

2019

Direct Visualization of Single Molecule Amyloid Beta Peptides in Action by High-Speed Atomic Force Microscopy

Lei Feng
University of Wollongong

Follow this and additional works at: <https://ro.uow.edu.au/theses1>

University of Wollongong

Copyright Warning

You may print or download ONE copy of this document for the purpose of your own research or study. The University does not authorise you to copy, communicate or otherwise make available electronically to any other person any copyright material contained on this site.

You are reminded of the following: This work is copyright. Apart from any use permitted under the Copyright Act 1968, no part of this work may be reproduced by any process, nor may any other exclusive right be exercised, without the permission of the author. Copyright owners are entitled to take legal action against persons who infringe their copyright. A reproduction of material that is protected by copyright may be a copyright infringement. A court may impose penalties and award damages in relation to offences and infringements relating to copyright material.

Higher penalties may apply, and higher damages may be awarded, for offences and infringements involving the conversion of material into digital or electronic form.

Unless otherwise indicated, the views expressed in this thesis are those of the author and do not necessarily represent the views of the University of Wollongong.

Recommended Citation

Feng, Lei, Direct Visualization of Single Molecule Amyloid Beta Peptides in Action by High-Speed Atomic Force Microscopy, Doctor of Philosophy thesis, Australian Institute for Innovative Materials, University of Wollongong, 2019. <https://ro.uow.edu.au/theses1/789>

Research Online is the open access institutional repository for the University of Wollongong. For further information contact the UOW Library: research-pubs@uow.edu.au



UNIVERSITY
OF WOLLONGONG
AUSTRALIA

Direct Visualization of Single Molecule Amyloid Beta Peptides in Action by High-Speed Atomic Force Microscopy

Lei Feng

Primary Supervisor: Prof. Michael Higgins

Co-supervisors: Dr Paul Molino, Prof. Gordon Wallace

This thesis is presented as part of the requirement for the conferral of the degree:

Doctor of Philosophy

University of Wollongong
Australian Institute for Innovative Materials

September 2019

Certification

I, Lei Feng, declare that this thesis, submitted in fulfilment of the requirements for the award of Doctor of Philosophy, at the Australian Institute for Innovative Materials, University of Wollongong, is wholly my own work except where specific references or acknowledgements are made. The thesis has not been submitted for a degree to any other university or institution.

Lei Feng

September, 2019

Preface

Publications

1. Feng, L., H. Watanabe, P. Molino, G.G. Wallace, S.L. Phung, T. Uchihashi, and M.J. Higgins, Dynamics of Inter-Molecular Interactions Between Single A β 42 Oligomeric and Aggregate Species by High-Speed Atomic Force Microscopy. *Journal of Molecular Biology*, 2019. 431(15): p. 2687-2699.
2. Kakinen, A., Y. Xing, N. Hegoda Arachchi, I. Javed, L. Feng, A. Faridi, A.M. Douek, Y. Sun, J. Kaslin, T.P. Davis, M.J. Higgins, F. Ding, and P.C. Ke, Single-Molecular Heteroamyloidosis of Human Islet Amyloid Polypeptide. *Nano Letters*, 2019.

Conference Proceedings

1. **Poster**: Visualizing the Kinetics of Amyloid Beta Peptide Interactions using High-Speed Atomic Force Microscopy. International Conference On Nano-medicine and Nanotechnology(ICONN), Wollongong.2018.01.29-02.02
2. **Oral**: Visualizing Amyloid Beta Peptide Dynamics using High-Speed Atomic Force Microscopy.8th International Nano-medicine Conference, Sydney.2017.07.03-05
3. **Oral**: Visualizing Amyloid Beta Peptide Dynamics using High-Speed Atomic Force Microscopy. The 8th Biennial Australia Colloid and Interface Symposium, Coffs Harbour. 2017.01.29-02.02
4. **Poster**: Visualizing the Kinetics of Amyloid Beta Peptide Interactions using High-Speed Atomic Force Microscopy International Electromaterials Science Symposium, Wollongong. 2017.02.08-02.10
5. **Poster**: “Watching” Protein-Conducting Polymer Interactions in Action using High-Speed AFM International Electro-materials Science Symposium, Wollongong 2015.02.11-02.13

Abstract

Alzheimer's disease (AD) has recently been labelled the 'twenty-first century plaque' and it has been estimated that more than 40 million people around the world suffer from this progressive disease. Within the amyloid hypothesis in Alzheimer's disease, current focus has shifted to earlier stages of amyloid beta ($A\beta$) peptide assembly, involving soluble oligomers and smaller aggregates that are more toxic to cells compared to their morphological distinct fibril forms. Critical to the $A\beta$ field is unlocking the molecular-level kinetic pathways or mechanisms of oligomerization, leading to the culprit subset or specific species of $A\beta$ oligomer populations responsible for the disease etiology. However, since the protein aggregation is highly dynamic, involving temporally and kinetically controlled processes, and also very difficult to monitor in the early stages, a key challenge is understanding dynamic $A\beta$ at the single molecule level under physiologically relevant conditions such as liquid.

Therefore, to probe the combined structural-dynamics of $A\beta$ peptides, High-Speed Atomic Force Microscope (HS-AFM) was used, as it enables direct observation of single molecules at sub-molecular spatial resolution and with time resolution of up to 50 milliseconds. For example, the main inventors of HS-AFM, Toshio Ando and his co-workers, produced real-time videos of the walking mechanism of a single Myosin V along an actin filament. Such movies existed before only as animations, but have now become reality due to the advent of HS-AFM. The thesis comprises 5 chapters, including introduction, 3 experimental and conclusion/future work.

In Chapter 1, we introduce and provide background to Alzheimer's disease and the evolution of hypothesis explaining the disease pathogenesis, including current hypothesis

focusing on the role of amyloid fibrils versus oligomers. This is followed by descriptions of the mechanisms and kinetics underlying the nucleation and growth of amyloid fibrils and oligomers, and a brief overview of current and treatments and therapies in Alzheimer's disease. Finally, we highlight current approaches for molecular level characterization of amyloid and its importance in understanding the disease.

In chapter 2, the molecular structures and dynamic diffusion of A β 42 peptides were characterized using HS-AFM and corresponding classification based on their structural dimensions demonstrated the presence of oligomer and larger aggregate species. In addition, based on HS-AFM movies, an analysis method was developed to quantify the kinetic parameters for interactions between the different A β species. The interactions between oligomers occurred more frequently, with binding consisting of a single exponential decay of lifetime at 0.55 ± 0.22 s for A β _{15-20nm} and 0.72 ± 0.28 s for A β _{36nm}, respectively. In contrast, the larger aggregates exhibited kinetic heterogeneity and could form long-lived, stable complexes. Inevitably, the latter may lead to the formation of different complexes or alloforms, which is known to contribute to difficulties in identifying A β oligomer toxicity and has implications for mechanisms underlying neuronal death accompanying Alzheimer's disease.

In chapter 3, the effect of different environmental factors such as peptide concentration, solution pH and incubation time on the A β morphology, dimensions and dynamics were investigated using samples prepared ex-situ. The effects of concentration and incubation time were minimal, whereas a decrease in solution pH was found to significantly accelerate the formation of intermediate aggregates. In-situ HS-AFM experiments involving changing the solution pH, i.e. changing from neutral to acidic conditions, during imaging to directly observe the real-time nucleation and growth of the A β oligomers and aggregates. A single molecule analysis approach based on HS-AFM was applied to quantify rate determining kinetic constants

of the different nucleating forms of A β . The findings revealed that assembly mechanisms of newly formed and existing peptides exhibited separate pathways during the nucleation processes.

In chapter 4, having characterized the morphology and dynamics of the A β peptides, their interactions with nanoparticles were investigated on the basis that the use of nanomaterials is an emerging approach to control the aggregation process, or even sequester the toxic species. Thus, as a model system, the dynamics and structural analysis of silica nanoparticles were characterized followed by a co-deposition with A β peptides to investigate silica nanoparticle-A β peptide interactions. Kinetic analysis showed that an increase in nanoparticle size caused a significant decrease in diffusion, which in turn led to an increase binding lifetime. The implications for the effect of nanoparticle size and diffusion on the kinetic analysis are discussed. Finally, Chapter 5 provides conclusions together with recommended directions for future work.

Acknowledgement

Undertaking this PhD has been a truly once-in-a-lifetime experience for me. I was lucky enough to have many of you, who gave me kind support, and helped on the path toward this dissertation.

Firstly, I would like to express my great appreciation to my supervisor, Professor Michael Higgins. Thank you for your motivating enthusiasm, endless patience and tireless encouragement. Thank you for the long-hours of chats on both research guidance and life. Thank you to my co-supervisor, Dr Paul Molino, for your great support, technical assistance and inspiration throughout the project. Thank you to Professor Gordon Wallace for the general advice and professional foresight of the research.

A special thanks to the Intelligent Polymer Research Institute (IPRI) for providing a prestigious research environment and funding support. I would like to express special thanks to (Chinese Scholarship Council) CSC for the sponsorship. I would like also to acknowledge Professor. Takayuki Uchihashi for providing me with technical advice on the HS-AFM instrument. Thanks to all the research visitors and collaborators I have been involved with, including Jessica Kretzmann, Arura Clayton and Aleksandr Kakinen.

To all the staff members and students in IPRI, I am grateful to have all of you in this journey and many thanks for your general help. Many thanks to my friends in IPRI, Dr Hongrui Zhang, Dr. Tian Zheng, Dr Yan Zong, Dr Christina Puckert, Dr Brianna Knowles, Mr. Alex Nagle, Ms Dan Yang, Ms Xinrui Zhang, Mr. Nuwan Hegoda Arachchi , Ms Buddhika Galagedarage Dona, Mr Shuai Zhang, Mr Yu Ge, Mr Chen Zhao, Mr Yong Zhao, Dr Jay Choi. It is a great memory and pleasure to work and play with you guys!

Last, but most important, thanks to my parents. Thanks for your support, both financial and emotional, your love and trust over the years.

Abbreviations

AD	Alzheimer's disease
ADDL's	A β -derived diffusible ligands
AFM	Atomic Force Microscopy
APP	Amyloid precursor protein
A β	Amyloid-beta
BBB	Blood brain barrier
BSA	Bovine serum albumin
C60	Fullerene
CD	Circular Dichroism
CGMD	Coarse grained molecular dynamics
Chels	Cholinesterase inhibitors
CNS	Central nerve system
DFS	Dynamic force spectroscopy
DPD	Dissipative particle dynamics
EGCg	Epigallocatechin-3-gallate
EA	Activation energy
EBD	Electron-beam deposition
FLIM	Fluorescence lifetime imaging microscopy

Fps	Frames per second
FTIR	Fourier transform infrared Spectroscopy
GAG	Glycosaminoglycan
HCl	Hydrochloric acid
HF488	Hilyte-Fluor 488
HFIP	1,1,1,3,3,3-hexafluoro-2-propanol
HMW	High molecular weight
HS-AFM	High speed-atomic force microscopy
KLVFF	16-20 residues, sequence of amyloid beta
K_e	Elongation rate constant
LMW	Low molecular weight
LTP	long-term potentiation
Met35	Oxidized Methionine-35 residue
MSD	Mean square displacement
MTT	3-(4,5-dimethylthiazol-2-yl)2,5-diphenyltetrazolium bromide
MW	Molecule weight
NaOH	Sodium hydroxide
NFTs	Neurofibrillary tangles
NMDA	N-methyl-d-aspartate
N-mers	Nucleus

PEGylated	Polyethylene glycol
PF	Protofibrils
PHFs	Paired helical filaments
PI3	Phosphatidylinositol-3-kinase
QLS	Quasielastic light scattering
RB	Rose Bengal
r.m.s	Root mean square
SEM	Scanning electron microscopy
SH3	SRC Homology 3 Domain
SiNP	Silica nanoparticle
SMFS	Single molecule force spectroscopy
SPs	Senile plaques
Ss-NMR	Solid-state nuclear magnetic resonance
T	Temperature
TTR	Transthyretin
TIRFM	Total Internal Reflection Fluorescence Microscopy
ThT	Thioflavin-T
TV3326	[(N-propargyl-(3R) aminoindan-5-y1)-ethyl methyl carbamate]
VMRI	Volumetric Magnetic Resonance Imaging
XRD	X-ray diffraction

k_{off} Disassociation rate constant

$\langle t \rangle$ Mean lifetime

Table of contents

Certification.....	2
Preface	3
Abstract.....	4
Acknowledgement	7
Abbreviations.....	9
Table of contents	13
List of Figures	16
List of Tables	23
List of Supplementary Movies	24
Chapter 1: Introduction	26
1.1 Neurodegenerative and Alzheimer’s disease	26
1.2 Pathogenic Hallmarks of AD.....	26
1.2.1 Senile plaques and neurofibrillary tangles.....	26
1.2.3 A β cascade hypothesis.....	29
1.2.4 ADDL’s hypothesis.....	31
1.3 Pathways of A β assembly	34
1.3.1 Kinetics of oligomer and fibril formation.....	34
1.3.2 Nucleation mechanisms of amyloid formation.....	36
1.3.3 Effect of A β state on the pathway of aggregation.....	39
1.3.4 Effects of environmental conditions.....	41
1.4 Current treatments and clinical therapies.....	44
1.4.1 Cholinesterase inhibitor treatments.....	44
1.4.2 Anti-amyloid therapies.....	45
1.4.3 Metal ions	47
1.4.4 Multi-target directed compounds.....	48
1.5 Alternative strategies.....	49
1.5.1 Nanoparticles (NPs).....	49
1.5.2 Nanomaterials.....	51
1.5.3 Photoexcitation Effects	52
1.5.4 Electrical Stimulation: A new paradigm for therapy.....	52

1.6 Molecular characterization of A β	53
1.6.1 Structural measurements	54
1.6.2 Fluorescence spectroscopy	59
1.7 High-Speed AFM: Combined Structural-Dynamics of A β Interactions	62
1.8 Overarching Aims	68
Chapter 2: Dynamics of Inter-Molecular Interactions between Single A β_{42} Oligomeric and Aggregate Species by HS-AFM	70
2.1 Introduction	70
2.2 METHODS	73
2.2.1 Preparation of A β solutions and reagents	73
2.2.2 Remodification of HS-AFM Cantilever Tips	73
2.2.3 High-Speed Atomic Force Microscopy (HS-AFM) imaging in liquid	74
2.2.4 Data analysis of HS-AFM images	74
2.3 Results/Discussion	77
2.3.1 Structural Dimensions of Different A β_{42} Species	77
2.3.2 Surface Diffusion and Interactions of Different A β_{42} Species	84
2.3.3 Kinetic Parameters of Single Molecule A β_{42} Binding	88
2.4 Conclusions	92
Chapter 3: Visualizing Real-Time Nucleation and Growth Mechanisms of Single A β_{42} Oligomers	94
3.1 Introduction	94
3.2 Materials and Methods	99
3.2.1 Preparation of A β_{42} samples	99
3.2.2 High-Speed Atomic Force Microscopy	99
3.2.3 Statistics analysis	101
3.3 Results/Discussion	102
3.3.1 Ex-situ A β : Effect of concentration, incubation time and pH	102
3.3.2 In-situ amyloid beta nucleation process	107
3.4 Conclusion	116
3.4.1 Factors in ex-situ: concentration, pH and incubation time govern the aggregation of A β peptides	116
3.4.2 In-situ amyloid nucleation process A β	117
Chapter 4: Molecular Interactions between A β peptide and Silica Nanoparticles Visualized by HS-AFM	121
4.1 Introduction	121
4.2 Materials and Methods	125
4.2.1 Preparation of A β_{42} and Silica Nanoparticle Samples	125

4.2.2 HS-AFM Imaging/ Data analysis	125
4.3 Result and Discussion.....	127
4.3.1 Silica nanoparticles (SiNP).....	127
4.3.2 Imaging of Co-deposited SiNP - A β ₄₂	128
4.3.3 Diffusion of SiNP and A β Comparison.....	132
4.3.4 Interactions and Kinetics of Co-deposited SiNP - A β ₄₂	135
4.4 Conclusion.....	137
Chapter 5: Conclusion and Outlook	143
5.1 Conclusions	143
5.2 Outlook	145
Chapter 6: Appendix	147
Chapter 7: Reference	154

List of Figures

Figure 1. 1. Ultrastructure of neurofibrillary tangles formed by paired helical filaments. (A) Longitudinal sections of filaments. $1.5 \mu\text{m} \times 1.0 \mu\text{m}$ (B) filaments cut in cross section. $3.75 \mu\text{m} \times 2.50 \mu\text{m}$ [15].	28
Figure 1. 2 Early amyloid cascade hypothesis. The APP produced mainly via 2 ways: (i) APP is first cleaved at residues 15-17 by the APP ‘secretase’. This cleavage event produces fragments that can not form to amyloid deposition. (ii) Several studies suggested that APP can also processed by the endosomal- lysosomal pathway, in which the entire A β P sequence and in further the amyloid deposition are formed. Eventually these deposition lead to the neurofibrillary tangles and cell death [32].	29
Figure 1. 3. TEM and AFM images of oligomeric and fibrillar A β_{40} , A β_{42} . TEM images of A β_{40} , A β_{42} fibrils were acquired through prolonged incubation in PBS under stagnant conditions. Scale bar is 200nm. AFM Images were recorded in $2 \mu\text{m} \times 2 \mu\text{m}$ contact mode with oligomers formed in Tris-buffered saline (TBS) after 24 h and tapping mode with fibrils formed in 10 mM HCl after 24h [33, 34].	30
Figure 1. 4. Different A β_{42} assemblies. (A) TEM images of Amylospheroids formed in A β_{42} solution (0.1 μM in 50% PBS) after an 8h slow rotation, scale bar 20nm. (B) AFM images of A β_{42} annular structured assemblies, the inset represents a $50 \times 50 \text{nm}$ topography image of annular assemblies. (C) AFM image of toxic globular oligomers of A β_{42} (ADDLs) [67-69].	32
Figure 1. 5. Diagram of ADDLs hypothesis shows all the elements involved with AD [77].	33
Figure 1. 6. Schematic of the nucleation-dependent polymerization model of A β aggregation. It reveals two phases are revealed during the amyloid aggregation: (i) the nucleation phase/lag phase, in which monomers undergo conformational changes/misfolding and consequently form oligomeric nuclei, (ii) the elongation phase/ growth phase, in which the nuclei rapidly grow by additional monomers to form larger aggregates or fibrils eventually [6].	35
Figure 1. 7. A simple scheme shows the kinetic curve for amyloid formation above barely the crucial concentration C_R [87].	36
Figure 1. 8. Kinetics of different pathways underlying the amyloid formation. (a) Primary nucleation from monomers, (b) Elongation by addition of monomers to existing aggregates. The secondary nucleation shows the combination of both monomeric and aggregated species and finally the fibrils formed at fragmentation stage. (c) Monomer-dependent secondary nucleation from monomers on	

surface of fibrils or aggregates. (d) monomer-independent fragmentation. All the monomers are coloured in green while the aggregates or fibrils are coloured blue [99]..... 37

Figure 1. 9. Measurement of oligomers populations with radiolabelling method and cell viability assays. (A) Samples of monomers and monomers mixed with preformed fibrils were incubated followed by size-exclusion chromatography and liquid scintillation counting. The numbers of oligomers fractions are shown below. (no fibrils for light blue bar and added fibrils for dark blue bar) (B) Probing the chromatography fractions with antibodies further confirms the enhanced production of small oligomers in the presence of fibril. Time $\Delta t_1=24$ mins. (C) Measurement of reduced cell viability for reactions without (light blue bars) and with (dark blue bars) a small concentration of added fibrils under the same conditions as in A and after filtration through a 200-nm filter. Values are averages over nine measurements at $\Delta t_2 =5, 6, 7$ mins. Grey bars represent initial monomers and end fibrils reaction time points. (D) Comparison of kinetic measurement between two conditions. The rapid increase in the slope with added fibrils (dark blue) and consequent shorter lag time suggest the rapid formation of new aggregates through secondary nucleation [100]..... 38

Figure 1. 10. Amyloid state and its relationship with the structure and conformation of the proteins. The amyloid structure is highly affected by the amyloid state. It is believed that peptides or some large fragments are natively unfolded structure and eventually formed amyloid fibrils that are rich in β - sheet structure. During the whole aggregation process, the different states corresponds to various structures [102]..... 40

Figure 1. 11. Arrhenius plot shows the temperature dependent fibril formation [111]. 41

Figure 1. 12. The effect of pH on the fibril formation of $A\beta_{42}$, as a function of rate constant of fibril formation. The aggregation of $5\mu\text{M}$ wild-type (\bullet), H6A (\square), H13A (\square) or H14A (Δ) mutant of $A\beta_{42}$ in 20mM ammonium acetate, 100mM NaCl with continuous agitation in the presence of $3.3\mu\text{M}$ ThT at 25°C at different pH values [112]. 43

Figure 1. 13. Effects of pH 5.8 and pH 7.4 $A\beta_{42}$ aggregates on the viability of PC12 cells. Aliquots from pH 7.4 (\blacktriangle) or pH 5.8 (\blacklozenge) $A\beta_{42}$ aggregates or the non-aggregates (\square) were incubated with PC12 cells for 48h and the cell viability assay was conducted by MTT inhibition method [120]. 43

Figure 1. 14. Cu^{2+} accelerates $A\beta$ growth and increases the cytotoxicity. (a) Average of 9 growth curves recorded Apo in red and Cu^{2+} in blue. The fluorescence ThT signal is normalized at maximal intensity. $A\beta_{40}$ concentrated at $5\mu\text{M}$, HEPES buffer 50mM, 160mM NaCl at 30°C . (b) Time to reach half-maximal fluorescence (t_{50}) in two experiments with 0 (red), 1 (mid-blue) or 0.5 (dark blue) mole equivalents of Cu^{2+} ions. The presence of Cu^{2+} typically halves the time taken to form fibrils. Error bars are for standard from nine traces. (c) Cell viability comparison [151]. 48

Figure 1. 15. Schematic illustration of the inhibition of $A\beta$ aggregation by photo-excited RB [175].. 52

Figure 1. 16. Schematic of the electro-cell. This purpose build cell is used to measure the real-time auto-fluorescence and circular dichroism of the protein solution exposed to electric fields of differing strength and frequency [179].	53
Figure 1. 17. Structure of native protein transthyretin (TTR) and TTR amyloid fibrils.(A) Amide I region from the FTIR spectrum of native TTR. (B) Ribbon diagram of native TTR tetramer.(C) Amide I region from the FTIR spectrum of TTR fibrils. (D)Electron Microscopy (EM) images of TTR fibrils [184].	55
Figure 1. 18. Atomic Force Microscopy images of standard prepared ADDLs (A), mature fibrils (B)and highly magnified part of the fibrils along with an ADDL subunit (C). All the samples were imaged in air using tapping mode [185].	56
Figure 1. 19. (a)-(c) AFM images of A β ₄₂ peptides and (d)-(f) proposed models of the A β ₄₂ monomer, dimer and tetramer [186]. Image scan size: 150 nm *150 nm	56
Figure 1. 20. (a) AFM images of time dependence of A β ₄₀ proto-fibril assembly at(scale bar:500nm*500nm) 2, 7 and 18 days. (b) AFM images show the temperature dependence of A β ₄₀ proto-fibril assembly. Scale bar: 1000*1000nm [187].	57
Figure 1. 21. (i) A series of AFM images depicting the development of multiple A β proto-fibril from a common core. Imaging scan size 2.5 μ m*2.5 μ m.(ii) A schematic outlining a possible mechanism for the fibrillization of A β [188].	58
Figure 1. 22. Experimental techniques employing ThT. (a) Structure of ThT (top). The two planer segments of ThT whose mutual rotation defines its chirality (bottom). (b) Early histology using Thioflavin-T to stain primary kidney amyloid. (c) Total Internal Reflection Fluorescence microscopy (TIRFM) image of branched glucagon fibrils stained with ThT. (d) Characteristic increase in ThT fluorescence upon binding to amyloid fibrils.(e) Protein concentration effects on the fibrillization kinetics measured by ThT fluorescent. The rapid onset of fibrillization induced through seeding is also shown [190-193].	60
Figure 1. 23. (A)Time-course of fibril formation at pH 7.5 and 37°C monitored using ThT fluorescence. (B) Observation of A β (1-40) amyloid fibril growth by TIRFM [194].	61
Figure 1. 24. Kinetics of HF488-labeled A β ₄₀ Fibril Formation Monitored by Fluorescence Lifetime Imaging. The colour coding of images and histograms relate to the colour bar on the right. The HF488-labeled A β ₄₀ concentration was 5 μ M, and the peptide was diluted into 50 mM phosphate buffer sodium at pH 7.4 [195].	62
Figure 1. 25. Schematic illustration showing HS-AFM system and devices. (a) All devices contained in the HS-AFM system and main devices like different functional scanners, the stage designed for sample	

and cantilever, and piezo control platform. (b) SEM image of a small cantilever for HS-AFM. The inset shows an electron beam deposited tip grown on the original tip. (c) An advanced scanner designed for narrow scanning area imaging [203]..... 64

Figure 1. 26. Visualization of walking M5-HMM molecules. (a) HS-AFM film strip showing unidirectional processive movement of M5-HMM in $1\mu\text{M}$ ATP. Scan size: $130 \times 65 \text{ nm}^2$, scale bar: 30 nm. (b) Schematic of two-headed bound M5-HMM (c) Schematic of the movement explanation in d and e.(d)(e) HS-AFM film strips showing the hand-over-hand movement in $1\mu\text{M}$ ATP. (d) Scan size: $150 \times 75 \text{ nm}^2$, scale bar: 50 nm (e) Scan size: $130 \times 65 \text{ nm}^2$, scale bar: 30 nm. All the images showing here are captured at scan rate: 146.7ms per frame [223]. 66

Figure 1. 27. HS-AFM imaging of $\text{A}\beta_{42}$. (A) Schematic diagram of HS-AFM measurement including HS-AFM cantilever, sample ($\text{A}\beta_{42}$ fibrils and intermediates) and substrate mica. (B) Clipped HS-AFM images at different time point during the fibrils growth. (Scale bar, 300nm) (C) Height profile of selected part of the fibrils as labelled (A to B) at 1800s [224]..... 67

Figure 2. 1. Morphology and dimensions of $\text{A}\beta_{42}$. (a) Representative HS-AFM image of $\text{A}\beta$ species on mica surface in PBS (Scan size: 500nm, imaging rate: 2frames/second). (b-e) Histograms of dimensions, area (b), height (c), width (d) and length (e). (f) Representative HS-AFM images (from left to right) of $\text{A}\beta_{15-20\text{nm}}$, $\text{A}\beta_{36\text{nm}}$, $\text{A}\beta_{\text{Agg}}$ and disordered or unstructured $\text{A}\beta$ monomer. 78

Figure 2. 2. Scatter plots of different dimensions, width (a) length (b), height (c), versus area of $\text{A}\beta$ species..... 82

Figure 2. 3. Filmstrip from HS-AFM movies showing the diffusion of individual $\text{A}\beta_{15-20\text{nm}}$ (a), $\text{A}\beta_{36\text{nm}}$ (b), and $\text{A}\beta_{\text{Agg}}$ (c) molecules. In each filmstrip, the solid coloured circle delineates the current frame position of the individually tracked $\text{A}\beta_{42}$ species, while dashed circles denote the series of positions from the previous frames. (Imaging rate: 2frames/second) 84

Figure 2. 4. MSD versus time plot of individually tracked $\text{A}\beta_{15-20 \text{ nm}}$ (black), $\text{A}\beta_{36 \text{ nm}}$ (red) and $\text{A}\beta_{\text{Agg}}$ (blue) molecules. $\text{MSD} = \langle |r(t) - r(0)|^2 \rangle$, where $\langle \rangle$ means the average, $r(t)$ is the position of each molecule in determined time t , $r(0)$ is the reference position of each molecule. (b) Average diffusion coefficient of $8.7 \pm 0.44 \text{ nm}^2 \text{ s}^{-1}$ ($\text{A}\beta_{15-20 \text{ nm}}$), $1.1 \pm 0.06 \text{ nm}^2 \text{ s}^{-1}$ ($\text{A}\beta_{36 \text{ nm}}$) and $0.4 \pm 0.01 \text{ nm}^2 \text{ s}^{-1}$ ($\text{A}\beta_{\text{Agg}}$) obtained by fitting slopes in panel a. Errors are standard deviation, $n = >10$ molecules. 86

Figure 2. 5. Filmstrip from HS-AFM movies showing (a) sequence of interactions between $\text{A}\beta_{15-20\text{nm}}$ (1 and 2) and $\text{A}\beta_{\text{Agg}}$ (3) involving binding of $\text{A}\beta_{15-20\text{nm}}$ (2) on top of $\text{A}\beta_{\text{Agg}}$ (3) (stacking to form complex 2 + 3). (b) Continuation of sequence in (a) showing formation of elongated structure due to interactions of $\text{A}\beta_{15-20\text{nm}}$ (1 and 4) with complex (2 + 3). Scale bar:25nm. Imaging rate: 5frames/s..... 87

Figure 2. 6. Single molecule kinetics data analysis based on HS-AFM. (a-c) HS-AFM filmstrips showing interactions between (a) $A\beta_{15-20nm}$ - $A\beta_{Agg}$, (b) $A\beta_{15-20nm}$ - $A\beta_{36nm}$, and (c) $A\beta_{15-20nm}$ - $A\beta_{15-20nm}$. Molecules in contact (green 'on) are in the bound state. Imaging rate: 5frames/s. (d-e) Representative traces of single molecule lifetimes. (g-i) Life-time distributions for the bound state of (g) $A\beta_{15-20nm}$ - $A\beta_{Agg}$, (h) $A\beta_{15-20nm}$ - $A\beta_{36nm}$, and (i) $A\beta_{15-20nm}$ - $A\beta_{15-20nm}$. Distributions in (h) and (i) are fit to a single exponential decay..... 89

Figure 3. 1. Morphology and structural dimensions of different concentration $A\beta_{42}$ peptides. (A-C) Representative HS-AFM image of 20ug/ml, 50ug/ml and 100ug/ml concentrated $A\beta_{42}$ peptides diffuse on the surface of mica. (Scan scale: 500*500nm, imaging rate: 1frame/second. (a-f) Histograms of different structural dimensions distributions. Area (a, c, e), Height (b, d, f). (g-i) Scatter plots of area and height shows their relationship..... 104

Figure 3. 2. Morphology and structural dimensions of different incubation time $A\beta_{42}$ peptides. (A-C) Representative HS-AFM image after 1h, 2h and 4h incubation of $A\beta_{42}$ peptides diffuse on the surface of mica. (Scan scale: 500*500nm, imaging rate: 1frame/second. (a-f) Histograms of different structural dimensions distributions. Area (a, c, e), Height (b, d, f). (g-i) Scatter plots of area and height shows their relationship..... 106

Figure 3. 3. Morphology and structural dimensions of $A\beta_{42}$ peptides incubated in different pH solution. (A-C) Representative HS-AFM image of $A\beta_{42}$ peptides diffuse on the surface of mica in different pH solution. (Scan scale: 500*500nm, imaging rate: 1frame/second. (a-f) Histograms of different structural dimensions distributions. Area (a, c, e), Height (b, d, f). (g-i) Scatter plots of area and height shows their relationship..... 107

Figure 3. 4. In-situ $A\beta_{42}$ peptides nucleation process at pH 3. (a) HS-AFM Film strip shows the morphology of $A\beta_{42}$ diffusion on mica surface before the Spike (neutral condition, pH 7.4 20ug/ml), nucleation stage between spike and growth stage and the stable growth stage after the rapid nucleation process. Scale bar: 50nm. Imaging rate: 2frame/sec. (b) $A\beta_{42}$ peptide numbers distribution among different stages. (c) Surface roughness of $A\beta_{42}$ on mica surface (d) Average height of $A\beta_{42}$ peptides distribution (e) Average Size of $A\beta_{42}$ peptides..... 111

Figure 3. 5. In-situ $A\beta_{42}$ peptides nucleation process in alkaline condition. (a) HS-AFM Film strip shows the morphology of $A\beta_{42}$ diffusion on mica surface before the Spike (neutral condition, pH 7.4 20ug/ml), spike and growth stage. Scale bar: 50nm. Imaging rate: 2frame/sec. (b) $A\beta_{42}$ peptide numbers distribution among different stages. (c) Surface roughness of $A\beta_{42}$ on mica surface. 112

Figure 3. 6. HS-AFM film strip shows the size and position changes of existing peptides appear all the time (dash black circle number 1,2 and 3 as labelled) and newly formed peptides only appeared after the Spike (dash red circle number 4,5,6 and 7 as labelled)..... 114

Figure 3. 7. The tracking size and height of existing peptides and newly formed peptides. (a)(b) Representative existing peptides of number 1,2 and 3 shows the size and height changes with the time growing. (c)(d) Representative newly formed peptides of number 4, 5 and 6 shows the size and height changes with the time growing. 115

Figure 4. 1. Morphology and structural dimensions of Silica Nanoparticles. (a) Representative HS-AFM image of Silica Nanoparticles diffuse on the surface of mica. (Scan scale: 500*500nm, imaging rate: 1frame/second) Histograms of different structural dimensions distributions Area (b), Height (c), Width (d) and Length (e) of Silica Nanoparticles.(f) Spherical and string morphology of various structural silica nanoparticles..... 128

Figure 4. 2. HS-AFM film strips shows the morphology of silica nanoparticles diffusion on mica surface before the Spike and the co-existing phase of nanoparticles and peptides after Spike. Scale bar: 50nm. Imaging rate: 1frame/sec..... 129

Figure 4. 3. In-situ spiking process that silica nanoparticles interacting with Aβ₄₂ peptides. (a) Numbers distribution of Silica nanoparticles co existing with Aβ₄₂ peptides among different stages. (i) Only silica nanoparticles, (ii) silica nanoparticles and Aβ₄₂ peptides.(b) Surface roughness of silica nanoparticles on mica (c) Surface roughness of silica nanoparticles with injected Aβ₄₂ peptides. ... 130

Figure 4. 4. Statistical analysis before and after the spike. (a)(b)(c)Representative snapshots of HS-AFM showed pure silica nanoparticles on mica and silica nanoparticles co existing with amyloid-beta peptides. Dimensions comparison among peptides, silica nanoparticles and co existing complexes. (d)(e)(f)(g) represent for Length, Width , Height and Area respectively, errors are standard deviation. 132

Figure 4. 5. (a) Mean square displacement (MSD)verse time plot of individual tracked nanoparticles with different size. $MSD = \langle |r(t) - r(0)|^2 \rangle$, where $\langle \rangle$ means the average, $r(t)$ is the position of each particle in determined time t , $r(0)$ stands for the reference spot of each particle. $n \Rightarrow 30$. Black line represents for the size of particles is less than 12nm, red line shows particles range with 12-18nm and blue line stands for particles larger than 18nm. (b) Diffusion Co-efficient scatters of different size particles fitted by nonlinear curve fit (red line for Asymptotic1 fitting). 133

Figure 4. 6. Dynamics and Interactions between silica nanoparticles.(a)HS-AFM film strip showed binding processes between a small particle (no.1) and a relative large one(no.2).(b)HS-AFM filmstrip

showed representative interaction processes between two similar size particles. Scale bar:25nm, 5frames/sec. (c) A representative figure showing the time ‘on’and ’off’ state, where number 1 refers to a binding state while number 0 refers to an unbound state. (d)Lifetime distributions for the bound state of particles with size range around 12nms. Distribution is fit to a single exponential decay (e) The binding time ‘on’ within the interactions versus the size of active nanoparticles. Distribution is fit to a polynomial order 2 curve. 134

Figure 4. 7. Dynamics and interactions between silica nanoparticles and peptides.(a)Representative HS-AFM filmstrip shows the process between single Aβ42 peptide and nanoparticle. Scale bar: 25nm. Scan rate :2frames/sec. (b) Diffusion Co-efficient of silica nanopartilces and Aβ42 peptides with similar size. Green (Aβ42)and red (Nps)lines are fit by nonlinear curve fit (Asymptotic1).(c)Comparison of the diffusion ability among single nps, Aβ42 peptides and the mixture of both. Average diffusion co-efficient of 0.46±0.1 nm²/s (nps),7.95±1.94 nm²/s (Aβ42)and 2.05±0.4 nm²/s (mixture).Errors are standard deviation. N=>20 molecules.(d)Lifetime distributions for the bound state between particles and Aβ42 peptides with similar size around 12nms. Detailed information is shown in Table 4. 1 ... 136

Figure A1. Length histogram of the Aβ peptides. we have an inset figure specifically for the length greater than 40nm to illustrate that some unstructured species normally have transient structure with unique higher values of ~up to 100nm..... 147

Figure A2. AFM cross-sectional analysis show how we track the dynamics and measure the structural dimension of these less well structured Aβ₄₂ species..... 148

Figure A3. Relationship between length and width shows a linear correlation. 149

Figure A4. Image line profile of cross-section on individual molecules. Represent three single peptides appearing on mica surface and present dynamic changes on the lateral dimensions as well as the height. 150

Figure A5. Morphology and structural dimensions of Silica Nanoparticles and amyloid-beta42 peptides injection during the first five minutes. (a) Representative HS-AFM image of Silica Nanoparticles and peptide diffusion on the surface of mica. (Scan scale: 500*500nm, imaging rate: 1frame/second) Histograms of different structural dimensions distributions Area (b), Height (c), Width (d) and Length (e) of Silica Nanoparticles and peptides. 151

Figure A6. Morphology and structural dimensions of Silica Nanoparticles and amyloid-beta42 peptides injection after 30 minutes. (a) Representative HS-AFM image of Silica Nanoparticles and peptides diffuse on the surface of mica. (Scan scale: 500*500nm, imaging rate: 1frame/second) Histograms of different structural dimensions distributions Area (b), Height (c), Width (d) and Length (e) of Silica Nanoparticles and peptides 151

List of Tables

Table 1. 1. Current treatments and approved therapies available for AD [133].	45
Table 1. 2. Some NPs proposed for the treatment of Alzheimer's disease [168].	50
Table 1. 3. Studies on the dynamic events of proteins by using HS-AFM.	65
Table 2. 1. Summary of properties of different A β species	91
Table 4. 1. Individual silica nanoparticles interactions	140
Table 4. 2. Table for silica nanoparticle binding associated with size	141
Table 4. 3. Table for interaction between peptides and silica nanoparticles	142

List of Supplementary Movies

S 1. HS-AFM movie of A β ₄₂ species diffusing on the mica surface. Scan size 500*500nm, scan rate 2frame/sec. x5 video playing speed.	152
S 2. HS-AFM movie of A β ₄₂ species fast diffusing and capturing transient structured species.	152
S 3. HS-AFM movie of A β _{15-20nm} diffusing and tracking processes. Dash line refers to the original position and solid line represent the current position.	152
S 4. HS-AFM movie of A β _{36nm} diffusing and tracking processes. Dash line refers to the original position and solid line represent the current position.	152
S 5. HS-AFM movie of A β _{agg} diffusing and tracking processes. Dash line refers to the original position and solid line represent the current position.	152
S 6. HS-AFM movie of whole processes of dynamic interactions between different A β species. The mechanism that elongation and stacking of the peptides assembly also revealed during the process.	152
S 7. HS-AFM movie of interaction process between A β _{15-20nm} and A β _{agg} . Dash line refers to the original position and solid line represent the current position.	152
S 8. HS-AFM movie of interaction process between A β _{15-20nm} and A β _{36nm} . Dash line refers to the original position and solid line represent the current position.	152
S 9. HS-AFM movie of interaction process between A β _{15-20nm} and A β _{15-20nm} . Dash line refers to the original position and solid line represent the current position.	152
S 10. HS-AFM movie of 50 μ g/ml A β ₄₂ species diffusing on the mica surface. Scan size 500*500nm, scan rate 2frame/sec.	152
S 11. HS-AFM movie of 100 μ g/ml A β ₄₂ species diffusing on the mica surface. Scan size 500*500nm, scan rate 1frame/sec.	152
S 12. HS-AFM movie of 20 μ g/ml A β ₄₂ species diffusing on the mica surface after 2hours incubation in pH 7. Scan size 500*500nm, scan rate 1frame/sec.	152
S 13. HS-AFM movie of 20 μ g/ml A β ₄₂ species diffusing on the mica surface after 4hours incubation in pH 7. Scan size 500*500nm, scan rate 1frame/sec.	152
S 14. HS-AFM movie of 20 μ g/ml A β ₄₂ species diffusing on the mica surface after 1hours incubation in pH 3. Scan size 500*500nm, scan rate 1frame/sec.	152
S 15. HS-AFM movie of 20 μ g/ml A β ₄₂ species diffusing on the mica surface after 1hours incubation in pH 11. Scan size 500*500nm, scan rate 1frame/sec.	152
S 16. HS-AFM movie of 20 μ g/ml A β ₄₂ species diffusing on the mica surface after 2hours incubation in pH 3. Scan size 500*500nm, scan rate 1frame/sec.	152
S 17. HS-AFM movie of 100 μ g/ml A β ₄₂ species diffusing on the mica surface after 4hours incubation in pH 3. Scan size 500*500nm, scan rate 1frame/sec.	152
S 18. HS-AFM movie of 100 μ g/ml A β ₄₂ species diffusing on the mica surface after 20hours incubation in pH 3. Scan size 500*500nm, scan rate 1frame/sec.	152
S 19. HS-AFM movie of 20 μ g/ml A β ₄₂ species diffusing on the mica surface after spike, inducing decreased solution pH from 7.0 to 3.0. Scan size 500*500nm, scan rate 1frame/sec.	152
S 20. HS-AFM movie of 20 μ g/ml A β ₄₂ species diffusing on the mica surface after spike, inducing increased solution pH from 7.0 to 11.0. Scan size 500*500nm, scan rate 1frame/sec.	152
S 21. HS-AFM movie of no.3 peptide nucleation processes after spike. Scale bar 20nm. Scan rate 5frames/sec.	152

S 22. HS-AFM movie of no.4 peptide nucleation processes after spike. Scale bar 22nm. Scan rate 5frames/sec.	152
S 23. HS-AFM movie of no.5 peptide nucleation processes after spike. Scale bar 18nm. Scan rate 5frames/sec.	153
S 24. HS-AFM movie of silica nanoparticles diffusing on mica. Scan size 500*500nm, scan rate 1frame/sec.	153
S 25. HS-AFM movie of silica nanoparticles diffusing on mica. Scan size 500*500nm, scan rate 1frame/sec.	153
S 26. (1)(2) HS-AFM movie of in-situ interactions between silica nanoparticles and injected A β ₄₂ peptides. Scan size 500*500nm, scan rate 1frame/sec.	153
S 27. HS-AFM movie of in-situ interactions between silica nanoparticles and injected A β ₄₂ peptides. Scan size 500*500nm, scan rate 1frame/sec.	153
S 28. HS-AFM movie of single molecular interactions between silica nanoparticles. Scan size 250*150nm, scan rate 5frames/sec.	153
S 29. HS-AFM movie of single molecular interactions between silica nanoparticles and A β ₄₂ peptides. Scan size 100*100nm, scan rate 2frames/sec.	153

Chapter 1: Introduction

1.1 Neurodegenerative and Alzheimer's disease

Neurodegenerative diseases such as Alzheimer's disease, Parkinson's disease and Huntington's disease are major threats to human health and welfare in the modern world [1-5]. Aberrant folding and abnormal accumulation of proteins in the brain are increasingly being realised as the major pathological hallmarks of these neurodegenerative disorders [6, 7]. Alzheimer's disease (AD) is an irreversible, progressive neurodegenerative disorder that destroys people's memory, reduces their ability to perform daily activities and even affects their personality. It represents the most common progressive disease and is the leading cause of dementia in the elderly, currently affecting more than 40 million people around the world [8]. It was first identified by Dr. Alois Alzheimer more than 100 years ago, with common clinical symptoms including memory loss and cognitive and functional abilities decline that are believed to contribute to the cause of death in AD.

1.2 Pathogenic Hallmarks of AD

1.2.1 Senile plaques and neurofibrillary tangles

In AD, the accumulation of amyloid-beta ($A\beta$) peptide outside of neurons is believed to contribute to the formation of senile plaques and accumulation of unusual protein tau inside neurons, referred as the tangles. These protein structures were first observed in 1901 by Dr. Alois Alzheimer who detected neurofibrillary tangles and senile plaques in the brain of a patient by using the silver impregnation method [9-13]. However, it was only after the late 1960s when newly emerging tools of research, i.e. electron microscopy (EM), were developed

that the observation of these proteins in the brain of patients with AD started to progress further. For example, Kidd et al. [14] visualized the ultrastructure of neurofibrillary tangles formed by paired helical filaments in 1963 and Terry et al. [15, 16] captured the senile plaques with a core of amyloid fibrils in 1964 as shown in Figure 1. 1. Quantitative measurements regarding the relationship between the degree of dementia and the number of plaques or tangles in each cortex were also examined by comparing the brains of diseased and healthy patients in vivo [17, 18]. These early studies provided a clear identification for the two abnormal proteins (A β and tau) and basis for the development of the molecular pathogenesis of AD. The brain changes associated with AD mentioned above significantly affect the communication between neurons and lead to the neuron cell death [19-21]. In these cases, eventually, the brains of people with advanced AD dramatically shrink due to the cell loss and corresponding synaptic loss, which is believed associating with the toxic species of A β peptide.

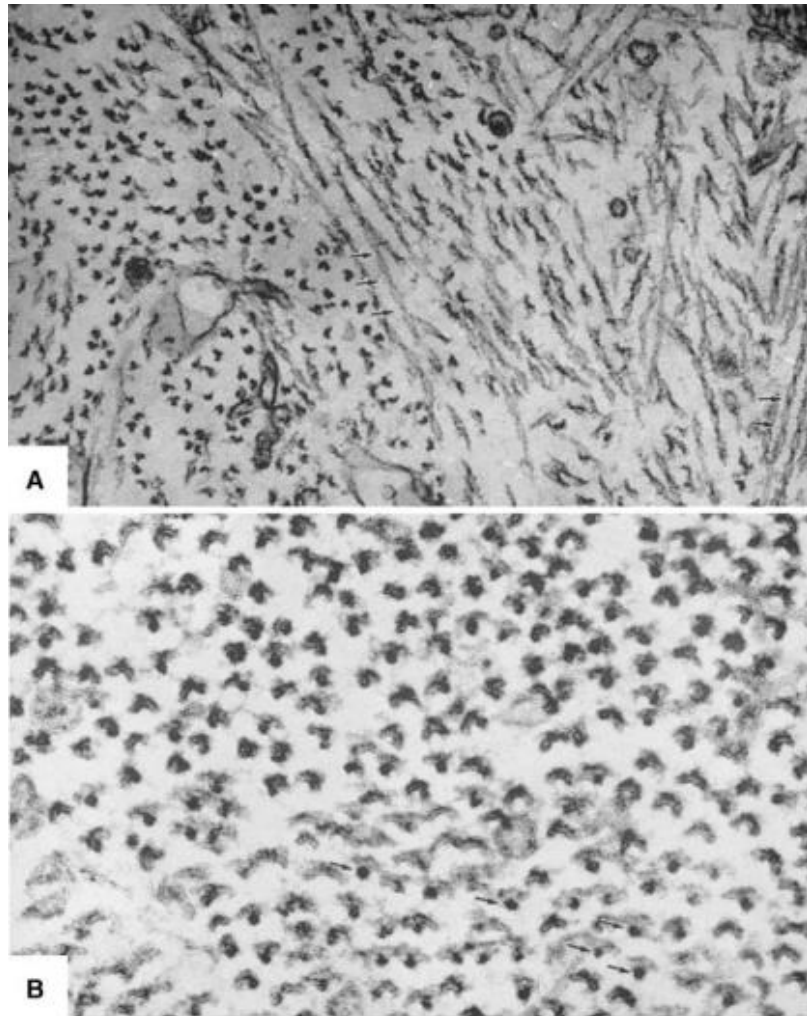


Figure 1. 1. Ultrastructure of neurofibrillary tangles formed by paired helical filaments. (A) Longitudinal sections of filaments. $1.5 \mu\text{m} \times 1.0 \mu\text{m}$ (B) filaments cut in cross section. $3.75 \mu\text{m} \times 2.50 \mu\text{m}$ [15].

Together with the emerging role of the cholinergic system (i.e. neurotransmitter acetylcholine signalling in neurons) in memory and learning, the first cholinergic hypothesis of AD was established more than thirty years ago according to findings of a strong correlation between cholinergic abnormalities and the numbers of plaques and tangles [22-26]. According to this hypothesis, the cognitive dysfunction behaviour related to AD is attributed to the decline in cholinergic neurotransmission [27], which indicated that drugs like cholinesterase inhibitors could potentially be used for treatment against the disease, however, the therapeutic treatments were proven to only be able to relieve temporary symptoms in AD [28-31].

Since these early observations, the field has largely been built on a few main hypothesis. Over the years, the amyloid cascade hypothesis has been pursued extensively though this has been more recently challenged by the hypothesis involving soluble A β protein assemblies such as A β -derived diffusible ligands (ADDL's) [32, 33].

1.2.2 A β cascade hypothesis

Progress in the diagnosis of AD during the last 30 years has culminated in the amyloid-cascade hypothesis that describes the etiologic and pathogenic mechanisms of AD. This hypothesis is explained by the excessive deposition of A β peptides in the form of extracellular plaques, as well as neurofibrillary tangles in the brain. To initially produce the abhorrent A β peptide, the modification of the A β precursor protein (APP) is thought to occur via 2 pathways (Figure 1. 2) [34]. In the first pathway, the APP is cleaved by β -secretase and then followed by γ -secretase cleavage though this pathway does not result in formation of amyloid. Alternatively, cleavage by lysozyme in the endosomal-lysosomal compartment results in formation of A β peptide that is believed to accumulate to form the amyloid plaques and tangles.

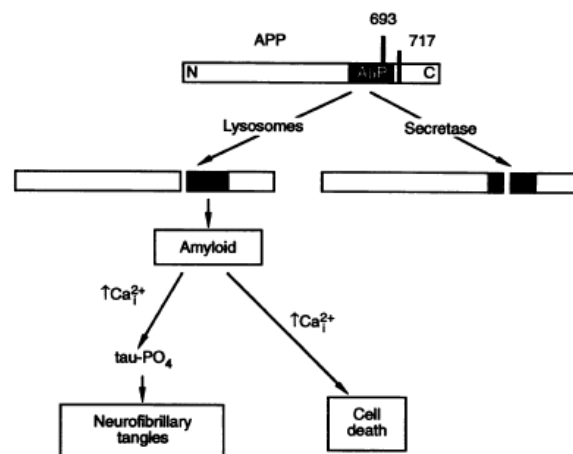


Figure 1. 2 Early amyloid cascade hypothesis. The APP produced mainly via 2 ways: (i) APP is first cleaved at residues 15-17 by the APP 'secretase'. This cleavage event produces fragments that can not form to amyloid deposition. (ii) Several studies suggested that APP can also processed by the endosomal- lysosomal pathway, in which the entire A β P sequence and in further the amyloid deposition are formed. Eventually these deposition lead to the neurofibrillary tangles and cell death [34].

Amyloid beta peptide ($A\beta$) comprises 39–43 amino acids and amyloid fibrils are the dominant structures in senile plaques (SPs). The fibrils and plaques can physiologically induce the neurotoxicity directly, or indirectly by the formation of neurofibrillary tangles (NFTs), resulting in the formation of intracellular paired helical filaments (PHFs) and ultimately neuronal cell death. A growing number of genetic studies revealed that the identified mutants are highly correlated with the increased formation of total $A\beta$ or fibrils. Specifically, the fibrillogenic $A\beta_{42}$, a 42 amino acid proteolytic product from APP, is postulated as the main component in the pathogenic process, leading to the formation of insoluble oligomers or fibrils. (Figure 1. 3)

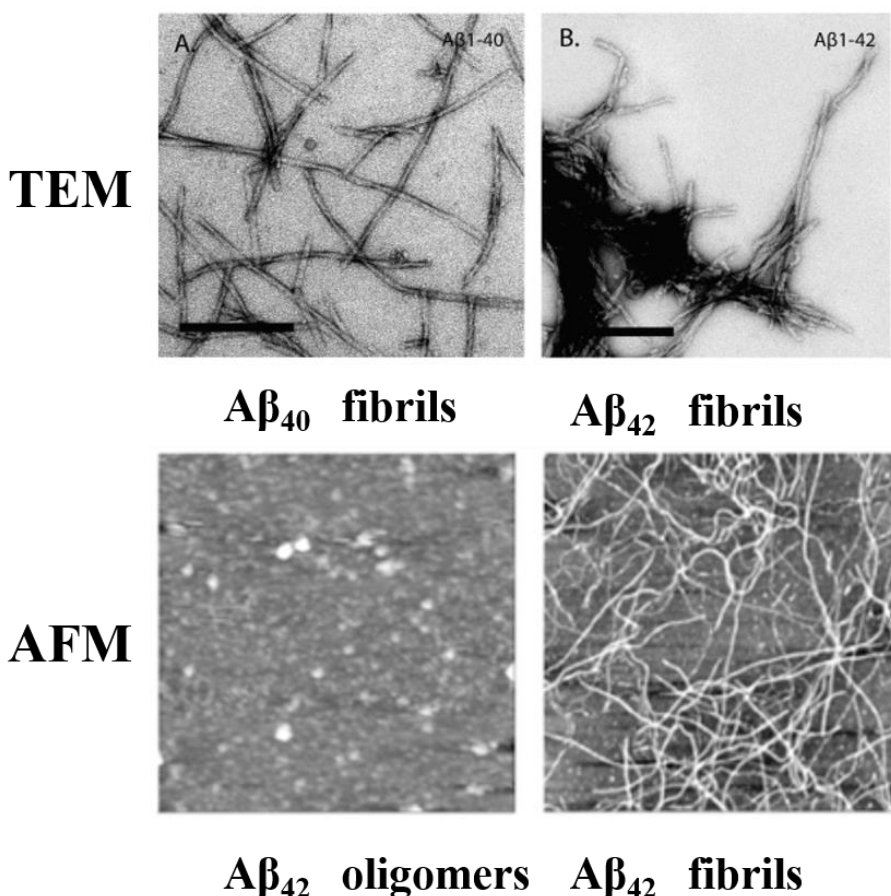


Figure 1. 3. TEM (Transmission Electron Microscopy) and AFM (Atomic Force Microscopy) images of oligomeric and fibrillar $A\beta_{40}$, $A\beta_{42}$. TEM images of $A\beta_{40}$, $A\beta_{42}$ fibrils were acquired through prolonged incubation in PBS under stagnant conditions. Scale bar is 200nm. AFM Images were recorded in $2\ \mu\text{m} \times 2\ \mu\text{m}$ contact mode with oligomers formed in Tris-buffered saline (TBS) after 24 h and tapping mode with fibrils formed in 10 mM HCl after 24h [35, 36].

In recent times, the amyloid cascade hypothesis has been debated on several aspects, largely concerning the implication that A β oligomers and other pre-fibrillary assemblies, and not the plaques and tangles per se, are primarily responsible for AD. The caveats for the amyloid cascade hypotheses include the 1) lack of correlation between neurofibrillary amyloid burden and neuronal dysfunction [37], 2) neurotoxicity of soluble A β peptide assemblies can also explain an amyloid plaque-independent pathology [38], 3) oligomer-induced functional memory loss that occurs before the neuronal death, and 4) concentration of soluble A β oligomers in the brain plasma as opposed to the concentration of fibrils [39]. Over time these observations have led to renewed suggestions that soluble A β oligomers and pre-fibrillary assemblies, rather than mature fibril deposits comprised in plaques, hold the clues to understanding the mechanisms of neurotoxicity in AD [39-45]. Several studies have since confirmed that A β oligomers are potent neurotoxins [45-47]. A β pre-fibrillary assemblies are also associated with many other protein-misfolding diseases like Parkinson's disease, Huntington's disease and Systemic Amyloidosis [41, 48, 49].

1.2.3 ADDL's hypothesis

Increasing evidence suggested that oligomeric and pre-fibrillary structures are key neurotoxic effectors in AD [38, 46, 50-53]. The complexity of their A β assembly is apparent due the existence of several prototypes, forms and structures. Studies have confirmed various A β assemblies (Figure 1. 4), each given their own terminology, including monomeric A β conformers [54], oligomers [46, 53, 55-58], ADDLs [59], protofibrils (PF) [60, 61], A β *56 [62], paranuclei [63-65], amylospheroids [66], annular assemblies [67], amyloid pores [46, 67, 68], and A β balls [69]. Owing to this diversity and complexity, elucidating their relevance to AD pathogenesis remains a challenge. Nevertheless, a growing number of studies

demonstrating their toxicity has seemingly caused a shift towards developing therapeutic strategies based on these pre-fibrillary A β assemblies. Henceforth, the longstanding hypothesis that amyloid fibrils are considered as the only active molecular pathogen has given way to a new paradigm associating with small toxins and we use the term ADDL to describe these small soluble oligomeric structural A β aggregates.

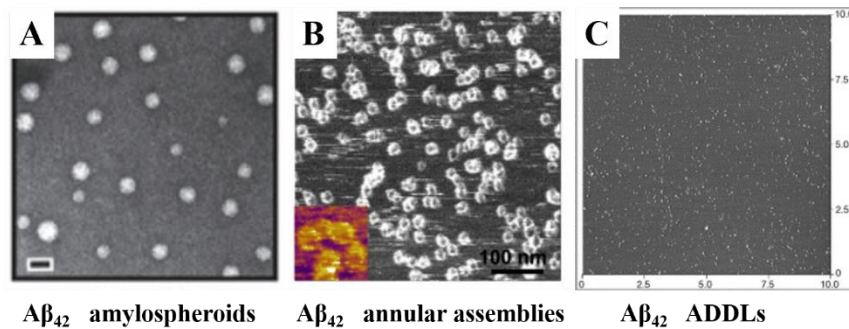


Figure 1. 4. Different A β_{42} assemblies. (A) TEM images of Amylospheroids formed in A β_{42} solution (0.1 μ M in 50% PBS) after an 8h slow rotation, scale bar 20nm. (B) AFM images of A β_{42} annular structured assemblies, the inset represents a 50*50nm topography image of annular assemblies. (C) AFM image of toxic globular oligomers of A β_{42} (ADDLs) [32, 70, 71].

In 1995 Oda et al. [72] proposed that soluble aggregated A β complexes rather than A β fibrils were the molecular pathogens of AD. They demonstrated that the complexes of A β_{42} formed in the presence of clusterin have a significant suppression effect on the A β aggregation and surprising enhancement of the neurotoxicity [73, 74]. Subsequent studies on the neurotoxic effect of ADDLs in synaptic loss and associated memory dysfunction, particularly the action in the neural signal transduction pathway, as well as cultured hippocampal neurons were first described by Lambert et al. [46, 75]. In addition, ADDLs were also found to be responsible for the long-term potentiation (LTP) inhibition and consequential neurological dysfunction, which was believed to directly cause the memory loss of AD [76-78]. Characterization of ADDL's in both *in-vitro* and *in-vivo* studies have not only revealed the detailed biological structure of these toxic oligomers but also provided a fundamental basis for understanding their role in AD, which is schematically outlined in Figure 1. 5 [38, 46, 59, 76, 79-83]. Although ADDLs have

been defined as a neurotoxic subset of A β ₄₂ oligomers, knowledge of their precise structure and definitive conclusion on their cytotoxic assemblies is still limited.

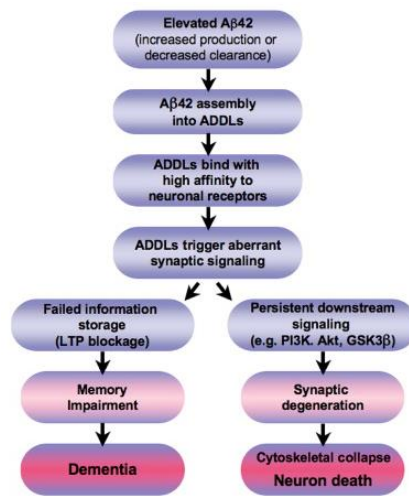


Figure 1. 5. Diagram of ADDLs hypothesis shows all the elements involved with AD [79].

As such, although A β is commonly believed to be a causative factor in AD, the role of mature fibrils and non-fibrillar structural A β species in the pathogenesis of AD remains unclear. Recently, however, *in vivo* studies demonstrated that these oligomeric species of A β ₄₂ are highly correlated with the severity of neurodegeneration in AD while some *in vitro* studies also confirmed the neurotoxicity of these non-fibrillar structures such as oligomers, ADDL's and proto-fibrils [84]. Karie et al. [85] reported that oligomers can inhibit neuronal viability 10 times more than mature fibrils and the toxicity increased 40-fold compared to non-aggregated peptides, indicating oligomers are the active species of the A β peptide that ultimately cause the synaptic loss and AD related degenerative disease.

1.3 Pathways of A β assembly

1.3.1 Kinetics of oligomer and fibril formation

The mechanisms by which A β monomers aggregate to form oligomers and fibrils have been extensively studied, as identifying the pathways leading to toxic species is viewed as critical for targeting with therapies. One of the well-known pathways is called nucleation-dependent polymerization reactions (shown in Figure 1. 6) [6]. In this reaction, a slow nucleation step initially occurs, producing a ‘lag phase’ during assembly, followed by a rapid fibril elongation step. To prove this transition, extensive X-ray diffraction and electron microscope studies have shown that the end product consists of characteristic, β -sheet-rich fibrils [39]. However, the polymerization processes revealed unexpected complexity in the numbers, types and structures of these aggregates. For example, a defined ‘on-pathway’ assembly required self-assembly of monomers into a nucleus, which is essential for the fibril elongation phase. On the other hand, an ‘off-pathway’ during fibril formation is associated with formation of distinct structural aggregates such as Annulus or Amylospheroid [86, 87] that represent globular assemblies. Related studies have confirmed that these globular assemblies will not form fibrils but they do have rich β -sheet structure content, which is believed to exist at the C terminus [88-90]. Compared to amylospheroids, which have spheroid structures with diameter around 15 nm, amyloid balls are larger spheroid species formed only by A β ₄₀ at high concentrations (300–600 μ M) [60]. It is believed that this high concentration of soluble A β might be associated with an interesting model of amyloid plaques, which is discovered in some brain disorders like Parkinson’s and Huntington diseases [57].

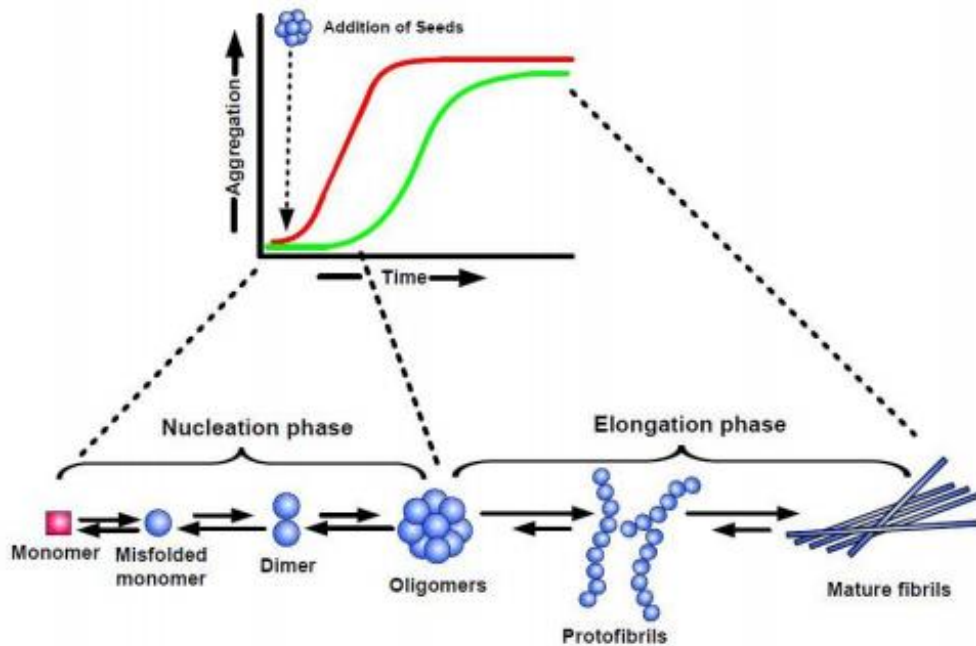


Figure 1. 6. Schematic of the nucleation-dependent polymerization model of A β aggregation. It reveals two phases are revealed during the amyloid aggregation: (i) the nucleation phase/lag phase, in which monomers undergo conformational changes/misfolding and consequently form oligomeric nuclei, (ii) the elongation phase/ growth phase, in which the nuclei rapidly grow by additional monomers to form larger aggregates or fibrils eventually [6].

As mentioned above, peptides can form various structural and types of soluble aggregates through the nucleation-dependent polymerization and one distinct feature of this process is the lag time before these aggregates are detectable, in which the dimers, trimers and eventually the nucleus (n-mers) will be formed [91]. However, this nucleation phase/lag phase is thermodynamically unfavourable and processes step by step while the elongation phase/growth phase is much more favourable and occurs quickly, which means the kinetic of amyloid formation can be well represented by the sigmoidal curve with a lag phase followed by the elongation phase (Figure 1. 6 green curve). In addition, the rate of formation of nuclei will be significantly determined by the seed concentration and additional seeds/nuclei will gradually increase the rate of aggregation by reducing the lag time (Figure 1. 6 red curve). Although this lag time is extremely concentration dependent, the effects on the formation of nucleus such as the structure, size of oligomers and the transition mechanisms are still not clear

[92-94]. A simple schematic example is shown in Figure 1. 7 to illustrate the general stages of A β fibrillation.

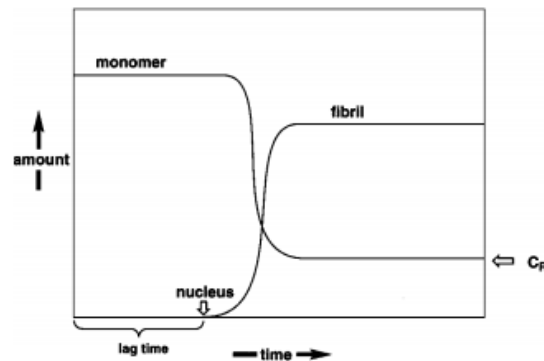


Figure 1. 7. A simple scheme shows the kinetic curve for amyloid formation above barely the crucial concentration C_R [91].

1.3.2 Nucleation mechanisms of amyloid formation

A β aggregation is a complicated process, involving various structural conformation changes and self-assembly of A β monomers to form rich β -sheet structural intermediates, protofibrils and mature filaments [66]. During the early stage of A β aggregation, two important microscopic steps involved in the nucleation-dependent polymerization are referred to as the primary and secondary pathways [95-97]. The primary pathway, such as homogeneous nucleation [95], is defined as a spontaneous process in which new soluble monomers can associate into existing aggregates or fibrils at a rate only dependent on the concentration of monomers (As shown in Figure 1. 8a, where k_n is the nucleation rate constant, $[m]$ is monomer concentration and n_c is represented as length of the smallest growth component fibril) and subsequent addition of the monomers will eventually elongate the fibrils (As shown in Figure 1. 8b, where $[f]$ is the fibril number concentration) [98]. The secondary pathway, where the concentration of existing fibrils is the determining factor, can be classified into monomer-dependent secondary nucleation and monomer-independent fragmentation (As shown in Figure 1. 8c and 8d, where $[M]$ refers to the total fibril mass concentration) [99-102]. In the monomer-

dependent secondary nucleation, several monomers combine to form a fibril by the presence of another fibril, the rate equation represented here is analogous to that for primary nucleation while the $[M]$ accounts for the fact that longer fibrils have more sites for the reaction. The fragmentation is defined by the fibrils break into two separate shorter fibrils and the rate equation is associated with fragmentation rate constant and individual fibril concentration. Figure 1. 8 below show these different kinetic pathways of amyloid fibril formation [103].

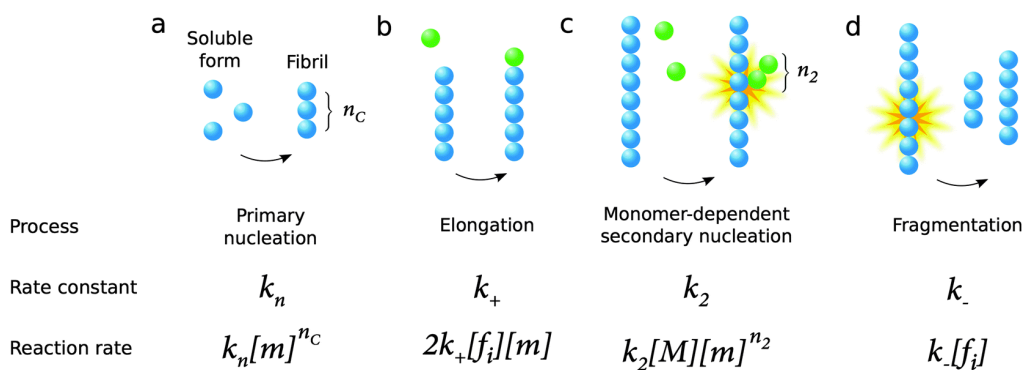


Figure 1. 8. Kinetics of different pathways underlying the amyloid formation. (a) Primary nucleation from monomers, (b) Elongation by addition of monomers to existing aggregates. The secondary nucleation shows the combination of both monomeric and aggregated species and finally the fibrils formed at fragmentation stage. (c) Monomer-dependent secondary nucleation from monomers on surface of fibrils or aggregates. (d) monomer-independent fragmentation. All the monomers are coloured in green while the aggregates or fibrils are coloured blue [103].

Determining the fundamental steps in the structural evolution of fibrils and associated kinetics during these nucleation processes is important for therapeutic targets. Recently, Cohen et al. [104] suggested that monitoring and control of the secondary nucleation pathway during the $A\beta$ aggregation is potentially an effective strategy to sequester the neurotoxic oligomers. For example, depending on the monomer concentration, the rate of both oligomer and fibril formation and the resulting cytotoxic effects can be directly detected by selective radiolabelling methods and cell viability assays, which is shown in Figure 1. 9. In addition, a critical concentration of $A\beta$ fibrils determined the pathway or assembly mechanism of $A\beta$ aggregation is also emphasised in the study, suggesting a potential approach to target precisely

certain structural species and control the amyloid pathways by adjusting the additional fibril concentration. Lomakin et al. [105] also reported the concentration-dependence of fibril elongation rate and the correlated fibril length from the quantitative analysis of different A β nucleation stages including pre-nucleation, nucleation and elongation process by quasielastic light scattering spectroscopy (QLS). The size of fibril nuclei and A β oligomers with corresponding rate constant of formation for fibrils are also determined. Thus, the complexity and diversity of factors influencing the nucleation of fibrils and kinetic parameters of growth could be essentially solved by these proposed models and technical examination.

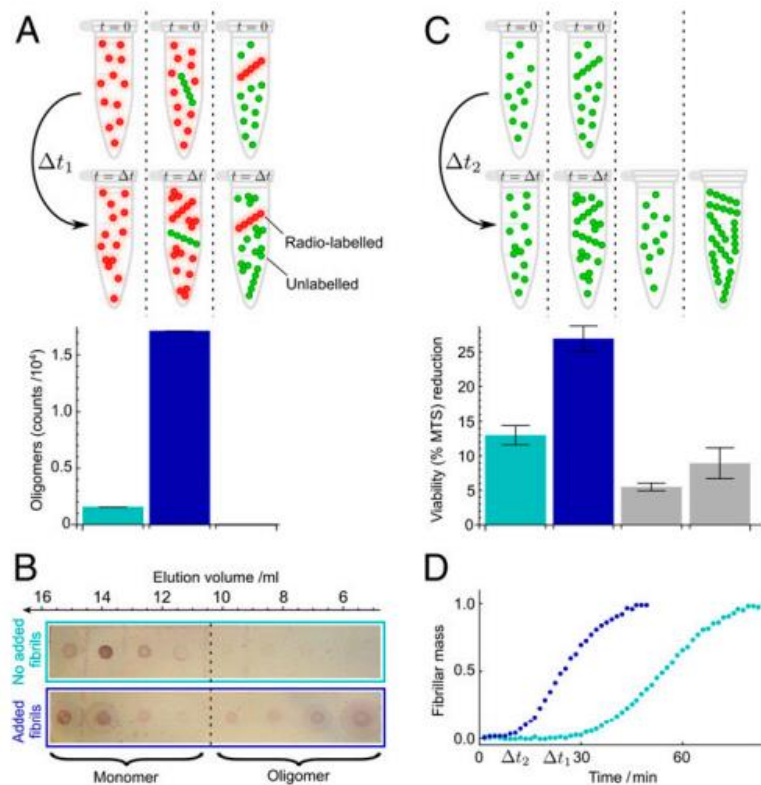


Figure 1. 9. Measurement of oligomers populations with radiolabelling method and cell viability assays. (A) Samples of monomers and monomers mixed with preformed fibrils were incubated followed by size-exclusion chromatography and liquid scintillation counting. The numbers of oligomers fractions are shown below. (no fibrils for light blue bar and added fibrils for dark blue bar) (B) Probing the chromatography fractions with antibodies further confirms the enhanced production of small oligomers in the presence of fibril. Time $\Delta t_1=24$ mins. (C) Measurement of reduced cell viability for reactions without (light blue bars) and with (dark blue bars) a small concentration of added fibrils under the same conditions as in A and after filtration through a 200-nm filter. Values are averages over nine measurements at $\Delta t_2=5, 6, 7$ mins. Grey bars represent initial monomers and end fibrils reaction time points. (D) Comparison of kinetic measurement between two conditions. The rapid increase in the slope with added fibrils (dark blue) and consequent shorter lag time suggest the rapid formation of new aggregates through secondary nucleation [104].

1.3.3 Effect of A β state on the pathway of aggregation

The multiplicity of A β state, in which the polypeptide chains adopted to form a well-defined structure, can be generally classified into native state with functional structures, misfolded state with disordered or partially ordered conformations and various structural intermediate aggregates. Proteins can biologically adopt various other conformation states in addition to the native structure. Tuomas P.J. Knowles and his co-workers demonstrated the amyloid state and its association with protein misfolding disease [106]. For example (as shown in Figure 1. 10), particularly for those large or folded proteins functioning in native state, they can adopt intermediate conformations before becoming fully folded. In addition, some partially folded proteins may also adopt misfolded structures or aggregates, which is essential for specific functional reasons such as the intracellular translocation requirements. Therefore, it was proposed that formation of amyloid structures is not only associated with a small number of diseases, but also that it suggests that the typical form of molecular structure should be related to its functional state or the stages where they will be adopted [107]. To fully elucidate the details on the relationship between A β states and their corresponding preferred protein structures, it is important to characterize the nature and properties of different A β states in which these particular structural molecules can be found [7, 107]. From another point of view, the study on the amyloid state can also provide unique insights into the nature of the functional forms of peptides and proteins, as well as understanding the conversion and the manner in which the peptides tend to aggregate or maintain the specific state [108-110].

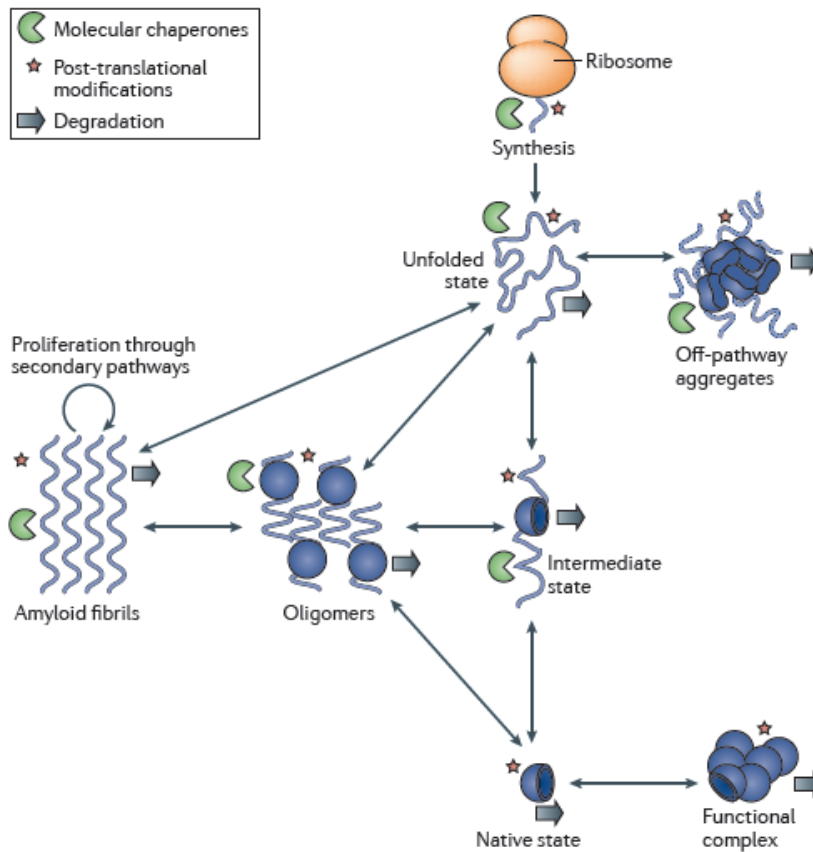


Figure 1. 10. Amyloid state and its relationship with the structure and conformation of the proteins. The amyloid structure is highly affected by the amyloid state. It is believed that peptides or some large fragments are natively unfolded structure and eventually formed amyloid fibrils that are rich in β -sheet structure. During the whole aggregation process, the different states corresponds to various structures [106].

Amyloid structures have different features from the native conformation, in which the property of kinetic and thermodynamic stability will become a key factor to determine [111, 112]. It has been recognized that measurements of kinetics and thermodynamics are fundamentally important not only for analysing experimental measurements in terms of reaction mechanisms but also for predicting aggregation behaviour under conditions in which such parameters cannot be measured [113]. While thermodynamics of various amyloid states describes whether or not a transition from one state to another is spontaneous, the analysis of kinetics will mainly emphasize how fast a transition could take place [113, 114].

1.3.4 Effects of environmental conditions

Kinetic processes of amyloid aggregation are not only dependent on the concentrations of the protein but also associated with some other factors such as the temperature, incubation time, metal ions or liquid pH. For example, Kusumoto et al. showed that the fibril elongation rate constant (K_e) is increased significantly by two orders of magnitude as the temperature increases from 4°C to 40°C. This temperature dependent K_e follows the Arrhenius equation: $K_e = A \exp(-E_A/kT)$, where A is the pre-exponential factor, E_A is the activation energy for the reaction and T is the absolute temperature, resulting in higher activation energy and indicating a possible conformational transition activity (Figure 1. 11) [115]. Ann Tiiman et al. [116] similarly reported that fibril formation is accelerated at higher temperature and lag time decreased from 10°C to 45°C, however, at lower temperatures (4°C) and at physiological pH oligomers were formed, revealing the conditions suitable for the production of the oligomeric neuro-toxic species in AD [117-120].

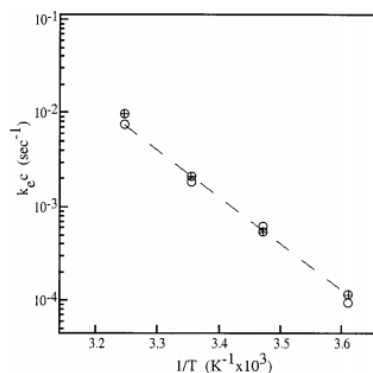


Figure 1. 11. Arrhenius plot shows the temperature dependent fibril formation [115].

A growing number of studies revealed that the fibrillation process is independent of pH in the range from 7 to 9, whereas the rate constant of fibril formation dramatically decreases at lower pH, indicating an effect of protonation of histidine groups [121-123]. In acidic solution, the protonated histidine will not be able to form salt bridge with aspartic acidic residues, as

suggested in fibrillogenesis, rather the positively charged histidine will repel each other in the structure of the forming fibrils, resulting the inhibition of the fibril formation. Further addition of different mutants (H6A, H13A and H14A) were investigated to identify essential histidine for the A β fibrillation and reveal inhibition mechanisms, which is shown in Figure 1. 12 [116]. It has been shown that the pH dependence of the fibrillation rate of H6A is similar to the wild type A β ₄₂ while the fibrillation rate of H13A and H14A mutants are constant in the whole pH range, suggesting that the protonation of H6A will not affect the fibril formation and both histidine H13A and H14A inhibit the fibril formation. The pH dependency of A β aggregation under acidic conditions sheds light on the peptide oligomerization and the corresponding cytotoxicity issues of oligomeric A β . Yeu Su et al. [124] examined the structure and neurotoxic effects of aggregates formed in different pH conditions and revealed that only aggregates that formed at pH 5.8 induced a significant inhibition of 3-(4,5-dimethylthiazol-2-yl)2,5-diphenyltetrazolium bromide (MTT) reduction, which is a colorimetric assay for assessing cell metabolic activity, resulting in the death of PC12 cells (Figure 1. 13). Additional results from a reliable neuronal cells detecting assay, annexin-V staining assay, further confirmed that the aggregates formed at pH 5.8 contributed to the apoptosis of PC12 cells. These findings, along with many current in vitro studies have been done in accordance with the finding that cell organelles are filled with acidic components of senile plaques in the brain of patients with AD [125].

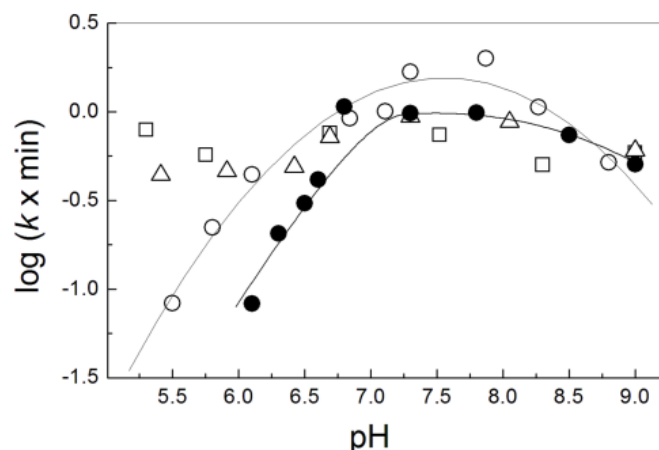


Figure 1. 12. The effect of pH on the fibril formation of A β ₄₂, as a function of rate constant of fibril formation. The aggregation of 5 μ M wild-type (●), H6A (□), H13A (□) or H14A (Δ) mutant of A β ₄₂ in 20mM ammonium acetate, 100mM NaCl with continuous agitation in the presence of 3.3 μ M ThT at 25°C at different pH values [116].

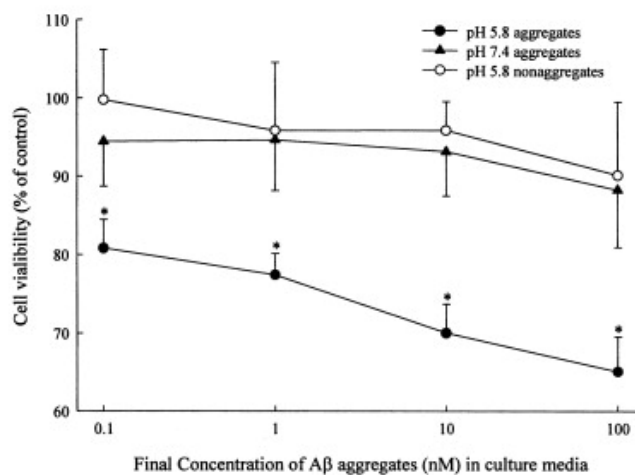


Figure 1. 13. Effects of pH 5.8 and pH 7.4 A β ₄₂ aggregates on the viability of PC12 cells. Aliquots from pH 7.4(▲) or pH 5.8(●)A β ₄₂ aggregates or the non-aggregates (□) were incubated with PC12 cells for 48h and the cell viability assay was conducted by MTT inhibition method [124].

Fundamental knowledge of the A β ₄₂ assembly process in terms of comprehension of both the kinetics and mechanisms of the A β ₄₂ aggregation, combined with the understanding of popular pathways and various effectors in the progress. It is realizable to maintain the specific structural protein species by regulating the protein concentrations at different aggregation phases and by controlling the rates of the conversion between them. This will be highly meaningful for various strategies proposed to suppress the production of the toxic oligomeric species [126-129]. Therefore, the controllable process between different

aggregation stages can be achieved by either disrupting the process of their formation or promoting the pathways of their moving [130, 131]. The development of drugs that reduce the risk of aggregation by decreasing the concentration and formation rates of the toxic protein species has been an area of interest in recent times. Herein, an overview of the treatments and strategies involved are presented below.

1.4 Current treatments and clinical therapies

1.4.1 Cholinesterase inhibitor treatments

The neuropathology of AD is characterized by early cholinergic neuronal loss, resulting in decreased cholinergic transmission [132, 133]. Therefore, various cholinesterase inhibitors have been introduced firstly by delaying the breakdown of acetylcholine, which is important for the nerve cell communication and memory neurotransmission [134]. In addition, a recently developed drug, Memantine, belonging to the N-methyl-d-aspartate (NMDA) receptor (and one of the three types of ionotropic glutamate receptors), is shown to be capable of blocking excess glutamate that can damage or kill nerve cells [135]. However, these treatments can only provide symptomatic relief or delays in the progression state and cannot reverse the course of the disease.

In addition to the Memantine mentioned above, at present only four cholinesterase inhibitors (ChEIs), Tacrine, Donepezil, Rivastigmine, and Galantamine are recognized and approved by the U.S. Food and Drug Administration for treatment of AD [136]. Depending on the different stage of the disease, these drugs all exhibit reasonable neuroprotective activity and work by blocking the enzyme acetylcholinesterase so that the levels of acetylcholine in the synaptic cleft can be maintained or elevated. Table 1. 1 [137] provides a brief summary of these drugs. The success in symptomatic treatments led to the alternative development of functional

drugs. For example, Phenserine, an inhibitor of acetylcholinesterase and capable of improving cognitive function in dogs and rodents, was clinically tested in AD patients and showed successful results to attenuate the progression of AD [138]. Other therapeutic targets such as M1 muscarinic receptor agonists AF102B, AF150(S) and AF267B have also been investigated and reported as cognitive enhancers with potential to modify AD [139, 140]. The effect of nicotinic receptor agonists on cognitive functions of AD patients have also been investigated for many years and currently most of them are in preclinical stages [141, 142].

Table 1. 1. Current treatments and approved therapies available for AD [137].

Name	Disease stage	Symptomatic activity
Tacrine	Mild-moderate	Increase cholinergic transmission
Rivastigmine		
Galantamine		
Donepezil	All stages	Increase cholinergic transmission
Memantine	Moderate -severe	Decreases glutamate excitotoxicity

1.4.2 Anti-amyloid therapies

1.4.2.1 Prevent A β aggregation

Although the pathology of AD and identification of toxic species from diverse A β structures, forms and aggregates are still unclear, targeting the neurotoxic activity of A β oligomers has provided a fundamental basis for the development of compounds and drugs that aim to purposefully suppress the A β oligomerization [39].

Tramiprosate, a glycosaminoglycan (GAG), was developed as the first generation of anti-amyloid aggregation drugs designed to interfere with soluble monomeric A β species, maintaining it in non-fibril form, and thus preventing oligomerization and aggregation [143].

Clinical trials of patients with mild to moderate AD demonstrated promising efficacy in the treatment for cognitive function improvement and stabilization of neurologic deficits [144]. The beneficial effects of those anti-amyloid aggregations compounds have also attracted some clinical investigation such as the longitudinal Volumetric Magnetic Resonance Imaging (VMRI) measurements of the decreasing atrophic hippocampus in patients with mild to moderate AD, revealing their significant capabilities of improvement for cognition [145]. However, due to the low bioavailability and the side effect of toxicity issue associated with the tau aggregation, the development of tramiprosate still requires further clinical evaluation and recently some related projects have been terminated [146]. Some other inhibitors of A β aggregation such as scyllo-inositol and Epigallocatechin-3-gallate (EGCg) worked via a similar mechanism to prevent and even disassociate aggregates by binding to initially forming A β species. These drugs were well tolerated and showed significant benefits in clinical trials [147, 148].

1.4.2.2 Promote A β clearance

An alternative approach to therapy in AD is to directly reduce the levels of A β in the brain, which can be theoretically manipulated or balanced by the levels of A β degrading enzymes. Therefore, many small molecule activators that function to ultimately reduce the A β levels have been investigated. For example, the inhibitors of plasminogen activator inhibitor-1 have proven to increase the A β catabolism and may constitute a reliable therapeutic approach to lower the levels of A β in brain [149]. Recently, neprilysin was also implicated as a promising A β degrading enzyme target since it can significantly reduce the levels of A β deposits in transgenic mouse models [150]. However, further evaluation of these compounds and characterization of the delivery approaches are poorly understood and require further testing.

1.4.3 Metal ions

Accumulating evidence shows that transition metal ions and generated oxidative stress are involved in the pathogenesis of AD [151-154]. In vitro studies indicate that physiological concentrations of zinc and copper can accelerate A β aggregation and increase A β toxicity [155-157]. As shown in Figure 1. 14a and 14b, the analysis of fibril growth kinetics, metal-free A β preparation takes more than 70 ± 2 h to reach half maximal fluorescence while the fibril formation time is nearly halved at 38 ± 2 h for the same preparation with Cu $^{2+}$ ions. The increased cytotoxicity induced by copper ions was also emphasized in Figure 1. 14c. The concentration of iron in the brain of AD patients is also elevated [158]. A β peptide has a strong positive reduction potential and displays high-affinity binding for Zn $^{2+}$, Cu $^{2+}$ and Fe $^{3+}$ ions [159]. Therefore, various metal chelating agents are potentially effective in attenuating the effects of A β . PBT-2, one of the analogues of 8-hydroxyquinoline, has distinct chelating properties, with good blood brain barrier (BBB) permeability, and widely used to inhibit zinc and copper ions from binding to A β to accelerate clearance of A β oligomers. Subsequent clinical trials with PBT-2 also confirmed its improvement in the memory and cognition in AD animal models though further clarification of the safety, tolerability and efficacy are still needed [160, 161]. Another metal ion-based system, Met35, participates in redox reactions and has potential to modulate oxidative stress. Hou et al. [162] have reported that oxidation of Met35 to Met35(O) significantly reduces the rate of amyloid formation and alters fibril morphology. Bitan and Teplow [55] reported similar findings when Met35(O) A β_{42} does not form pentamer/hexamer (paranuclei) which self-associate to form larger oligomers, but rather oligomerizes similarly to A β_{40} , indicating the role of Met35(O) in blocking the formation of paranuclei and in controlling the pathway of A β oligomerization. However, the high affinity property of these chelators may pose harmful effects when undesirable metal binding occurs in

other tissues. Thus, an effective delivery approach for chelation combined with precise targeting methods will provide significant therapeutic options for clinical treatment.

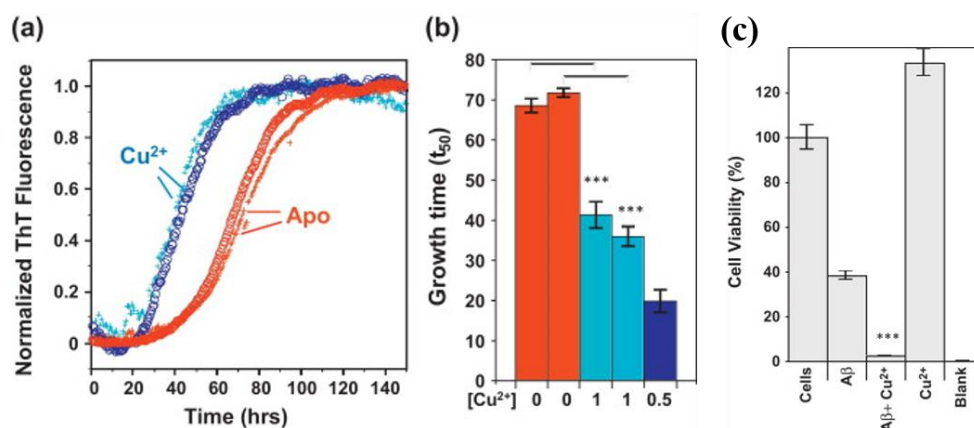


Figure 1. 14. Cu²⁺ accelerates A β growth and increases the cytotoxicity. (a) Average of 9 growth curves recorded Apo in red and Cu²⁺ in blue. The fluorescence ThT signal is normalized at maximal intensity. A β ₄₀ concentrated at 5 μ M, HEPES buffer 50mM, 160mM NaCl at 30°C. (b) Time to reach half-maximal fluorescence (t₅₀) in two experiments with 0 (red), 1 (mid-blue) or 0.5 (dark blue) mole equivalents of Cu²⁺ ions. The presence of Cu²⁺ typically halves the time taken to form fibrils. Error bars are for standard from nine traces. (c) Cell viability comparison [155].

1.4.4 Multi-target directed compounds

The complexity of pathology in AD has inspired researchers to develop multifunctional drugs for various central nerve system (CNS) targets [163]. These multifunctional compounds will interact via different mechanisms so that the specific benefits or symptomatic improvements can be achieved [164]. For instance, a novel neuroprotective drug called TV3326 [(N-propargyl-(3R) aminoindan-5-yl)-ethyl methyl carbamate] possesses both cholinesterase and monoamine oxidase inhibitory ability, thus can clinically increase the cholinergic neurotransmission, levels of dopamine, serotonin and adrenaline in the brain, and provide cognitive benefits [164]. TV3326 also has antioxidant properties and can modulate APP processing and cellular signalling pathway, preventing cell death [165]. Similar acting compounds of M-30 and Memoquin are also believed to be promising drugs for the anti-AD [165, 166].

Despite the symptomatic relief that has been achieved using the aforementioned therapies and drugs in AD, which provided a promising basis for the development of clinical treatments, in particular those targeting A β oligomerization and aggregation, unfortunately none of them have made it successfully through clinical trials and approved for use at present. One of the issues posed is that such drugs may be ineffective in treatment of patients diagnosed with AD, as current diagnosis may represent late-stage or post-AD where the pathogenic mechanisms of A β oligomerization and aggregation have already passed. In addition, another challenge as mentioned is the current lack of understanding of ADDL's in AD, particularly their role in early stages and failure to identify which A β oligomers/aggregates are responsible among their many diverse forms [167]. Alternatively, some emerging approaches to antibodies or chemical compounds targeting A β oligomers will be further summarized below.

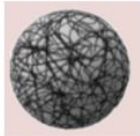
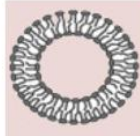


1.5 Alternative strategies

1.5.1 Nanoparticles (NPs)

Currently more than 98% of potential available drugs can't transfer from blood to brain effectively due to the physical barriers and BBB which is actually a cellular 'fence' to protect brain from hazardous substances in the blood flow. For example, most of the current potential iron chelators, as discussed above, are of relatively high molecular weight and are limited by the poor transference across the BBB. Although modified lower molecular weight chelators have shown a better ability to penetrate the BBB, the toxicity issue for the treatment of chelation therapy are becoming serious [168, 169]. However, as the development of NPs advanced in efficient drug delivery and improved drug targeting ability, nanoparticles conjugated with metal ions are demonstrated as a new therapy option [170].

Beyond that, engineered NPs with size around 3-200nm and made of biocompatible materials can be proposed to solve the problem of enhancing transport of drugs from blood to brain [171]. Advancement in the encapsulation and surface modification of NPs also guarantee the pharmaceuticals against degradation as well as increase their half-life time since most of the NPs will be rapidly cleared by the reticuloendothelial system and mainly sequestered in liver and spleen [172]. In order to make the particles suitable for BBB crossing to allow their diffusion within the brain, it is also crucial to control the size of NPs below 200nm diameter which is estimated as the largest pores present in extracellular spaces in the human brain tissue [173]. Some functionalized NPs with potential drugs proposed for the treatment of AD are listed below. (See Table 1.2)

Table 1. 2. Some NPs proposed for the treatment of Alzheimer’s disease [172].

Type		Size	Drugs
Polymeric NPs		1–1000 nm	Curcumin Neuroprotective peptide Rivastigmine Estradiol S14G-humanin Anti A β antibody
Liposomes		200 nm to 500 μ m	Curcumin or curcumin derivatives Phosphatidic acid Cardiolipin XO4 Glycofused benzopyrane
Solid lipid NPs		50–1000 nm	Piperine
Gold NPs		1–150 nm	A β -binding peptide

While there is a growing interest in the application on the NPs in biomedical field, many issues remain to be considered, including the critical questions of the potential toxic effect of NPs to human health. Current research data has only shown that NPs' size, size distribution, purity, shape, composition, surface coating, surface charge and surface reactivity result in a different distribution, accumulation and transport of NPs to different organs, as well as across the BBB [174-176]. It should be noted that most neurotoxicity studies performed so far have focused on metal and carbon-based NPs. Thus it is difficult to apply a general rule regarding brain toxicity of NPs and the benefits of NPs must be weighed against their potential toxic effects. So far, in fact, the toxicity of NPs has not been fully understood and a complete understanding of the molecular and pathogenic events of AD is also desired. However, drug-loaded multi-functionalization NPs remain a viable option for the effective treatment of AD [172, 177]. It should also be noted that the current nano-medicine treatments for AD therapy are still limited to preclinical studies.

1.5.2 Nanomaterials

With the development of nanotechnology, and the emergence of a range of nanomaterials and NPs for use in a variety of biomedical applications, the development of anti-AD therapies based on nanotechnologies is seen as a promising avenue for investigation. For example, Zaixing Yang et al. [178] revealed that graphene and graphene-oxide nano-sheets can significantly inhibit A β peptide monomer fibrillation and extract a large number of peptides from preformed amyloid fibrils. In this study, the results from AFM imaging studies showed that mature amyloid fibrils can be disassociated into small pieces, further removed by graphene oxides, and cell viability assays demonstrated that graphene oxide can significantly decrease the A β cytotoxicity. These findings provided a fundamental basis for understanding the mechanisms of graphene-A β protein interactions and Nano-therapies for AD [178].

1.5.3 Photoexcitation Effects

Environmental factors play an important role in the progression of AD. Joon Seok Lee [179] found that photo-excited Rose Bengal (RB) strongly inhibits Alzheimer's $A\beta_{42}$ aggregation compared to RB exposed under dark conditions (Figure 1. 15). RB under green LED illumination interfered with an early step in the pathway of $A\beta_{42}$ self-assembly and inhibited the conformational transition from monomers into toxic β -sheet-rich structure. Therefore, utilizing photo-excited RB provide another potential strategy for effective suppression of $A\beta$ aggregation and cytotoxicity.

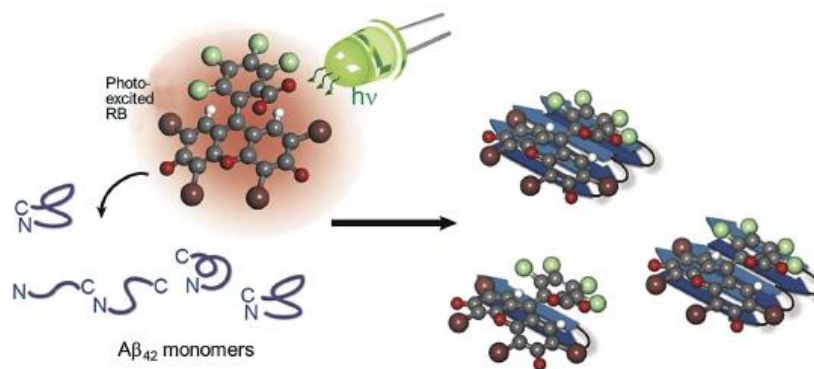


Figure 1. 15. Schematic illustration of the inhibition of $A\beta$ aggregation by photo-excited RB [179].

1.5.4 Electrical Stimulation: A new paradigm for therapy

As we have witnessed, more electronic devices have been successfully developed in medical area nowadays, especially in the bionics such as the bionic ear [180] , cardiac pacemakers [181] and devices that provide electrical stimulation for bone regrowth [182]. Not only huge money invested trying to find suitable drugs for treatment, but also people have to consider the side-effect or toxicity of the conventional pharmaceuticals. Therefore, a new therapy that involving deep brain stimulators for treatment of protein-aggregation disorders are potentially exciting options in the future.

Recently, Innocent Bekard et al. [183] and his group propose a model whereby the electrophoretic motion of the proteins leads to a frictional force that results in protein unfolding (Figure 1. 16). They measured the effect of a low strength oscillating electric field on the conformation of Bovine serum albumin (BSA) and Lysozyme and confirmed that electric force applied during electric field exposure was significant to perturb the tertiary structure of both BSA and Lysozyme. They establish intrinsic protein fluorescence as a sensitive tool to study the dynamics of the tertiary structure of native proteins in response to stress. Circular dichroism is used to quantitatively explore the solution conformation of peptides and poly-peptides. In addition, prolonged electric field exposure resulted in significant frictional energy dissipation in the proteins. This observation that weak electric fields have the ability to dissipate energy in proteins, and then result in the unfolding of the proteins, provides for potential health implications.

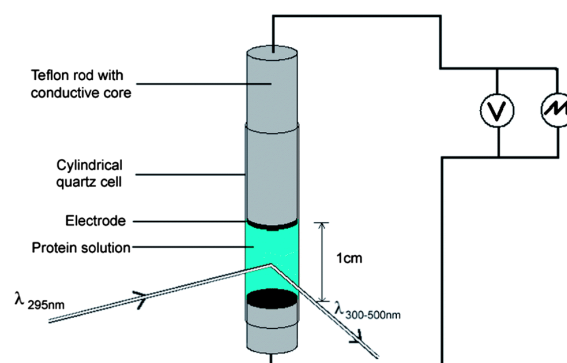


Figure 1. 16. Schematic of the electro-cell. This purpose build cell is used to measure the real-time auto-fluorescence and circular dichroism of the protein solution exposed to electric fields of differing strength and frequency [183].

1.6 Molecular characterization of A β

Unravelling the molecular structures of A β species and the process of amyloid aggregation are thought of as two key aspects for revealing the molecular mechanisms of AD. In the following

section, the different approaches used to characterize A β and their dynamic interactions are summarized.

1.6.1 Structural measurements

Structural analysis of individual A β peptides, including aggregates, has been extensively elucidated using techniques such as Fourier transform infrared (FTIR) spectroscopy, Circular Dichroism (CD), Solid-state nuclear magnetic resonance (ss-NMR) spectroscopy and X-ray crystallography [184, 185]. These methods will normally provide fundamental data regarding the secondary structures of A β peptides and corresponding morphologies. For example, Liping Yu et al. applied NMR to characterize the soluble A β oligomers and identified a mixed parallel and antiparallel β -sheet structure in these soluble A β forms, which is different from the fibrils that only contains β -sheet structure [186].

1.6.1.1 FTIR spectroscopy

FTIR has been widely used to detect the presence of β -sheet secondary structure, which is a specific type of β -sheet fragment detected by X-ray diffraction (XRD) encompassed in the amyloid fibrils [187]. This β -sheet secondary structure is detected by the presence of a band near 1620cm^{-1} when examining the amide I region ($1600\text{-}1700\text{cm}^{-1}$) of the spectrum of A β fibril samples. Zandomeneghi et al. [188] distinguished amyloid fibrils and native β -sheet proteins from the amide I region of their infrared spectra. They revealed a common group of fibrillary structures, derived from various aggregates, which were distinct from the native β -sheet proteins (Figure 1. 17). Moreover, this study suggested a potential therapeutic strategy by inhibiting or disrupting the formation of structures associated with toxicity.

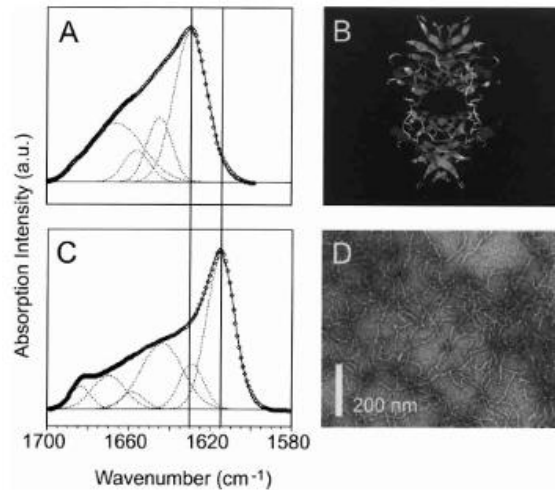


Figure 1. 17. Structure of native protein transthyretin (TTR) and TTR amyloid fibrils.(A) Amide I region from the FTIR spectrum of native TTR. (B) Ribbon diagram of native TTR tetramer.(C) Amide I region from the FTIR spectrum of TTR fibrils. (D)Electron Microscopy (EM) images of TTR fibrils [188].

1.6.1.2 Atomic Force Microscopy (AFM)

Atomic Force Microscopy (AFM) has been widely applied to characterize the structures and to distinguish soluble oligomeric A β peptides from highly aggregated fibrils. As shown in Figure 1. 18A, Hepler et al. [189]successfully captured the ADDLs in a globular structure with approximately 3-5nm in height while the long strand accumulated fibrils were observed in Figure 1. 18B. Interestingly in Figure 1. 18C, a highly magnified image of an isolated subunit, which is referred as the globular oligomer, was observed next to a fibrillary strand that consist of nine of these globular subunits arranged in a helically twisted bundle [189].

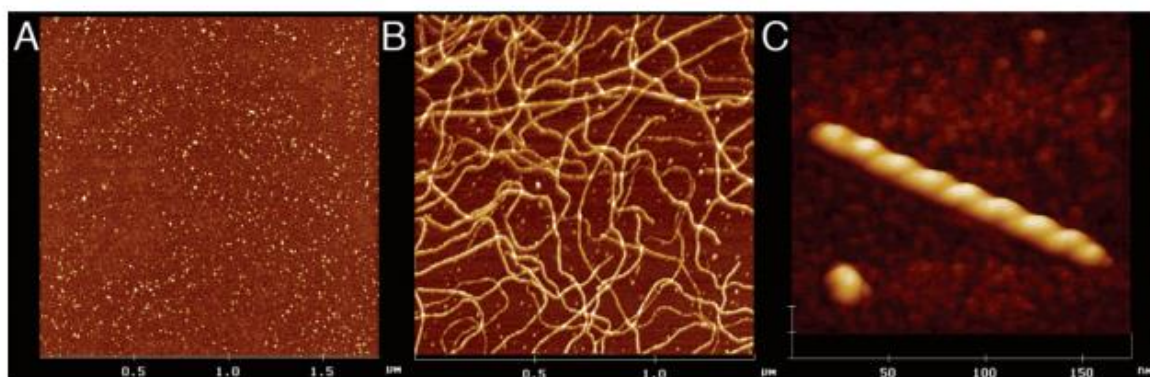


Figure 1. 18. Atomic Force Microscopy images of standard prepared ADDLs (A), mature fibrils (B) and highly magnified part of the fibrils along with an ADDL subunit (C). All the samples were imaged in air using tapping mode [189].

More Recently, Iris A. Mastrangelo et al. [190] investigated the structure and formation of these assemblies using AFM. By taking AFM images of various A β forms at early incubation times (<1h), they revealed that the assembly from monomers, to soluble oligomers and proto-fibrils, subsequently with observations resulting in a stacking mode of assembly has been proposed (Figure 1. 19). In this study, based on the molecular weight (MW) and associated dimensions such as length, width and height, low MW oligomers consisted of two to four monomeric units as shown in Figure 1. 19a, while the oligomers in Figure 1. 19b and 19c appear to be twice as large as the structure in Figure 1. 19a. The proposed models presented below in Figure 1. 19(d)-(f) are referred to the A β ₄₂ monomer, dimer and tetramer.

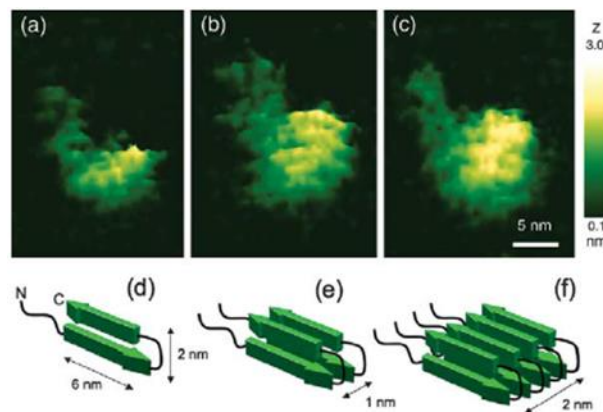


Figure 1. 19. (a)-(c) AFM images of A β ₄₂ peptides and (d)-(f) proposed models of the A β ₄₂ monomer, dimer and tetramer [190]. Image scan size: 150 nm *150 nm

Furthermore, the unique capacity of AFM to provide high-resolution images of single molecules over time has led to this technique becoming one of the main methods to follow the dynamics of amyloid fibril formation. AFM imaging has shown that A β fibril formation is a multistage process and indicates 4 main stages of assembly comprising diverse structures including the 1) earliest proto-fibrils that exist in the form of unstructured A β monomers, 2) subsequent proto-fibril elongation along with reversible disassociation, 3) proto-fibril to fibril

transition, which is not a reversible stage and finally 4) fibril elongation [191]. Additionally, the rate of elongation was dependent on the peptides concentration, temperature and ionic strength of the medium in a comparable experiment. As the AFM images show below, significant increases have been observed in the protofibril length with increasing incubation time at 2 days, 7 days and 18 days (Figure 1. 20a), and increasing temperature at 3°C, 18°C and 37°C respectively (Figure 1. 20b). The statistical analysis further revealed a decrease in the numbers of the protofibrils with the increasing time and temperature, indicating that coalescence of smaller protofibrils contributes to the protofibril elongation. In addition, statistical result of an averaged shorten length of protofibrils with the decreasing numbers in diluted condition suggested an irreversible assembly progress [191].

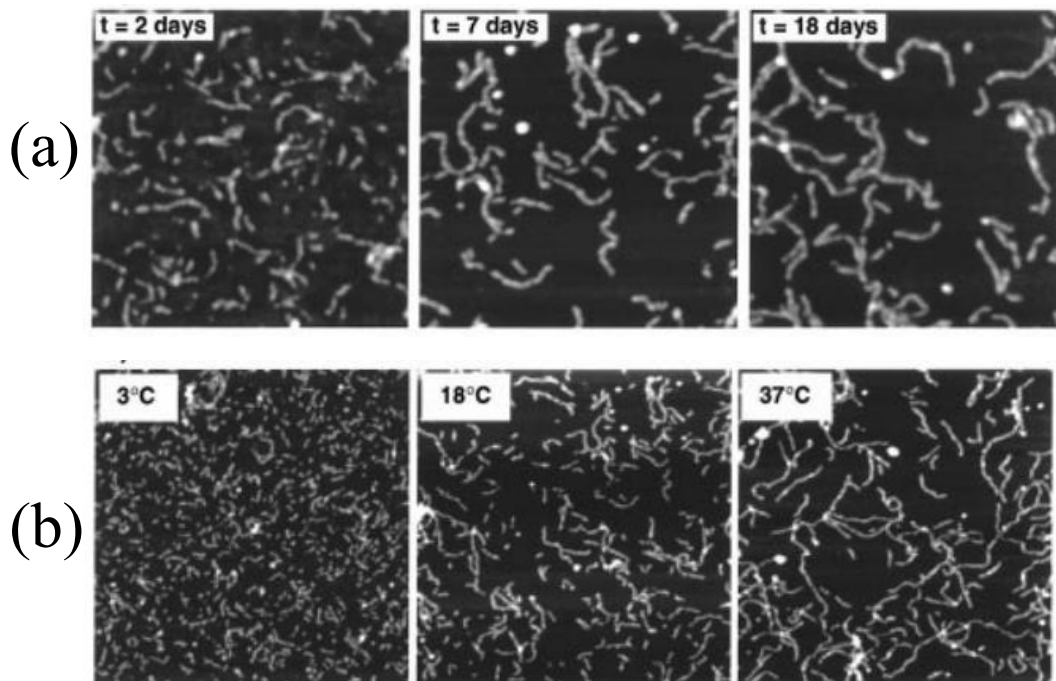


Figure 1. 20. (a) AFM images of time dependence of A β 40 proto-fibril assembly at (scale bar: 500nm*500nm) 2, 7 and 18 days. (b) AFM images show the temperature dependence of A β ₄₀ proto-fibril assembly. Scale bar: 1000*1000nm [191].

The first in-situ AFM visualization, which means the fibrils formation is occurring locally without isolating it from other systems, of proto-fibril formation from single aggregate units of A β peptides that were 83.3 ± 18.2 nm wide with height at 4.5 ± 2.8 nm was reported by H.K.L Blackley et al. [192]. In addition to observing the growth of the proto-fibrils (Figure

1. 21 (i)) and based on these findings, the authors proposed a mechanism for fibrillization of A β (Figure 1. 21 (ii)). Importantly, this work demonstrated the possibility of observing the binding of two single molecular aggregates during the early stages of proto-fibril formation and understand the conditions that either activated or inhibited the aggregation processes [193].

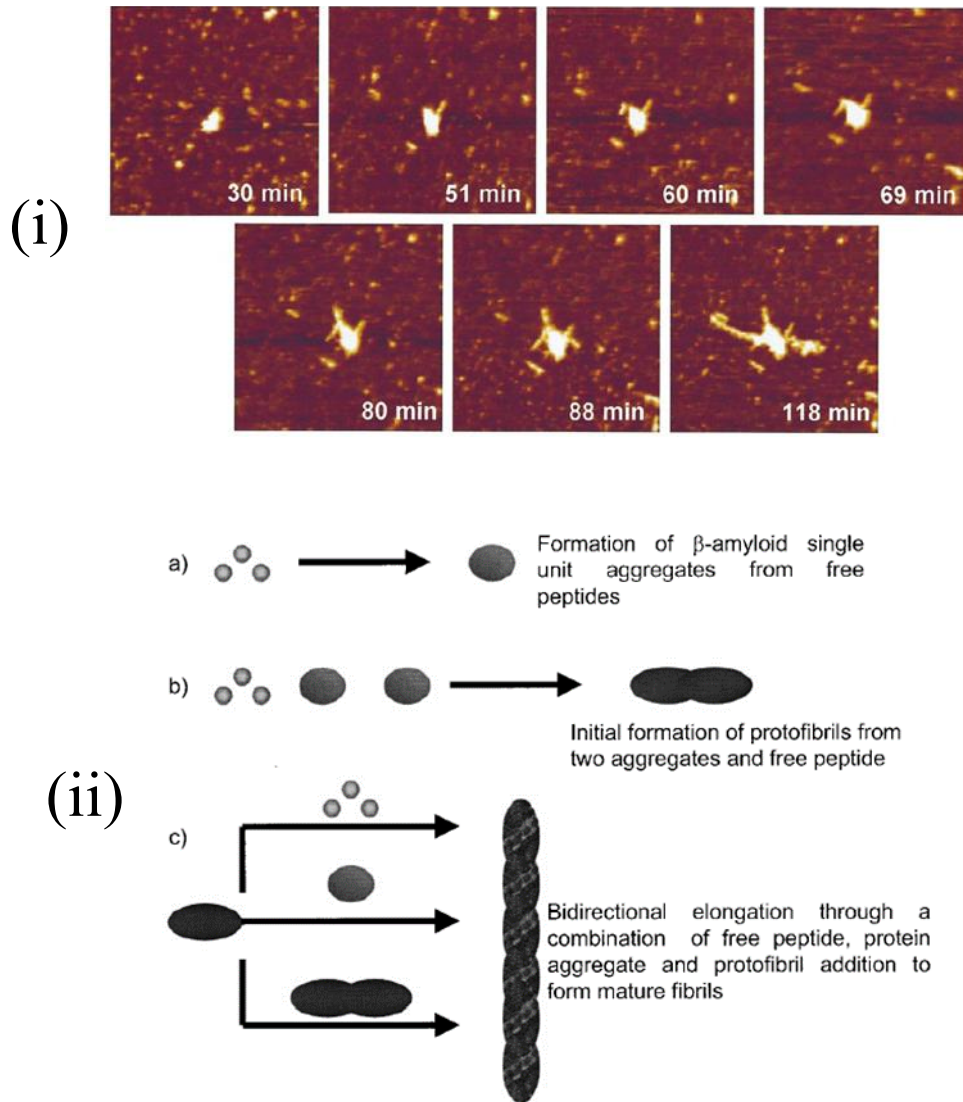


Figure 1. 21. (i) A series of AFM images depicting the development of multiple A β proto-fibril from a common core. Imaging scan size 2.5 μ m*2.5 μ m.(ii) A schematic outlining a possible mechanism for the fibrillization of A β [192].

1.6.2 Fluorescence spectroscopy

1.6.2.1 Internal Reflection Fluorescence Microscopy (TIRFM)

In histological detection and microscopic observations, Congo red dye has been extensively used for staining in amyloidosis. However, this method is too cumbersome for routine use due to the time-consuming nature and low efficiency and reproducibility of the preparation. In contrast, fluorescent stains such as ThT (Thioflavin T), a benzothiazole dye, (Figure 1. 22a) only shows fluorescence upon binding to a specific molecular entity (e.g. amyloid misfolded aggregates or fibrils). It is commonly used as a diagnostic tool for mature amyloid fibril structures both in vitro and in vivo and Vassar et al. was the first to demonstrate this feature in 1959 [194, 195]. They reported that ThT will selectively bind to amyloid deposits, leading to a significant increase in fluorescence brightness as shown in Figure 1. 22b and 22c. Further investigations of the characterization of binding properties and fluorescence provided fundamental support for the importance of the ThT spectroscopic measurement. As the example shows in Figure 1. 22e, Lindgren et al. [196] demonstrated the dye thioflavin T spectroscopic as an efficient method to monitor in situ process of amyloid aggregation with different concentration conditions. In this study, a dramatic increase in the emission fluorescence spectrum upon binding to amyloid fibrils was firstly identified as shown in Figure 1. 22d, then the fibrillation kinetics was measured as the concentration increased [196].

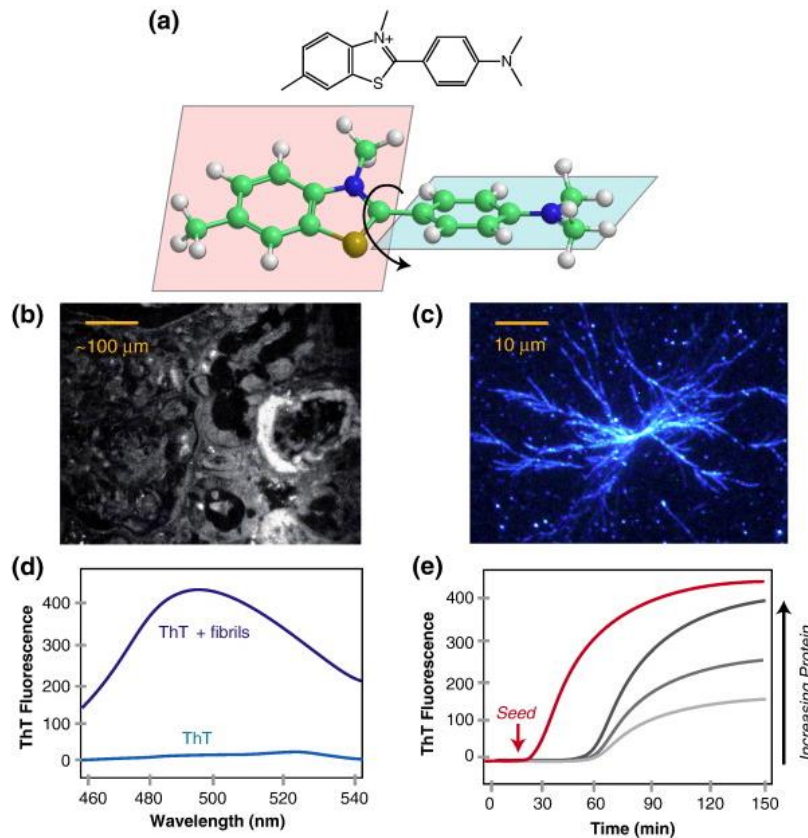


Figure 1. 22. Experimental techniques employing ThT. (a) Structure of ThT (top). The two planer segments of ThT whose mutual rotation defines its chirality (bottom). (b) Early histology using Thioflavin-T to stain primary kidney amyloid. (c) Total Internal Reflection Fluorescence microscopy (TIRFM) image of branched glucagon fibrils stained with ThT. (d) Characteristic increase in ThT fluorescence upon binding to amyloid fibrils. (e) Protein concentration effects on the fibrillization kinetics measured by ThT fluorescent. The rapid onset of fibrillization induced through seeding is also shown [194-197].

In addition, Ban et al. [198] (Figure 1. 23) employed total TIRFM combined with the thioflavin T (ThT) to observe and track the growth of individual fibrils directly. The ability to follow the process of fibril growth provided the great opportunity to not only analyse the kinetics of the reactions, but also for the testing and evaluation of potent inhibitors or therapeutic targets.

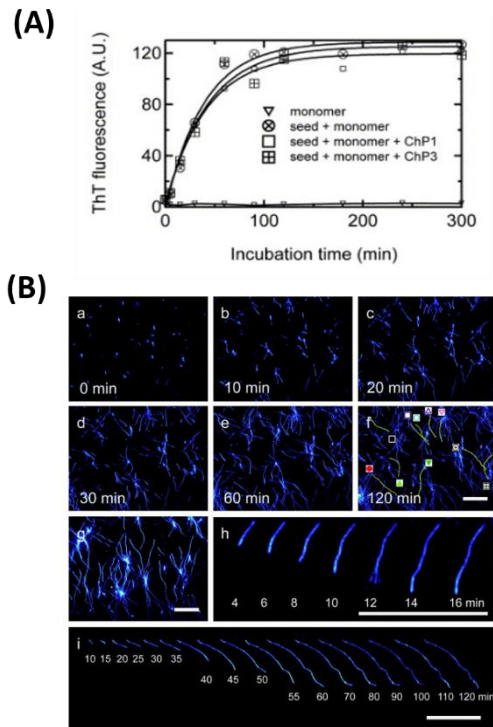


Figure 1. 23. (A) Time-course of fibril formation at pH 7.5 and 37°C monitored using ThT fluorescence. (B) Observation of Aβ(1-40) amyloid fibril growth by TIRFM [198].

1.6.2.2 Fluorescence Lifetime Imaging Microscopy (FLIM)

Intrinsic fluorescence spectroscopy has been suggested as another method capable of directly detecting the amyloid formation by specific spectral changes. Recently, Esbjorner et al. [199] employed fluorescence lifetime imaging microscopy (FLIM) to monitor amyloid formation and study the kinetics of aggregation of Aβ₄₀ and Aβ₄₂ during their cellular uptake and the following trafficking activity in live neuronal cells. In this work, the changes in the fluorescence lifetime of covalently linked dye label HF488 was sensitively recorded during the amyloid aggregation, and this method was proved useful in determining the existence of β-sheet structures, which is highly correlated with such lifetime. Figure 1. 24 below shows an example of kinetic measurement of HF488-labeled amyloid fibril formation. The decreased fluorescence lifetime is consistent with the deeper extent of the amyloid formation and the broader lifetime distribution, and the further aggregation progress is in good agreement with the increasing

population of aggregates. Moreover, the investigation of A β aggregation in the neuronal cells provided vital clues for understanding the role of A β aggregation in pathogenesis of AD.

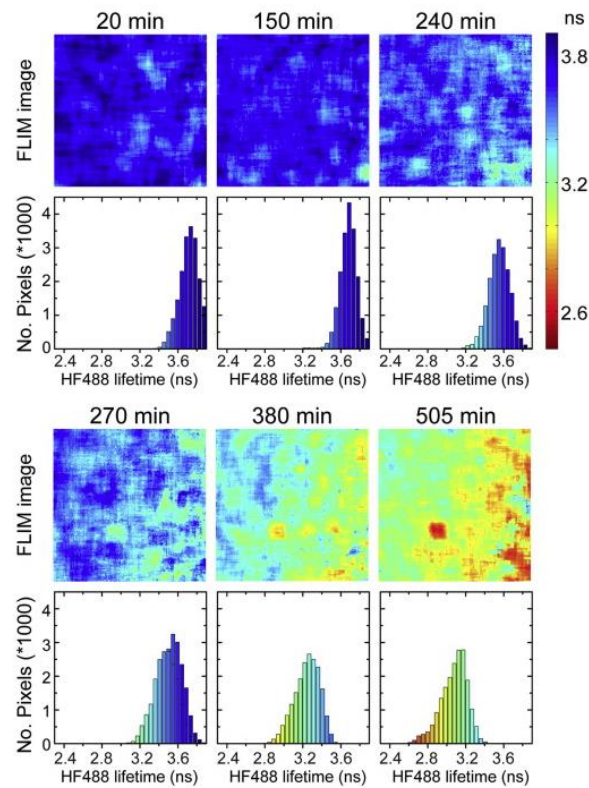


Figure 1. 24. Kinetics of HF488-labeled A β ₄₀ Fibril Formation Monitored by Fluorescence Lifetime Imaging. The colour coding of images and histograms relate to the colour bar on the right. The HF488-labeled A β ₄₀ concentration was 5 μ M, and the peptide was diluted into 50 mM phosphate buffer sodium at pH 7.4 [199].

1.7 High-Speed AFM: Combined Structural-Dynamics of A β Interactions

Since proteins are dynamic and the process of their misfolding or refolding are frequently associated with different transient intermediates, such as partially folded aggregates and spherical oligomers, very little is known about the mechanisms underlying these processes [107, 200, 201]. The difficulties in monitoring various structural A β forms or aggregates and lack of understanding on the dynamics of these transition interactions have further hindered related

research progress. While the development of bulk kinetics measurements such as ThT spectroscopy and fluorescence spectroscopy have provided significant insight into protein dynamics, they do not address the lack of understanding at the single molecule level. Even though single molecule fluorescent studies have been utilized successfully for detecting and tracking the amyloid formation process, there are still limitations in capturing structural information. Alternatively, AFM has been extensively used for providing structural information of single molecules, however, owing to its slow imaging speeds, i.e. several minutes per scan, the real-time dynamic information of single molecules is not realized. This is where the emergence of High-Speed Atomic Force Microscopy (HS-AFM) provides an exciting opportunity to contribute to an integrated approach with the aforementioned techniques; to enable the visualization of protein structural-dynamics. HS-AFM is beginning to bridge the gap by decreasing structural imaging times from minutes to milliseconds. It massively surpasses the capabilities of current AFM systems by enabling acquisition times of ~50 milliseconds per image (~ 20 frames/second). This takes AFM into the realm of video rate imaging that is defined as achieving speeds of ~ 12-13 frames/sec; the human eye needs to visualize a sequence of images at this speed in order to perceive motion.

To study the dynamics of proteins, single-molecule fluorescence microscopy [202, 203] and optical trapping apparatus [204] have been created and widely used over the last 20-30 years. These methods are reliant on recording the dynamic behaviour of optical biomarkers attached to the protein molecule of interest. Owing to this indirect measurement, one has to infer how the protein molecules are actually behaving behind the recorded data. Thus, a technique capable of directly observing both structure and functioning protein molecules in a “label-free” manner has long been desired. And to meet this desire, high-speed atomic force microscopy has been developed [205-207]. (Figure 1. 25)

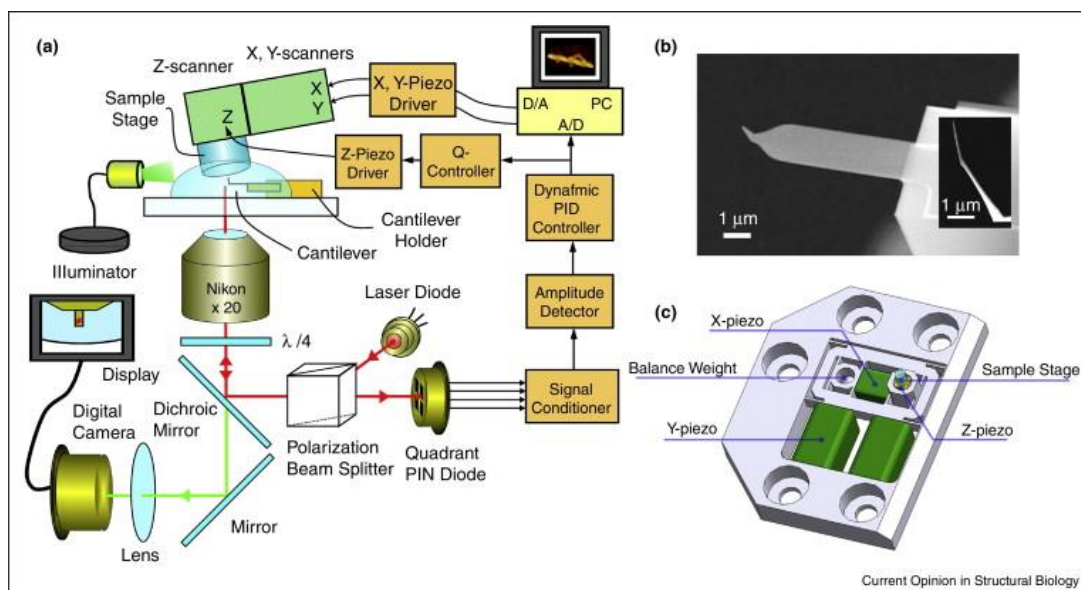


Figure 1. 25. Schematic illustration showing HS-AFM system and devices. (a) All devices contained in the HS-AFM system and main devices like different functional scanners, the stage designed for sample and cantilever, and piezo control platform. (b) SEM image of a small cantilever for HS-AFM. The inset shows an electron beam deposited tip grown on the original tip. (c) An advanced scanner designed for narrow scanning area imaging [207].

Over the past decade various developments in HS-AFM, including small modified AFM cantilevers (Figure 1. 25b), sample-stage advanced scanners (Figure 1. 25c) and optimised electronics shown in HS-AFM system (Figure 1. 25a), e.g. dynamic PID controller [208] and cantilever deflection detection system, have seen the practical use of HS-AFM come to fruition and used to address biological questions that have been difficult or impossible to address by other methods [209]. For example, a feedback control system has been implemented to maintain weak tip-sample interactions and an active damping method was introduced to eliminate scanners' mechanical resonant vibrations [210], which is responsible for the imaging rate, however, perhaps the most critical development was the fabrication and ability to accommodate the optical detection of very small cantilevers of $\sim 6\text{-}12\mu\text{m}$ in length and $2\mu\text{m}$ wide to achieve high resonant frequencies of $\sim 400\text{ kHz}$ to 1.2MHz in water (1.5MHz to 3.5MHz in air) yet retaining small spring constants ($\sim 0.1\text{-}0.2\text{N/m}$) that are suitable for imaging biomolecules. In addition, an electron beam deposited sharp tip ($\sim 1\mu\text{m}$ long and apex radius of $\sim 0.5\text{nm}$ in best case) can be post-fabricated by scanning electron microscopy (SEM) at the top

end of the original cantilever to acquire high resolution images. Imaging speed of HS-AFM is determined by various parameters, including the bandwidth of feedback control, scan range, scan lines, the spatial frequency and maximum possible phase delay. At present, the imaging rate has been greatly improved to over 20 frames per second (fps) without any significant disturbance to the biological function (e.g. tip force action on the sample) [207, 211, 212]. Because of the high imaging rate and low invasiveness to the sample, HS-AFM enables the directly visualization of dynamic structural changes and dynamic interactions occurring in individual molecules, which contribute directly to a wide development of single molecule dynamics visualization and major studies are list below [209]. (Table 1.3)

Table 1. 3. Studies on the dynamic events of proteins by using HS-AFM

Conformational Changes	<ul style="list-style-type: none"> -Photo-activated bacteriorhodopsin [213, 214] -Visualization of the motion of the Ca²⁺-pump [215] -Rotary catalysis of rotorless F₁-ATPase [216] -Agonist-induced height change of NMDA receptor [217]
Diffusion and interactions in membranes	<ul style="list-style-type: none"> -Diffusion and fusion of vacancy defects in streptavidin 2D crystals formed on SLB [218] -Membrane-mediated interaction between ATP-synthase c-rings [219] -Interaction of bR trimers with bR crystal edges in purple membranes [220]
	<ul style="list-style-type: none"> -Amyloid-like fibril formation by lithostathine [221]

Self-assembly processes	-Real-time visualization of assembling of a sphingomyelin-specific toxin on planar lipid membranes [222]
Dynamics occurring in intrinsically disordered proteins	-Visualization of intrinsically disordered regions of proteins [223] -Wiggling and shortening motion of a disordered region in CENP-T [224]
DNA–protein interactions	-Cleavage of DNA by type IIF restriction enzyme [225]
Diffusion and interactions on live cell surfaces	-Single molecule imaging of diffusion of crowded porin molecules on live bacterial outer surface [226]

One of the first striking results obtained by HS-AFM images was the direct visualization of myosin V molecules walking along actin filaments. The ability to capture molecular, dynamic behaviours (e.g. unidirectional movement of myosin V molecule with hand-over-hand manner, unfolding of the coiled-coil tail, foot stomp events in ATP and the lever-arm swing motor action) with different conformational structural transitions (Figure 1. 26) provided unprecedented insight [227].

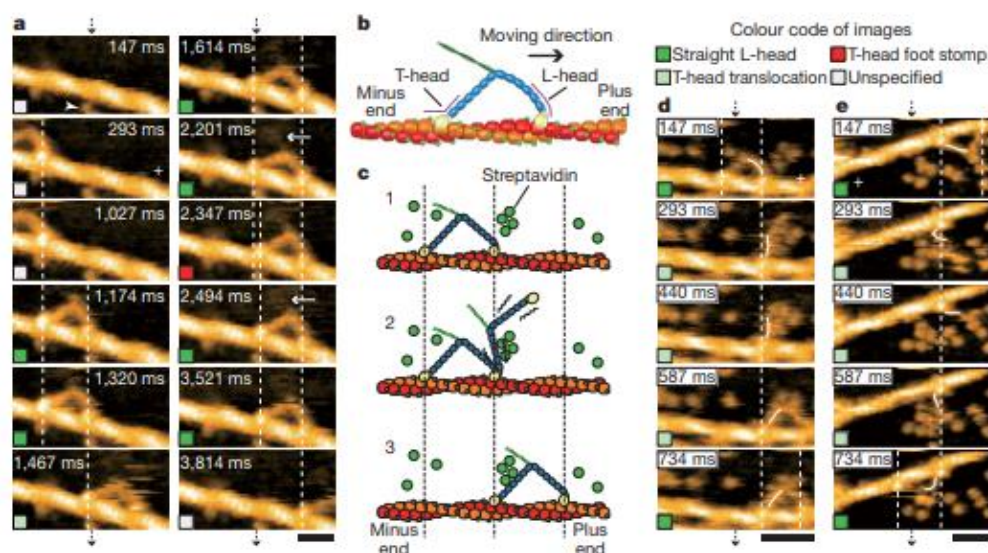


Figure 1. 26. Visualization of walking M5-HMM molecules. (a) HS-AFM film strip showing unidirectional processive movement of M5-HMM in $1\mu\text{M}$ ATP. Scan size: $130 * 65 \text{ nm}^2$, scale bar: 30 nm. (b) Schematic of two-headed bound M5-HMM (c) Schematic of the movement explanation in d and e.(d)(e) HS-AFM film strips showing the hand-over-hand movement in $1\mu\text{M}$ ATP. (d) Scan size: $150 * 75 \text{ nm}^2$, scale bar: 50 nm (e) Scan size: $130 * 65 \text{ nm}^2$, scale bar: 30 nm. All the images showing here are captured at scan rate: 146.7ms per frame [227].

The application of HS-AFM to study amyloid fibril dynamics has also appeared recently, with Watanabe et al. [228] revealing the structural features and assembly kinetics of $A\beta_{42}$ (Figure 1. 27). They revealed two different pathways of the fibril growth, including straight fibrillation and spiral growth. In addition, the findings of initial fibril nuclei structure dependent pathway and the bidirectional switching property between two growth models are also presented for the first time. This finding is consistent with the two distinct steps mechanisms named as dock-lock growth mechanism [229]: monomers will initially bind (dock to) to the fibrils surface in a fast timescale and followed by a slower timescale step associated with the lock process, which is involved with structure rearrangement.

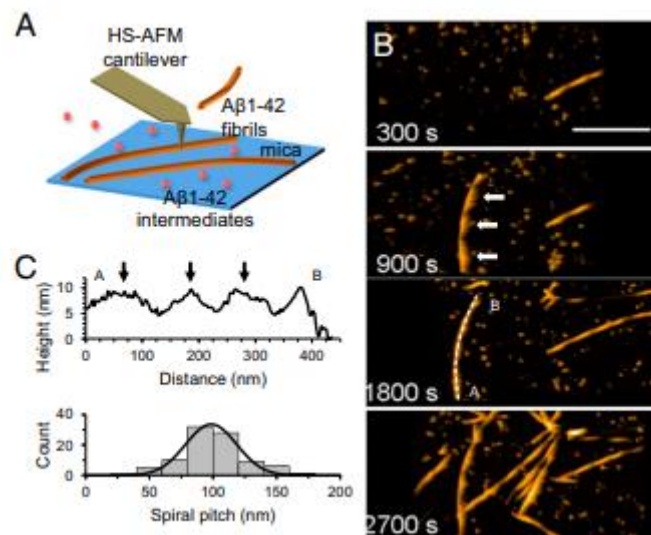


Figure 1. 27. HS-AFM imaging of $A\beta_{42}$. (A) Schematic diagram of HS-AFM measurement including HS-AFM cantilever, sample ($A\beta_{42}$ fibrils and intermediates) and substrate mica. (B) Clipped HS-AFM images at different time point during the fibrils growth. (Scale bar, 300nm) (C) Height profile of selected part of the fibrils as labelled (A to B) at 1800s [228].

S. Banerjee et al.[230] also successfully captured different forms of $A\beta_{42}$ oligomers with distinct structures and highlighted the dynamic significance of isolated cross-linked dimers, pentamers and heptamers. In this study, they found out that oligomers as large as heptamers are in a dynamic equilibrium with dimers and trimers, indicating the important role

of these two key types of oligomers in targeting and further sequestering higher order oligomers, which are considered possibly the most neurotoxic agents.

1.8 Overarching Aims

Within the amyloid hypothesis in Alzheimer's disease, current focus has shifted to earlier stages of amyloid beta ($A\beta$) peptide assembly, involving soluble oligomers and smaller aggregates which are more toxic to cells compared to their morphological distinct fibril forms. However, due to the diverse, parallel molecular interactions between various species at this earlier stage, (referred to the lag time stage shown in Figure. 1.7) along with associated monomer-dependent nucleation, elongation and fragmentation mechanisms, it become critical to unlock the molecular-level kinetic pathways involved with these transition mechanisms. Although the $A\beta_{42}$ peptide has been extensively studied, the detail on their dynamic interactions and associated kinetic analysis at the single molecule level is essentially void. This is due to the challenge acquiring high resolution structural information while simultaneously measuring the dynamics. For this reason, directly visualizing the first moments of $A\beta$ nucleation and subsequent growth into oligomeric forms or other amyloid assemblies has not been achieved despite it being a critical step (in the lag phase) underlying the amyloid aggregation process. Lastly, a growing number of nanomaterials have been introduced to modulate the $A\beta_{42}$ interactions, with a view for potential applications in diagnostics and treatment of disease.

Therefore, to gain a better understanding of the fundamental mechanisms of amyloid interactions responsible for the Alzheimer's disease, the thesis aims to use High-Speed AFM to:

Aim 1: Characterize the structure and dynamics of single molecule $A\beta_{42}$ peptides in liquid, including the intermolecular interactions occurring between the different assemblies of the peptide.

Aim 2: Directly visualize the real-time nucleation and growth mechanisms of single $A\beta_{42}$ peptides by applying in-situ HS-AFM whereby the sample condition is modified during imaging to initiate the growth mechanisms. Numerous factors confirmed to either inhibit or promote the aggregation such as metal ions, temperature and pH will be investigated.

Aim 3: Investigate the interactions between single nanoparticles, namely silica nanoparticles, and $A\beta_{42}$ peptides and to establish HS-AFM methodology and analysis for general characterization of protein – nanoparticle interactions at the single molecule (nanoparticle) level.

Chapter 2: Dynamics of Inter-Molecular Interactions between Single A β ₄₂ Oligomeric and Aggregate Species by HS-AFM

2.1 Introduction

Recent theory for pathogenesis in Alzheimer's disease (AD) implicate the accumulation of soluble amyloid beta (A β) oligomers [32, 231], generally consisting of low molecular weight monomeric, dimeric, tetrameric A β peptides [232], or higher molecular weight (~20 – 40 monomers) oligomers [190]. Due to their small size, high diffusion rate and permissivity to biological interactions, they are evidently more highly toxic, particularly with high-affinity for cellular ligands [233] e.g. neurosynapses. They are defined as basic proteins transformed into toxic forms that are structurally very distinct from their insoluble amyloid fibril successors found in plaques synonymous with AD [234, 235]. Their increasing discovery in patients [236], along with a growing number of *in-vitro* and animal studies demonstrating their toxicity [237, 238], has seen a shift from earlier amyloid 'cascade' hypotheses [239, 240], based on plaque and fibril neurodegeneration, toward understanding the protagonists of A β oligomer toxicity [235], including effects of size, morphology, homeostasis and biodistribution, leading to emergence of A β immunotherapies in clinical trials [137]. A fundamental challenge is identifying which subset or specific species of A β oligomers, amongst the apparent structural

diversity and polymorphism with transient states, are responsible for AD. Equally as important to more broadly elucidate potential targets for AD therapies will be understanding the molecular interaction kinetics that ultimately define the oligomerization pathway(s) leading to the toxic populations.

Thioflavin T-based fluorescence kinetic studies on A β revealing classical sigmoid growth kinetics [241-243], including initial lag, followed by nucleation and fibril formation phases, enable quick interrogation of amyloid or fibrillation blockers, e.g. antibodies, or the effects of amyloidogenic biological conditions such metal ion concentration [244, 245] and pH [245, 246]. The lag phase and slope of the nucleation phase partially indicates the rate at which oligomerization proceed however the kinetic contribution from specific, individual oligomer species are not differentiated. From a structural perspective, x-ray crystallography, electron microscopy and atomic force microscopy show that the oligomer species range from 2-50 nm in size [245, 247], displaying diverse structures and assemblies. Emerging techniques such as ion mobility coupled with mass spectroscopy enable measurement of A β oligomer population distributions, revealing potential assembly pathways and specifically dodecamers as terminal species that are yet to rearrange into a β -sheet structures and thus may represent toxic forms in AD [247-249]. Single molecule fluorescence measurements can probe oligomers present during the lag phase, showing they constitute a highly heterogeneous ensemble of species (~40 molecules) indicative of having undergone a stochastic polymer-like assembly process [250]. Up until now, only single molecule force spectroscopy (SMFS) based on atomic force microscopy (AFM) is used to experimentally determine single molecule kinetics parameters (e.g. dissociation constants) of intra-molecular A β interactions [251]. However, this is currently only configured for the interaction between two monomers [252, 253], effectively limiting measurements to dimerization kinetics. Exploring kinetics of very early stages of

oligomerization, with seemingly fast transition states, are investigated by theoretical and computational simulations [254-256] in the absence of molecular-level experimental data.

To date, a significant mismatch exists between high resolution structural imaging with poor temporal resolution versus inherently fast dynamic spectroscopy but which lacks the ability to directly visualize molecular structure. This is where the use of high-speed AFM (HS-AFM as shown in Figure. 1.25) provides a unique opportunity to study the molecular structural determinants of kinetics by decreasing structural imaging times of single molecules from minutes to millisecs, i.e. ~15-20 images per second [212, 257, 258]. Related to amyloid peptides, HS-AFM studies report on the structural flexibility of α -synuclein monomers and dimers associated with Parkinson's disease [259], dynamic formation of A β protofibrils [228], and structural dynamics of A β oligomers, including specified trimers, pentamers and heptamers [230]. Here, we develop a new analysis based on HS-AFM movies to produce lifetime traces, enabling the first extraction of kinetics assigned to inter-molecular interactions between different types of single molecule A β ₄₂ oligomers and aggregate forms. In doing so, we discover interesting kinetic phenomenon once the A β ₄₂ species reach dimensions associated with larger aggregate species.

2.2 METHODS

2.2.1 Preparation of A β solutions and reagents

Amyloid-beta protein fragment 1-42 (A β 42 peptide) was purchased as a lyophilized solid and more than 95% purity was guaranteed by HPLC from Sigma-Aldrich (High Performance Liquid Chromatography). ADDL's from A β 42 peptide were prepared according to previous methods of [190, 260]. Firstly, 1mg lyophilized solid peptides were dissolved in HFIP (1,1,1,3,3,3-hexafluoro-2-propanol) to prevent aggregation and then aliquoted into 50 small microcentrifuge tubes. After 30-minutes incubation at room temperature in a chemical fume hood, the HFIP was allowed to evaporate for 60 minutes and the re-lyophilized peptides stored at -20°C. Aqueous solutions were prepared by dissolving peptides into PBS (pH 7.4) at concentration of 20 μ g/ml and then vortex mixing for 20 sec prior to use.

2.2.2 Remodification of HS-AFM Cantilever Tips

High resonance frequency (0.8-1.2MHz) cantilevers with low spring constants (0.1-0.2Nm⁻¹) specially designed for High-Speed AFM (HS-AFM) imaging were obtained from Olympus (BL-AC10DS). The silicon nitride cantilevers consisted of a beak-like tip upon which we further deposited a carbon-based tip by electron-beam deposition (EBD) [261, 262]. The carbon tip was sharpened by argon or oxygen plasma etching to produce a significantly smaller tip radius of ~3 nm compared to the original tip (25-100 nm) of the commercial cantilever, which enabled improved imaging stability and resolution [263, 264]. After imaging, the carbon tip could be completely removed by plasma etching and the cantilever remodified for reuse.

2.2.3 High-Speed Atomic Force Microscopy (HS-AFM) imaging in liquid

To prepare samples for imaging, 2ul of 20 $\mu\text{g/ml}$ A β 42 peptide in PBS was pipetted onto a 1.5 mm diameter freshly cleaved mica disk on a glass slide (Cat No. 7101) and incubated for 2 mins. 2ul of fresh PBS was then added and pipetted in/out of the sample solution, and this was repeated several times to exchange the sample solution in order to remove excess A β 42 peptides that had not adsorbed onto the mica surface. The sample was then placed into the liquid cell for HS-AFM imaging. HS-AFM imaging was performed using an ANDO-model (Research Institute of Biomolecule Metrology Co., Ltd., Japan) in tapping mode with high frequency, small cantilevers (BL-AC10, Olympus) remodified with the carbon-tip, as described above. During imaging, the free oscillation amplitude of the cantilever was set to ~ 2 nm and the set point amplitude was kept to $\sim 90\%$ of the free amplitude. An XY scanner with range of $4 \mu\text{m} \times 4 \mu\text{m}$ and z scanner (700 nm) with scan speeds of normally 2-4 frames/sec for 500 nm scans was used. For higher resolution scans of 200 nm $5-10$ frames/sec was applied. For 200 nm \times 200 nm or smaller area imaging. During imaging, a relatively large gain force can be applied without any effects to the interactions to improve the quality of image owing to the short time of force action (~ 100 ns). Thus in the experiment, different types of dynamic events occurring in the biological environment can be visualized.

2.2.4 Data analysis of HS-AFM images

A Matlab computer program was developed to segment molecules in HS-AFM images. The program had four main stages: 1) background image estimation; 2) background subtraction and contrast enhancement; 3) image segmentation using the Otsu's algorithm; 4) connected component labelling and object measurement.

In Stage 1, the background image was estimated by applying image erosion followed by image dilation. Let $I(x, y)$ be an input HS-AFM image, where x and y are the horizontal and vertical coordinate, respectively. To compute the eroded image I_e , the pixel at location (x, y) was set as the *minimum* of all pixels in a local neighbourhood of image I :

$$I_e(x, y) = \mathbf{min} I(R(x, y))$$

In our experiments, the local neighbourhood R was selected as a circular region of radius 15 centred at pixel location (x, y) . Next, to compute the dilated image I_b , the pixel at location (x, y) was set as the *maximum* of all pixels in a local neighbourhood of image I_e :

$$I_b(x, y) = \mathbf{max} I_e(R(x, y))$$

The dilated image $I_b(x, y)$ was considered as estimation of the image background.

In Stage 2, the background image was subtracted from the input image: $I_d = I - I_b$. The difference image I_d contained mostly the foreground (i.e. the molecules). To improve the contrast of the foreground and consequently the segmentation accuracy, the difference image I_d was scaled linearly to the full intensity range [0, 255].

In Stage 3, the enhanced difference image was segmented using the Otsu's algorithm. In this algorithm, a threshold is applied to separate the image into two classes: foreground and the image background. This threshold is selected to minimize the intra-class variance and maximize the inter-class variance and. In other words, this algorithm increases the similarity between pixels belonging to the same class, while decreases the similarity between pixels belonging to different classes.

In Stage 4, connected component labelling was applied to each group of connected pixels into a single region (molecule). For each region, several properties were measured, including width, height, bounding-box coordinates, centroid, perimeter, area, and eccentricity.

In addition, the length and width of peptides were validated using the cross-section analysis in the Igor Pro software. Using the above properties, molecules were also tracked across multiple frames of a HS-AFM video sequence.

However, we also applied the function of filter to some videos, especially for the height measurement, to better observe the individual molecules and their dynamic interactions. Owing to this, some darker regions may appear in these snapshot images and slightly affect the real height value of peptides that adsorbed in these darker areas, then we did manually analysis using line height profile in Igor (HS-AFM software) with the filter on versus off to calculate a correction factor for the height data.

All the data collected from the experimental results were repeated more than three times and the reproducible results were shown as representative group.

2.3 Results/Discussion

2.3.1 Structural Dimensions of Different A β ₄₂ Species

HS-AFM images with scan sizes of 500 nm taken at imaging rates of 2 frames/sec were used to characterize the structure and dimensions of the A β ₄₂ peptide. A representative snapshot of a single frame at time = 10s revealed adsorbed peptides with surface density of ~ 30 -40 molecules/ μm^2 , primarily comprising small, globular-like structures of different sizes (Figure 2. 1a). Corresponding movies with duration of 500 secs show the differently sized peptide species with varying surface diffusion speeds (*Supplementary Movie S1*). For statistical analysis of structural dimensions, Matlab software algorithms were firstly used to desegment imported avi movies into individual frames followed by automatic threshold detection of frame objects to obtain parameters such as area (nm^2), width (nm), length (nm) and height (average pixel intensity) (*See Methods Section*). In addition, tip broadening effects are expected to occur when the object's size is below the radius of tip curvature and therefore the lateral dimensions still represent an overestimation [42]. Histogram analysis of the area showed three distinct peak distributions at 180 nm^2 , 400 nm^2 and 700 nm^2 (Figure 2. 1b), indicating the existence of at least three different forms of A β ₄₂ peptide(s). From the width and length histograms (Figure 2. 1d and e), the main peak distributions occurred at 15 nm and 20 nm, respectively, indicating the size of the most abundant A β ₄₂ peptide species. In addition, a second peak distribution occurred at higher values of 36 nm, particularly for the width (Figure 2. 1d) and a similar range of higher values is observed in skewed (non-normal; right tail) histogram of length (Figure 2. 1e). Two other main observations included a much smaller peak distribution between 6-12 nm (Figure 2. 1e, arrow) specifically for length and sampling of significantly higher values of \sim up to 100 nm but with no clear distribution (Figure A1). For the height, two clear peak distributions are observed at $\sim 2.8 \text{ nm}$ and another at 9.2 nm (Figure 2. 1c).

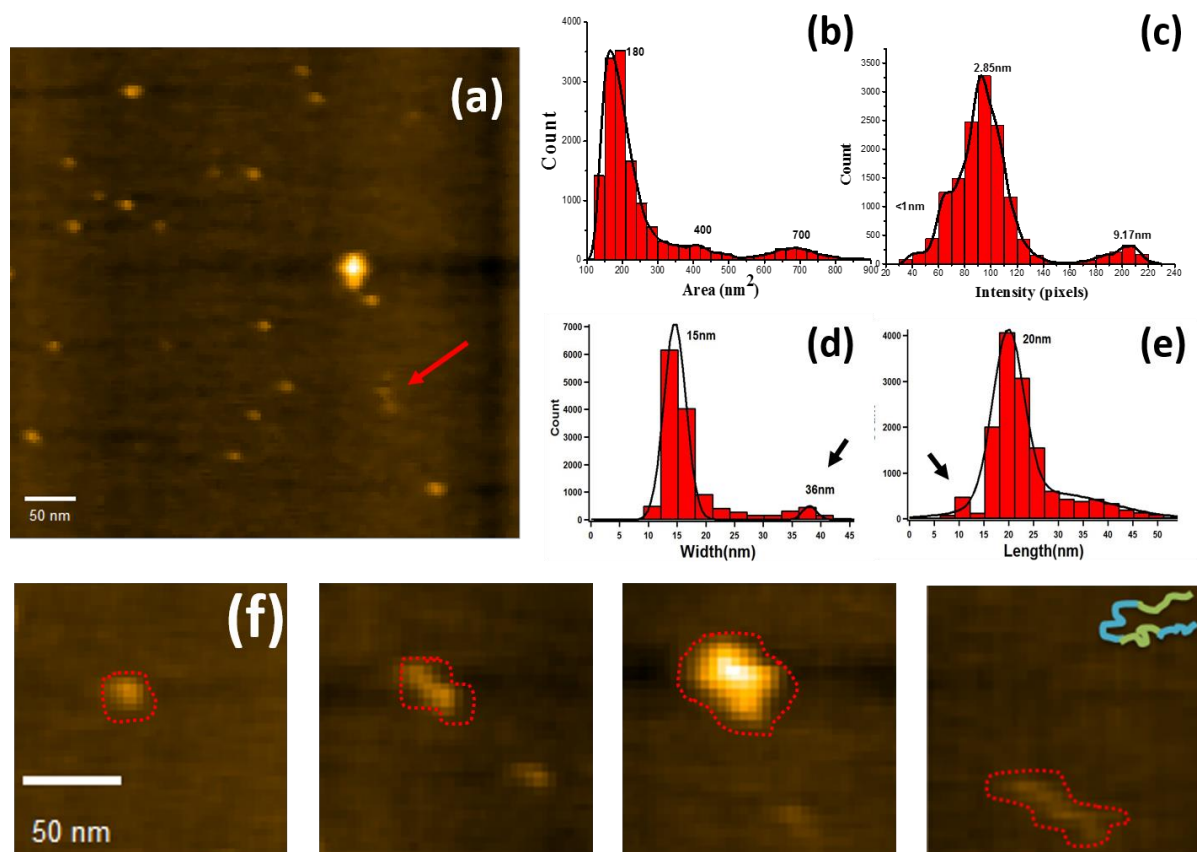


Figure 2. 1. Morphology and dimensions of $A\beta_{42}$. (a) Representative HS-AFM image of $A\beta$ species on mica surface in PBS (Scan size: 500nm, imaging rate: 2frames/second). (b-e) Histograms of dimensions, area (b), height (c), width (d) and length (e). (f) Representative HS-AFM images (from left to right) of $A\beta_{15-20nm}$, $A\beta_{36nm}$, $A\beta_{Agg}$ and disordered or unstructured $A\beta$ monomer.

The existence of different $A\beta_{42}$ peptide species based on their size distributions indicate that the preparation of samples from lyophilized solid peptides dissolved in 1,1,1,3,3,3-hexafluoro-2-propanol (HFIP) does not result in pure monomers but instead leads to associated oligomers and larger aggregates [265, 266]. This is somewhat contrary to the use of HFIP that constitutes a method typically used to minimize peptide aggregation. Once the peptides are resuspended in phosphate buffer saline they are immediately deposited onto the mica substrate for HS-AFM imaging (approximately after 20-30 min) and subsequently rinsed to remove excess free peptide. This sample preparation also does not allow sufficient time for the formation of amyloid fibrils [267], which was intentionally undertaken to only focus on the

interactions and dynamics of A β ₄₂ monomers, oligomers and larger aggregates as opposed to the processes of fibril formation as done by several others in AFM studies [192, 268].

Similar rounded structures of A β ₄₂ peptide species with dimensions on the order of a few nanometres up to tens of nanometres are routinely observed in A β ₄₀ and A β ₄₂ samples in AFM studies [269, 270]. Without the use of any solvent in the sample preparation, Prabhu et al. [271] similarly reveal a height range of 1.5-2.5 nm for A β ₄₂ to explain the presence of either monomers or small oligomers. Using super sharp tips for AFM imaging, Mastrangelo et al. [190] refer to low molecular weight (LMW) soluble A β ₄₂ oligomers mostly with height of ~ 1-2 nm and diameters ranging from 5-15 nm attributed to monomers or dimers (5-7 nm) and tetramers (~10-15 nm). In the same study based on the HFIP method, higher molecular weight (HMW) oligomers of 15-25 nm in diameter (reduced value after tip correction) with heights ranging from 3-6 nm indicated stacking of 2-3 monomers/dimers units. The HMW oligomers could also retain heights of 2nm, suggesting the formation of planar structures [190]. More recently, Banerjee and Siddhartha et al using HS-AFM show similar A β oligomer structures and distribution of sizes, including compact (5-7 nm), bilobed (20 nm) and larger aggregate structures, though are differently assigned to specific trimers, pentamers and heptamers, respectively [230]. A point of difference in this study is that a photochemical cross-linking method is used to enable isolation of A β according to their size and purity, giving a priori knowledge of the sample distribution.

Theoretical and experimental measurements give a size of ~ 1 – 1.5 nm for single A β monomers [255, 272, 273], thus our HS-AFM observations clearly represent several monomers and what appear to be mostly oligomers and larger aggregates. Previous AFM studies have shown that the lateral dimensions of A β , often up to tens of nanometers, exceeds the most probable height of 2 nm and which is also the case in this study. Specifically, the lateral dimensions were shown to vary linearly with the height, suggesting that the latter is actually a

true representation, i.e. the $A\beta$ is not perfectly spherical but more closely resemble oblate spheroids [274, 275]. As mentioned above, similar sizes of $A\beta_{42}$ measured by AFM have previously been attributed to various forms, including pentamers, tetramers, and HMW oligomers. Here, we refer to the most abundant distribution of $A\beta$ species with peak distributions of 2.8 nm and 15-20 nm (length-width) (and correlating to an area of 180 nm²), as $A\beta_{15-20nm}$, since defining an exact number of monomer units is difficult. For example, in this compact structure (Figure 2. 1f, far left image) the individual monomers cannot be resolved due to insufficient AFM tip resolution. The larger-sized species of 36-40 nm are referred to as $A\beta_{36nm}$ and effectively relate to a doubling of size compared to $A\beta_{15-20nm}$. The $A\beta_{36nm}$ form corresponds to images showing a bilobed structure, consisting of two rounded, compact structures lying planar on the mica surface (Figure 2. 1f, middle left image). Interestingly, similar 20 nm bilobed structures were recently observed by Banerjee and Siddhartha using HS-AFM and identified as pentamers produced using a photochemical cross-linking method [230]. We interpret $A\beta_{36nm}$ as consisting of significantly greater number of monomers, which also retain a height of 2.8 nm, indicating a planar structural configuration. $A\beta_{36nm}$ may however orientate themselves perpendicular to the substrate, giving a doubling in height of ~ 4 nm but the same footprint area as the $A\beta_{15-20nm}$ (Figure 2. 1f). This is responsible for a broadening of the height distribution in the histogram (Figure 2. 1c) and evident in further analysis of height values described below in Figure. 2.1c. The largest structures, presumably giving a peak area distribution of 700 nm², length/width values of $\sim > 40$ nm and up to 100 nm, and very distinct height distribution at 9.2 nm are clearly larger aggregates and referred to as $A\beta_{Agg}$ (Figure 2. 1f, middle right image). Furthermore, a small peak between 6 -12 nm for length (Figure 2. 1e, arrow) combined with heights of ~ 1 nm is more closely indicative of structures equivalent to dimensions of lower molecular weight (LMW) oligomers such as dimers, trimers or tetramers, as described in previous AFM studies [276, 277]. To date, a range of $A\beta_{42}$ oligomer structures,

generally referred to as amyloid-beta derived diffusible ligands (ADDLs), globulomers and protofibrils, are described in several reviews [278-280]. Contrary to early theories on A β ₄₂ existing in only stable monomeric or dimeric states, Teplow et al and others [73, 281] reveal a mixture of monomers, dimers, tetramers, and HMW oligomers, specifically ‘paranuclei’ (planar hexamers), stacked hexamers and dodecamers.

Additional less-well, structurally defined A β ₄₂ species, as opposed to the rounded conformations of A β _{15-20nm}, A β _{36nm}, A β _{Agg}, are observed transiently appearing in the HS-AFM movies (*Supplementary Movie S1*) and a representative snapshot given in Figure 2. 1f (far right image). However, due to their significantly lower heights of < 1 nm, they were not easily identified by automated threshold detection for analysis. In fact, they were most noticeable when observing movies as they appeared transiently, e.g. flickering of the height contrast, in a scan area for < 1-2 sec, indicating their fast surface diffusion (*Supplementary Movie S1*). *Supplementary Movie S2* more clearly indicates the appearance of these species by freezing the relevant frames. Separate AFM cross-sectional analysis show these A β ₄₂ forms to be ~ 25-30 nm in size and ~ 1 nm in height (Figure A2). We suggest that these forms are associated with significantly smaller, soluble A β ₄₂ monomers that are known to be largely disordered or unstructured in solution [190], although exact details of their transient conformational states or dynamics is unclear. Recent studies using FRET analysis show that both A β ₄₀ and A β ₄₂ comprise an ensemble of rapidly reconfiguring unfolded states, with no long-lived conformational states [282]. Molecular dynamics simulations support that the peptides have configurations consistent with random polymer chains, with the vast majority of conformations lacking significant secondary structure [273, 283]. When considering tip broadening effects, the measured size of 25-30 nm correlates to an estimated contour length of an unfolded A β ₄₂ monomer (i.e. 42 amino acids ~ 20 nm).

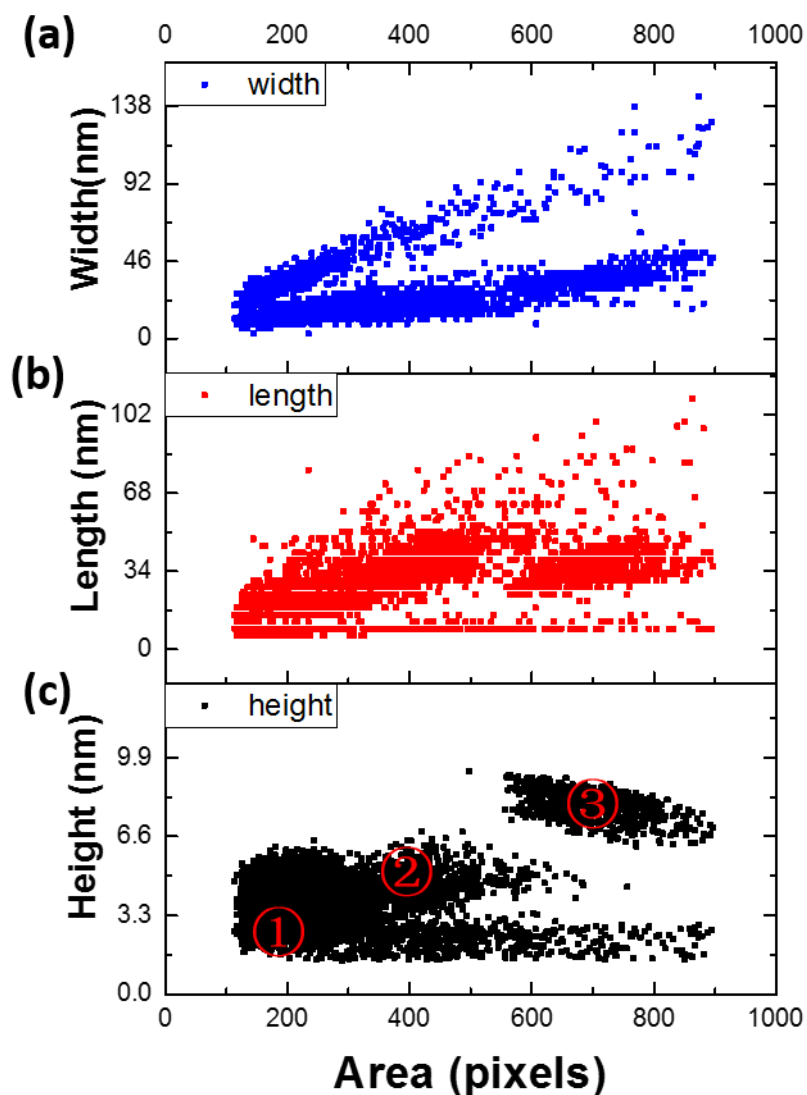


Figure 2. 2. Scatter plots of different dimensions, width (a) length (b), height (c), versus area of A β species.

The relationship between the dimensional parameters (length, width, height, area) is shown in Figure 2.2 to better understand the structural configurations of the different A β_{42} species. Importantly, it is noted that Figure 2.2 represents the preformed A β_{42} species arising from the sample preparation, i.e. lyophilized peptide from HFIP followed by resuspension in PBS, as opposed to their formation after deposition on the mica surface. Herein, the length versus width shows a linear relationship (Figure A3), indicating the different peptide species generally retain a spherical structure as their size increases, which is also qualitative evident in

the HS-AFM images in Figure 2. 1. Two different linear trends for width (or length) versus area values are observed (Figure 2. 2a and b); the first trend (i) shows that as expected a change in both width (or length) is proportional to the area. In contrast, the second trend (ii) shows a significantly smaller, or negligible increase in width (length) as a function of increasing area. This is due to the analysis method whereby the width and length are defined as increasing in value in the y-scan and x-scan directions, respectively. Thus, the effective width or length approaches zero if measured in the opposing scan direction. A height versus area plot reveals a region (1) where the height remains constant at ~ 2.5 nm with increasing area up to 800 nm^2 (Figure 2. 2c). This indicates preformed aggregates can exist as planar structures with constant height and presumably form by the lateral addition of monomers. In contrast, regions (2) and (3) show an increase in height, firstly to 4.8 nm and then 7.8 nm, respectively. Specifically, the increase to 4.8 nm, while retaining the area of $\sim 200 \text{ nm}^2$, suggests this may be related to perpendicular reorientation of the larger $A\beta_{42}$ species, e.g. $A\beta_{36\text{nm}}$, on the mica surface. At heights of 4.8 nm, further increases in the area to 400 nm^2 , indicates the preformed aggregates can increase in size in both 2D and 3D. However, no further height increases are observed for areas of 200 nm^2 and 400 nm^2 . This interestingly leads to a ‘jump’ in height and area to 7.8 nm and area $600\text{-}800 \text{ nm}^2$, respectively, for the $A\beta_{\text{Agg}}$. These discrete changes in height as a function of area (Figure 2. 2c), suggests that there is likewise a formation of discrete, preformed $A\beta_{42}$ species, as opposed to randomly sized oligomers and aggregates, during the sample preparation of peptides.

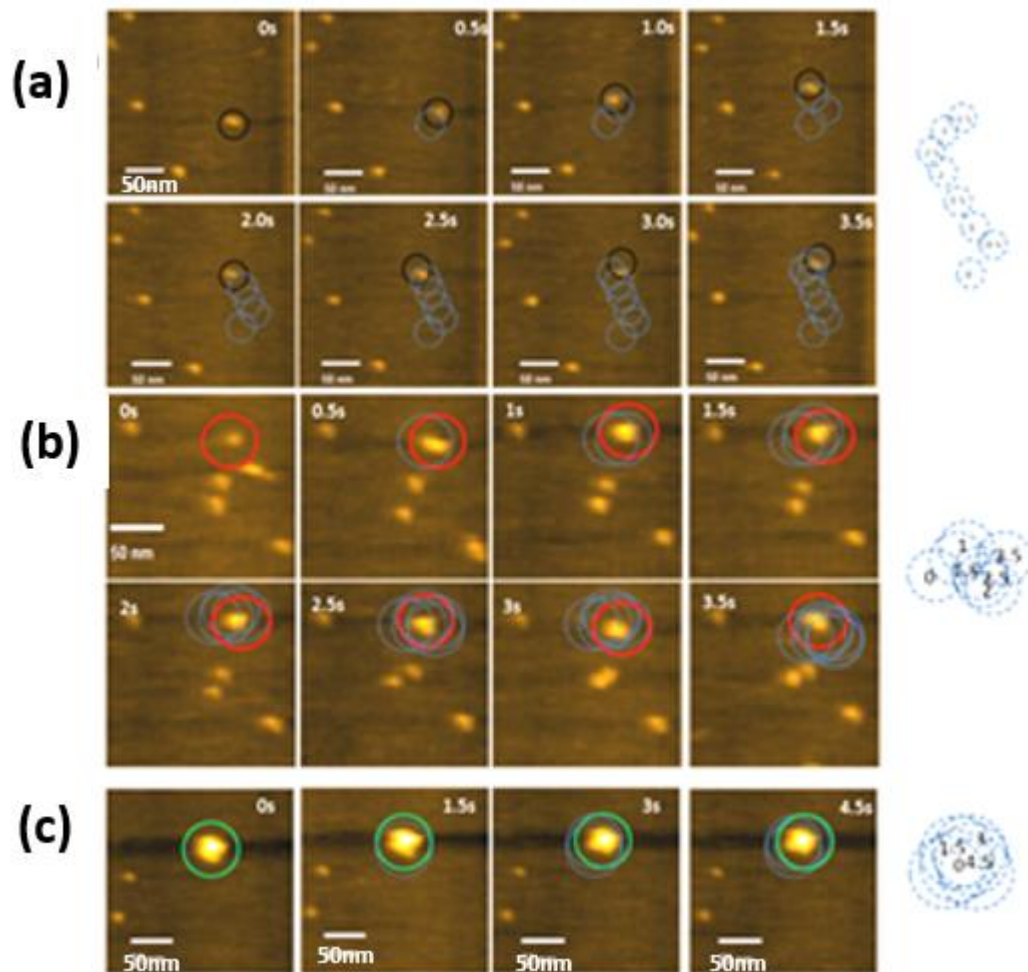


Figure 2. 3. Filmstrip from HS-AFM movies showing the diffusion of individual $A\beta_{15-20nm}$ (a), $A\beta_{36nm}$ (b), and $A\beta_{Agg}$ (c) molecules. In each filmstrip, the solid coloured circle delineates the current frame position of the individually tracked $A\beta_{42}$ species, while dashed circles denote the series of positions from the previous frames. (Imaging rate: 2frames/second)

2.3.2 Surface Diffusion and Interactions of Different $A\beta_{42}$ Species

Matlab software was used to automatically track the motion of the different $A\beta_{42}$ forms in movies (2 frames/sec) for a duration of 20 secs. In addition to Matlab software analysis, representative filmstrips showing their diffusion are given in Figure 2. 3 and further corresponding movies in *Supplementary, Movies S3, S4, S5*. In each filmstrip, the solid coloured circle delineates the current frame position of the individually tracked $A\beta_{42}$ species,

while dashed circles denote the series of positions from the previous frames. The distance moved by the $A\beta_{42}$ species decreases as their size increases from the $A\beta_{15-20nm}$, $A\beta_{36nm}$ to $A\beta_{70nm}$ (Figure 2. 3). Slopes of distance versus time plots of individually tracked $A\beta_{15-20nm}$, $A\beta_{36nm}$ and $A\beta_{70nm}$ further emphasizes the differences in diffusion speed (Figure 2. 4). Interestingly, ‘steps’ are found in the slopes of $A\beta_{15-20nm}$ and this occurs to a lesser extent for $A\beta_{36nm}$ but is not observed for $A\beta_{70nm}$ (Figure 2. 4a). The steps are due to a significant increase in the distance moved by the $A\beta_{15-20nm}$, i.e. up to 40-50 nm, within the period of a few frames. Following these steps, the $A\beta_{15-20nm}$ resumes its normal rate of diffusion. Reasons for the sudden bursts in diffusion speed are not fully clear though may relate to changes in surface-absorption [284]. Quantitative analysis of the average mean square displacement ($n = 10$) is shown in Figure 2. 4b, corresponding to diffusion coefficients of $3.51\pm 0.72\text{nm}^2 \text{sec}^{-1}$, $0.77\pm 0.38\text{nm}^2 \text{sec}^{-1}$ and $0.39\pm 0.22\text{nm}^2 \text{sec}^{-1}$, respectively. Further analysis of the fast diffusing monomers in Figure 2. 1f (far right image) and *Supplementary Movie S2* was not undertaken because these peptides only existed in the scan area for a period of 1~2 frames, as mentioned above. In this case, the monomers are able to traverse an entire scan area of 500 nm within a few seconds, giving an estimated speed of $> 2500 \text{ nm sec}^{-1}$. (See Table 2.1) It is worth mentioning that those unique activities with increased sizes can be also explained by the AFM imaging artifacts that normally caused by tracking a moving object [285].

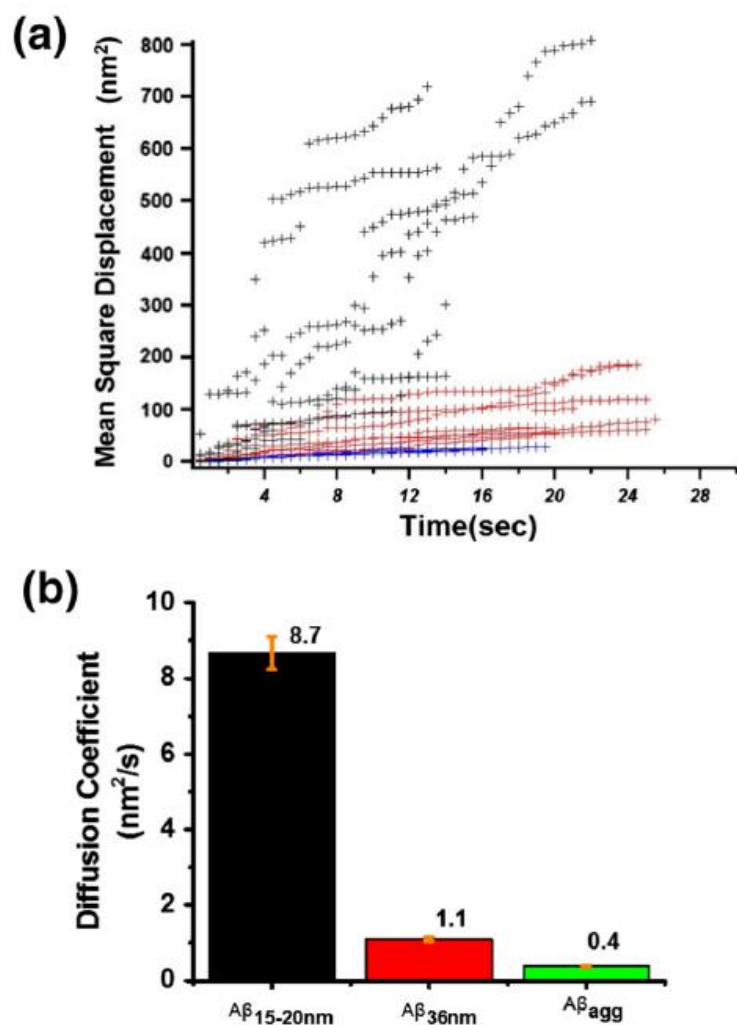


Figure 2. 4. MSD versus time plot of individually tracked Aβ_{15-20 nm} (black), Aβ_{36 nm} (red) and Aβ_{Agg} (blue) molecules. $MSD = \langle |r(t) - r(0)|^2 \rangle$, where $\langle \rangle$ means the average, $r(t)$ is the position of each molecule in determined time t , $r(0)$ is the reference position of each molecule. (b) Average diffusion coefficient of $8.7 \pm 0.44 \text{ nm}^2 \text{ s}^{-1}$ (Aβ_{15-20 nm}), $1.1 \pm 0.06 \text{ nm}^2 \text{ s}^{-1}$ (Aβ_{36 nm}) and $0.4 \pm 0.01 \text{ nm}^2 \text{ s}^{-1}$ (Aβ_{Agg}) obtained by fitting slopes in panel a. Errors are standard deviation, $n = >10$ molecules.

Representative filmstrips show examples of commonly observed interactions between the different preformed Aβ species, i.e. once deposited on the mica surface, namely where there was either 2D formation of elongated structures or addition of species in the z-direction giving increases in height (Figure 2. 5). For example, after 0.8 sec, an Aβ_{15-20nm} (2) moves closer to an Aβ_{Agg} (3) until they undergo binding at 1.4 sec and remain as a complex (2+3) for the remainder of the filmstrip (Figure 2. 5a). In this case, the complex (2+3) increases in width-length (and area). At 1.6 and 3.4 sec, further interactions within the complex (2+3) show the

$A\beta_{15-20nm}$ “rebinding” to the top of the $A\beta_{Agg}$, causing an increase in height (stacking in Figure 2. 5a) but no significant change in the area. Following this in Figure 2. 5b, $A\beta_{15-20nm}$ (1) and a new $A\beta_{15-20nm}$ (4) enter the scan area and both interact with complex (2+3) (4.0 secs), resulting in elongation and formation a small, protofibril-like structure. To visualize the dynamics of the entire process, see *Supplementary Movie S6*. These collective interactions involve interactions occurring in the z-direction ($2 \leftrightarrow 3$) and x-y direction ($1 \leftrightarrow \text{complex } (2+3) \leftrightarrow 4$), demonstrating a combined growth process to form new $A\beta$ species. In general, these types of interactions are dynamic and qualitatively could be either short-lived or long-lived, for example, the protofibril structures were only transient compared to more stable HMW oligomer/aggregate complexes.

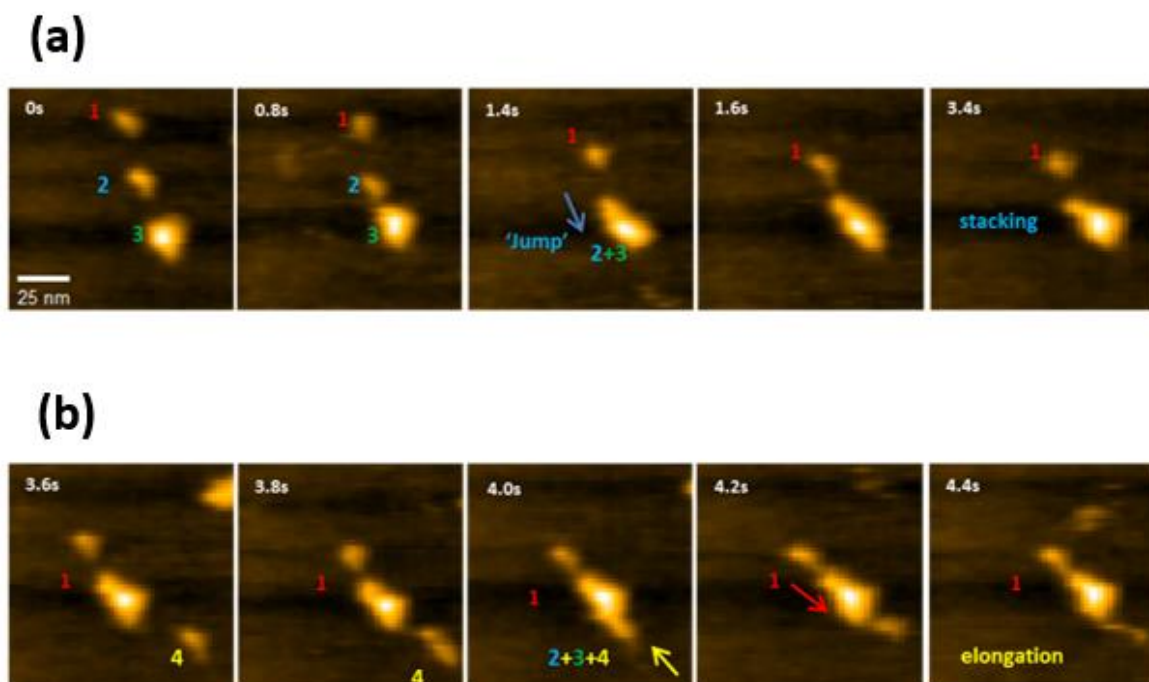


Figure 2. 5. Filmstrip from HS-AFM movies showing (a) sequence of interactions between $A\beta_{15-20nm}$ (1 and 2) and $A\beta_{Agg}$ (3) involving binding of $A\beta_{15-20nm}$ (2) on top of $A\beta_{Agg}$ (3) (stacking to form complex 2 + 3). (b) Continuation of sequence in (a) showing formation of elongated structure due to interactions of $A\beta_{15-20nm}$ (1 and 4) with complex (2 + 3). Scale bar:25nm. Imaging rate: 5frames/s

2.3.3 Kinetic Parameters of Single Molecule A β 42 Binding

The ability to directly ‘watch’ single molecule interactions in action between the different A β ₄₂ species provides a unique opportunity to quantify kinetics underlying the process of oligomerization. Here, we quantify the binding kinetics by measuring the amount of time two molecules spend in physical contact, which is defined by the formation of image contrast between the two molecules. Significantly, we extract kinetic parameters, e.g. mean lifetime $\langle t \rangle$ and dissociation rate constant, k_{off} ($1/\langle t \rangle$), for specific interactions between the A β _{15-20nm} \leftrightarrow A β _{15-20nm}, A β _{15-20nm} \leftrightarrow A β _{36nm}, and A β _{15-20nm} \leftrightarrow A β _{Agg} (Figure 2. 6a-c). An important distinction for this type of HS-AFM-based analysis is involvement of the peptide-surface (mica) interaction and its role in diffusion-limited effects on the intrinsic association/dissociation rates of the A β species. For instance, the A β species can come in contact via diffusion, after which they undergo binding at a rate governed by their intrinsic association rate constant. Conversely, the A β species dissociate with an intrinsic rate constant, after which they move apart via diffusion. Therefore, the time spent in contact between two species is may be influenced by diffusion, which as shown in Figure 2. 3 differs depending on the size of the A β species.

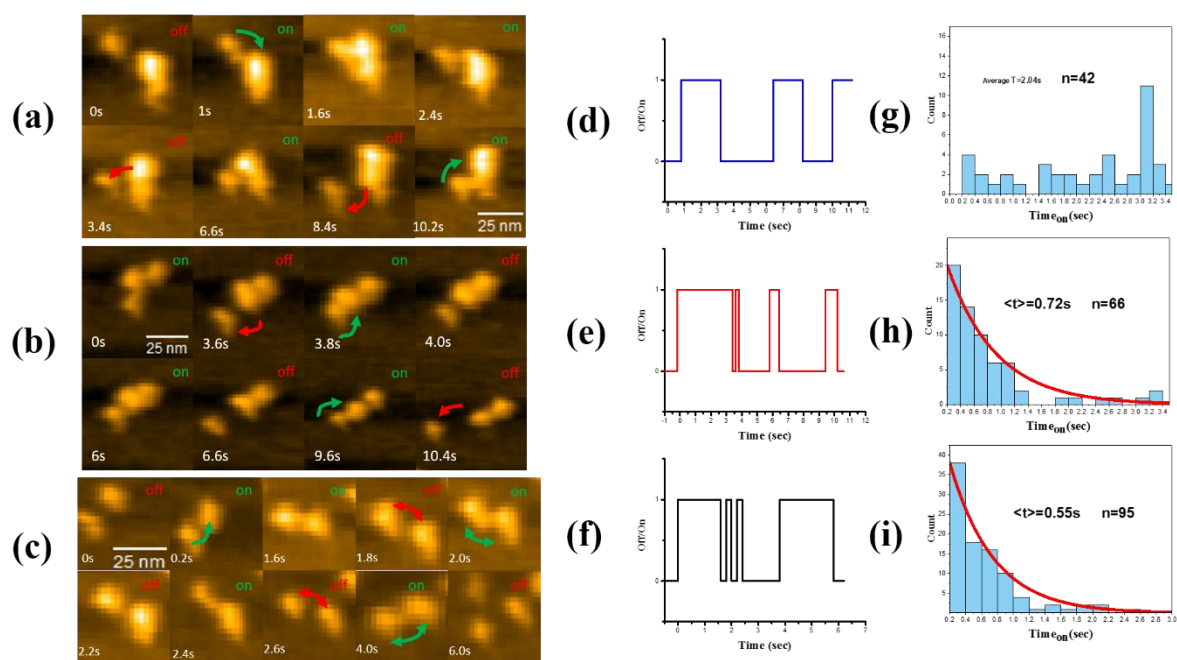


Figure 2. 6. Single molecule kinetics data analysis based on HS-AFM. (a-c) HS-AFM filmstrips showing interactions between (a) $A\beta_{15-20nm}-A\beta_{Agg}$, (b) $A\beta_{15-20nm}-A\beta_{36nm}$, and (c) $A\beta_{15-20nm}-A\beta_{15-20nm}$. Molecules in contact (green 'on') are in the bound state. Imaging rate: 5frames/s. (d-e) Representative traces of single molecule lifetimes. (g-i) Life-time distributions for the bound state of (g) $A\beta_{15-20nm}-A\beta_{Agg}$, (h) $A\beta_{15-20nm}-A\beta_{36nm}$, and (i) $A\beta_{15-20nm}-A\beta_{15-20nm}$. Distributions in (h) and (i) are fit to a single exponential decay.

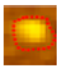
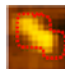
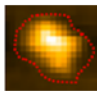
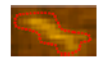
For this analysis, the binding is directly visualized as being 'on' or 'off' (Figure 2. 6a-c) to produce single-molecule lifetime traces (Figure 2. 6d-f) that are analogous to those commonly obtained using fluorescence techniques, e.g. single molecule FRET [286, 287]. *Supplementary Movies S7, S8, S9* show corresponding movies of the different $A\beta$ interactions represented in filmstrips in Figure 2. 6a-c. Life-time distributions for the bound state show a single exponential decay law for the $A\beta_{15-20nm} \leftrightarrow A\beta_{15-20nm}$ and $A\beta_{15-20nm} \leftrightarrow A\beta_{36nm}$ (Figure 2. 6h-i), indicating a single step binding process that yields one characteristic lifetime for these types of interactions. A mean lifetime $\langle t \rangle = 0.55 \pm 0.22$ sec, with dissociation rate constant k_{off} ($1/\langle t \rangle$) = 1.82 sec^{-1} , for the $A\beta_{15-20nm} \leftrightarrow A\beta_{15-20nm}$ compared to the $A\beta_{15-20nm} \leftrightarrow A\beta_{36nm}$ with a mean lifetime = 0.72 ± 0.28 sec ($k_{off} = 1.39 \text{ sec}^{-1}$), indicating the latter to some extent forms more tightly bound complexes due to its slower dissociation rate. It could also be that the slower dissociation rate is partially governed diffusion, whereby with the order of the magnitude slower diffusing $A\beta_{36nm}$ on the mica surface, even weaker interactions are sufficient to keep them in contact for measurable periods of time. In contrast, lifetime distributions for the $A\beta_{15-20nm} \leftrightarrow A\beta_{Agg}$ show a randomized histogram of shorter-lived through to longer-lived complexes (Figure 2. 6g), indicating a distribution of interactions energies or barriers that the $A\beta_{15-20nm} \leftrightarrow A\beta_{Agg}$ complex must overcome in order to dissociate. When considering the effects of diffusion, the $A\beta_{Agg}$ is also an order of magnitude slower compared to the $A\beta_{15-20nm}$ and effectively static on the mica surface, with the an $A\beta_{15-20nm}$ acting as a faster diffusing ligand. Under these conditions, the $A\beta_{15-20nm}$ diffusion may influence the dissociation rate, however, it is not expected to significantly alter the energy landscape of the unbinding pathway(s). Thus, the randomized histogram is suggested to be intrinsic to the $A\beta_{15-20nm} \leftrightarrow$

$A\beta_{Agg}$ interaction and is different to an exponential decay of lifetimes, indicating all molecules undergo the same process with a single well defined energy barrier, as the case for the $A\beta_{15-20nm} \leftrightarrow A\beta_{15-20nm}$ and $A\beta_{15-20nm} \leftrightarrow A\beta_{36n}$ complexes in Figure 2. 6h-i.

Kinetic parameters for single molecule $A\beta$ peptide interactions have only previously been determined by another AFM-based technique, single molecule force spectroscopy (SMFS). For the SMFS, a monomeric peptide is attached to a substrate, for example via a heterobifunctional cross-linker molecule such as N-hydroxysuccinimide-polyethylene glycol-maleimide [288], and the opposing monomer is bound to the AFM cantilever tip [289]. By bringing the peptide functionalized tip into contact with the substrate, the measurement of single molecule unbinding forces as function of loading rate, referred to as dynamic force spectroscopy (DFS), enables kinetic and thermodynamic parameters to be extracted, yielding a useful comparison of k_{off} and bond lifetimes. Yu et al. [253] carried out DFS measurements to understand the amyloid related misfolding and aggregation of α -synuclein in Parkinson's disease. At pH 5, a single energy barrier to unbinding of single α -synuclein monomers, or dimer dissociation, gave k_{off} of $\sim 3.74 \pm 1.99 \text{ sec}^{-1}$ with lifetimes of 0.27 sec. More weakly bound $A\beta_{40}$ monomer-monomer interactions give k_{off} of $\sim 9.4 \pm 1.50 \text{ sec}^{-1}$ with shorter lifetimes of $0.1 \pm 0.01 \text{ sec}$ at pH 7 [290]. Lv et al. [251] compared both $A\beta_{40}$ and $A\beta_{42}$, giving k_{off} of $9.0 \pm 2.4 \text{ sec}^{-1}$ ($0.11 \pm 0.03 \text{ sec}$) and $5.7 \pm 0.3 \text{ sec}^{-1}$ ($0.18 \pm 0.01 \text{ sec}$), respectively, revealing stronger inter-peptide interactions for $A\beta_{42}$ than for $A\beta_{40}$. Specifically for $A\beta_{42}$ monomer-monomer unbinding, Hane et al. [291] tested multiple DFS models (Bell-Evans and Friddle-De Yoreo), giving k_{off} of $\sim 7-12 \text{ sec}^{-1}$ with lifetimes of 0.14 – 0.09 sec, while comparable k_{off} of $\sim 12.5 \pm 9.62 \text{ sec}^{-1}$ and lifetimes of $0.09 \pm 0.7 \text{ sec}$ were obtained in a further study on the effect of copper ions [292]. From these SMFS studies, it is now understood that $A\beta$ dimeric complexes have high stability, dissociating over a period of seconds, i.e. $\sim 5 - 12 \text{ sec}^{-1}$, due to the monomers adopting antiparallel binding structures as shown in MD simulations

[293]. This is very different to intramolecular interactions of monomers that occur on much shorter micro-to-nanoseconds timescales [294], suggesting that the dimerization process measured in SMFS may be an important protagonist in the early aggregation process. To date, the peptide functionalization in SMFS studies is only configured for the interaction between two monomers [252, 253] i.e. dimerization, though it is expected that clever functionalization strategies in future will enable SMFS on a range of A β oligomer structures. Using our HS-AFM-based analysis theoretically allows for kinetic information on multitude of combinatorial A β interactions, including those consisting of multiple monomer units.

Table 2. 1. Summary of properties of different A β species

Summary of A β properties	A β_{15-20} nm	A β_{36} nm	A β_{Agg}	Unstructured A β
				
Width (nm)	15.4 ± 3.2	16.5 ± 4.6	35.7 ± 3.8	–
Length (nm)	19.0 ± 5.1	34.4 ± 6.8	34.1 ± 10.7	25.5 ± 4.4 ^a
Height (nm)	2.8 ± 0.7	2.8 ± 0.7	9.2 ± 2.5	1.1 ± 0.3 ^a
Area (nm ²)	177 ± 60.4	385 ± 93.8	670 ± 80.4	–
Diffusion coefficient (nm ² s ⁻¹)	8.7 ± 0.44	1.1 ± 0.06	0.4 ± 0.01	>2500 ^a
Lifetime (s)	0.55 ± 0.22 ^b	0.72 ± 0.28 ^c	^d	–
k_{off} (s ⁻¹)	2.17 ± 0.87 ^b	1.64 ± 0.64 ^c	^d	–

Width, length and height values of A β_{15-20} nm, A β_{36} nm, and A β_{Agg} obtained from histograms in Fig. 1 and Supplementary Fig. 2. Extraction of values from HS-AFM videos using MATLAB algorithm of automated threshold detection. Peak values and error (fit width) are obtained from multi-peak fitting (Igor Pro, Wavemetrics).

^a For the unstructured A β , length and height values obtained by cross-sectional analysis in HS-AFM software (Wavemetrics, Igor Pro). Diffusion coefficient estimated from diffusion speed of 100 nm/s; therefore, MSD > 100 nm². For diffusion coefficient, $D = MSD/4t$, then $D > 10^4/4 = 2500$ nm² s⁻¹. Errors are standard deviation.

^b Lifetime and k_{off} for interactions between A β_{15-20} nm ↔ A β_{15-20} nm.

^c Lifetime and k_{off} for interactions between A β_{36} nm ↔ A β_{15-20} nm. Errors from fitting exponential decay in Fig. 6h and i.

^d A β_{36} nm show randomized lifetime histograms; thus, no lifetime and k_{off} is obtained.

2.4 Conclusions

Significantly, the HS-AFM analysis suggests that the formation of aggregates such as $A\beta_{agg}$ are driven by kinetic heterogeneity, indicating a shift in the mechanism of oligomerization. We attribute this “opportunistic” or permissive binding to the presence of different conformation states of the $A\beta_{agg}$, resulting in a variety of accessible interacting groups. Inevitably, this is likely to lead to the formation of different complexes or alloforms, which is known to contribute to the complexity and challenges in identifying $A\beta$ oligomer toxicity. Equally for ensemble kinetic measurements, nucleation-limited aggregation of $A\beta_{40}$ peptide is shown to be controlled by a stochastic factor inherent in the nucleation process, leading to substantial macroscopic heterogeneity [295]. More recently, Nag et al. [296] refer to ‘metastable’ $A\beta_{40}$ oligomers that are thermodynamically unstable but show a large kinetic barrier, which is mostly entropic in origin. The monomers are said to be entangled in the initial oligomeric state, with multiple intra- and intermolecular hydrophobic interactions aiding in their entanglement. At the single molecule level, Orte et al. [297] recently report on stochastic behaviour in early stages of oligomer fibril formation by the SH3 domain from bovine phosphatidylinositol-3-kinase (PI3-SH3). Using two-color single-molecule fluorescence they show that although the size distribution of detected SH3 oligomers remains virtually constant with increasing aggregation time, they constitute a highly heterogeneous ensemble of species, which is explained by a stochastic polymer-like assembly process [297]. Molecular dynamics simulations of the early steps of aggregation provide evidence that the associating and initially monomeric polypeptide chains can sample and stabilize early aggregates of considerably different structures [298], with considerable conformational flexibility, thereby enabling the formation of very different conformational arrangements [299]. Such observations are testament to oligomers showing a high degree of polymorphism, as a result of stochastic

fluctuations in polypeptide chain dynamics. Evidence is increasingly pointing to heterogeneity as a protagonist in aggregation. For example, variations in oligomer conformation and associated interactions, and not just specificity in oligomer size, may be responsible for biological toxicity, as demonstrated for HypF-N protein [300]. Our study contributes to this emerging narrative by quantifying the kinetic parameters of different A β species consisting of oligomers and aggregate forms, in particular confirming a distinct change in the energy (binding) landscape occurring at the onset of interactions with aggregate species, i.e. A β _{Agg}.

In conclusion, single molecule kinetic data can make significant contributions to 'kinetic' distribution models that depict aggregation pathways, but which still lack the assignment of fully quantitative kinetic constants to their various pathways. The sizes and distribution of A β ₄₂ species presented here agree with previous AFM studies but in particular the HS-AFM movies emphasizes the dynamic and transient states that exist within and between the different species. In assimilating to current models, the findings show that interactions between smaller A β species (A β _{15-20nm} and A β _{36nm}) present a single exponential decay of lifetimes, while interactions with larger aggregates is driven by a type of kinetic heterogeneity. The latter enables the formation of long-lived, stable A β aggregates. It is necessary in future HS-AFM studies to investigate the influence of peptide-surface interactions and diffusion parameters on quantitative analysis of kinetic parameters; though such studies are also relevant to the effects of cell membrane surfaces and other intracellular substrates that may play a role in the formation of A β oligomers/aggregates. In addition, implementing well-defined A β peptides, e.g. comprising recombinant peptides or those with structures known *a priori*, will assist in rationalizing AFM characterization of peptide dimensions and together with new insights on A β dynamics from HS-AFM, exciting advances in understanding A β ₄₂ interactions can be explored.

Chapter 3: Visualizing Real-Time Nucleation and Growth Mechanisms of Single A β ₄₂ Oligomers

3.1 Introduction

Alzheimer's disease (AD) is a neurodegenerative disorder characterized by the presence of senile plaques and neurofibrillary tangles [301-305]. Recent studies on the conformational structure and aggregation of A β species have revealed that a subset of soluble, non-fibrillar A β [46, 72], referred to as amyloid β -derived diffusible ligands (ADDLs) [58, 68], are primarily responsible for neurotoxicity instead of fibril-induced neuronal death described by the earlier "amyloid cascade hypothesis" [34]. Several studies have shown that soluble oligomeric A β species may be the initial effectors of neurodegeneration rather than A β fibrils [306-309]. Similarly, for all types of A β peptide assemblies, the soluble oligomers and larger aggregates formed during the A β aggregation are reportedly more toxic than some initial species such as monomers [59, 104, 310].

Evidently, the molecular mechanisms and kinetics associated with the formation of pathological A β oligomers and aggregates, involving monomer-dependent nucleation processes is of significant interest. In primary nucleation, the growth of individual nuclei only involves monomer addition and can occur in bulk solution (homogeneous nucleation) or at a surface which is not already made up of the monomer (heterogeneous nucleation). A monomer-dependent secondary nucleation process, whereby the surface of an existing structure made up

of the same monomer, e.g. amyloid fibril, “catalyses” the growth of new nuclei, was more recently discovered for A β ₄₂ and since demonstrated for other proteins such as islet amyloid polypeptide and α -synuclein in Parkinson’s disease [103, 311-313]. This secondary nucleation mechanism explains the shortening of the lag-phase fibril growth through addition of pre-formed fibrils, or “seeds”, into a monomer solution. As mentioned, while the general consensus is that toxicity is mainly associated with oligomers above the amyloid fibrils, recent in vitro studies further reveal a strong toxic effect from A β oligomers produced by secondary nucleation of monomers on fibril surfaces [104, 314, 315]. Herein, an understanding of these nucleation processes, leading to the formation of toxic oligomers, serves to identify potential therapeutics that either control or inhibit their growth process.

Various studies have shown that an acidic pH environment, higher peptide concentration, extending incubation times, and even the presence of a solid substrate are important predictive factors in promoting amyloid deposition [316-319]. Moreover, in-vitro studies have shown that A β is not an intrinsically insoluble peptide and the solubility (and toxicity) of A β peptide is critically dependent on the aqueous environmental conditions such as pH [320, 321]. For example, the α -helical structure of A β ₄₂ is favoured at pH 1 to 4 while the neurotoxic β -sheets as well as fibril formation occur under acidic conditions from pH 4 to 7 [320, 322-324]. In addition, A β ₄₂ peptides are shown to self-assemble rapidly from insoluble aggregates into fibrils at pH 5.0 in comparison with pH 7.4 [316, 317]. By reducing the pH to 4.6, the native conformation of A β peptides can change into less-ordered structural aggregates during the fibril growth stage [325]. Klug et al. [326] also demonstrated that A β aggregation induced by low pH occurred via a different pathway that is associated with slow aggregation process of stable A β species.

Studies on the effect of peptide concentration have reported that A β ₄₀ formed a stable dimer at relatively low concentration of 25 μ g/ml, while high concentrations significantly

promoted the formation of helix structures, which are believed to inhibit or slow fibrillogenesis. Thus, the latter leads to greater formation of intermediate aggregates [327, 328]. Lomakin et al. have demonstrated that there is a critical A β concentration for the aggregates to spontaneously initiate fibrillogenesis [191, 329]. In addition, the rate of nucleation depends on both the aggregate and monomer concentrations [104].

Monomer interactions with surfaces can also play a role, with two main factors (intrinsic and extrinsic) widely reported to affect the monomer-dependent nucleation processes and subsequently alter the lag phase [103]. For example, a growing number of mutants in A β sequence variants in the amyloid precursor protein (APP) gene (e.g. A21G (Flemish), E22G (Arctic), E22K (Italian), E22Q (Dutch) and the D23N (Iowa) amino acid substitutions) have been identified as beneficial intrinsic agents for clinical relief treatment [330-332]. Extrinsic factors generally include other peptides and proteins [333-336], membranes [337, 338], nanoparticles and substrates [339-344], smaller molecules [345, 346], pH and temperatures [104, 347, 348]. In particular for the effects of surface area, where the catalysis or inhibition of aggregation will be determined by the protein to surface area ratio and the strength of surface attractive forces [342, 349].

Theories of A β monomer-dependent nucleation processes are based on macroscopic kinetic measurements showing classical sigmoid shaped curves that typically consist of three different phases, including lag, growth and plateau phase [350, 351]. During the lag phase, which generally represents the time that is required for nuclei to grow, there also exists a myriad of diverse, parallel molecular interactions occurring between different species, such as the nuclei, intermediates, oligomers and aggregates, involving the aforementioned monomer-dependent nucleation as well as other elongation and fragmentation processes [352-354]. In fact, many of these molecular interactions are ongoing during all phases, and the overall macroscopic (averaged) measurement cannot distinguish between the different molecular

interactions. In particular, the initial nucleus are suggested to form within milliseconds, though characterizing such molecular events at short-timescales in bulk analysis where the detection sensitivity is limited, e.g. not enough aggregate has formed, is a challenge [355, 356]. The concentration of oligomers is also low and they are also highly transient, similarly making it difficult to elucidate their role in the growth process and compounded by a lack of experimental techniques to directly quantify kinetics of single molecule A β species. Therefore, there remains the question as to which molecular interactions occur during these phases, particularly at early time-points where nuclei, oligomer and aggregate species are produced, as this is important for understanding the fundamental mechanisms of amyloid formation.

Herein, we use High-Speed Atomic Force Microscopy (HS-AFM) to directly visualize the formation and growth of nuclei, followed by their subsequent interactions with existing seeds and inter-molecular interactions to produce new aggregates. HS-AFM enables the visualization of protein structural-dynamics and is beginning to bridge the gap by decreasing structural imaging times from minutes to millisecs [357]. It massively surpasses the capabilities of current AFM systems by enabling acquisition times of ~50 milliseconds per image (~ 20 frames/second). This takes AFM into the realm of video rate imaging that is defined as achieving speeds of ~ 12-13 frames/sec, coupled with the ability to achieve 1-2 nanometer lateral image resolution, this technique has recently been used to visualize dynamics of A β in 'action', including the interactions between single oligomeric and aggregated species [358]. We specifically investigate A β on a solid substrate (mica), where a local concentration of diffusing monomers exist at the liquid-solid interface, and through a pH-triggered nucleation process are able to directly visualize the growth of single nuclei followed by the formation of single oligomers and aggregates in real-time.

3.2 Materials and Methods

3.2.1 Preparation of A β ₄₂ samples

Amyloid-beta protein fragment 1-42 (A β ₄₂ peptide) was purchased as a lyophilized solid and more than 95% purity was guaranteed by HPLC from Sigma-Aldrich (High Performance Liquid Chromatography). A β ₄₂ peptide samples were prepared according to previous methods of [319, 347]. 1 mg of lyophilized solid peptides were firstly dissolved in (1,1,1,3,3,3-hexafluoro-2-propanol (HFIP) to prevent aggregation and then aliquot into 50 small microcentrifuge tubes. After 30 minutes incubation at room temperature in a chemical fume hood, the HFIP peptide solutions were allowed to evaporate for 60 minutes and the re-lyophilized peptides stored at -20°C. Lyophilized peptides were solubilized using phosphate-buffered saline (PBS) (pH 7.4) at a concentration of either 20 μ g/ml, 50 μ g/ml or 100 μ g/ml and then vortex mixing applied for 20 seconds prior to use. To investigate the effect of pH on peptide samples, two different methods were used. The ex-situ method involved either maintaining a pH of 7 (i.e. using the peptide samples solubilized in PBS) or adjusting the pH to 3 or 11 by addition of HCl or NaOH prior to depositing the peptide solution on a mica substrate for HS-AFM imaging, as described below. Alternatively, the in-situ method involved firstly depositing the peptide solution in PBS (pH 7) for HS-AFM imaging and then during the imaging using a pipette to inject 2 μ l of concentrated HCl or NaOH into the sample solution. After 'spiking' the sample solution, further mixing could be applied by withdrawing/injecting the solution via pipetting.

3.2.2 High-Speed Atomic Force Microscopy

To prepare samples for imaging, 2 μ l of the A β ₄₂ peptide solution was pipetted onto a 1.5 mm diameter freshly cleaved mica disc (Cat No. 7101) and incubated for 2 minutes to allow the

peptides to adsorb onto the mica surface. 2 μ l of fresh PBS was then added and pipetted in/out of the sample solution, and this was repeated several times to exchange the sample solution in order to remove excess A β ₄₂ peptides that had not adsorbed onto the mica surface. The sample was then placed into the liquid cell of the HS-AFM. HS-AFM imaging was performed using an ANDO-model (Research Institute of Biomolecule Metrology Co., Ltd., Japan) in tapping mode with high frequency, small cantilevers (BL-AC10, Olympus) remodified with the carbon-tip, as described above. During imaging, the free oscillation amplitude of the cantilever was set to \sim 2 nm and the set point amplitude was kept to \sim 90% of the free amplitude. The maximum possible scanning rate is calculated as $R_{\max} = (\lambda f)/(2WN)$, where λ is the amplitude, f is feedback bandwidth, W is the scanning size and N is the corresponding number of scan lines. A non-electrode wide scanner with range of 4 μ m * 4 μ m, z scanner with maximum height of 700 nm were used with typical scan speeds of 2-4 frames/sec for 500 nm scans. Higher resolution scans of 200 nm were taken at 5-10 frames/sec with 550-275 lines/sec. HS-AFM imaging was performed on samples of different peptide concentrations (20 μ g/ml, 50 μ g/ml or 100 μ g/ml), incubation times (1h, 2h and 4h) of the peptide in the PBS (pH 7) prior to commencing the imaging, and pH of 3, 7, and 11 using either the ex-situ or in-situ method. The imaging was performed for a typical duration of 10 minutes to 120 minutes or until it was clear that tip quality had reduced, presumably due to adhesion of peptides on the tip. For each sample condition at least three separate imaging experiments using new tips were performed. The operation of the HS-AFM and collection of the AFM movies was obtained by modified software in Igor Pro, Wave metrics. AFM movies were either analysed using Igor Pro or exported as an AVI. Movie file for further analysis using Matlab algorithms.

3.2.3 Statistics analysis

Values obtained from the Matlab analysis of HS-AFM movies included the peptide area, intensity (height), width and length as mentioned in Chapter 2. All data analysis and histograms were produced using Igor Pro, Wave metrics. Multi-peak fitting with Lorentzian or Gaussian functions were applied to the histograms. The peak values shown in histograms are representative size of each species of peptide (with error bars indicated). Origin was used to plot the peptide area versus intensity in Fig.3.1, 3.2, 3.3 (g, h, i).

3.3 Results/Discussion

3.3.1 Ex-situ A β : Effect of concentration, incubation time and pH

3.3.1.1 Concentration

Ex-situ preparation of samples was used to assess the effect of sample conditions such as A β concentration, solution pH and incubation time on the formation of oligomer or aggregate species. The A β_{42} peptide was resuspended in PBS solution (in Eppendorf tubes) at either different A β_{42} concentrations of 20, 50, 100 $\mu\text{g/ml}$ or pH of 3, 7, or 11 (20 $\mu\text{g/ml}$ A β_{42} in PBS by addition of HCl or NaOH). After approximately 30 minutes, these samples were deposited on the mica surface and imaged with the HS-AFM. To investigate the effect of time, 20 $\mu\text{g/ml}$ A β_{42} solutions at pH 7 were incubated for either 1 hr, 2 hr or 4 hr prior to imaging with HS-AFM. In all samples, HS-AFM imaging commenced \sim 2-5 min after the peptides had been allowed to adsorb to the mica, i.e. the time required to align the laser and approach the tip to sample surface. Three representative snapshots taken from HS-AFM movies at 1.0 frames/sec at time = 1.0 sec of A β_{42} peptides prepared with solution concentrations of 20 $\mu\text{g/ml}$, 50 $\mu\text{g/ml}$ and 100 $\mu\text{g/ml}$ are shown in Figure 3.1A-C. Corresponding movies with duration of 500 secs (*supplementary Movie S1, S10 and S11*) show the peptide dynamics, particularly their surface diffusion and, in many cases, physical interactions occurring between the peptides. For 20 $\mu\text{g/ml}$ samples at pH 7, particulate or globular structures of various sizes were observed with surface density of \sim 30-40 molecules/ μm^2 and exhibited three area distributions at $170 \pm 34\text{nm}^2$, $410 \pm 67\text{nm}^2$ and $645 \pm 37\text{nm}^2$ and two height distributions at $3.2 \pm 1.2\text{nm}$ and $7.7 \pm 0.8\text{nm}$ (Figure 3.1a and 3.1b). These different distributions of the A β dimensions are in agreement with the three main species observed in the previous chapter, referred to as A $\beta_{15-20\text{nm}}$, A $\beta_{36\text{nm}}$ and A β_{agg} , and ascribed to the existence of A β_{42} oligomers and larger aggregates that represent

pre-formed species arising from the sample preparation, i.e. lyophilized peptide from HFIP followed by resuspension in PBS, as opposed to their formation after deposition on the mica surface. Increasing the A β ₄₂ sample concentration to 50 and 100 μ g/ml retained the three main distributions for area though the peak values appeared to shift to lower values (Figure 3.1a-c), while the lower height distribution clearly showed an increase in peak value to the point where at 100 μ g/ml the two height distributions effectively coalesced to form a single distribution. Scatter plots of the height (pixel intensity) versus area (Figure 3.1g-i) with identical scales also clearly distinguished the 3 main A β ₄₂ distributions at 20 μ g/ml (Figure 3.1g), which were increasingly overlapping and less distinct at the higher concentrations of 50 μ g/ml (Figure 3.1d) and 100 μ g/ml (Figure 3.1f). A β with concentration range from 20 μ g/ml to 100 μ g/ml deposited on mica surface all exhibited three main populations although a slightly decrease in area and increase in height occurred with increased concentration, suggesting an interesting trend: the decreasing peptide size is correlated to the increasing height, and the Figure 3.1g-i showing relation between these two parameters indicated the tendency toward formation of a single population.

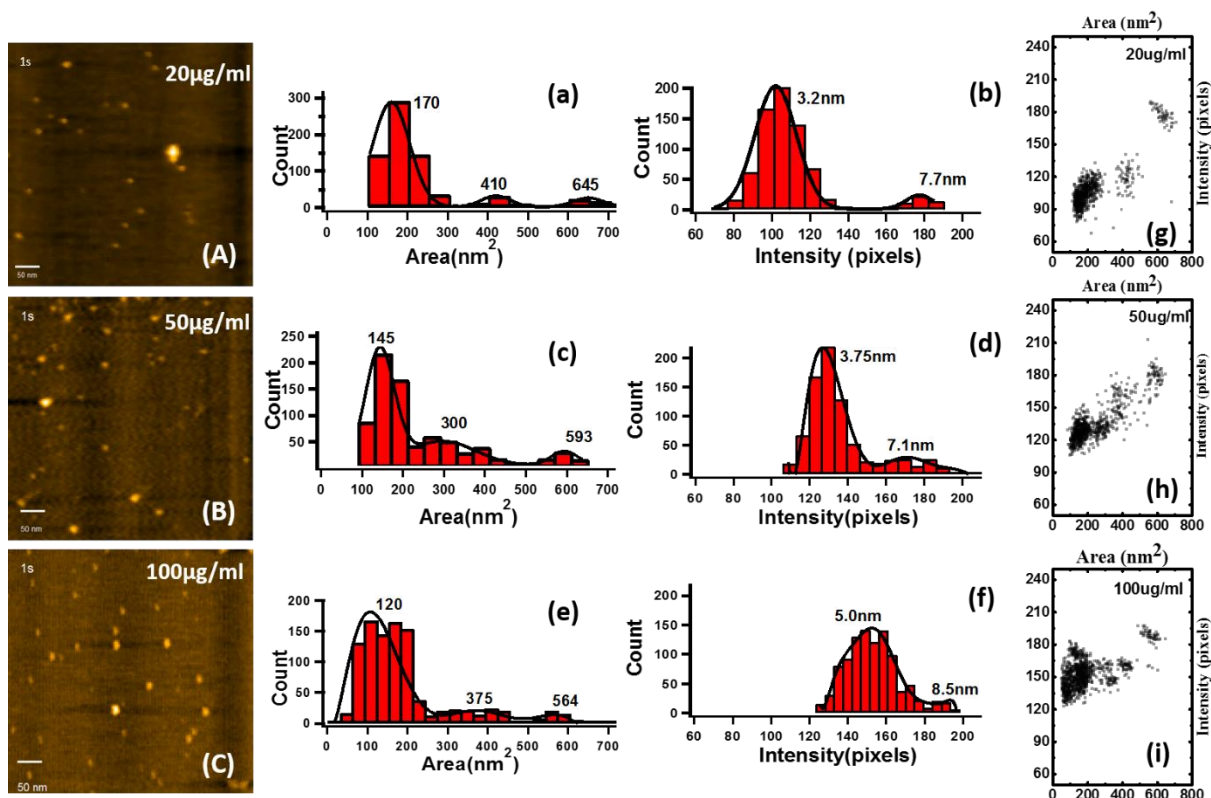


Figure 3. 1. Morphology and structural dimensions of different concentration Aβ₄₂ peptides. (A-C) Representative HS-AFM image of 20 μg/ml, 50 μg/ml and 100 μg/ml concentrated Aβ₄₂ peptides diffuse on the surface of mica. (Scan scale: 500*500nm, imaging rate: 1frame/second. (a-f) Histograms of different structural dimensions distributions. Area (a, c, e), Height (b, d, f). (g-i) Scatter plots of area and height shows their relationship.

3.3.1.2 Incubation time

Starting from intact lyophilized solid peptides, and then after 1 h, 2 h or 4 h incubation in PBS at neutral pH 7, the peptides were imaged at 1 frame/sec with a scan area of 500nm. Corresponding snapshots from movies of peptides after 1 h incubation are equivalent to those in Figure 3.1A that were taken under the same conditions (i.e. 20 μg/ml, pH 7 and 1 h incubation) and displayed in Figure 3.2A again for comparison with the longer incubation times. (*Supplementary Movie S1, S12 and S13*) After 2 h and 4 h incubation, three similar peak distributions for area were observed in Figure 3.2c and Figure 3.2e, respectively. However, there appeared to be no significant difference in the peak values compared to 1 h incubation. In contrast, similar to increasing concentration, increasing the incubation time to 2 and 4 h

resulted in a comparable increase in height of the peptides (Figure 3.2d and Figure 3.2f). At 2 h incubation, the main height distribution increased to a peak value of 4.3 nm, with a further increase to 4.6 nm occurring at 4 h incubation. Both of the longer incubation times also continued to show the secondary distribution at higher peak values of 7.4 (2 h) and 8.6 nm (4 h) (Figure 3.2d and Figure 3.2f). Similarly, scatter plots of height versus area showed that the three main populations became less distinct with increasing incubation time, primarily due to the increasing height values. In summary, the effect of peptide concentration and incubation time both showed the involvement of the three distinct area, and two height distributions of the A β , as observed in the previous chapter (and displayed again for comparison in Figure 3.1A and 3.2A). These arise from pre-formed structure in the sample preparation. It is observed that by increasing either concentration or incubation time of samples prepared ex-situ, there is some modification to these preformed structures, namely an increase in size apparent from a measured increase in height by approximately 40-50%.

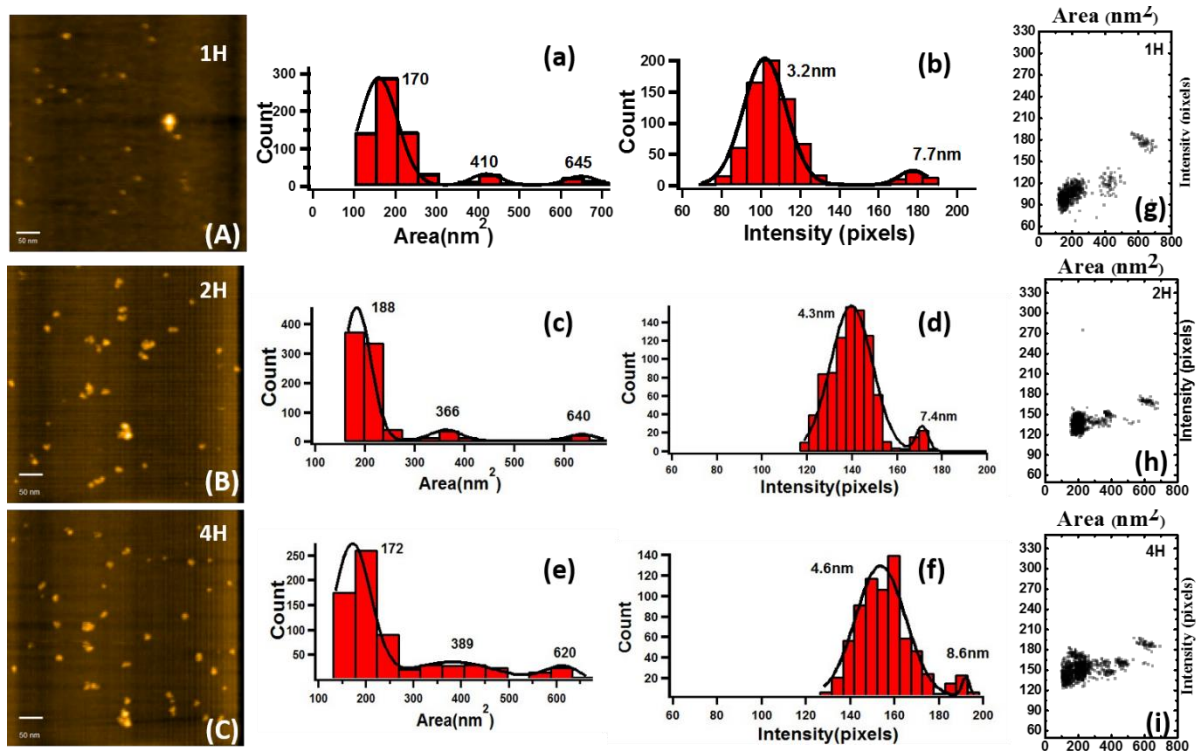


Figure 3. 2. Morphology and structural dimensions of different incubation time A β ₄₂ peptides. (A-C) Representative HS-AFM image after 1h, 2h and 4h incubation of A β ₄₂ peptides diffuse on the surface of mica. (Scan scale: 500*500nm, imaging rate: 1frame/second. (a-f) Histograms of different structural dimensions distributions. Area (a, c, e), Height (b, d, f). (g-i) Scatter plots of area and height shows their relationship.

3.3.1.3 Effect of Solution pH

Filmstrip from HS-AFM movies of 20 μ g/ml peptide samples at pH 3 (Figure 3.3A), pH 7 (Figure 3.3B) and pH 11 (Figure 3.3C) showed distinct differences, especially with regards to the presence of larger A β peptides formed under acidic conditions. (*Supplementary Movie S1, S14 and S15*) In addition, a significantly lower number of adsorbed peptides with surface density \sim 10-20 molecules/ μ m² were observed under alkaline conditions (pH 11) compared to neutral and acidic pH, with values of \sim 30-40 molecules/ μ m² and \sim 55-66 molecules/ μ m², respectively. Compared to the histogram analysis of the neutral solution condition (plotted in Figure 3.3B for comparison), only two peak distributions for area at 251 nm² and 620 nm² were observed for pH 3 (Figure 3.3a), with the former, main distribution representing almost a doubling in size of the peptides. In addition, the two peak height distributions showed an 50-80 percentage increase in size to 4.3 nm and 13.5 nm (Figure 3.3b), which again was equivalent to a \sim doubling in height compared to the pH 7. It is worth mentioning that the observation of proto-fibrils and mature fibrils were also achieved after longer incubation time in pH 3, (*Supplementary Movie S16, S17 and S18*) however, no further analysis was conducted due to the fact that species formed at early stage are of more interest. In contrast, at pH 11, only one peak distribution for area was observed at 108 nm² (Figure 3.3e), corresponding to a single height distribution of 2.5 nm (Figure 3.3f). Scatter plots of the height versus area interestingly showed that at pH 3 the peptides from the main distribution for area with peak value of 251 nm² were responsible for both height distributions. For example, most of the peptides within the main area distribution corresponded to heights of 4.3 nm, but a smaller sub-population corresponded to the heights at 13.5 nm, i.e. values $>$ approximately 300 pixels in Figure 3.3g.

Furthermore, the larger area peptides at 620 nm² actually had similar heights to those smaller peptides representing the main distribution (Figure 3.3g). Evidently, under the alkaline conditions the scatter plots confirmed the existence of only a single distribution of peptides (Figure 3.3i). Owing to the huge changes under the acidic conditions, we further pursued the effect of low pH for in-situ experiments, as described below.

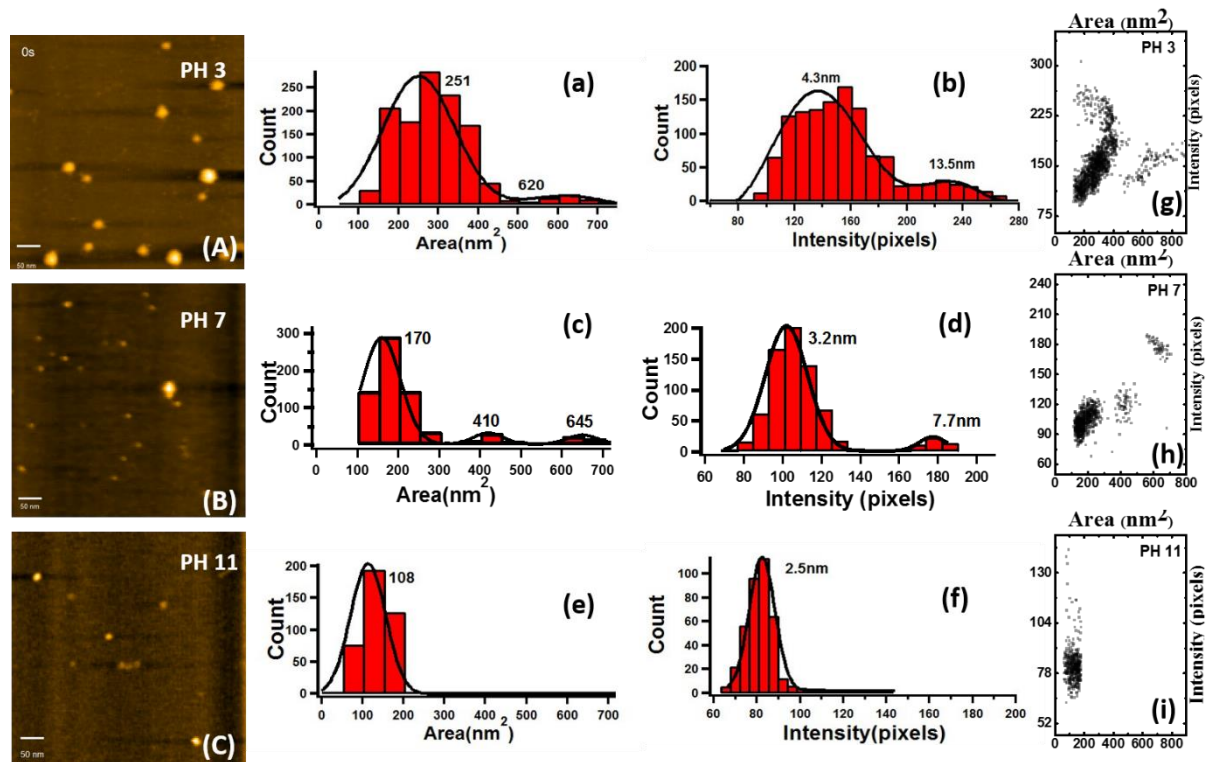


Figure 3. 3. Morphology and structural dimensions of A β ₄₂ peptides incubated in different pH solution. (A-C) Representative HS-AFM image of A β ₄₂ peptides diffuse on the surface of mica in different pH solution. (Scan scale: 500*500nm, imaging rate: 1frame/second. (a-f) Histograms of different structural dimensions distributions. Area (a, c, e), Height (b, d, f). (g-i) Scatter plots of area and height shows their relationship.

3.3.2 In-situ amyloid beta nucleation process

In the previous chapter and this study, the different A β oligomers and aggregates are already pre-formed or assembled during the sample preparation and prior to deposition on the mica surface. However, an understanding of their origin and formation directly from the A β monomer requires observations of early stages such as initial nucleation steps and subsequent

growth. Since the range of A β concentration and incubation time used in ex-situ sample preparation resulted in only pre-formed structures, with relatively small change in their dimensions, it was not expected that these sample conditions would enable in-situ HS-AFM observation of dynamic nucleation and/or growth processes, at least within the timeframe of the HS-AFM experiments. Further to this, the typical duration of the HS-AFM imaging, e.g. 10mins – 2 hours, is significantly shorter than the general time (\sim typically days) for A β_{42} aggregate or fibril formation, which is also dependent on various environmental factors [359, 360]. In contrast, low pH, acidic conditions, produced a greater number (\sim 55-66 molecules/ μm^2) of significantly larger oligomers or aggregates within a relatively short period of time, i.e. 2 hours. In addition, the difference in their morphology and dimensions (Figure 3.4a and 3.6a-b) compared to pre-formed structures (Figure 3.3A-C) suggested that the low pH conditions produced newly formed species and/or induced significant growth of the existing ones. These observations are supported by previous studies that have shown differences in the dynamic formation of the aggregates as a function of pH [361, 362]. Henceforth, it was anticipated that changing to a low pH solution during HS-AFM imaging of the A β_{42} could enable in-situ observations of dynamic pH-dependent processes. To perform these experiments, imaging was initially performed at pH 7 for several minutes until the image was optimised. Whilst continuing the imaging, 2 μl of a 1mg/ml concentrated HCl solution (or NaOH for comparison) was then injected into the liquid cell. After an initial instability resulting in loss of the image, the imaging could be resumed within approximately 20 seconds by adjusting the imaging parameters.

A representative filmstrip with different time-points of an in-situ experiments involving “spiking” with acidic solution is shown in Figure 3.4a. (*Supplementary Movie S19*) We were able to identify four different phases during the imaging process, including i) pre-spike, ii) pre-nucleation, iii) nucleation, and iv) equilibrium growth. These are explained by correlating the

filmstrip images in Figure 3.4a with quantitative analysis of the particle count (Figure 3.4b) and r.m.s surface roughness (Figure 3.4c) versus the time. The particle count is a measure of the number of nucleating A β peptides on the mica, while the surface roughness measured from each movie frame is reflective of both the change in count and size of the particles, i.e. surface roughness increases as more particles nucleate and grow. Prior to spiking with HCl, the A β peptides are observed to be diffusing on the mica surface (Figure 3.4a, frame = 0 sec). During this pre-spike phase (i) there was no significant change in the particle count (Figure 3.4b, frame = 0-30 sec) and surface roughness (Figure 3.4c, frame = 0-30 sec). After spiking with HCl (Figure 3.4a, frame = 30 sec), the perturbation by injecting the solution typically caused the tip to lift from the surface, resulting in loss of imaging. In these cases, the set point oscillation amplitude of the cantilever was re-adjusted to resume imaging of the surface within 20 secs. Qualitative observations of subsequent frames from 30 to 130 sec did not clearly show a change in the number of peptides on the mica surface, though some of the existing peptides showed an increase in size (Figure 3.4a, frame – 30-130 sec). During this period, which was referred to as the pre-nucleation phase (ii), the analysis of particle count showed an increasing fluctuation in values between ~ 0-20 (Figure 3.4b(ii)), while the r.m.s. surface roughness showed a gradual increase from 0.95 nm to 1.03 nm (Figure 3.4c (ii)). Thus, the pre-nucleation phase was characterized by a slow rate of nucleation, involving possible formation of new A β and increased growth of existing A β . Later on at 135 sec, a rapid increase in the appearance of smaller peptides was observed, in addition to the continued growth of existing A β peptides. Analysis of both particle count (Figure 3.4b (iii)) and surface roughness (Figure 3.4c (iii)) from this time-point (135 sec) showed an increase in their values until ceasing at approximately 170 sec. Thus, this period between 135 – 170 sec was referred to as the nucleation phase (iii). Beyond this period (Figure 3.4a, frame – 300 - 400 sec), referred to as the equilibrium growth phase (iv), a significant number of the smaller peptides remained on the mica surface while

both new and existing A β peptide continued to increase in size. This equilibrium growth phase (iv) correlated to a slower rate of increasing r.m.s. surface roughness (Figure 3.4c (iv)), however also showed an unexpected decrease in the particle count (Figure 3.4b (iv)). For the latter, it appeared that the decrease in particle count was due to a decrease in those monomers covering the mica surface, i.e. the mica appeared “cleaner” in regions during the growth phase compared to the nucleation phase, suggesting the consumption of surface adsorbed species during the nucleation/growth process.

Quantitative analysis of the particle height versus time also revealed a similar nucleation and growth profile, including i) pre-spike, ii) pre-nucleation, iii) nucleation, and iv) equilibrium growth (Figure 3.4d). During the pre-spike (i) and pre-nucleation (ii) phases, heights of ~ 3 nm (115 pixel intensity) were observed and rapidly increased to ~ 4 nm (130-140 pixel intensity) during the nucleation (iii) phase after which the height increase proceeded more slowly during the subsequent growth (iv) phase (Figure 3.4d). Similar analysis of the peptide area versus time showed that during the pre-spike phase (i) and pre-nucleation phase (ii) the majority of peptides had an area of ~160-200 nm², which then rapidly decreased (during the nucleation phase) before levelling out to ~120-160nm² in the equilibrium growth phase. The latter can be explained by the increasingly number of newly formed species that have smaller area, which significantly lowers the average area value per frame, compared to those in the earlier pre-spike phase and pre-nucleation phases.

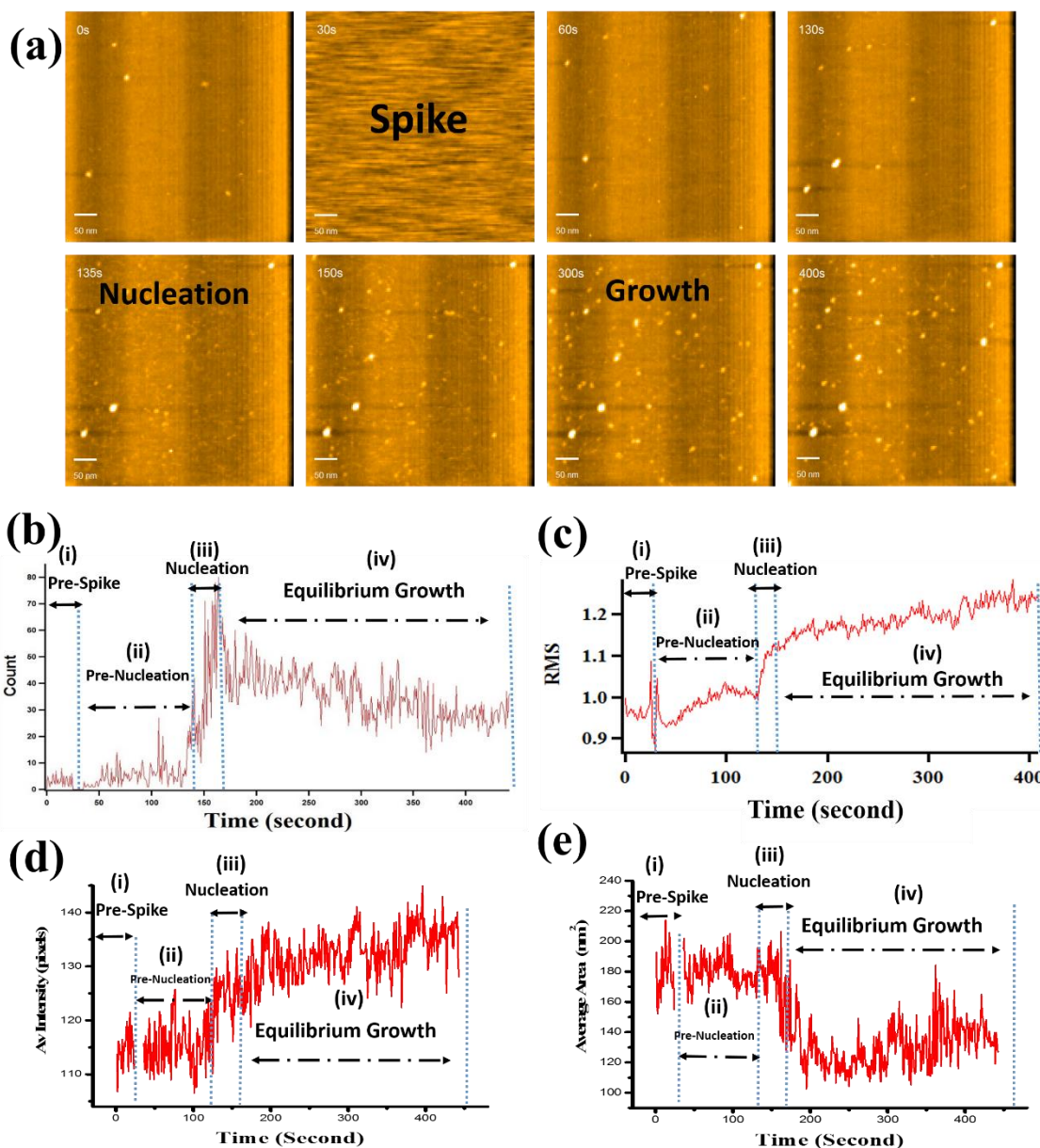


Figure 3. 4. In-situ A β 42 peptides nucleation process at pH 3. (a) HS-AFM Film strip shows the morphology of A β 42 diffusion on mica surface before the Spike (neutral condition, pH 7.4 20 μ g/ml), nucleation stage between spike and growth stage and the stable growth stage after the rapid nucleation process. Scale bar: 50nm. Imaging rate: 2frame/sec. (b) A β 42 peptide numbers distribution among different stages. (c) Surface roughness of A β 42 on mica surface (d) Average height of A β 42 peptides distribution (e) Average Size of A β 42 peptides.

For comparison, similar experiments were conducted in alkaline condition at pH 11. Figure 3.5a shows a filmstrip of different time points, including prior to the ‘spike’ (0 sec), the spike (30 sec) and several subsequent frames out to \sim 380 sec. (*supplementary Movie S20*) Prior to spike, fewer peptides were observed with a low surface density of \sim 10 molecules/ μ m² that is consistent with the results shown in the imaging of ex-situ samples. After the spike, the

surface density remained the same, with most of the existing peptides (black dash circle at =133s) showing minimal surface diffusion. For the remainder of the imaging duration until to 383 sec, no other significant changes were observed. These observations were confirmed by the subsequent analysis of particle count and r.m.s. surface roughness versus time (Figure 3.5b and 3.5c). In these analyses, there was not change in their values post spike, referred to as the stable phase (ii). The increase in surface roughness during the spike is artefact due to loss the loss of imaging.

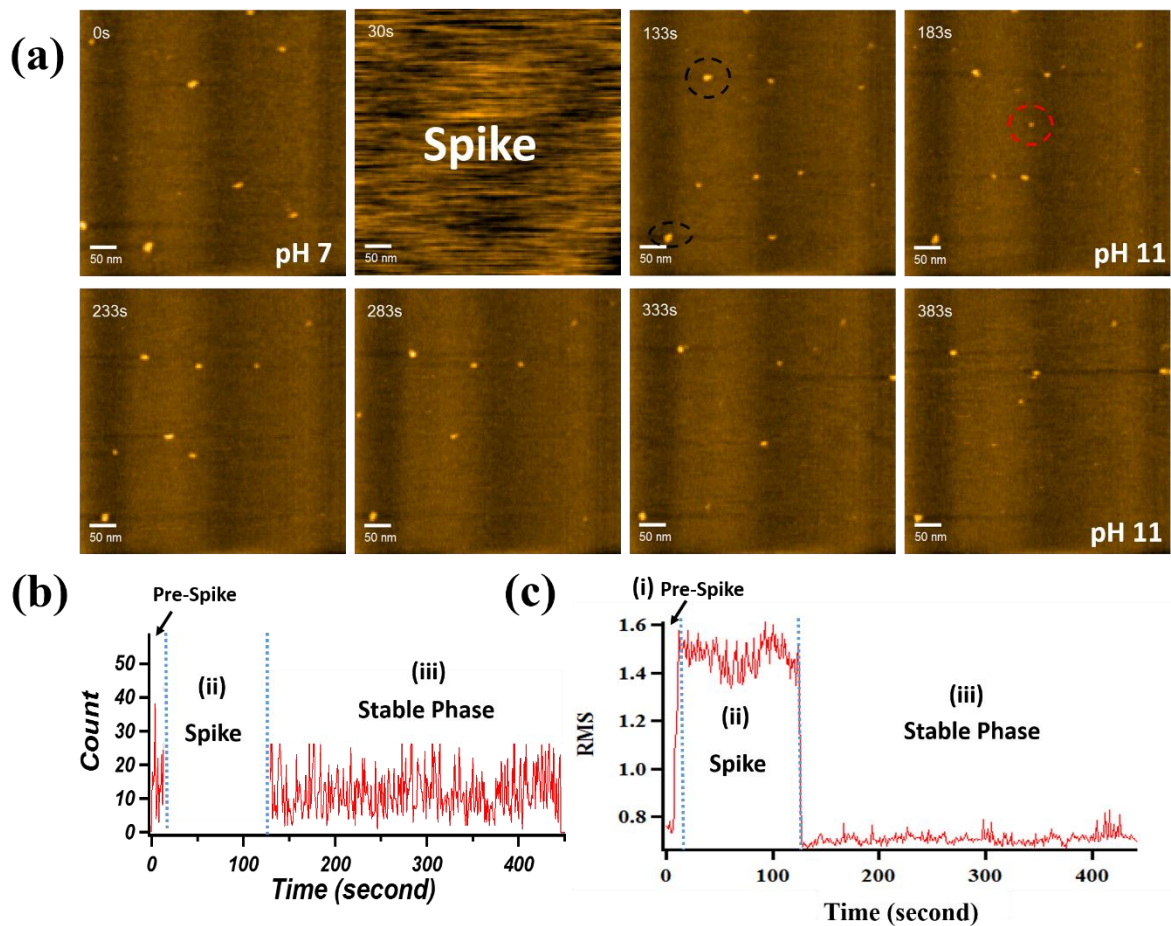


Figure 3. 5. In-situ $A\beta_{42}$ peptides nucleation process in alkaline condition. (a) HS-AFM Film strip shows the morphology of $A\beta_{42}$ diffusion on mica surface before the Spike (neutral condition, pH 7.4 20 $\mu\text{g/ml}$), spike and growth stage. Scale bar: 50nm. Imaging rate: 2frame/sec. (b) $A\beta_{42}$ peptide numbers distribution among different stages. (c) Surface roughness of $A\beta_{42}$ on mica surface.

Further analysis of the dynamic nucleation and growth process at the single particle level is shown in Figures 3.6 and 3.7. In particular, high resolution images of individual molecules were captured and shown in *Supplementary Movie S21, S22 and S23*. Figure 3.6a-b show representative filmstrips before and after spiking with the HCl, with individual particles labelled (no.1-6) for the analysis. From 0-12 secs before the spike, three individual peptides labelled 1-3 were observed to be diffusing freely on the mica surface (*supplementary Movie S19*). This free diffusion phenomena last for 30 seconds until the spiking process, during which the diffusion ability at $8.1 \pm 0.5 \text{ nm}^2/\text{s}$ is consistent with our previous work in neutral condition ($8.7 \pm 0.44 \text{ nm}^2/\text{s}$ for $A\beta_{15-20\text{nm}}$). After spiking these existing peptides (labelled 1-3) are diffusing slower at $\sim 5.8 \pm 0.36 \text{ nm}^2/\text{s}$ and during 64 – 84 sec in the pre-nucleation phase, there is no significant observation though a few newly formed peptides appeared (Figure 3.6b). During the nucleation phase at 154 sec, a significantly greater number of newly formed peptides appeared, with those labelled from 4-6 selected for the analysis. Frames at later time-points of 174 sec and 354 sec indicate that newly formed peptides (dash red circles) and previously existing peptides (dash black circles) co-exist on the mica surface. Figure 3.6c-d show zoomed in images of existing $A\beta$ (3) and newly formed $A\beta$ (5) as they increase in size after spiking the sample with HCl. Additional analysis on the cross-section of individual zoomed in peptides emphasized the dynamic changes on the lateral dimensions as well as the height (Figure A4).

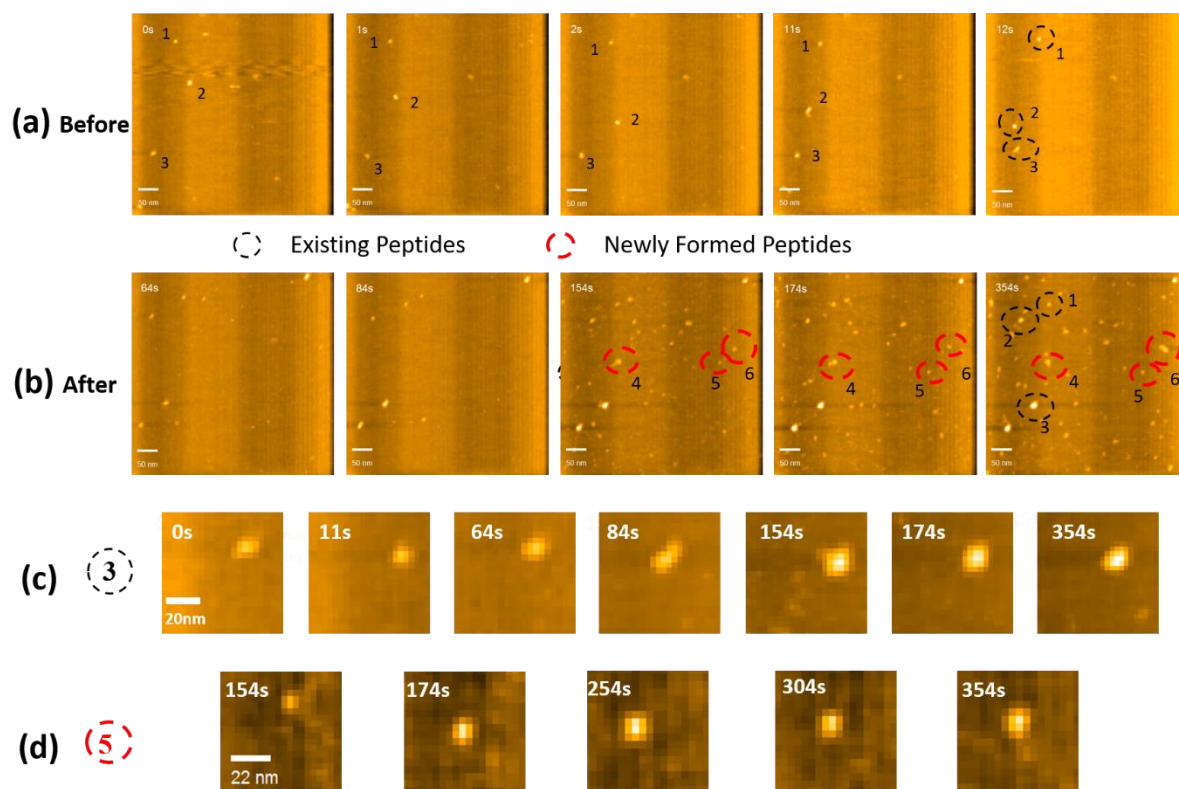


Figure 3. 6. HS-AFM film strip shows the size and position changes of existing peptides appear all the time (dash black circle number 1,2 and 3 as labelled) and newly formed peptides only appeared after the Spike (dash red circle number 4,5 and 6 as labelled).

Kinetic traces of the area and height versus time of those individual peptides labelled in Figure 3.6, including both newly formed and existing peptides, are shown separately in Figure 3.7. For the existing peptides during the pre-nucleation phase (ii), there was significant variation in the area growth rates (nm^2/s) between the peptides (Figure 3.7a). For example, $\text{A}\beta$ (3) showed a faster growth rate ($\sim 1.50 \text{ nm}^2/\text{s}$) followed by $\text{A}\beta$ (2) ($\sim 0.71 \text{ nm}^2/\text{s}$) whereas $\text{A}\beta$ (1) did not appear to increase in area. Beyond the pre-nucleation phase, the area of each peptide effectively plateaued however some fluctuations in the values were still observed (Figure 3.7a). Similarly, for heights of the same existing peptides (Figure 3.7b), equivalent profiles of the traces were observed suggesting that the nucleation and growth is proportional in lateral (area) and normal (height) directions, i.e. sphere-forming growth. For the newly formed peptides, $\text{A}\beta$ (6) appeared after nucleation stage phase (iii) and both the area and height increased during equilibrium growth stage phase (iv) (Figure 3.7c and 3.7d). For the other two peptides, $\text{A}\beta$ (4),

A β (5), it was difficult to observe their initial growth during the nucleation phase (iii) though small increases were observed in the height trace (Figure 3.7d). In the later growth phase (iv) the traces plateaued though again showed fluctuations that we interpret as secondary nucleation process.

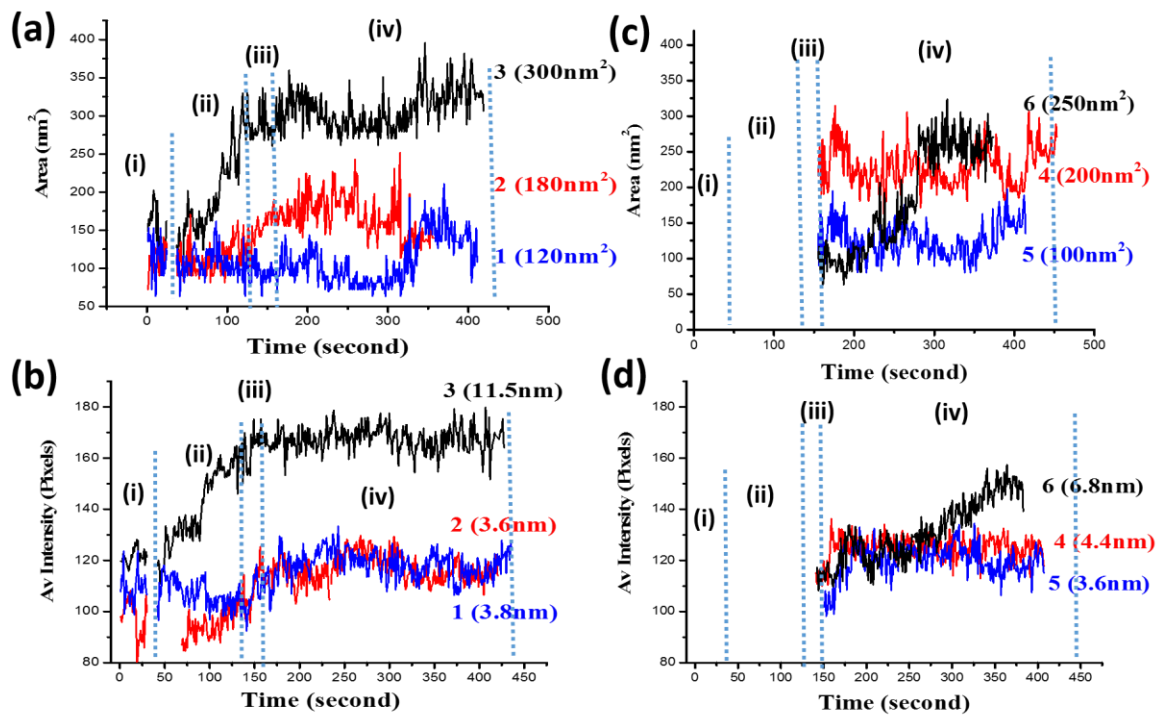


Figure 3. 7. The tracking size and height of existing peptides and newly formed peptides. (a)(b) Representative existing peptides of number 1,2 and 3 shows the size and height changes with the time growing. (c)(d) Representative newly formed peptides of number 4, 5 and 6 shows the size and height changes with the time growing.

3.4 Conclusion

3.4.1 Factors in ex-situ: concentration, pH and incubation time govern the aggregation of A β peptides

One of the key environmental factors believed to influence the A β aggregation process, leading to toxic β -sheet rich oligomeric structures, is the pH [124, 320]. It is also proposed that A β aggregation in the brain may occur in the lysosomal compartments where the pH is about 5.5 [363-368]. Brain injury can also lower the local pH, which in turn may lead to AD [369]. Therefore, understanding the effect of solution pH on the ability to initiate formation of oligomers and aggregates is imperative. Previous AFM studies show that the amyloid aggregation and proto-fibrils formation are very pH-dependent. At neutral pH, A β peptides have limited solubility and produce only spherical aggregates with predominantly β -sheet secondary structure, whereas at acidic pH 4.9 formation of mature amyloid fibrils and proto-fibril can be observed [370, 371]. Similarly, both the ex-situ and in-situ HS-AFM imaging shows that acidic conditions significantly accelerate the peptide aggregation as opposed to alkaline conditions that appears to have a minimal effect. In particular, in-situ imaging revealed that almost immediately after spiking with HCl, the growth of existing peptides occurs followed by a rapid nucleation event that produced mostly newly formed peptides.

These observations relate to a pH-driven protonation/de-protonation of A β residues, previously shown to lead to a change in the net molecular charge from ~ -3 at pH 7 to 0 at acidic pH [372]. Lowering the pH from 7.4 to 6.6 is also shown to reduce the zeta potential of A β_{42} from -35 mV to -25 mV, respectively. A β_{1-40} , has a pI at approximately pH 5.3 [320] though is suggested to be only weakly charged until pH 9 (based on pKa analysis of individual peptides) and becomes strongly charged at pH 12. For closely related A β_{42} , the higher pH

condition likewise increases charge on the monomer, resulting in the presence of stabilized, soluble A β ₄₂ nanoparticles of size ~50 nm [373]. Due to the presence of the mica surface, its pH-dependent surface charge will also play a role in the nucleation and growth observed in the in-situ HS-AFM imaging. Silanol groups of mica are assumed to control the pH-dependent surface charge [374], giving a reduction in zeta surface potential [375] and weak attractive forces at low pH (as opposed to long-range repulsive forces at higher pH) [376].

Therefore, we suggest that two general pH-drive mechanisms, based on the monomer and mica substrate, enable visualization of nucleation and growth of the A β ₄₂ in Figure 3.4a. Firstly, minimisation of mica surface charge at low pH will facilitate surface adsorption of the monomer, which is interpreted as the appearance of the initial surface covering of A β ₄₂ at the onset of the nucleation phase (Figure 3.4a, at 135 sec). In this and previous chapters, this effect may also explain why monomers are not clearly observed at neutral pH, with only the pre-formed larger oligomers and aggregates present on the mica surface. The inability for the monomer to adsorb to the surface at neutral pH would make them difficult to image and may relate to the observation in the chapter 1 of the less well, structurally defined A β ₄₂ species that transiently appeared in the HS-AFM movies and exhibited very fast diffusion (> 100nm/sec). Once the monomer has adsorbed to the surface, minimization of its surface charge too, will then facilitate the binding of additional monomers diffusing toward the surface, leading to nucleation and growth. In addition, the charge minimization of the existing oligomers also facilitate their continual growth during the pre-nucleation phase through to the subsequent nucleation and growth phases.

3.4.2 In-situ amyloid nucleation process A β

Some of the earliest studies on nucleation and growth of amyloid beta fibrils describe that a key factor in fibrillogenesis was the spontaneous self-assembly of A β monomers into what were

described as “micelles” of ~ 14 nm in size [374], or perhaps now more commonly referred to as oligomeric structures. Specifically at low pH, these early models proposed mechanisms of homogenous (primary) nucleation involving the self-assembly of monomers at a critical concentration, or alternatively the heterogeneous (secondary) nucleation where the nucleation process occurred on non-A β seeds, i.e. a substrate [374]. The homogenous (primary) nucleation is a relatively simple model, intuitively providing a physical description of the aggregation pathway and for most part is able to explain the macroscopically observed kinetics [375]. Similarly, such models propose that the rate-limiting step, causing the “lag-phase” in kinetic growth studies, is due to the initial formation of nuclei that eventually become large enough to grow spontaneously [376]. A consequence of adding a nucleus or “seeds” into a monomer solution is a rapid aggregation process that can proceed without the need for priori nucleation formation [377]. For example, the presence of undissolved small A β nanoparticles, or seeds, or even a substrate surface, i.e. surface of the sample container, could initiate aggregation. This underlies the mechanism of heterogeneous (secondary) nucleation, which was confirmed by showing that the addition of “seeds” into a monomer solution caused a shortening of the lag phase proportional to the seed concentration [104]. Hence, current descriptions of homogenous (primary) nucleation involve the growth of individual nuclei through only monomer addition, typically in bulk solution (homogeneous nucleation), while secondary nucleation occurs on the surface of an existing amyloid structure, e.g. amyloid fibril, which “catalyses” the growth of new nuclei. Elucidating such molecular pathways in which the toxic forms can be sequestered or promoted are essential for potential therapeutic treatments. For example, Cohen et al. [315] suggested a strong connection between the toxicity and the species produced from secondary nucleation of monomers and this correlation further supported by in vitro studies indicating the significant role of secondary nucleation in AD pathogenesis [104, 315, 378]. In particular,

Meisl et al. [350, 379] found a saturation phenomenon of secondary nucleation occurred in high concentration when the pH switched may also be involved in these combined processes.

Based on the above definitions, we interpret two processes of nucleation and growth of the A β ₄₂ on the mica surface at low pH. Firstly, the observed growth of the existing oligomers and aggregates follows a heterogeneous secondary nucleation process whereby monomers add to existing “seeds” in the sample. This can be initiated immediately after a change in the solution pH and predominately proceeds during the pre-nucleation phase (ii). Analysis of single oligomer kinetics indicates that similar sized seeds can growth at different rates, typically in the range of 0.71-1.5 nm²/sec and 0-0.71nm²/sec of area, for a duration of ~ 100 sec before the growth plateaus. In addition, there is no observation of new seeds being released, or “budding-off”, into the solution during this process, as has previously been described for catalysis of nuclei from amyloid fibril surfaces [380] (shown in Figure 1.1a (chapter 1)). In contrast, the catalysis of nucleating species via the mica substrate is representative of a heterogeneous (secondary) nucleation process and appears to be initiated by a significant increase in peptide surface adsorption at the beginning of the nucleation phase (iii) which lasts for ~ 30 secs. While it is difficult to precisely determine when they first appear (due to resolution limit of AFM), their growth rate and final dimensions are equivalent in range to those of the existing seeds. Interestingly, many of the newly formed species could be observed diffusing on the surface and interacting with each other, similarly to that shown in chapter 1, and in some cases eventually form stable complexes. Hence, their diffusion can provide for subsequent interactions between the different structural peptides such as peptides binding, elongation and aggregation [381].

Lastly, pH-dependent structural formation of peptides has been revealed by a wide range of methods including antiparallel β -sheet structure investigated by Solid state NMR [382] and detection of aggregates by ThT [383]. Other emerging high resolution studies such as

circular dichroism spectroscopy [384], fourier transform infrared spectroscopy [385] and X-ray diffraction have also been demonstrated [386, 387].

While HS-AFM has previously revealed the dynamic growth of fibrils [221, 228, 388] and binding of single oligomers/aggregates in our previous work [358], this is to our knowledge the first time that A β nucleation and growth processes have been directly visualized at the single molecule level. In doing so, we show that various pathways exist within the one system, including nucleation of new species, growth of existing seeds, and formation of new species through diffusion and binding - emphasizing the complexity of multiple microscopic processes that potentially occur during a lag phase and lead to macroscopic differences in bulk aggregation kinetics.

Chapter 4: Molecular Interactions

between A β peptide and Silica

Nanoparticles Visualized by HS-AFM

4.1 Introduction

The abnormal generation of plaques comprising amyloid fibrils is central to pathological diagnosis of neurodegenerative diseases, including Alzheimer's disease (AD), Parkinson's disease, type II diabetes and some types of cancers [389, 390]. For decades, extensive research has been undertaken to investigate the underlying causes and explore potential therapies for AD, yet unfortunately no effective treatments or drugs have successfully made it through clinical trials. One issue is that very little is understood about the molecular mechanisms through which the A β peptide induces the cytotoxicity. Up until recently, various structurally distinct forms of A β aggregates, including oligomers and aggregated intermediates, have been revealed as the toxic species [391-394]. Therefore, strategies that include the prevention or interference of A β aggregation have become a significant focus in targeting the toxic species and determining their role in the pathology of AD.

A large number of aggregation inhibitors have been explored as potential drug candidates for directly targeting the A β formation. Traditional inhibitors can be generally classified in two major groups, small biomolecules as binding partners of A β or peptides including modified peptides and designer peptides. For example, three different casein kinase

protein inhibitors were shown to decrease the amount of A β produced when interacting with A β peptides [395, 396]. Some organic molecules such as the chelator, clioquinol, have also been shown to inhibit fibrillization [397-402]. In addition, some designer peptides such as A β KLVFF, iA β ₅ and A β _{16-20e}, which are derived from original fragments of protein have also shown to inhibit fibril formation, and reduce the toxicity or disassembly of fibrils [403-406]. However, few of these inhibitors can be identified as potent clinical drugs due to their strong side effects.

With the rapid development of nanomedicine, nanoparticles (NP's) are becoming a major cornerstone for drug delivery, molecular diagnostics, regenerative medicine and medical imaging [407-411]. Thus, the interactions between nanomaterials and biomolecules have been widely explored and shed light on how nanomaterials can be utilized in diagnostics and treatments of disease. In particular, NP's have attracted significant interest in AD therapies due to their great adsorption capacity, ease of surface modification and ability to cross the blood brain barrier [412, 413]. Multiple NPs, including polymeric [339, 341, 414-416], inorganic [417-420], magnetic [421-423] and fullerene (carbon-based) [424-430] based particles have demonstrated the ability to inhibit A β aggregation or fibrillation. Aggregation of A β in vitro can be photo-thermally ablated through the short irradiation of A β peptide bound functionalised gold particles [431-433]. Majzik.A et al. [434] revealed chain-like structures of A β aggregates on gold nanoparticles decorated with cysteine- and LPFFD-OH, indicating that the functionalized gold NP's have significant effects on the conformation and structure of the aggregates. Even as early as the late 90's, fullerene (C60) derivatives were shown to have neuroprotective properties by reducing neural cell death caused by A β peptide [424]. More recently, fullerene nanoparticles were found to strongly inhibit the A β aggregation by specifically binding to the central hydrophobic motif, KLVFF (16-20 residues, sequence of amyloid beta) of A β peptide [425]. Numerous other nanoparticles have been reported to be

efficient at preventing A β peptide aggregation and reducing their cytotoxicity [414, 418, 432, 435-437]. For example, Ashwini S.Pai et al. [438] demonstrated the inhibitory effects of (Polyethylene glycol) PEGylated phospholipid nanomicelles on the A β_{42} aggregation and proposed this conventional nanomedicine carrier as a new potential therapeutic agent [438]. Fluorinated nanoparticles were shown to induce an α -helical structure in A β_{40} , consequently preventing fibril formation, while polymeric nanoparticles are also capable of blocking active sites responsible for A β aggregation [339, 414]. Conversely, hydrogenated nanoparticles were shown to accelerate β -sheet structure formation, leading to fibrillogenesis [439]. Similarly, TiO $_2$ nanoparticles have been found to promote A β aggregation by exhibiting a strong adsorption capacity for A β peptide at high concentrations [440].

The underlying effects of NPs on A β aggregation, which is expected to be determined by the NP's composition and surface characteristics such as particle size, shape, surface charge and modifications, remains largely unclear. Furthermore, evaluating kinetics of the A β -nanoparticle interactions, particularly at the single molecular level, also represents a challenge [435]. For example, it is seemingly insurmountable to experimentally measure the kinetic rate constant of a single A β -NP interaction within a complex mixture. Largely in the absence of experimental data, molecular dynamics simulations have been widely used to reveal the molecular mechanisms of interactions between protein and nanoparticles [441, 442]. Ding H et al. [443] applied dissipative particle dynamics (DPD) simulations to investigate the effect of protein adsorption on the delivery of nanoparticles. Coarse grained molecular dynamics (CGMD) simulations have proven to be another powerful tool for the study of nanoparticles interacting with biological systems, by which a growing number of simulation approaches along with various proposed molecular modelling packages have been introduced. Slaven et al. [444] utilized this method to investigate the effects of NPs on amyloid beta aggregation and

found that the ratio of NP/proteins plays an important role in determining the aggregation inhibition or promotion.

Despite the aforementioned molecular dynamic simulation approaches, experimental tools with the ability to resolve both structure and dynamics at the molecular level are required. This is where High-Speed Atomic Force Microscopy (HS-AFM) is beginning to address the need for “structural-dynamics” by enabling direct visualization of label-free single molecules, with imaging speeds of 10-20 frames per second (fps) in liquid [207, 221]. While HS-AFM has previously been used to reveal dynamics of A β fibril formation and oligomeric intermediates, including our work on intra-molecular binding kinetics between different types of A β oligomers and aggregates [221, 228, 230, 358], this study to our knowledge is first to report on the dynamics of A β -nanoparticle interactions, and more generally the nanoparticles themselves. HS-AFM was employed to characterize the structural information and dynamics of silica nanoparticles (LUDOX HS-40 colloidal silica), followed by a co-deposition with A β ₄₂ peptides to investigate SiNPs-A β interactions. We applied the single molecule kinetic analysis established in the previous chapter, which is based on image contrast in HS-AFM movies, to understand the A β -nanoparticle interactions. The applicability and considerations of the analysis, particularly when measuring interaction kinetics in the presence of a substrate is discussed.

4.2 Materials and Methods

4.2.1 Preparation of A β ₄₂ and Silica Nanoparticle Samples

LUDOX HS-40 colloidal silica (12nm diameter), amyloid-beta protein fragment 1-42 (A β ₄₂ peptide) were purchased from Sigma-Aldrich. The silica-nanoparticle solution was prepared as 40wt % in water and then 100ml silica-nanoparticle solution was diluted to 20wt% in 50ml PBS solution prior to use. A β ₄₂ peptide solution was prepared by dissolving 1mg lyophilized solid peptides into HFIP to prevent the aggregation and then aliquot into 50 small microcentrifuge tubes. After half an hour incubation at room temperature in a chemical fume hood, the HFIP was allowed to evaporate for 60 minutes and the re-lyophilized peptides stored at -20°C. Aqueous solutions were prepared by dissolving peptides into PBS (PH 7.4) at concentration of 20 μ g/ml and then vortex mixed for 20 sec prior to use.

4.2.2 HS-AFM Imaging/ Data analysis

To prepare samples for HS-AFM imaging, 2 μ l of the silica nanoparticle solution was pipetted onto a 1.5 mm diameter freshly cleaved mica disc (Cat No. 7101) and incubated for 2 minutes to allow the particles to adsorb onto the mica surface. 2 μ l of fresh PBS was then added and pipetted in/out of the sample solution, and this was repeated several times to exchange the sample solution in order to remove excess particles that had not adsorbed onto the mica surface. The sample was then placed into the liquid cell of the HS-AFM and imaging was performed (Research Institute of Biomolecule Metrology Co., Ltd., Japan) in tapping mode with high frequency, small cantilevers (BL-AC10, Olympus) remodified with the carbon-tip, as described above. For experiments involving co-deposition and imaging of both the silica nanoparticles and A β ₄₂, stable HS-AFM imaging of the silica nanoparticles was firstly achieved, as described above. Following this, 10 μ l of a 1 μ g/ml A β ₄₂ peptide solution was then

injected into the liquid cell and further mixed by pipetting in/out whilst continuing imaging of the silica nanoparticles. This injection of the A β ₄₂ solution and mixing typically perturbed or caused a loss of the imaging, e.g. the tip lifts of the surface, though stable imaging could easily be reattained after optimization of the feedback gains, set point and amplitude. During imaging, the free oscillation amplitude of the cantilever was set to ~2 nm and the set point amplitude was kept to ~ 90% of the free amplitude. The maximum possible scanning rate is calculated as $R_{max} = (\lambda f) / (2WN)$, where λ is the amplitude, f is feedback bandwidth, W is the scanning size and N is the number of corresponding scan lines. A non-electrode wide scanner with range of 4 μm * 4 μm and z scanner (700 nm) with scan speeds of normally 1-4 frames/sec for 500 nm scans was used. For higher resolution scans of 200 nm, 5-10 frames/sec with 550-275 lines/sec was applied.

Data analysis of the values obtained from the Matlab software was investigated as mentioned in Chapter 2.

4.3 Result and Discussion

4.3.1 Silica nanoparticles (SiNP)

HS-AFM movies were taken at 1 frame/sec with 500nm scan size to visualize the silica nanoparticles in phosphate buffer solution on a mica substrate. A representative single frame reveals the silica nanoparticles exhibit a degree of size variation (e.g. some larger aggregates are present), with surface density of $\sim 100\text{-}120$ NP's/ μm^2 (Figure 4.1a). Corresponding movies show the surface diffusion of these nanoparticles, including dynamic, physical interactions occurring between individual NP's where they are observed to come into contact for various periods of time (typically on the order of seconds) and then separate or diffuse away (*Supplementary Movies 24 and 25*). High resolution images show the NP's mostly have a spherical morphology though also appear to assemble or aggregate into various string-like morphologies (Figure 4.1f). Statistical analysis of the NP dimensions was obtained from Matlab software designed to segment imported (movie) AVI.file into individual frames, automatically detect all objects, and analyse parameters such as XY coordinates, eccentricity, perimeter, area, height (pixels intensity), width and length. Histograms of the area showed two distinct peak distributions (Figure 4.1b), including the most abundant NP's with area of 105 ± 36.8 nm² and a smaller distribution at 520 ± 48.4 nm² that is indicative of aggregated NP. Histograms of the length and width (Figure 4.1d, e) showed peak distributions of 12.9 ± 3.2 nm and 11.0 ± 2.7 nm, respectively, confirming spherical NP with effective diameters correlating to the nominal size of ~ 12 nm for these commercially available SiNPs (Ludox HS 40). A smaller sampling of larger widths at ~ 30 nm was observed (Figure 4.1e), presumably related to the aggregated NPs. Similarly, analysis of the height gave two peak distributions at 2.1 ± 0.9 nm and 5.8 ± 1.1 nm correlating to the main and aggregated NP's (Figure 4.1c). However, the NP height was significantly lower than the expected NP size (12 nm) [445, 446],

indicating an imaging artefact causing an underestimation of the actual height. Normally tip broadening can overestimate the lateral dimensions though anomalies in z-height are also reported and previously shown to be due to frequency shift in response to tip-sample interaction when imaging nanoparticles in tapping mode [447].

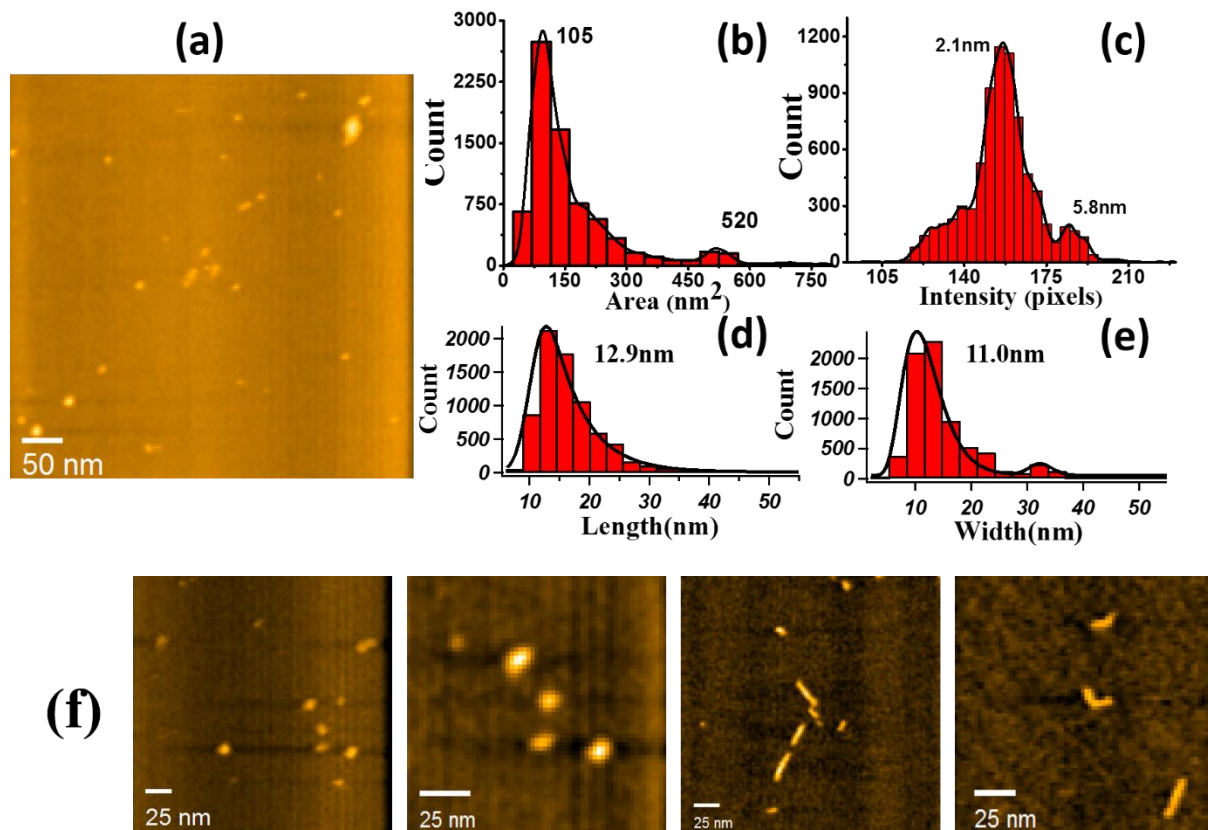


Figure 4. 1. Morphology and structural dimensions of Silica Nanoparticles. (a) Representative HS-AFM image of Silica Nanoparticles diffuse on the surface of mica. (Scan scale: 500*500nm, imaging rate: 1frame/second) Histograms of different structural dimensions distributions Area (b), Height (c), Width (d) and Length (e) of Silica Nanoparticles.(f) Spherical and string morphology of various structural silica nanoparticles.

4.3.2 Imaging of Co-deposited SiNP - A β ₄₂

HS-AFM imaging was performed on samples comprising both SiNP and A β ₄₂ on the mica surface in PBS. In these experiments, SiNP were first deposited on the surface and stable imaging achieved at 1 frame/sec, as performed above for their analysis in Figure 4.1, prior to

then injecting a small volume (10 μ l) of a 1 μ g/ml A β ₄₂ solution. Two representative examples of movie filmstrips show the time-course of the experiments from 0-500 sec, including the initial frame of only SiNPs (defined as 0 sec), injection or ‘spiking’ with A β ₄₂ at 170 sec, followed by imaging of SiNP and A β ₄₂ coexisting on the surface until 500 sec (Figure 4.2). Corresponding movies are given in *Supplementary Movies 26 and 27*. Immediately after spiking with A β ₄₂ peptide, the perturbation caused by injecting the solution caused instability in the imaging, i.e. lifting up of the cantilever tip from the surface, resulting in loss of imaging (Figure 4.2, at 170 sec). In this case, the imaging set-point was readjusted to resume stable imaging typically within < 30 sec. Beyond this point from 200 – 500 sec duration, it was evident that an increasing number of A β ₄₂ peptides appeared on the surface.

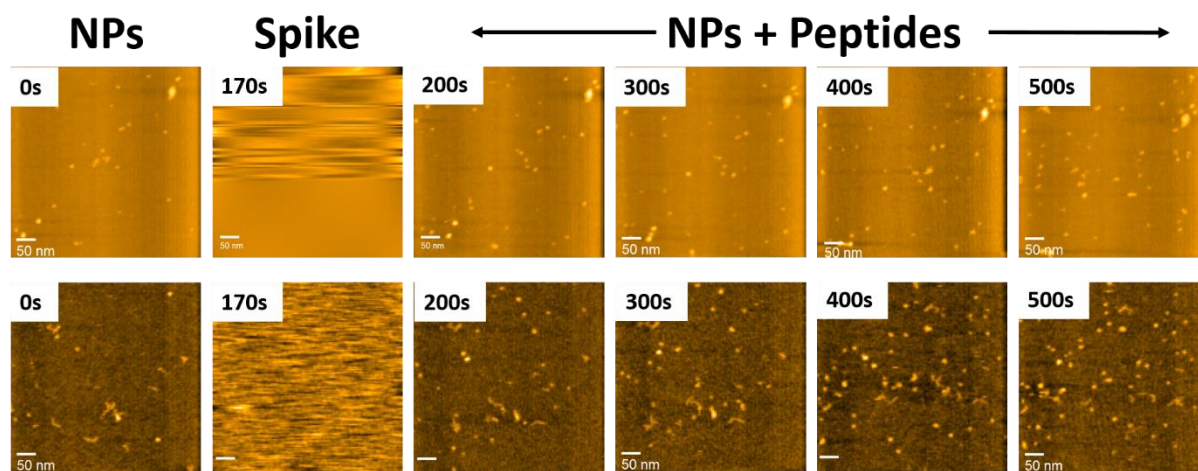


Figure 4. 2. HS-AFM film strips shows the morphology of silica nanoparticles diffusion on mica surface before the Spike and the co-existing phase of nanoparticles and peptides after Spike. Scale bar: 50nm. Imaging rate: 1frame/sec.

To confirm the qualitative observations in Figure 4.2, analysis of both the object count in each frame and root mean square (r.m.s.) surface roughness versus imaging time is shown in Figure 4.3. Prior to spiking with A β ₄₂, the object count only represented the number of SiNPs in each frame, which reached a constant value ~20-25 NP’s per frame (Figure 4.3a, NP’s (i)).

After spiking, the object count significantly increased to a combined ~ 30 -40 NP's- $A\beta_{42}$ per frame (Figure 4.3a, NP's + $A\beta_{42}$ (ii)), indicating the addition of the $A\beta_{42}$ on the mica surface. Similarly for the r.m.s. roughness, an increase in value from 0.7 nm before spiking to 0.9 after spiking indicated an increasing number of $A\beta_{42}$ adsorbing to the mica surface (Figure 4.3b and 4.3c). Despite confirming the co-existence of the SiNP- $A\beta_{42}$, qualitatively distinguishing them from each other directly from the movies was difficult due to their similar morphology and size. Hence, further analysis was undertaken to compare their size dimensions and diffusion speed.

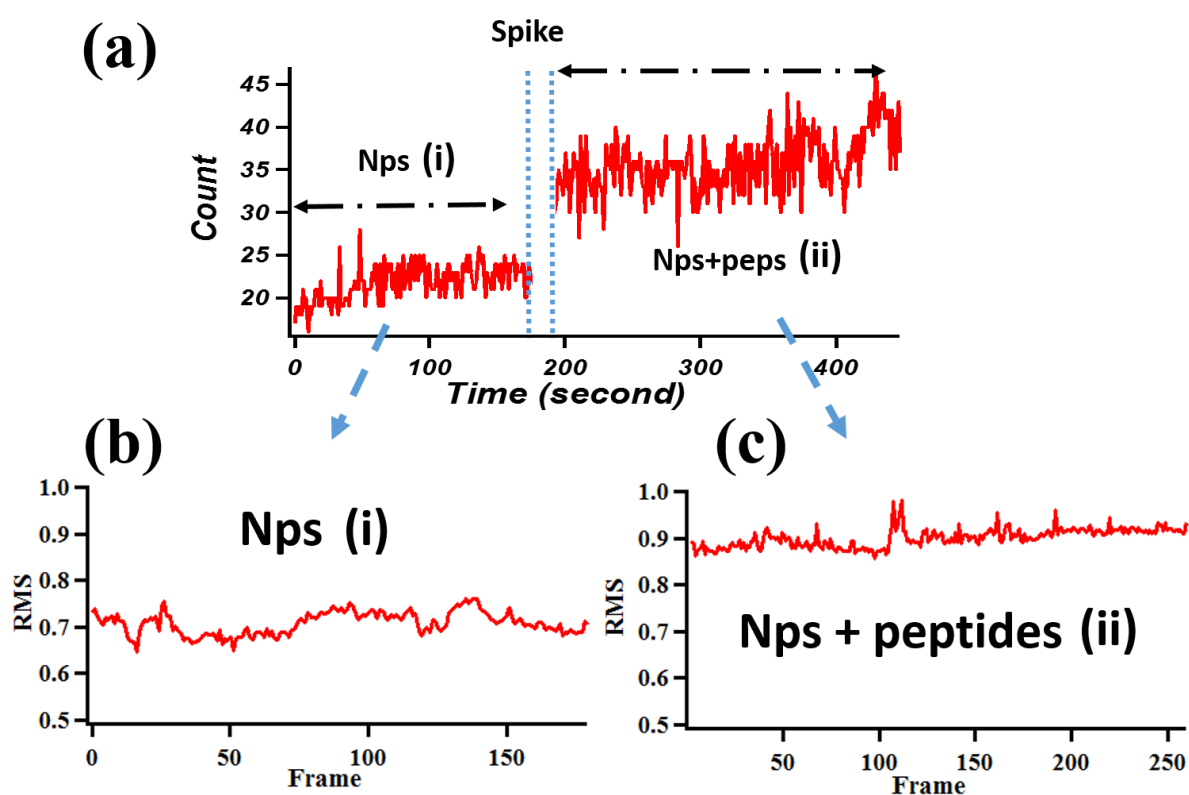


Figure 4. 3. In-situ spiking process that silica nanoparticles interacting with $A\beta_{42}$ peptides. (a) Numbers distribution of Silica nanoparticles co existing with $A\beta_{42}$ peptides among different stages. (i) Only silica nanoparticles, (ii) silica nanoparticles and $A\beta_{42}$ peptides.(b) Surface roughness of silica nanoparticles on mica (c) Surface roughness of silica nanoparticles with injected $A\beta_{42}$ peptides.

Histogram analysis of area, height, length and width was performed on the co-deposited SiNP- $A\beta_{42}$ samples on frames within the first 5 min and also after 30 min of spiking with $A\beta_{42}$ (Figure A5 and A6). From these histograms, the peak distribution values (represent the values of main species at different stages) with errors (e.g. width of Gaussian fit) are compared (Figure

4.4d-g) along with their representative images at 0 sec (NP's only), and 5 min and 30 min after spiking, in Figure 4.4a-c. Firstly, object detection from the images (Figure 4.4a-c) indicated an increasing number of A β 42 after spiking, with values reaching ~30-45 NP's/ A β 42 per frame and ~45-70 NP's/ A β 42 per frame after 5 min and 30 min, respectively (Figure A5 and A6).

After 5 min, the peak value for area (Figure 4.4g, blue bar) reduced to 80 nm² compared to 105 nm² for the NP's only, while a slight decrease in values also occurred for length (12.1 nm) and width (10.1 nm) however these decreases in the dimensions of the co-deposited SiNP-A β 42 were not statistically significant. In contrast, a corresponding increase in height to 2.8 nm (Figure 4.4f, blue bar) suggests that interactions such as possible adsorption of A β 42 onto SiNP and/or rearrangement of their conformation may be involved. After 30mins, the peak distribution values for area, length and width, show an increase in values (Figure 4.4, magenta bar) compared to both the NP's only and NP's-A β 42 after 5 min. The exception was height which remained equivalent and was not statistically different. For comparison, the dimensions of the most abundant A β (A β _{15nm}) obtained previously in Chapter 2 are also included in Figure 4.4 (red bar) and indicate that the A β _{15nm} oligomer is similar in height but has significantly greater lateral dimensions. This analysis shows that individual A β and SiNP have a distinct size difference, with the A β of ~ 15-20 nm and SiNP of ~ 12 nm that closely matches its commercially reported value. However, analysis of co-deposited NP's-A β 42 reveals the size is more equivalent to the SiNP, with no distinct separate distributions observed in the histograms. Thus, distinguishing between the two NP and A β immediately after co-deposition was difficult. After 30 min, there appeared to be an increase in NP's-A β 42 size, suggesting either their binding or aggregation though the size remained smaller than the A β only.

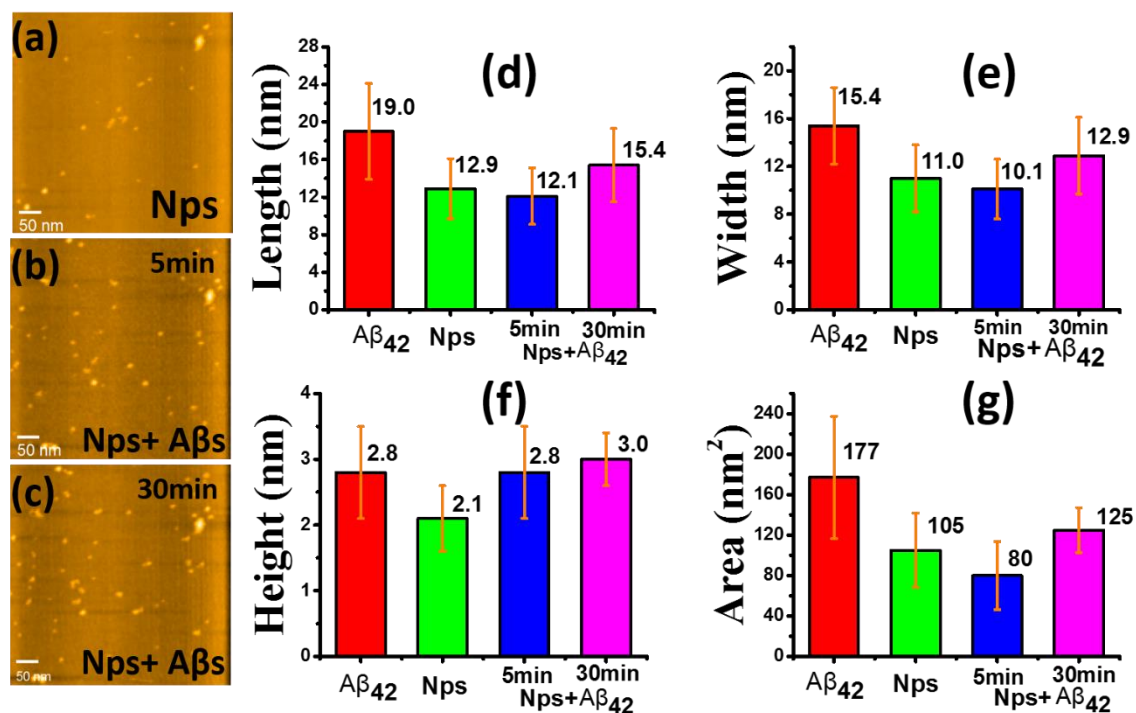


Figure 4. 4. Statistical analysis before and after the spike. (a)(b)(c) Representative snapshots of HS-AFM showed pure silica nanoparticles on mica and silica nanoparticles co existing with amyloid-beta peptides. Dimensions comparison among peptides, silica nanoparticles and co existing complexes. (d)(e)(f)(g) represent for Length, Width, Height and Area respectively, errors are standard deviation. The numbers of molecule calculated for the bar graphs are at least 25 molecules each frame for single measurement, though the numbers will reach to around 75 for the total three separate measurements.

4.3.3 Diffusion of SiNP and Aβ Comparison

To quantify surface diffusion, individual SiNPs were tracked ($n=30$) in Matlab software and analysis of mean square displacement (MSD) of single SiNPs as a function of time was plotted (Figure 4.5a). In addition, the different sizes of the SiNPs are indicated in Figure 4.5a to assess the effect of particle size on the surface diffusion, revealing that surface diffusion decreased (lower MSD slopes) with increasing SiNP size (Figure 4.5a). (Table 4. 1) In the calculated diffusion coefficient, this effect was observed as an exponential decrease in the diffusion coefficient with increasing particle size, indicating a particle-size dependency that may be due to a direct effect (molecular size) or indirectly by influencing the particle-surface interactions, e.g. due to change in particle-surface contact area. In particular, it was found that, irrespective of particle size, the diffusion range of $\sim 0.6 - 5.8 \text{ nm}^2/\text{s}$ for SiNP was significantly slower than

the diffusion of similar sized A β ₄₂ oligomers ($\sim 8.3 - 9.2 \text{ nm}^2/\text{s}$) but faster than the larger A β ₄₂ aggregates ($\sim 0.4 \text{ nm}^2/\text{s}$) measured in the previous chapter 2.

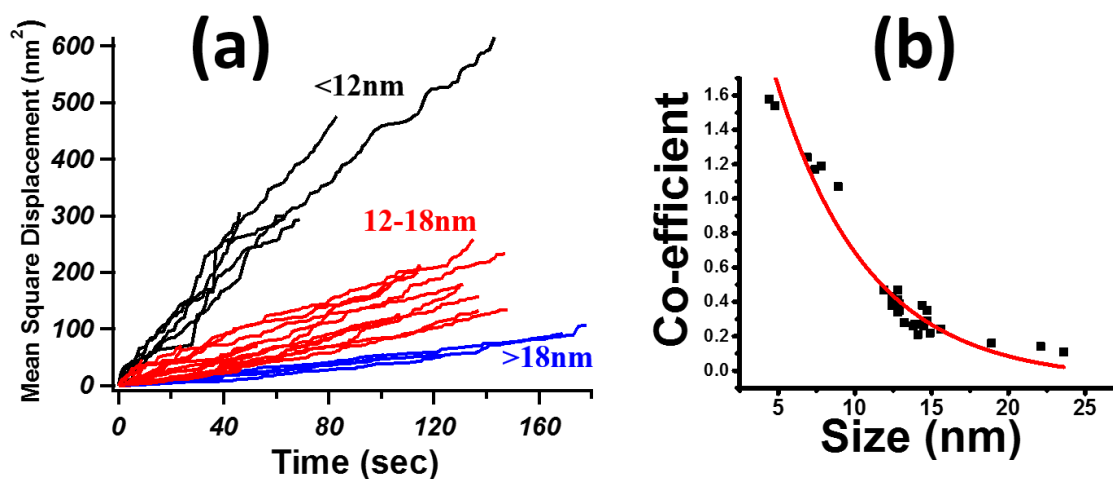


Figure 4. 5. (a) Mean square displacement (MSD) versus time plot of individual tracked nanoparticles with different size. $MSD = \langle |r(t) - r(0)|^2 \rangle$, where $\langle \rangle$ means the average, $r(t)$ is the position of each particle in determined time t , $r(0)$ stands for the reference spot of each particle. $n \Rightarrow 30$. Black line represents for the size of particles is less than 12nm, red line shows particles range with 12-18nm and blue line stands for particles larger than 18nm. (b) Diffusion Co-efficient scatters of different size particles fitted by nonlinear curve fit (red line for Asymptotic1 fitting).

Based on previous analysis established in Chapter 2 for quantifying single molecule kinetic parameters for A β - A β binding, we applied the same analysis to single SiNP-SiNP interactions in samples with SiNP only. A representative filmstrip (5 frame/sec) showing the analysis process is shown in Figure 4.6a and 4.6b, with the corresponding movie given in *Supplementary Movie S28*. Starting at time = 0 sec, three SiNPs of varying size (labelled 1, 2 and 3) are observed to be freely diffusing on the mica surface. After 0.2 sec, SiNP (1) attaches to a larger SiNP (2) and both remain as a complex (1+2) until time point 1.0 s. During this period, the complex (1+2) increases in both width and length, and exhibits slower surface diffusion. SiNP(1) then dissociates from SiNP (2) and diffuses away at 1.0 sec but then undergoes binding (SiNP(1+2) at 1.4s) and dissociation again (1.6s). Subsequent SiNP-SiNP interactions did not occur again until timeframe 8.8 - 34.4s (Figure 4.5b). During this period, a new SiNP (4) entered the scan area (8.8s) and interacted with SiNP (3) (10 sec), undergoing

initial ‘binding’ and then unbinding until 32.6s. By measuring the amount of time the two SiNPs spent in physical contact, as demonstrated by ‘on’ or ‘off’ in Figure 4.6c, lifetime distributions could be produced to extract kinetics parameters such as mean lifetime $\langle t \rangle$, binding rate K_{on} and dissociation rate K_{off} (Figure 4.6d). Exponential decay functions fitted to lifetime distributions gave a mean lifetime of $\langle t \rangle = 4.55$ sec, with K_{off} of $1/\langle t \rangle = 0.22$ s for the interaction between SiNPs (Figure 4.6d). Importantly, the relationship between the SiNP size and the time ‘on’ for binding is shown in Figure 4.5e, (Table 4.2) which indicates an increasing exponential-like relationship. Hence, the latter is inversely correlated to the size-dependence of the diffusion coefficient in Figure 4.5b, indicating that the kinetic parameters are directly influenced by the surface diffusion of the SiNP. The implications of this on the HS-AFM analysis of interactions are discussed further below.

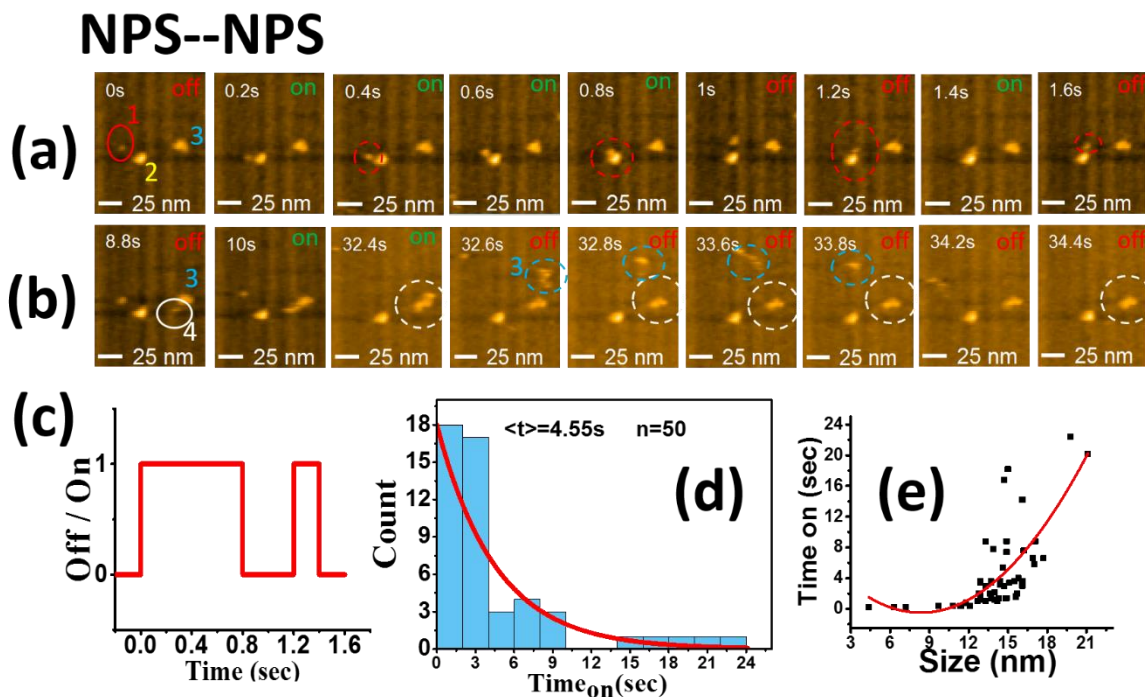


Figure 4. 6. Dynamics and Interactions between silica nanoparticles.(a)HS-AFM film strip showed binding processes between a small particle (no.1) and a relative large one(no.2).(b)HS-AFM filmstrip showed representative interaction processes between two similar size particles. Scale bar:25nm, 5frames/sec. (c) A representative figure showing the time ‘on’and ‘off’ state, where number 1 refers to a binding state while number 0 refers to an unbound state. (d)Lifetime distributions for the bound state of particles with size range around 12nm. Distribution is fit to a single exponential decay (e) The binding time ‘on’ within the interactions versus the size of active nanoparticles. Distribution is fit to a polynomial order 2 curve.

4.3.4 Interactions and Kinetics of Co-deposited SiNP - A β ₄₂

As demonstrated from the previous chapter, the A β ₄₂ peptides were observed to diffuse significantly faster than the SiNP (cf. $\sim 8.3 - 9.2 \text{ nm}^2/\text{s}$ versus $\sim 0.6 - 5.8 \text{ nm}^2$). To confirm this observation in samples comprising the co-deposited SiNP and A β ₄₂, individual objects with sizes ranging from $\sim 10 \text{ nm}$ to 20 nm were individually tracked for $> 200 \text{ s}$ to calculate their diffusion coefficients. The average coefficient was found to be $2.05 \pm 0.04 \text{ nm}^2/\text{s}$ (Figure 4.7a), which was higher than the pure SiNP ($0.46 \pm 0.01 \text{ nm}^2/\text{s}$) but much lower than the A β ₄₂ only ($7.95 \pm 1.99 \text{ nm}^2/\text{s}$) (Figure 4.7a). Importantly, two different distributions of diffusion coefficient were observed within the same size range (Figure 4.7b), suggesting that delineation of separate SiNP and A β ₄₂ diffusion speeds within the co-deposited sample. Therefore, despite their similar dimensions, it was possible to identify either SiNP or A β ₄₂ based on their diffusion speed, especially since the diffusion of A β ₄₂ exhibited close to 16 times faster speeds than SiNP. Having the ability to identify the SiNP and A β ₄₂, the same kinetic analysis was used to quantify single molecule kinetics of SiNP-A β ₄₂ interactions, with a representative filmstrip at 2 frame/sec shown in Figure 4.7a. (*Supplementary Movie S29*) At time 0 sec, a single A β ₄₂ (1) (green circle) was observed to freely diffuse and then bind to a SiNP labelled (2) (red circle) at 2.5 sec to form a complex (1+2) that increases in height. In subsequent frames, the complex (1+2) undergoes repeated dissociation and rebinding. Table 4. 3 shows a list of 20 different SiNP-A β interactions that were analysed from the HS-AFM movies, with corresponding values of size and diffusion coefficient given for each SiNP and A β participating in the interaction. Analysis of time ‘on’ for binding and exponential decay fit to lifetime distribution in Figure 4.7d gave a mean lifetime $\langle t \rangle$ at 1.15s and K_{off} of 0.87s, indicating that affinity between A β ₄₂ – SiNP interactions was significantly weaker than the interaction between two SiNPs. However,

as mentioned above, due to the apparent dependence of binding lifetimes on the particle size and/or diffusion the implications of this analysis are discussed further below.

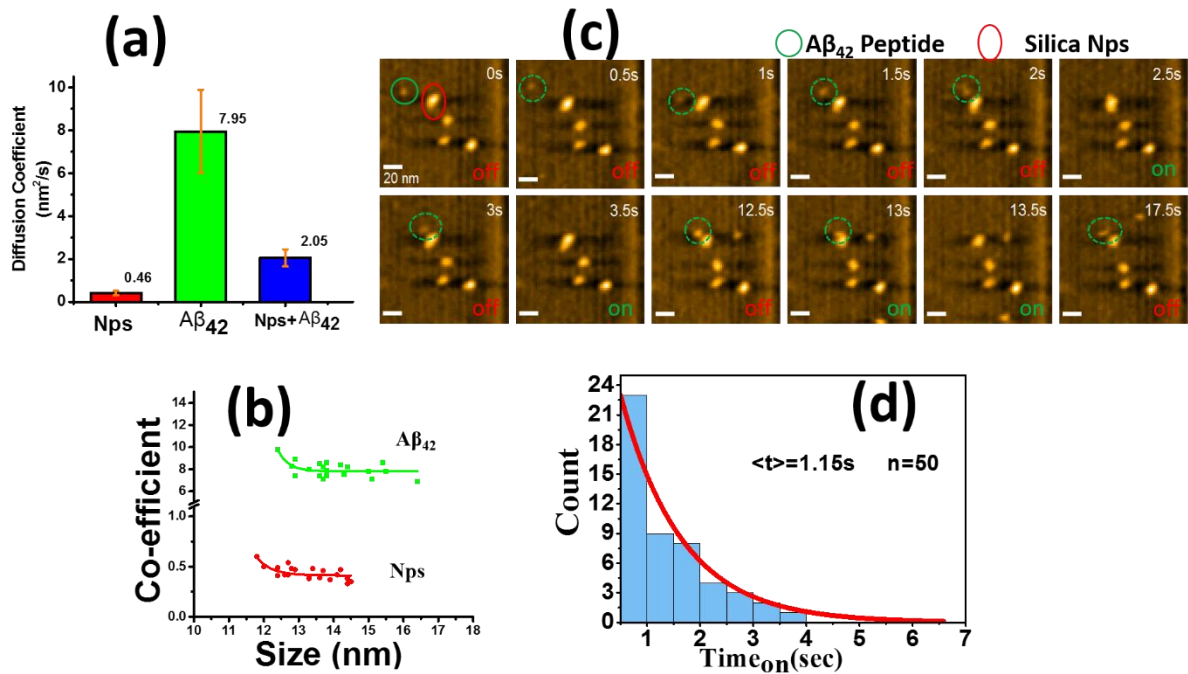


Figure 4. 7. Dynamics and interactions between silica nanoparticles and peptides.(a)Representative HS-AFM filmstrip shows the process between single Aβ₄₂ peptide and nanoparticle. Scale bar: 25nm. Scan rate :2frames/sec. (b) Diffusion Co-efficient of silica nanopartilces and Aβ₄₂ peptides with similar size. Green (Aβ₄₂)and red (Nps)lines are fit by nonlinear curve fit (Asymptotic1).(c)Comparison of the diffusion ability among single nps, Aβ₄₂ peptides and the mixture of both. Average diffusion co-efficient of 0.46±0.1 nm²/s (nps),7.95±1.94 nm²/s (Aβ₄₂)and 2.05±0.4 nm²/s (mixture).Errors are standard deviation. N=>20 molecules.(d)Lifetime distributions for the bound state between particles and Aβ₄₂ peptides with similar size around 12nm. Detailed information is shown in Table 4. 1.

4.4 Conclusion

Understanding the diffusion of nanoparticles in fluids is important for a wide range of therapeutic applications, for example in drug delivery, with typical diffusion coefficients for nanoparticles on the order of $10^{-12} \text{ m}^2/\text{s}$ ($1000 * 10^4 \text{ nm}^2/\text{s}$). Ellina A. M et al. [448] have detailed the effects of particle size, medium viscosity and components of the liquid medium on nanoparticle diffusivity. For example, silica nanoparticles coated with polyethylene glycol exhibit an enhanced diffusion of $906 \pm 89 * 10^4 \text{ nm}^2/\text{s}$ in water, while thiolated nanoparticle diffusion decreases to $731 \pm 40 * 10^4 \text{ nm}^2/\text{s}$, even though their particle sizes are similar. This nanoparticle diffusion is however very different to those conditions under which the HS-AFM is operated, namely due to the presence of a solid substrate that clearly hampers the nanoparticle diffusivity. In the vicinity of the mica substrate, the calculated diffusion coefficients of both $A\beta_{42}$ and SiNP in this study and previous chapters are on the order of $1\text{-}10 \text{ nm}^2/\text{sec}$, approximately six orders of magnitude lower than nanoparticles allowed to “freely” diffuse in liquid [448, 449]. Previous work on single particle tracking of individual proteins (RAD54) on mica and MSD analysis using HS-AFM have revealed similar coefficients of $\sim 2 \text{ nm}^2/\text{sec}$ and likewise noted the discrepancy with reported diffusion coefficients of $96 \pm 89 * 10^6 \text{ nm}^2/\text{s}$ for globular proteins in water. Accordingly, reduced diffusion associated with surface interactions can be explained by physical adsorption theory [450] whereby weak adhesion forces, such as the Van der Waals forces between the particle and surface, affects the surface driven Brownian motion.

In the previous chapter $A\beta_{15-20\text{nm}} \leftrightarrow A\beta_{15-20\text{nm}}$ interactions gave a mean lifetime $\langle t \rangle = 0.55 \pm 0.22 \text{ sec}$ ($k_{\text{off}} (1/\langle t \rangle) = 1.82 \text{ sec}^{-1}$) compared to the $A\beta_{15-20\text{nm}} \leftrightarrow A\beta_{36\text{nm}}$ with a mean lifetime $= 0.72 \pm 0.28 \text{ sec}$ ($k_{\text{off}} = 1.39 \text{ sec}^{-1}$), indicating that interactions with the larger-sized $A\beta_{36\text{nm}}$ form a more tightly bound complex due to the slower dissociation rate (lower k_{off}).

Nevertheless, it was clarified that a slower dissociation rate could be partially governed by diffusion, as the slower diffusing $A\beta_{36nm}$ on the mica surface may influence the time it spends in contact with another peptide, i.e. it take longer to diffuse away and hence a longer time “on” will be recorded in the HS-AFM analysis. Similarly, in the previous chapter 1, the largest $A\beta$ aggregate, $A\beta_{Agg}$, had an order of magnitude lower diffusion coefficient than both the $A\beta_{15-20nm}$ and $A\beta_{36nm}$, and hence so too may influence the binding lifetime. Furthermore, in this chapter, it was clearly evident that increasing SiNP particle size caused a decrease in diffusion (Figure 4.6e) but also conversely an increase the binding lifetime (time “on”) (Figure 4.7d), suggesting that differences in particle size influence diffusion which in turn affects the measured time “on” or binding lifetimes.

When considering the aforementioned effect of diffusion, we conclude that caution must be taken when assessing kinetic parameters based on the HS-AFM analysis. For example, the lower K_{off} value of the SiNP-SiNP interaction indicates a longer bound-state compared to the SiNPs- $A\beta_{42}$ peptide interaction. However, the slower diffusivity of the SiNPs could contribute to their lower K_{off} , as explained above. Similarly, the lower K_{off} of both SiNP-SiNP and SiNP- $A\beta_{42}$ interactions compared to $A\beta_{42}$ - $A\beta_{42}$ interactions measured in the previous chapter (with the exception of the larger $A\beta_{42}$ aggregate) possibly result from the slower SiNP diffusion and/or faster $A\beta_{42}$ diffusion. One other observation is that while the time “on” exponentially increases with particle size, the effect did not occur until the particle size reached > 12-13nm, suggesting that analysis of smaller particles in Figure 4.6e may differ from larger aggregates. Despite this, at this early stage in development of HS-AFM for analysis of single molecule or nanoparticle interactions the effect of particle diffusion on the kinetic analysis needs to be further investigated.

In light of above, there are still aspects of the kinetics analysis that cannot be explained by diffusion. For example in the previous chapter, while the diffusion ability of different sized

$A\beta_{15-20\text{nm}}$ and $A\beta_{36\text{nm}}$ species was significantly different by ~8 times, the binding lifetimes were similar, e.g. 0.55 ± 0.22 sec and 0.72 ± 0.28 sec for $A\beta_{15-20\text{nm}}$ and $A\beta_{36\text{nm}}$, respectively. Additionally, as mentioned above, the $A\beta_{\text{Agg}}$ diffuses significantly slower compared to the $A\beta_{15-20\text{nm}}$ and equivalent to the $A\beta_{36\text{nm}}$. Yet under these conditions, the $A\beta_{\text{Agg}}$ shows a “stochastic” lifetime of binding that cannot be explained by its lower diffusion. From these findings, further investigation is required to validate the HS-AFM analysis of binding kinetics. It is suggested through appropriate experimental design that binding kinetics could be analyzed by 1) keeping one particle fixed and the other freely diffusing, 2) using a nanoparticle substrate rather than freely diffusing nanoparticles and 3) controlling the surface diffusion of particles by modifying the surface.

Table 4. 1. Individual silica nanoparticles interactions

Number	Silica Nanoparticles		Number	Silica Nanoparticles	
	Size (nm)	MSD/Co-E		Size (nm)	MSD/Co-E
1	4.4	1.58	16	13.8	0.26
2	7.8	1.19	17	14.5	0.26
3	4.8	1.54	18	14.5	0.29
4	6.9	1.24	19	23.6	0.11
5	7.4	1.17	20	14.9	0.22
6	8.9	1.07	21	14.5	0.35
7	11.9	0.47	22	15.6	0.24
8	14.4	0.38	23	12.8	0.41
9	18.9	0.16	24	12.8	0.47
10	13.2	0.28	25	11.9	0.47
11	13.9	0.27	26	12.4	0.43
12	14.4	0.38	27	12.9	0.39
13	12.9	0.37	28	14.1	0.21
14	14.7	0.29	29	12.8	0.34
15	12.9	0.35	30	12.8	0.37

Table 4. 2. Table for silica nanoparticle binding associated with size

Active NPs		Active NPs		Active NPs	
Size (nm)	Time _{on} (s)	Size (nm)	Time _{on} (s)	Size (nm)	Time _{on} (s)
4.4	0.2	15.6	1.6	16.1	3.6
6.3	0.2	15.7	2	15.8	4
7.2	0.2	12.8	2	17	5.8
11.4	0.4	13.6	2	17.7	6.6
9.7	0.4	12.9	2	16.9	6.6
10.8	0.4	14	2.2	14.9	7.4
12.1	0.4	13.3	3	14.9	8.8
11.8	0.8	14.7	3	16.1	14.2
14.2	1	16.1	3	14.7	16.8
12.7	1	14.4	3.2	15	18.2
13.3	1	12.9	3.4	21.1	20.2
14	1.2	13.7	3.4	19.8	22.4
12.9	1.2	15.1	3.4	17.1	8.8
13.7	1.4	15.5	3.6	16.2	7.6
14.8	1.4	13.7	3.6	14.6	5.4
14.9	1.4	12.9	3.6	13.3	8.8
14.3	1.4	14.4	3.6	13.9	7.8

Table 4. 3. Table for interaction between peptides and silica nanoparticles

Number	Peptides		nanoparticles	
	size	MSD/Co-E	size	MSD/Co-E
1	13.8	7.9	13.4	0.48
2	15	7.8	14.1	0.42
3	13.6	7.4	12.7	0.54
4	12.8	8.3	12.4	0.49
5	14.4	8.2	13.6	0.39
6	14.2	8.4	14.5	0.35
7	15.1	7.1	13.3	0.38
8	13.8	7.4	12.8	0.48
9	13.7	7.1	12	0.5
10	12.9	8.9	12.4	0.41
11	14.3	7.5	12.9	0.47
12	15.4	8.6	13.9	0.37
13	12.9	7.4	14.4	0.33
14	13.3	8	13.3	0.39
15	13.7	8.2	12.7	0.42
16	16.4	6.9	12.6	0.42
17	15.5	7.8	14.4	0.38
18	13.8	8.6	13.7	0.46
19	12.4	9.8	11.8	0.6
20	13.6	8.5	14.2	0.47

Chapter 5: Conclusion and Outlook

5.1 Conclusions

The structural characterization and dynamics interactions between $A\beta_{42}$ peptides were investigated by High Speed Atomic Force Microscopy, which is capable of directly visualization of single molecules and proteins at sub-nanometre structural level with millisecond temporal resolution in liquid. Analysis of dimensions revealed up to three main $A\beta_{42}$ species distributions, $A\beta_{15-20nm}$, $A\beta_{36nm}$ and $A\beta_{agg}$, in addition to the appearance of fast diffusive monomers when compared to the larger $A\beta_{42}$ species. Prior to the peptides interaction analysis, quantitative measurement of molecular diffusion was also conducted by tracking individual molecules with the designed software Mat-lab and the results showed the mean square displacement (MSD) have a linear dependence relation with the molecule size, with $8.7 \pm 0.44 \text{ nm}^2/\text{s}$, $1.1 \pm 0.06 \text{ nm}^2/\text{s}$ and $0.4 \pm 0.01 \text{ nm}^2/\text{s}$ for $A\beta_{15-20nm}$, $A\beta_{36nm}$ and $A\beta_{agg}$ respectively. Additionally, the relationship between different parameters also suggested a potential model for the peptide assembly, which is termed as combined lateral additional elongation step with height stacking process.

Significantly, we established a new platform based on image contrast in the captured videos to quantify reaction rate determining kinetics constants for interactions between different $A\beta_{42}$ species. The results showed that interaction between smaller $A\beta_{15-20nm}$ to $A\beta_{agg}$ followed by a type of kinetic heterogeneity with the lifetime at 2.04s while the lifetime for $A\beta_{15-20nm}$ - $A\beta_{15-20nm}$ and $A\beta_{15-20nm}$ to $A\beta_{36nm}$ are very short and both fit to a single exponential decay, with 0.55s and 0.72s respectively, indicating significant different pathways for interactions between different species to overcome the energy barrier and the complexity of

various structural aggregates will hinder the advancement on the A β toxicity identification and proper targeting.

Different environmental factors such as peptide concentration, incubation time and solution pH were investigated under *ex-situ* conditions by HS-AFM. The results indicated that the effect of peptide concentration and incubation time on the structural morphology and diffusion of peptides was minimal, however, a decrease in solution pH accelerated the formation of toxic β -sheet rich oligomeric structures. Further *in-situ* HS-AFM imaging of this pH-induced aggregation process was able to observe the real-time nucleation and growth of single A β , including elucidating distinct separate pathways leading to formation of A β oligomers.

Having characterized the A β_{42} peptide, silica nanoparticles were introduced to investigate their interactions with the peptide. The silica nanoparticles (SiNPs) were found to be 12nm in diameter and exhibited significantly slower diffusion (coefficient at 0.46 ± 0.1 nm²/s) compared to similar sized A β_{42} peptides (7.95 ± 1.94 nm²/s). In samples co-deposited with SiNP and A β_{42} it was difficult to distinguish them based on size, though clear difference in their diffusion enabled their identification for further analysis. Subsequently, kinetic analysis of real-time interactions between SiNPs and peptides showed that the particle size had a significant effect on diffusion, which in turn influenced determination of binding lifetimes in the kinetic analysis. Hence, further investigation on the effects of diffusion on the kinetic analysis at single molecule level is still needed.

5.2 Outlook

Protein aggregation is believed as a highly complex problem at molecular level, with little clarity around the kinetic mechanisms [451]. Despite the extensive literature, currently there is much more to be understood on the processes of aggregation, including nucleation, polymerization, elongation and fibrillation [452]. Also, many hypotheses of the amyloid beta aggregation lacks a precise definition on molecular kinetic equation due to the mathematical complexity [112]. Therefore, there is a disconnect between the fundamental parameters such as the transient rate constants or structural dimensions and corresponding species due to these confused nomenclature.

It has been widely demonstrated that prefibrillar assemblies of amyloid peptide, such as soluble oligomers or protofibrils, instead of mature end-stage amyloid fibrils are the main toxic species in protein misfolding diseases [59]. However, the pathway(s) by which normal monomeric forms of the peptide become intermediates or fibrils that are associated with toxicity is still uncertain. In this case, approaches based on *in vivo* cell culture experiments to assess the toxicity of structural intermediates, for example the oligomers and aggregates identified by HS-AFM could be useful. Similarly, assessing toxicity of samples based on *a priori* characterization of molecular forms of A β could also be applied more generally to the problem of protein aggregation. Elucidating the structure and associated toxicity will provide a fundamental basis for development of potential targeting via therapeutic drugs.

Lastly, as an alternative to antibodies and other chemical compounds [453, 454], nanomaterials such as the carbon nanomaterials [455, 456] have been shown to have inhibitory/promoting effects on the protein aggregation. In addition, the combination of these two classes of materials is believed as a compromising way to assess or control the cytotoxicity due to their dispersibility in liquid. Therefore, the diversity of these nanomaterials and protein forms may

bring a tremendous potential for both structural and dynamic characterization requirements. The application of HS-AFM imaging with single molecule dynamic analysis will then provide unprecedented opportunity to elucidate a wide range of molecular interactions [457].

Chapter 6: Appendix

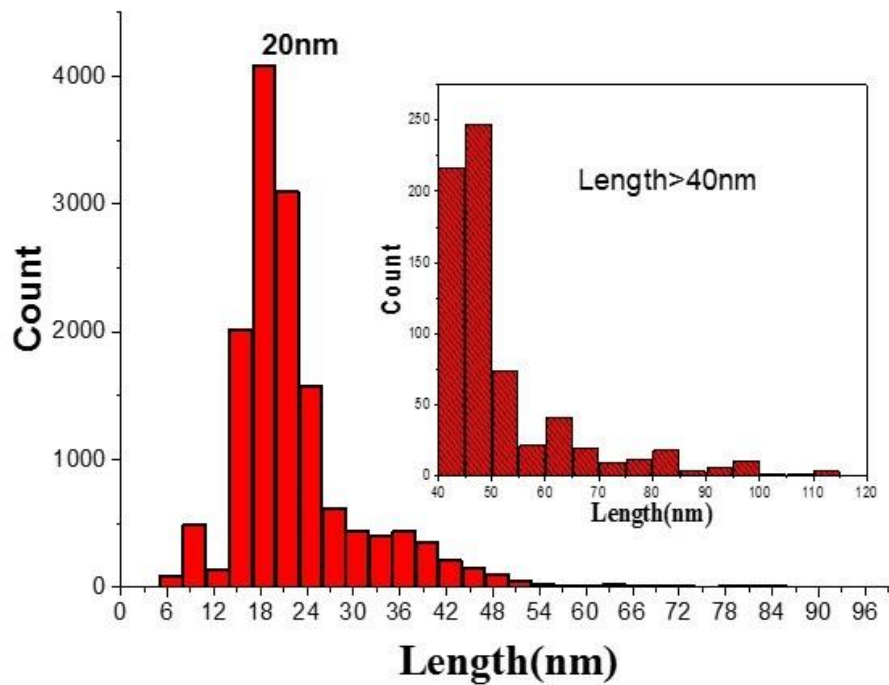


Figure A1. Length histogram of the A β peptides. we have an inset figure specifically for the length greater than 40nm to illustrate that some unstructured species normally have transient structure with unique higher values of ~up to 100nm.

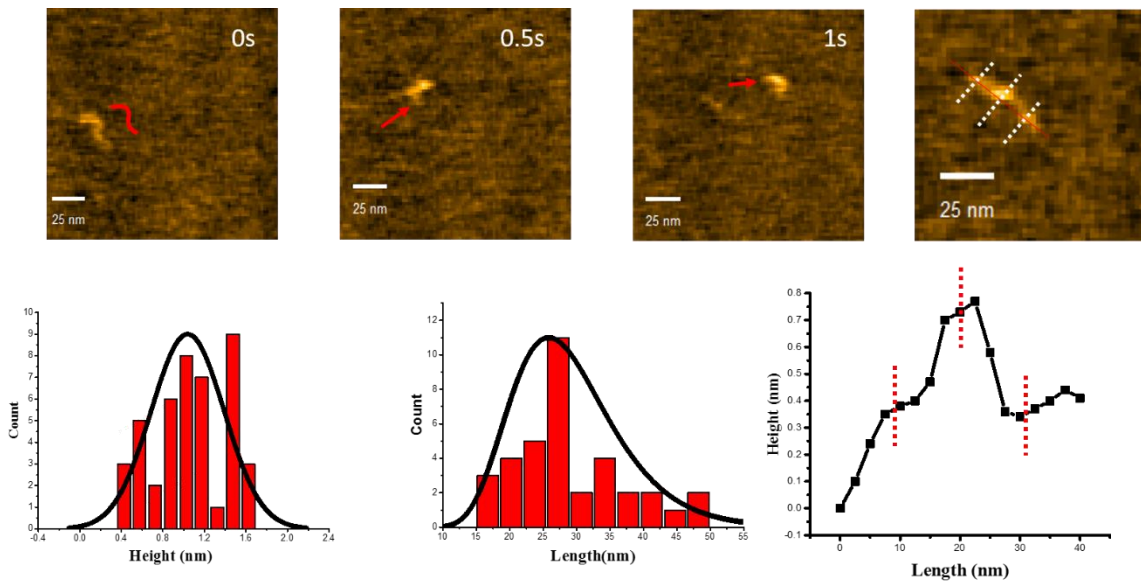


Figure A2. AFM cross-sectional analysis show how we track the dynamics and measure the structural dimension of these less well structured $A\beta_{42}$ species.

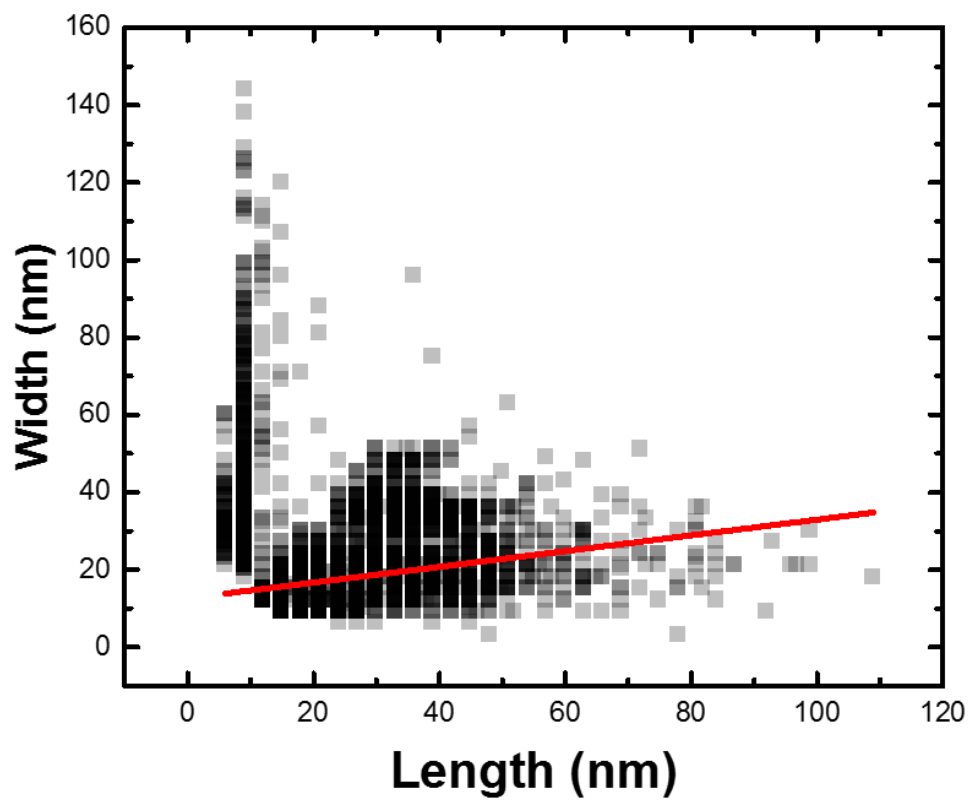


Figure A3. Relationship between length and width shows a linear correlation.

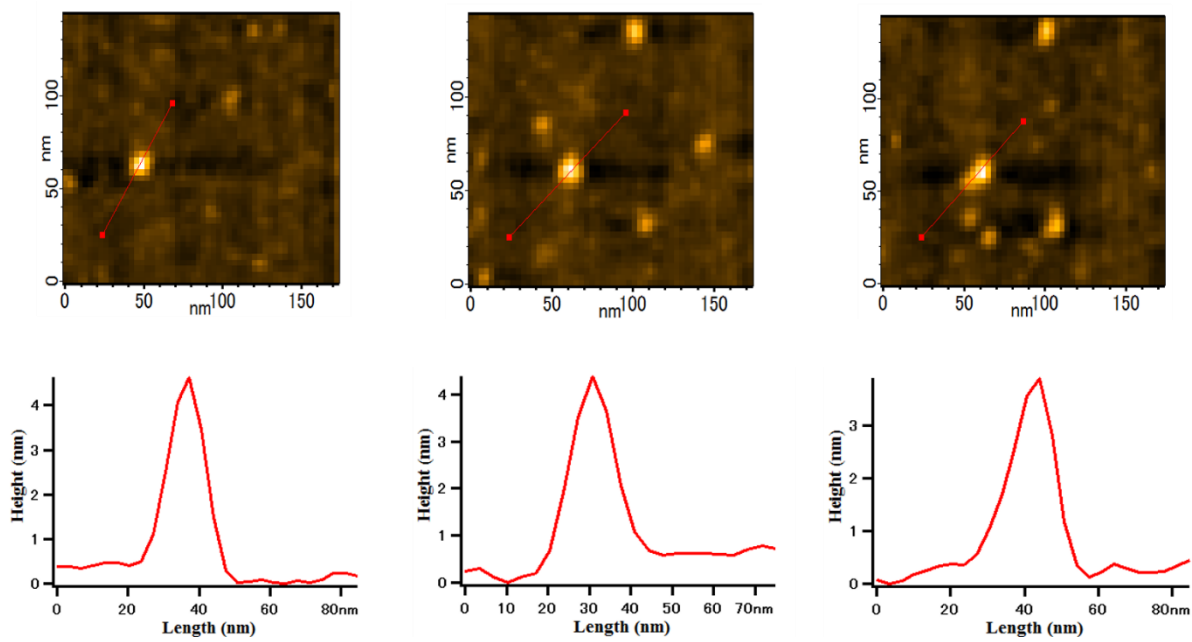


Figure A4. Image line profile of cross-section on individual molecules. Represent three single peptides appearing on mica surface and present dynamic changes on the lateral dimensions as well as the height.

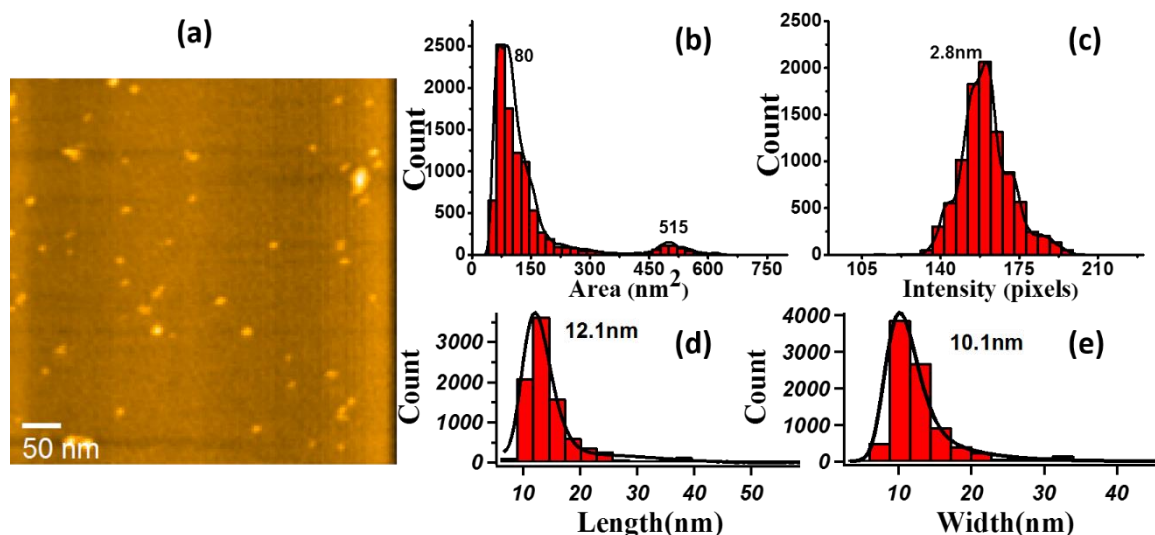


Figure A5. Morphology and structural dimensions of Silica Nanoparticles and amyloid-beta42 peptides injection during the first five minutes. (a) Representative HS-AFM image of Silica Nanoparticles and peptide diffusion on the surface of mica. (Scan scale: 500*500nm, imaging rate: 1frame/second) Histograms of different structural dimensions distributions Area (b), Height (c), Width (d) and Length (e) of Silica Nanoparticles and peptides.

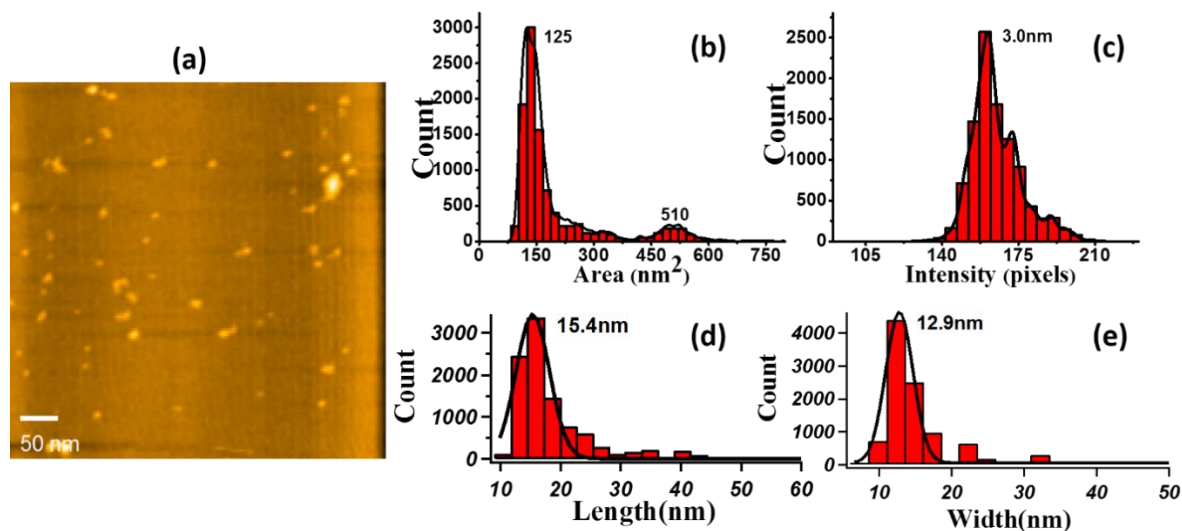


Figure A6. Morphology and structural dimensions of Silica Nanoparticles and amyloid-beta42 peptides injection after 30 minutes. (a) Representative HS-AFM image of Silica Nanoparticles and peptides diffuse on the surface of mica. (Scan scale: 500*500nm, imaging rate: 1frame/second) Histograms of different structural dimensions distributions Area (b), Height (c), Width (d) and Length (e) of Silica Nanoparticles and peptides

- S 1. HS-AFM movie of A β ₄₂ species diffusing on the mica surface. Scan size 500*500nm, scan rate 2frame/sec. *5 video playing speed.
- S 2. HS-AFM movie of A β ₄₂ species fast diffusing and capturing transient structured species.
- S 3. HS-AFM movie of A β _{15-20nm} diffusing and tracking processes. Dash line refers to the original position and solid line represent the current position.
- S 4. HS-AFM movie of A β _{36nm} diffusing and tracking processes. Dash line refers to the original position and solid line represent the current position.
- S 5. HS-AFM movie of A β _{agg} diffusing and tracking processes. Dash line refers to the original position and solid line represent the current position.
- S 6. HS-AFM movie of whole processes of dynamic interactions between different A β species. The mechanism that elongation and stacking of the peptides assembly also revealed during the process.
- S 7. HS-AFM movie of interaction process between A β _{15-20nm} and A β _{agg}. Dash line refers to the original position and solid line represent the current position.
- S 8. HS-AFM movie of interaction process between A β _{15-20nm} and A β _{36nm}. Dash line refers to the original position and solid line represent the current position.
- S 9. HS-AFM movie of interaction process between A β _{15-20nm} and A β _{15-20nm}. Dash line refers to the original position and solid line represent the current position.
- S 10. HS-AFM movie of 50 μ g/ml A β ₄₂ species diffusing on the mica surface. Scan size 500*500nm, scan rate 2frame/sec.
- S 11. HS-AFM movie of 100 μ g/ml A β ₄₂ species diffusing on the mica surface. Scan size 500*500nm, scan rate 1frame/sec.
- S 12. HS-AFM movie of 20 μ g/ml A β ₄₂ species diffusing on the mica surface after 2hours incubation in pH 7. Scan size 500*500nm, scan rate 1frame/sec.
- S 13. HS-AFM movie of 20 μ g/ml A β ₄₂ species diffusing on the mica surface after 4hours incubation in pH 7. Scan size 500*500nm, scan rate 1frame/sec.
- S 14. HS-AFM movie of 20 μ g/ml A β ₄₂ species diffusing on the mica surface after 1hours incubation in pH 3. Scan size 500*500nm, scan rate 1frame/sec.
- S 15. HS-AFM movie of 20 μ g/ml A β ₄₂ species diffusing on the mica surface after 1hours incubation in pH 11. Scan size 500*500nm, scan rate 1frame/sec.
- S 16. HS-AFM movie of 20 μ g/ml A β ₄₂ species diffusing on the mica surface after 2hours incubation in pH 3. Scan size 500*500nm, scan rate 1frame/sec.
- S 17. HS-AFM movie of 10 0 μ g/ml A β ₄₂ species diffusing on the mica surface after 4hours incubation in pH 3. Scan size 500*500nm, scan rate 1frame/sec.
- S 18. HS-AFM movie of 100 μ g/ml A β ₄₂ species diffusing on the mica surface after 20hours incubation in pH 3. Scan size 500*500nm, scan rate 1frame/sec.
- S 19. HS-AFM movie of 20 μ g/ml A β ₄₂ species diffusing on the mica surface after spike, inducing decreased solution pH from 7.0 to 3.0. Scan size 500*500nm, scan rate 1frame/sec.
- S 20. HS-AFM movie of 20 μ g/ml A β ₄₂ species diffusing on the mica surface after spike, inducing increased solution pH from 7.0 to 11.0. Scan size 500*500nm, scan rate 1frame/sec.
- S 21. HS-AFM movie of no.3 peptide nucleation processes after spike. Scale bar 20nm. Scan rate 5frames/sec.
- S 22. HS-AFM movie of no.4 peptide nucleation processes after spike. Scale bar 22nm. Scan rate 5frames/sec.

- S 23. HS-AFM movie of no.5 peptide nucleation processes after spike. Scale bar 18nm. Scan rate 5frames/sec.
- S 24. HS-AFM movie of silica nanoparticles diffusing on mica. Scan size 500*500nm, scan rate 1frame/sec.
- S 25. HS-AFM movie of silica nanoparticles diffusing on mica. Scan size 500*500nm, scan rate 1frame/sec.
- S 26. (1)(2) HS-AFM movie of in-situ interactions between silica nanoparticles and injected A β ₄₂ peptides. Scan size 500*500nm, scan rate 1frame/sec.
- S 27. HS-AFM movie of in-situ interactions between silica nanoparticles and injected A β ₄₂ peptides. Scan size 500*500nm, scan rate 1frame/sec.
- S 28. HS-AFM movie of single molecular interactions between silica nanoparticles. Scan size 250*150nm, scan rate 5frames/sec.
- S 29. HS-AFM movie of single molecular interactions between silica nanoparticles and A β ₄₂ peptides. Scan size 100*100nm, scan rate 2frames/sec.

Chapter 7: Reference

1. Niccoli, T. and L. Partridge, *Ageing as a risk factor for disease*. Current Biology, 2012. **22**(17): p. R741-R752.
2. Emerit, J., M. Edeas, and F. Bricaire, *Neurodegenerative diseases and oxidative stress*. Biomedicine & pharmacotherapy, 2004. **58**(1): p. 39-46.
3. Seeley, W.W., et al., *Neurodegenerative diseases target large-scale human brain networks*. Neuron, 2009. **62**(1): p. 42-52.
4. Soto, C., *Unfolding the role of protein misfolding in neurodegenerative diseases*. Nature Reviews Neuroscience, 2003. **4**(1): p. 49.
5. Lee, V.M., M. Goedert, and J.Q. Trojanowski, *Neurodegenerative tauopathies*. Annual review of neuroscience, 2001. **24**(1): p. 1121-1159.
6. Roychoudhuri, R., et al., *Amyloid β -protein assembly and Alzheimer disease*. Journal of Biological Chemistry, 2009. **284**(8): p. 4749-4753.
7. Chiti, F. and C.M. Dobson, *Protein misfolding, functional amyloid, and human disease*. Annu. Rev. Biochem., 2006. **75**: p. 333-366.
8. Association, A.s., *2013 Alzheimer's disease facts and figures*. Alzheimer's & dementia, 2013. **9**(2): p. 208-245.
9. Graeber, M.B. and P. Mehraein, *Reanalysis of the first case of Alzheimer's disease*. European archives of psychiatry and clinical neuroscience, 1999. **249**(3): p. S10-S13.
10. Lee, J.H., *Alois Alzheimer: Defining, Understanding, and Delineating Dementia*. THE PPEREVIEW, 2017: p. 13.
11. Maurer, K. and U. Maurer, *Alzheimer: The Life of a Physician and the Career of a Disease*. 2003: Columbia University Press.
12. Maurer, K., S. Volk, and H. Gerbaldo, *Auguste D and Alzheimer's disease*. The Lancet, 1997. **349**(9064): p. 1546-1549.
13. Spielmeyer, W., *Alzheimers Lebenswerk*. Zeitschrift für die gesamte Neurologie und Psychiatrie, 1916. **33**(1): p. 1-44.
14. Kidd, M., *Paired helical filaments in electron microscopy of Alzheimer's disease*. Nature, 1963. **197**(4863): p. 192.
15. Terry, R.D., N.K. Gonatas, and M. Weiss, *Ultrastructural studies in Alzheimer's presenile dementia*. The American journal of pathology, 1964. **44**(2): p. 269.
16. Terry, R.D., *The fine structure of neurofibrillary tangles in Alzheimer's disease*. 1963.
17. Wilcock, G. and M. Esiri, *Plaques, tangles and dementia: a quantitative study*. Journal of the neurological sciences, 1982. **56**(2-3): p. 343-356.
18. Tomlinson, B.E., G. Blessed, and M. Roth, *Observations on the brains of demented old people*. Journal of the neurological sciences, 1970. **11**(3): p. 205-242.
19. Villemagne, V.L., et al., *Amyloid β deposition, neurodegeneration, and cognitive decline in sporadic Alzheimer's disease: a prospective cohort study*. The Lancet Neurology, 2013. **12**(4): p. 357-367.
20. Jack Jr, C.R., et al., *Serial PIB and MRI in normal, mild cognitive impairment and Alzheimer's disease: implications for sequence of pathological events in Alzheimer's disease*. Brain, 2009. **132**(5): p. 1355-1365.
21. Reiman, E.M., et al., *Brain imaging and fluid biomarker analysis in young adults at genetic risk for autosomal dominant Alzheimer's disease in the presenilin 1 E280A kindred: a case-control study*. The Lancet Neurology, 2012. **11**(12): p. 1048-1056.
22. Drachman, D.A. and J. Leavitt, *Human memory and the cholinergic system: a relationship to aging?* Archives of neurology, 1974. **30**(2): p. 113-121.

23. Drachman, D.A. and B. Sahakian, *Memory and cognitive function in the elderly: a preliminary trial of physostigmine*. Archives of Neurology, 1980. **37**(10): p. 674-675.
24. Bartus, R.T., et al., *The cholinergic hypothesis of geriatric memory dysfunction*. Science, 1982. **217**(4558): p. 408-414.
25. Perry, E., *Acetylcholine and Alzheimer's disease*. The British Journal of Psychiatry, 1988. **152**(6): p. 737-740.
26. Bartus, R.T., *On neurodegenerative diseases, models, and treatment strategies: lessons learned and lessons forgotten a generation following the cholinergic hypothesis*. Experimental neurology, 2000. **163**(2): p. 495-529.
27. Auld, D.S., et al., *Alzheimer's disease and the basal forebrain cholinergic system: relations to β -amyloid peptides, cognition, and treatment strategies*. Progress in neurobiology, 2002. **68**(3): p. 209-245.
28. Toogood, P., *Acetylcholinesterase inhibitors in the treatment of Alzheimer's disease*. Canadian Pharmacists Journal, 2001. **134**(1): p. 29.
29. Gauthier, S., *Advances in the pharmacotherapy of Alzheimer's disease*. Cmaj, 2002. **166**(5): p. 616-623.
30. Giacobini, E., *Cholinesterase inhibitors stabilize Alzheimer's disease*. Annals of the New York Academy of Sciences, 2000. **920**(1): p. 321-327.
31. Giacobini, E., *Cholinesterase inhibitor therapy stabilizes symptoms of Alzheimer disease*. Alzheimer Disease & Associated Disorders, 2000. **14**(1): p. S3-S10.
32. Klein, W.L., *A β toxicity in Alzheimer's disease: globular oligomers (ADDLs) as new vaccine and drug targets*. Neurochemistry international, 2002. **41**(5): p. 345-352.
33. Selkoe, D.J., *Alzheimer's disease: genes, proteins, and therapy*. Physiological reviews, 2001. **81**(2): p. 741-766.
34. Hardy, J.A. and G.A. Higgins, *Alzheimer's disease: the amyloid cascade hypothesis*. Science, 1992. **256**(5054): p. 184-186.
35. Bra, K., et al., *Scanning electron microscopy as a tool for evaluating morphology of amyloid structures formed on surface plasmon resonance chips*. Data in brief, 2018. **19**: p. 1166-1170.
36. Cerf, E., et al., *Antiparallel β -sheet: a signature structure of the oligomeric amyloid β -peptide*. Biochemical Journal, 2009. **421**(3): p. 415-423.
37. Outeiro, T.F. and J. Tetzlaff. *Mechanisms of disease II: cellular protein quality control*. in *Seminars in pediatric neurology*. 2007. Elsevier.
38. Ferreira, S.T., M.N. Vieira, and F.G. De Felice, *Soluble protein oligomers as emerging toxins in Alzheimer's and other amyloid diseases*. IUBMB life, 2007. **59**(4 - 5): p. 332-345.
39. Haass, C. and D.J. Selkoe, *Soluble protein oligomers in neurodegeneration: lessons from the Alzheimer's amyloid β -peptide*. Nature reviews Molecular cell biology, 2007. **8**(2): p. 101.
40. Lansbury, P.T. and H.A. Lashuel, *A century-old debate on protein aggregation and neurodegeneration enters the clinic*. Nature, 2006. **443**(7113): p. 774.
41. Baglioni, S., et al., *Prefibrillar amyloid aggregates could be generic toxins in higher organisms*. Journal of Neuroscience, 2006. **26**(31): p. 8160-8167.
42. Caughey, B. and P.T. Lansbury Jr, *Protofibrils, pores, fibrils, and neurodegeneration: separating the responsible protein aggregates from the innocent bystanders*. Annual review of neuroscience, 2003. **26**(1): p. 267-298.
43. Hardy, J. and D.J. Selkoe, *The amyloid hypothesis of Alzheimer's disease: progress and problems on the road to therapeutics*. science, 2002. **297**(5580): p. 353-356.
44. Kirkitadze, M.D., G. Bitan, and D.B. Teplow, *Paradigm shifts in Alzheimer's disease and other neurodegenerative disorders: the emerging role of oligomeric assemblies*. Journal of neuroscience research, 2002. **69**(5): p. 567-577.
45. Klein, W.L., G.A. Krafft, and C.E. Finch, *Targeting small A β oligomers: the solution to an Alzheimer's disease conundrum?* Trends in neurosciences, 2001. **24**(4): p. 219-224.

46. Lambert, M.P., et al., *Diffusible, nonfibrillar ligands derived from A β 1–42 are potent central nervous system neurotoxins*. Proceedings of the National Academy of Sciences, 1998. **95**(11): p. 6448-6453.
47. De Felice, F.G., et al., *Targeting the neurotoxic species in Alzheimer's disease: inhibitors of A β oligomerization*. The FASEB journal, 2004. **18**(12): p. 1366-1372.
48. Mucke, L., et al., *High-level neuronal expression of A β 1–42 in wild-type human amyloid protein precursor transgenic mice: synaptotoxicity without plaque formation*. Journal of Neuroscience, 2000. **20**(11): p. 4050-4058.
49. Terry, R.D., et al., *Physical basis of cognitive alterations in Alzheimer's disease: synapse loss is the major correlate of cognitive impairment*. Annals of Neurology: Official Journal of the American Neurological Association and the Child Neurology Society, 1991. **30**(4): p. 572-580.
50. Watson, D., et al., *Physicochemical characteristics of soluble oligomeric A β and their pathologic role in Alzheimer's disease*. Neurological research, 2005. **27**(8): p. 869-881.
51. Walsh, D.M. and D.J. Selkoe, *A β oligomers—a decade of discovery*. Journal of neurochemistry, 2007. **101**(5): p. 1172-1184.
52. Millucci, L., et al., *Conformations and biological activities of amyloid beta peptide 25-35*. Current Protein and Peptide Science, 2010. **11**(1): p. 54-67.
53. Harper, J.D., et al., *Observation of metastable A β amyloid protofibrils by atomic force microscopy*. Chemistry & biology, 1997. **4**(2): p. 119-125.
54. Bitan, G., S.S. Vollers, and D.B. Teplow, *Elucidation of primary structure elements controlling early amyloid β -protein oligomerization*. Journal of Biological Chemistry, 2003. **278**(37): p. 34882-34889.
55. Bitan, G., et al., *A molecular switch in amyloid assembly: Met35 and amyloid β -protein oligomerization*. Journal of the American Chemical Society, 2003. **125**(50): p. 15359-15365.
56. Bitan, G., et al., *Amyloid β -protein (A β) assembly: A β 40 and A β 42 oligomerize through distinct pathways*. Proceedings of the National Academy of Sciences, 2003. **100**(1): p. 330-335.
57. Lesné, S., et al., *A specific amyloid- β protein assembly in the brain impairs memory*. Nature, 2006. **440**(7082): p. 352.
58. Hartley, D.M., et al., *Protofibrillar intermediates of amyloid β -protein induce acute electrophysiological changes and progressive neurotoxicity in cortical neurons*. Journal of Neuroscience, 1999. **19**(20): p. 8876-8884.
59. Walsh, D.M., et al., *Naturally secreted oligomers of amyloid β protein potently inhibit hippocampal long-term potentiation in vivo*. Nature, 2002. **416**(6880): p. 535.
60. Podlisny, M.B., et al., *Aggregation of secreted amyloid-protein into sodium dodecyl sulfate-stable oligomers in cell culture*. Journal of Biological Chemistry, 1995. **270**(16): p. 9564-9570.
61. Vigo - Pelfrey, C., et al., *Rapid Communication: Characterization of β - Amyloid Peptide from Human Cerebrospinal Fluid*. Journal of neurochemistry, 1993. **61**(5): p. 1965-1968.
62. Enya, M., et al., *Appearance of sodium dodecyl sulfate-stable amyloid β -protein (A β) dimer in the cortex during aging*. The American journal of pathology, 1999. **154**(1): p. 271-279.
63. Roher, A.E., et al., *Morphological and biochemical analyses of amyloid plaque core proteins purified from Alzheimer disease brain tissue*. Journal of neurochemistry, 1993. **61**(5): p. 1916-1926.
64. Taylor, B.M., et al., *Spontaneous aggregation and cytotoxicity of the β -amyloid A β 1–40: a kinetic model*. Journal of protein chemistry, 2003. **22**(1): p. 31-40.
65. Lashuel, H.A. and P.T. Lansbury, *Are amyloid diseases caused by protein aggregates that mimic bacterial pore-forming toxins?* Quarterly reviews of biophysics, 2006. **39**(2): p. 167-201.
66. Teplow, D.B., *Structural and kinetic features of amyloid β -protein fibrillogenesis*. Amyloid, 1998. **5**(2): p. 121-142.

67. Jellinger, K.A., *Recent advances in our understanding of neurodegeneration*. Journal of neural transmission, 2009. **116**(9): p. 1111-1162.
68. Walsh, D.M., et al., *Amyloid β -protein fibrillogenesis Structure and biological activity of protofibrillar intermediates*. Journal of Biological Chemistry, 1999. **274**(36): p. 25945-25952.
69. Walsh, D.M., et al., *Amyloid β -protein fibrillogenesis detection of a protofibrillar intermediate*. Journal of Biological Chemistry, 1997. **272**(35): p. 22364-22372.
70. Hoshi, M., et al., *Spherical aggregates of β -amyloid (amylospheroid) show high neurotoxicity and activate tau protein kinase I/glycogen synthase kinase-3 β* . Proceedings of the National Academy of Sciences, 2003. **100**(11): p. 6370-6375.
71. Pires, R.H., et al., *Distinct annular oligomers captured along the assembly and disassembly pathways of transthyretin amyloid protofibrils*. PLoS One, 2012. **7**(9): p. e44992.
72. Oda, T., et al., *Clusterin (apoJ) alters the aggregation of amyloid β -peptide (A β 1-42) and forms slowly sedimenting A β complexes that cause oxidative stress*. Experimental neurology, 1995. **136**(1): p. 22-31.
73. Bernstein, S.L., et al., *Amyloid- β protein oligomerization and the importance of tetramers and dodecamers in the aetiology of Alzheimer's disease*. Nature chemistry, 2009. **1**(4): p. 326-331.
74. Jack Jr, C.R., et al., *Hypothetical model of dynamic biomarkers of the Alzheimer's pathological cascade*. The Lancet Neurology, 2010. **9**(1): p. 119-128.
75. Krafft, G.A., et al., *Amyloid β protein (globular assembly and uses thereof)*. 2001, Google Patents.
76. Cerpa, W., M.C. Dinamarca, and N.C. Inestrosa, *Structure-function implications in Alzheimer's disease: effect of A β oligomers at central synapses*. Current Alzheimer Research, 2008. **5**(3): p. 233-243.
77. Knobloch, M., et al., *A β oligomer-mediated long-term potentiation impairment involves protein phosphatase 1-dependent mechanisms*. Journal of Neuroscience, 2007. **27**(29): p. 7648-7653.
78. Li, S., et al., *Soluble oligomers of amyloid β protein facilitate hippocampal long-term depression by disrupting neuronal glutamate uptake*. Neuron, 2009. **62**(6): p. 788-801.
79. Krafft, G.A. and W.L. Klein, *ADDLs and the signaling web that leads to Alzheimer's disease*. Neuropharmacology, 2010. **59**(4-5): p. 230-242.
80. Rowan, M., et al., *Synaptic memory mechanisms: Alzheimer's disease amyloid β -peptide-induced dysfunction*. 2007, Portland Press Limited.
81. Walsh, D.M., et al., *The role of cell-derived oligomers of A β in Alzheimer's disease and avenues for therapeutic intervention*. 2005, Portland Press Limited.
82. Marcello, E., R. Epis, and M. Di Luca, *Amyloid flirting with synaptic failure: towards a comprehensive view of Alzheimer's disease pathogenesis*. European journal of pharmacology, 2008. **585**(1): p. 109-118.
83. Viola, K., P. Velasco, and W.L. Klein, *Why Alzheimer's is a disease of memory: the attack on synapses by A β oligomers (ADDLs)*. The Journal of Nutrition Health and Aging, 2008. **12**(1): p. S51-S57.
84. Serrano-Pozo, A., et al., *Neuropathological alterations in Alzheimer disease*. Cold Spring Harbor perspectives in medicine, 2011. **1**(1): p. a006189.
85. Stine, W.B., et al., *In vitro characterization of conditions for amyloid- β peptide oligomerization and fibrillogenesis*. Journal of Biological Chemistry, 2003. **278**(13): p. 11612-11622.
86. Lashuel, H.A. and D. Grillo-Bosch, *In Vitro Preparation of Prefibrillar Intermediates of Amyloid- β and α Synuclein*, in *Amyloid Proteins*. 2005, Springer. p. 19-33.
87. Hane, F.T., B.Y. Lee, and Z. Leonenko, *Recent progress in Alzheimer's disease research, part 1: Pathology*. Journal of Alzheimer's Disease, 2017. **57**(1): p. 1-28.

88. Gellermann, G.P., et al., *A β -globulomers are formed independently of the fibril pathway*. *Neurobiology of disease*, 2008. **30**(2): p. 212-220.
89. Ahmed, M., et al., *Structural conversion of neurotoxic amyloid- β 1–42 oligomers to fibrils*. *Nature structural & molecular biology*, 2010. **17**(5): p. 561.
90. Wu, J.W., et al., *Fibrillar oligomers nucleate the oligomerization of monomeric amyloid β but do not seed fibril formation*. *Journal of Biological Chemistry*, 2010. **285**(9): p. 6071-6079.
91. Jerrett, J.T. and P.T. Lansbury Jr, *Seeding uOne-Dimensional Minireview Crystallization" of Amyloid: A Pathogenic Mechanism in Alzheimer's Disease and Scrapie?*
92. Andreu, J.M. and S.N. Timasheff, [5] *The measurement of cooperative protein self-assembly by turbidity and other techniques*, in *Methods in enzymology*. 1986, Elsevier. p. 47-59.
93. Asakura, S., *Polymerization of flagellin and polymorphism of flagella*. *Adv. Biophys.*, 1970. **1**: p. 99-155.
94. Eaton, W.A. and J. Hofrichter, *The biophysics of sickle cell hydroxyurea therapy*. *Science*, 1995. **268**(5214): p. 1142-1144.
95. Oosawa, F. and S. Asakura, *Thermodynamics of the Polymerization of Protein*. 1975: Academic Press.
96. Ferrone, F.A., J. Hofrichter, and W.A. Eaton, *Kinetics of sickle hemoglobin polymerization: II. A double nucleation mechanism*. *Journal of molecular biology*, 1985. **183**(4): p. 611-631.
97. Ferrone, F., [17] *Analysis of protein aggregation kinetics*, in *Methods in enzymology*. 1999, Elsevier. p. 256-274.
98. Oosawa, F. and M. Kasai, *A theory of linear and helical aggregations of macromolecules*. *Journal of molecular biology*, 1962. **4**(1): p. 10-21.
99. Cacciuto, A., S. Auer, and D. Frenkel, *Onset of heterogeneous crystal nucleation in colloidal suspensions*. *Nature*, 2004. **428**(6981): p. 404.
100. Ruschak, A.M. and A.D. Miranker, *Fiber-dependent amyloid formation as catalysis of an existing reaction pathway*. *Proceedings of the National Academy of Sciences*, 2007. **104**(30): p. 12341-12346.
101. Tanaka, M., et al., *The physical basis of how prion conformations determine strain phenotypes*. *Nature*, 2006. **442**(7102): p. 585.
102. Collins, S.R., et al., *Mechanism of prion propagation: amyloid growth occurs by monomer addition*. *PLoS biology*, 2004. **2**(10): p. e321.
103. Arosio, P., T.P. Knowles, and S. Linse, *On the lag phase in amyloid fibril formation*. *Physical Chemistry Chemical Physics*, 2015. **17**(12): p. 7606-7618.
104. Cohen, S.I., et al., *Proliferation of amyloid- β 42 aggregates occurs through a secondary nucleation mechanism*. *Proceedings of the National Academy of Sciences*, 2013. **110**(24): p. 9758-9763.
105. Lomakin, A., et al., *On the nucleation and growth of amyloid beta-protein fibrils: detection of nuclei and quantitation of rate constants*. *Proceedings of the National Academy of Sciences*, 1996. **93**(3): p. 1125-1129.
106. Knowles, T.P., M. Vendruscolo, and C.M. Dobson, *The amyloid state and its association with protein misfolding diseases*. *Nature reviews Molecular cell biology*, 2014. **15**(6): p. 384.
107. Dobson, C.M., *Protein folding and misfolding*. *Nature*, 2003. **426**(6968): p. 884.
108. Fändrich, M. and C.M. Dobson, *The behaviour of polyamino acids reveals an inverse side chain effect in amyloid structure formation*. *The EMBO journal*, 2002. **21**(21): p. 5682-5690.
109. Eisenberg, D. and M. Jucker, *The amyloid state of proteins in human diseases*. *Cell*, 2012. **148**(6): p. 1188-1203.
110. Dobson, C.M., *Protein misfolding, evolution and disease*. *Trends in biochemical sciences*, 1999. **24**(9): p. 329-332.
111. Wetzel, R., *Kinetics and thermodynamics of amyloid fibril assembly*. *Accounts of chemical research*, 2006. **39**(9): p. 671-679.

112. Morris, A.M., M.A. Watzky, and R.G. Finke, *Protein aggregation kinetics, mechanism, and curve-fitting: a review of the literature*. Biochimica et Biophysica Acta (BBA)-Proteins and Proteomics, 2009. **1794**(3): p. 375-397.
113. Knowles, T.P., et al., *Observation of spatial propagation of amyloid assembly from single nuclei*. Proceedings of the National Academy of Sciences, 2011. **108**(36): p. 14746-14751.
114. Qiang, W., K. Kelley, and R. Tycko, *Polymorph-specific kinetics and thermodynamics of β -amyloid fibril growth*. Journal of the American Chemical Society, 2013. **135**(18): p. 6860-6871.
115. Kusumoto, Y., et al., *Temperature dependence of amyloid β -protein fibrillization*. Proceedings of the National Academy of Sciences, 1998. **95**(21): p. 12277-12282.
116. Tiiman, A., et al., *In vitro fibrillization of Alzheimer's amyloid- β peptide (1-42)*. AIP Advances, 2015. **5**(9): p. 092401.
117. Dahlgren, K.N., et al., *Oligomeric and fibrillar species of amyloid- β peptides differentially affect neuronal viability*. Journal of Biological Chemistry, 2002. **277**(35): p. 32046-32053.
118. Johansson, A.S., et al., *Physicochemical characterization of the Alzheimer's disease - related peptides A β 1 - 42Arctic and A β 1 - 42wt*. The FEBS journal, 2006. **273**(12): p. 2618-2630.
119. Lin, M.-S., et al., *Investigation of the mechanism of β -amyloid fibril formation by kinetic and thermodynamic analyses*. Langmuir, 2008. **24**(11): p. 5802-5808.
120. Carrotta, R., et al., *Protofibril formation of amyloid β -protein at low pH via a non-cooperative elongation mechanism*. Journal of Biological Chemistry, 2005. **280**(34): p. 30001-30008.
121. Hou, L., et al., *Solution NMR studies of the A β (1- 40) and A β (1- 42) peptides establish that the Met35 oxidation state affects the mechanism of amyloid formation*. Journal of the American Chemical Society, 2004. **126**(7): p. 1992-2005.
122. Gaggelli, E., et al., *Copper homeostasis and neurodegenerative disorders (Alzheimer's, prion, and Parkinson's diseases and amyotrophic lateral sclerosis)*. Chemical reviews, 2006. **106**(6): p. 1995-2044.
123. Tycko, R., *Molecular structure of amyloid fibrils: insights from solid-state NMR*. Quarterly reviews of biophysics, 2006. **39**(1): p. 1-55.
124. Su, Y. and P.-T. Chang, *Acidic pH promotes the formation of toxic fibrils from β -amyloid peptide*. Brain research, 2001. **893**(1-2): p. 287-291.
125. Parasuraman, R. and J.V. Haxby, *Attention and brain function in Alzheimer's disease: a review*. Neuropsychology, 1993. **7**(3): p. 242.
126. Johnson, S.M., et al., *Native state kinetic stabilization as a strategy to ameliorate protein misfolding diseases: a focus on the transthyretin amyloidoses*. Accounts of chemical research, 2005. **38**(12): p. 911-921.
127. Razavi, H., et al., *Benzoxazoles as transthyretin amyloid fibril inhibitors: synthesis, evaluation, and mechanism of action*. Angewandte Chemie International Edition, 2003. **42**(24): p. 2758-2761.
128. De Strooper, B., R. Vassar, and T. Golde, *The secretases: enzymes with therapeutic potential in Alzheimer disease*. Nature Reviews Neurology, 2010. **6**(2): p. 99.
129. Bence, N.F., R.M. Sampat, and R.R. Kopito, *Impairment of the ubiquitin-proteasome system by protein aggregation*. Science, 2001. **292**(5521): p. 1552-1555.
130. Dobson, C.M., *In the footsteps of alchemists*. Science, 2004. **304**(5675): p. 1259-1262.
131. Ross, C.A. and M.A. Poirier, *Protein aggregation and neurodegenerative disease*. Nature medicine, 2004. **10**(7s): p. S10.
132. Morrison, J.H. and P.R. Hof, *Life and death of neurons in the aging brain*. Science, 1997. **278**(5337): p. 412-419.
133. Smale, G., et al., *Evidence for apoptotic cell death in Alzheimer's disease*. Experimental neurology, 1995. **133**(2): p. 225-230.
134. Parsons, C.G., et al., *Memantine and cholinesterase inhibitors: complementary mechanisms in the treatment of Alzheimer's disease*. Neurotoxicity research, 2013. **24**(3): p. 358-369.

135. Marder, K., *Memantine approved to treat moderate to severe Alzheimer's disease*. Current neurology and neuroscience reports, 2004. **4**(5): p. 349-350.
136. Noetzli, M. and C.B. Eap, *Pharmacodynamic, pharmacokinetic and pharmacogenetic aspects of drugs used in the treatment of Alzheimer's disease*. Clinical pharmacokinetics, 2013. **52**(4): p. 225-241.
137. Mangialasche, F., et al., *Alzheimer's disease: clinical trials and drug development*. The Lancet Neurology, 2010. **9**(7): p. 702-716.
138. Klein, J., *Phenserine*. Expert opinion on investigational drugs, 2007. **16**(7): p. 1087-1097.
139. Fisher, A., *M1 muscarinic agonists target major hallmarks of Alzheimer's disease—the pivotal role of brain M1 receptors*. Neurodegenerative Diseases, 2008. **5**(3-4): p. 237-240.
140. Fisher, A., *M1 muscarinic agonists target major hallmarks of Alzheimer's disease-an update*. Current Alzheimer Research, 2007. **4**(5): p. 577-580.
141. Dunbar, G.C., et al., *Effect of ispronicline, a neuronal nicotinic acetylcholine receptor partial agonist, in subjects with age associated memory impairment (AAMI)*. Journal of Psychopharmacology, 2007. **21**(2): p. 171-178.
142. Hilt, D., M. Gawryl, and G. Koenig, *Evp-6124: Safety, Tolerability and cognitive effects of a novel A7 nicotinic receptor agonist in Alzheimer's disease patients on stable donepezil or rivastigmine therapy*. Alzheimer's & Dementia: The Journal of the Alzheimer's Association, 2009. **5**(4): p. e32.
143. Wright, T.M., *Tramiprosate*. Drugs of today (Barcelona, Spain: 1998), 2006. **42**(5): p. 291-298.
144. Saumier, D., et al., *Domain-specific cognitive effects of tramiprosate in patients with mild to moderate Alzheimer's disease: ADAS-cog subscale results from the Alphase Study*. JNHA-The Journal of Nutrition, Health and Aging, 2009. **13**(9): p. 808-812.
145. Gauthier, S., et al., *Effect of tramiprosate in patients with mild-to-moderate Alzheimer's disease: exploratory analyses of the MRI sub-group of the Alphase study*. JNHA-The Journal of Nutrition, Health and Aging, 2009. **13**(6): p. 550-557.
146. Santa-Maria, I., et al., *Tramiprosate, a drug of potential interest for the treatment of Alzheimer's disease, promotes an abnormal aggregation of tau*. Molecular neurodegeneration, 2007. **2**(1): p. 17.
147. McLaurin, J., et al., *Cyclohexanehexol inhibitors of A β aggregation prevent and reverse Alzheimer phenotype in a mouse model*. Nature medicine, 2006. **12**(7): p. 801.
148. Mandel, S.A., et al., *Cell signaling pathways and iron chelation in the neurorestorative activity of green tea polyphenols: special reference to epigallocatechin gallate (EGCG)*. Journal of Alzheimer's Disease, 2008. **15**(2): p. 211-222.
149. Jacobsen, J.S., et al., *Enhanced clearance of A β in brain by sustaining the plasmin proteolysis cascade*. Proceedings of the National Academy of Sciences, 2008. **105**(25): p. 8754-8759.
150. Marr, R.A., et al., *Nepriylsin gene transfer reduces human amyloid pathology in transgenic mice*. Journal of Neuroscience, 2003. **23**(6): p. 1992-1996.
151. Prasad, K.N., et al., *Multiple antioxidants in the prevention and treatment of Alzheimer disease: analysis of biologic rationale*. Clinical neuropharmacology, 2000. **23**(1): p. 2-13.
152. Perry, G., et al., *Reactive oxygen species mediate cellular damage in Alzheimer disease*. Journal of Alzheimer's Disease, 1998. **1**(1): p. 45-55.
153. Casadesus, G., et al., *Alzheimer disease: evidence for a central pathogenic role of iron-mediated reactive oxygen species*. Journal of Alzheimer's disease, 2004. **6**(2): p. 165-169.
154. Kennard, M.L., et al., *Serum levels of the iron binding protein p97 are elevated in Alzheimer's disease*. Nature Medicine, 1996. **2**(11): p. 1230.
155. Viles, J.H., *Metal ions and amyloid fiber formation in neurodegenerative diseases. Copper, zinc and iron in Alzheimer's, Parkinson's and prion diseases*. Coordination Chemistry Reviews, 2012. **256**(19-20): p. 2271-2284.

156. Bush, A.I., et al., *Rapid induction of Alzheimer A beta amyloid formation by zinc*. Science, 1994. **265**(5177): p. 1464-1467.
157. Linder, M.C. and M. Hazegh-Azam, *Copper biochemistry and molecular biology*. The American journal of clinical nutrition, 1996. **63**(5): p. 797S-811S.
158. Markesbery, W.R., *The role of oxidative stress in Alzheimer disease*. Archives of neurology, 1999. **56**(12): p. 1449-1452.
159. Aguirre, P., et al., *Neuroprotective effect of a new 7, 8-dihydroycoumarin-based Fe²⁺/Cu²⁺ chelator in cell and animal models of Parkinson's disease*. ACS chemical neuroscience, 2016. **8**(1): p. 178-185.
160. Faux, N.G., et al., *PBT2 rapidly improves cognition in Alzheimer's Disease: additional phase II analyses*. Journal of Alzheimer's Disease, 2010. **20**(2): p. 509-516.
161. Adlard, P.A., et al., *Rapid restoration of cognition in Alzheimer's transgenic mice with 8-hydroxy quinoline analogs is associated with decreased interstitial Aβ*. Neuron, 2008. **59**(1): p. 43-55.
162. Hou, L., et al., *Methionine 35 oxidation reduces fibril assembly of the amyloid Aβ-(1-42) peptide of Alzheimer's disease*. Journal of Biological Chemistry, 2002. **277**(43): p. 40173-40176.
163. Youdim, M.B. and J.J. Buccafusco, *Multi-functional drugs for various CNS targets in the treatment of neurodegenerative disorders*. Trends in Pharmacological Sciences, 2005. **26**(1): p. 27-35.
164. Bajda, M., et al., *Multi-target-directed ligands in Alzheimer's disease treatment*. Current medicinal chemistry, 2011. **18**(32): p. 4949-4975.
165. Weinreb, O., et al., *Multifunctional neuroprotective derivatives of rasagiline as anti-Alzheimer's disease drugs*. Neurotherapeutics, 2009. **6**(1): p. 163-174.
166. Bolognesi, M.L., A. Cavalli, and C. Melchiorre, *Memoquin: a multi-target-directed ligand as an innovative therapeutic opportunity for Alzheimer's disease*. Neurotherapeutics, 2009. **6**(1): p. 152-162.
167. Selkoe, D.J., *Alzheimer's disease is a synaptic failure*. Science, 2002. **298**(5594): p. 789-791.
168. Porter, J., et al., *Relative oral efficacy and acute toxicity of hydroxypyridin-4-one iron chelators in mice [see comments]*. Blood, 1990. **76**(11): p. 2389-2396.
169. Hider, R., J. Porter, and S. Singh, *The design of therapeutically useful iron chelators*. The development of iron chelators for clinical use, 1994: p. 353-371.
170. Liu, G., et al., *Nanoparticle iron chelators: a new therapeutic approach in Alzheimer disease and other neurologic disorders associated with trace metal imbalance*. Neuroscience letters, 2006. **406**(3): p. 189-193.
171. Shang, L., K. Nienhaus, and G.U. Nienhaus, *Engineered nanoparticles interacting with cells: size matters*. Journal of nanobiotechnology, 2014. **12**(1): p. 5.
172. Gregori, M., M. Masserini, and S. Mancini, *Nanomedicine for the treatment of Alzheimer's disease*. Nanomedicine, 2015. **10**(7): p. 1203-1218.
173. Masserini, M., *Nanoparticles for brain drug delivery*. ISRN biochemistry, 2013. **2013**.
174. Sharifi, S., et al., *Toxicity of nanomaterials*. Chemical Society Reviews, 2012. **41**(6): p. 2323-2343.
175. Mahmoudi, M., et al., *Protein-nanoparticle interactions: opportunities and challenges*. Chemical reviews, 2011. **111**(9): p. 5610-5637.
176. Gnach, A., et al., *Upconverting nanoparticles: assessing the toxicity*. Chemical Society Reviews, 2015. **44**(6): p. 1561-1584.
177. Gagliardi, M., G. Bardi, and A. Bifone, *Polymeric nanocarriers for controlled and enhanced delivery of therapeutic agents to the CNS*. Therapeutic delivery, 2012. **3**(7): p. 875-887.
178. Yang, Z., et al., *Destruction of amyloid fibrils by graphene through penetration and extraction of peptides*. Nanoscale, 2015. **7**(44): p. 18725-18737.

179. Lee, J.S., B.I. Lee, and C.B. Park, *Photo-induced inhibition of Alzheimer's β -amyloid aggregation in vitro by rose bengal*. *Biomaterials*, 2015. **38**: p. 43-49.
180. Grayden, D.B., et al., *Implant design and development*. Cochlear implants: A practical guide, 2006: p. 1-20.
181. Achenbach, S., et al., *Effects of magnetic resonance imaging on cardiac pacemakers and electrodes*. *American heart journal*, 1997. **134**(3): p. 467-473.
182. Childs, S.G., *Stimulators of bone healing: Biologic and biomechanical*. *Orthopaedic Nursing*, 2003. **22**(6): p. 421-428.
183. Bekard, I. and D.E. Dunstan, *Electric field induced changes in protein conformation*. *Soft Matter*, 2014. **10**(3): p. 431-437.
184. Dobson, C.M., *Structural biology: prying into prions*. *Nature*, 2005. **435**(7043): p. 747.
185. Dobson, C.M., *Experimental investigation of protein folding and misfolding*. *Methods*, 2004. **34**(1): p. 4-14.
186. Yu, L., et al., *Structural characterization of a soluble amyloid β -peptide oligomer*. *Biochemistry*, 2009. **48**(9): p. 1870-1877.
187. Antzutkin, O.N., *Amyloidosis of Alzheimer's A β peptides: solid - state nuclear magnetic resonance, electron paramagnetic resonance, transmission electron microscopy, scanning transmission electron microscopy and atomic force microscopy studies*. *Magnetic Resonance in Chemistry*, 2004. **42**(2): p. 231-246.
188. Zandomenighi, G., et al., *FTIR reveals structural differences between native β - sheet proteins and amyloid fibrils*. *Protein Science*, 2004. **13**(12): p. 3314-3321.
189. Hepler, R.W., et al., *Solution state characterization of amyloid β -derived diffusible ligands*. *Biochemistry*, 2006. **45**(51): p. 15157-15167.
190. Mastrangelo, I.A., et al., *High-resolution atomic force microscopy of soluble A β 42 oligomers*. *Journal of molecular biology*, 2006. **358**(1): p. 106-119.
191. Harper, J.D., et al., *Assembly of A β amyloid protofibrils: an in vitro model for a possible early event in Alzheimer's disease*. *Biochemistry*, 1999. **38**(28): p. 8972-8980.
192. Blackley, H., et al., *In-situ atomic force microscopy study of β -amyloid fibrillization*. *Journal of molecular biology*, 2000. **298**(5): p. 833-840.
193. Lamert, M., A. Barlow, and B. Chromy, *Diffusible, nonfibrillar ligands derived from A β 1-42 are potent central nervous system neurotoxins*. *Proc Natl Acad Sci USA*, 1998. **95**(4): p. 6448-6453.
194. Biancalana, M. and S. Koide, *Molecular mechanism of Thioflavin-T binding to amyloid fibrils*. *Biochimica et Biophysica Acta (BBA)-Proteins and Proteomics*, 2010. **1804**(7): p. 1405-1412.
195. Vassar, P.S. and C. Culling, *Fluorescent stains, with special reference to amyloid and connective tissues*. *Archives of pathology*, 1959. **68**: p. 487-498.
196. Lindgren, M., K. Sörgjerd, and P. Hammarström, *Detection and characterization of aggregates, prefibrillar amyloidogenic oligomers, and protofibrils using fluorescence spectroscopy*. *Biophysical journal*, 2005. **88**(6): p. 4200-4212.
197. Andersen, C.B., et al., *Branching in amyloid fibril growth*. *Biophysical journal*, 2009. **96**(4): p. 1529-1536.
198. Ban, T., et al., *Direct observation of A β amyloid fibril growth and inhibition*. *Journal of molecular biology*, 2004. **344**(3): p. 757-767.
199. Esbjörner, E.K., et al., *Direct observations of amyloid β self-assembly in live cells provide insights into differences in the kinetics of A β (1-40) and A β (1-42) aggregation*. *Chemistry & biology*, 2014. **21**(6): p. 732-742.
200. Segel, D.J., et al., *Transient dimer in the refolding kinetics of cytochrome c characterized by small-angle X-ray scattering*. *Biochemistry*, 1999. **38**(46): p. 15352-15359.
201. Uversky, V.N., et al., *Association of partially-folded intermediates of staphylococcal nuclease induces structure and stability*. *Protein science*, 1999. **8**(1): p. 161-173.

202. Joo, C., et al., *Advances in single-molecule fluorescence methods for molecular biology*. Annu. Rev. Biochem., 2008. **77**: p. 51-76.
203. Moerner, W., *New directions in single-molecule imaging and analysis*. Proceedings of the National Academy of Sciences, 2007. **104**(31): p. 12596-12602.
204. Neuman, K.C. and S.M. Block, *Optical trapping*. Review of scientific instruments, 2004. **75**(9): p. 2787-2809.
205. Viani, M.B., et al., *Probing protein-protein interactions in real time*. Nature Structural & Molecular Biology, 2000. **7**(8): p. 644.
206. Ando, T., et al., *A high-speed atomic force microscope for studying biological macromolecules*. Proceedings of the National Academy of Sciences, 2001. **98**(22): p. 12468-12472.
207. Ando, T., *High-speed AFM imaging*. Current opinion in structural biology, 2014. **28**: p. 63-68.
208. Kodera, N., M. Sakashita, and T. Ando, *Dynamic proportional-integral-differential controller for high-speed atomic force microscopy*. Review of Scientific Instruments, 2006. **77**(8): p. 083704.
209. Ando, T., T. Uchihashi, and T. Fukuma, *High-speed atomic force microscopy for nano-visualization of dynamic biomolecular processes*. Progress in Surface Science, 2008. **83**(7-9): p. 337-437.
210. Kodera, N., H. Yamashita, and T. Ando, *Active damping of the scanner for high-speed atomic force microscopy*. Review of scientific instruments, 2005. **76**(5): p. 053708.
211. Ando, T., et al., *High-speed AFM and nano-visualization of biomolecular processes*. Pflügers Archiv-European Journal of Physiology, 2008. **456**(1): p. 211-225.
212. Picco, L., et al., *Breaking the speed limit with atomic force microscopy*. Nanotechnology, 2006. **18**(4): p. 044030.
213. Shibata, M., et al., *High-speed atomic force microscopy shows dynamic molecular processes in photoactivated bacteriorhodopsin*. Nature nanotechnology, 2010. **5**(3): p. 208.
214. Yamashita, H., et al., *Role of trimer-trimer interaction of bacteriorhodopsin studied by optical spectroscopy and high-speed atomic force microscopy*. Journal of structural biology, 2013. **184**(1): p. 2-11.
215. Yokokawa, M. and K. Takeyasu, *Motion of the Ca²⁺ - pump captured*. The FEBS journal, 2011. **278**(17): p. 3025-3031.
216. Uchihashi, T., et al., *High-speed atomic force microscopy reveals rotary catalysis of rotorless F1-ATPase*. Science, 2011. **333**(6043): p. 755-758.
217. Suzuki, Y., et al., *Visualization of structural changes accompanying activation of N-methyl-D-aspartate (NMDA) receptors using fast-scan atomic force microscopy imaging*. Journal of Biological Chemistry, 2013. **288**(2): p. 778-784.
218. Yamamoto, D., et al., *Anisotropic diffusion of point defects in a two-dimensional crystal of streptavidin observed by high-speed atomic force microscopy*. Nanotechnology, 2008. **19**(38): p. 384009.
219. Casuso, I., et al., *Experimental evidence for membrane-mediated protein-protein interaction*. Biophysical journal, 2010. **99**(7): p. L47-L49.
220. Yamashita, H., et al., *Dynamics of bacteriorhodopsin 2D crystal observed by high-speed atomic force microscopy*. Journal of structural biology, 2009. **167**(2): p. 153-158.
221. Milhiet, P.-E., et al., *Deciphering the structure, growth and assembly of amyloid-like fibrils using high-speed atomic force microscopy*. PLoS One, 2010. **5**(10): p. e13240.
222. Yilmaz, N., et al., *Real-time visualization of assembling of a sphingomyelin-specific toxin on planar lipid membranes*. Biophysical journal, 2013. **105**(6): p. 1397-1405.
223. Miyagi, A., et al., *Visualization of intrinsically disordered regions of proteins by high - speed atomic force microscopy*. Chemphyschem, 2008. **9**(13): p. 1859-1866.

224. Suzuki, A., et al., *Spindle microtubules generate tension-dependent changes in the distribution of inner kinetochore proteins*. The Journal of cell biology, 2011. **193**(1): p. 125-140.
225. Suzuki, Y., et al., *Visual analysis of concerted cleavage by type IIF restriction enzyme SfiI in subsecond time region*. Biophysical journal, 2011. **101**(12): p. 2992-2998.
226. Yamashita, H., et al., *Single-molecule imaging on living bacterial cell surface by high-speed AFM*. Journal of molecular biology, 2012. **422**(2): p. 300-309.
227. Kodera, N., et al., *Video imaging of walking myosin V by high-speed atomic force microscopy*. Nature, 2010. **468**(7320): p. 72.
228. Watanabe-Nakayama, T., et al., *High-speed atomic force microscopy reveals structural dynamics of amyloid β 1–42 aggregates*. Proceedings of the National Academy of Sciences, 2016. **113**(21): p. 5835-5840.
229. Esler, W.P., et al., *Alzheimer's disease amyloid propagation by a template-dependent dock-lock mechanism*. Biochemistry, 2000. **39**(21): p. 6288-6295.
230. Banerjee, S., et al., *Nanoscale dynamics of amyloid β -42 oligomers as revealed by high-speed atomic force microscopy*. ACS nano, 2017. **11**(12): p. 12202-12209.
231. Hardy, J.A. and G.A. Higgins, *Alzheimer's Disease: The Amyloid Cascade Hypothesis*. Science, 1992. **256**(5054): p. 184.
232. Catalano, S.M., et al., *The role of amyloid-beta derived diffusible ligands (ADDLs) in Alzheimer's disease*. Current topics in medicinal chemistry, 2006. **6**(6): p. 597-608.
233. Gong, Y., et al., *Alzheimer's disease-affected brain: Presence of oligomeric A β ligands (ADDLs) suggests a molecular basis for reversible memory loss*. Proceedings of the National Academy of Sciences of the United States of America, 2003. **100**(18): p. 10417-10422.
234. Hamley, I.W., *The Amyloid Beta Peptide: A Chemist's Perspective. Role in Alzheimer's and Fibrillization*. Chemical Reviews, 2012. **112**(10): p. 5147-5192.
235. Glabe, C.G. and R. Kaye, *Common structure and toxic function of amyloid oligomers implies a common mechanism of pathogenesis*. Neurology, 2006. **66**(1 suppl 1): p. S74.
236. Braak, H., E. Braak, and J. Bohl, *Staging of Alzheimer-Related Cortical Destruction*. European Neurology, 1993. **33**(6): p. 403-408.
237. Johnson, Robin D., et al., *Single-Molecule Imaging Reveals A β 42:A β 40 Ratio-Dependent Oligomer Growth on Neuronal Processes*. Biophysical Journal, 2013. **104**(4): p. 894-903.
238. Lesné, S., et al., *A specific amyloid- β protein assembly in the brain impairs memory*. Nature, 2006. **440**: p. 352.
239. Holtzman, D.M., C.M. John, and A. Goate, *Alzheimer's Disease: The Challenge of the Second Century*. Science translational medicine, 2011. **3**(77): p. 77sr1-77sr1.
240. Golde, T.E., L.S. Schneider, and E.H. Koo, *Anti-A β therapeutics in Alzheimer's disease: The Need for a Paradigm Shift*. Neuron, 2011. **69**(2): p. 203-213.
241. Sarroukh, R., et al., *Transformation of amyloid β (1–40) oligomers into fibrils is characterized by a major change in secondary structure*. Cellular and Molecular Life Sciences, 2011. **68**(8): p. 1429-1438.
242. Krimm, S. and J. Bandekar, *Vibrational spectroscopy and conformation of peptides, polypeptides, and proteins*, in *Advances in protein chemistry*. 1986, Elsevier. p. 181-364.
243. Xue, C., et al., *Thioflavin T as an amyloid dye: fibril quantification, optimal concentration and effect on aggregation*. Royal Society Open Science, 2017. **4**(1): p. 160696.
244. Ryu, J., et al., *Influence of multiple metal ions on β -amyloid aggregation and dissociation on a solid surface*. Biochemistry, 2008. **47**(19): p. 5328-5335.
245. Klug Genevieve, M.J.A., et al., *β - Amyloid protein oligomers induced by metal ions and acid pH are distinct from those generated by slow spontaneous ageing at neutral pH*. European Journal of Biochemistry, 2003. **270**(21): p. 4282-4293.
246. Foderà, V., et al., *Thioflavin T hydroxylation at basic pH and its effect on amyloid fibril detection*. The Journal of Physical Chemistry B, 2008. **112**(47): p. 15174-15181.

247. Korasick David, A. and J. Tanner John, *Determination of protein oligomeric structure from small - angle X - ray scattering*. Protein Science, 2018. **27**(4): p. 814-824.
248. Makin, O.S., et al., *Molecular basis for amyloid fibril formation and stability*. Proceedings of the National Academy of Sciences of the United States of America, 2005. **102**(2): p. 315.
249. Nelson, R., et al., *Structure of the cross- β spine of amyloid-like fibrils*. Nature, 2005. **435**: p. 773.
250. Kersey, F.R., W.C. Yount, and S.L. Craig, *Single-Molecule Force Spectroscopy of Bimolecular Reactions: System Homology in the Mechanical Activation of Ligand Substitution Reactions*. Journal of the American Chemical Society, 2006. **128**(12): p. 3886-3887.
251. Lv, Z., et al., *Mechanism of amyloid β -protein dimerization determined using single-molecule AFM force spectroscopy*. Scientific Reports, 2013. **3**: p. 2880.
252. Murat, M. and G.S. Grest, *Molecular Dynamics Simulations of the Force between a Polymer Brush and an AFM Tip*. Macromolecules, 1996. **29**(25): p. 8282-8284.
253. Yu, J., S. Malkova, and Y.L. Lyubchenko, *α -Synuclein Misfolding: Single Molecule AFM Force Spectroscopy Study*. Journal of Molecular Biology, 2008. **384**(4): p. 992-1001.
254. Ma, B. and R. Nussinov, *Simulations as analytical tools to understand protein aggregation and predict amyloid conformation*. Current Opinion in Chemical Biology, 2006. **10**(5): p. 445-452.
255. Baumketner, A., et al., *Amyloid β - protein monomer structure: A computational and experimental study*. Protein Science, 2006. **15**(3): p. 420-428.
256. Daura, X., et al., *Peptide folding: when simulation meets experiment*. Angewandte Chemie International Edition, 1999. **38**(1 - 2): p. 236-240.
257. Ando, T., *High-speed atomic force microscopy coming of age*. Nanotechnology, 2012. **23**(6): p. 062001.
258. Katan, A.J. and C. Dekker, *High-speed AFM reveals the dynamics of single biomolecules at the nanometer scale*. Cell, 2011. **147**(5): p. 979-982.
259. Lyubchenko, Y. and L. Shlyakhtenko, *Atomic Force Microscopy Imaging and Probing of Amyloid Nanoaggregates*. Handbook of Clinical Nanomedicine, 2016: p. 589-616.
260. Rechtes, M. and E. Gazit, *Self - assembly of peptide nanotubes and amyloid - like structures by charged - termini - capped diphenylalanine peptide analogues*. Israel Journal of Chemistry, 2010. **45**(3): p. 363-371.
261. Ando, T., et al., *High-speed atomic force microscopy for capturing dynamic behavior of protein molecules at work*. e-Journal of Surface Science and Nanotechnology, 2005. **3**: p. 384-392.
262. Ando, T., T. Uchihashi, and N. Kodera, *High-speed atomic force microscopy*. Japanese journal of applied physics, 2012. **51**(8S3): p. 08KA02.
263. Ando, T., T. Uchihashi, and N. Kodera, *High-Speed AFM and Applications to Biomolecular Systems*. Annual Review of Biophysics, 2013. **42**(1): p. 393-414.
264. Uchihashi, T., N. Kodera, and T. Ando, *Guide to video recording of structure dynamics and dynamic processes of proteins by high-speed atomic force microscopy*. nature protocols, 2012. **7**(6): p. 1193.
265. Janek, K., et al., *Study of the conformational transition of A β (1- 42) using d-amino acid replacement analogues*. Biochemistry, 2001. **40**(18): p. 5457-5463.
266. Fezoui, Y. and D.B. Teplow, *Kinetic Studies of Amyloid β -Protein Fibril Assembly DIFFERENTIAL EFFECTS OF α -HELIX STABILIZATION*. Journal of Biological Chemistry, 2002. **277**(40): p. 36948-36954.
267. Kowalewski, T. and D.M. Holtzman, *In situ atomic force microscopy study of Alzheimer's β -amyloid peptide on different substrates: New insights into mechanism of β -sheet formation*. Proceedings of the National Academy of Sciences, 1999. **96**(7): p. 3688-3693.

268. Harper, J.D., C.M. Lieber, and P.T. Lansbury Jr, *Atomic force microscopic imaging of seeded fibril formation and fibril branching by the Alzheimer's disease amyloid- β protein*. *Chemistry & biology*, 1997. **4**(12): p. 951-959.
269. Stine, W.B., et al., *Preparing Synthetic A β in Different Aggregation States*. *Methods in molecular biology* (Clifton, N.J.), 2011. **670**: p. 13-32.
270. Economou, N.J., et al., *Amyloid β -Protein Assembly and Alzheimer's Disease: Dodecamers of A β 42, but Not of A β 40, Seed Fibril Formation*. *Journal of the American Chemical Society*, 2016. **138**(6): p. 1772-1775.
271. Prabhu, Y., et al., *Adaptor protein 2-mediated endocytosis of the β -secretase BACE1 is dispensable for amyloid precursor protein processing*. *Molecular biology of the cell*, 2012. **23**(12): p. 2339-2351.
272. Sgourakis, N.G., et al., *The Alzheimer's peptides A β 40 and 42 adopt distinct conformations in water: a combined MD/NMR study*. *Journal of molecular biology*, 2007. **368**(5): p. 1448-1457.
273. Massi, F., et al., *Simulation study of the structure and dynamics of the Alzheimer's amyloid peptide congener in solution*. *Biophysical Journal*, 2001. **80**(1): p. 31-44.
274. Cizas, P., et al., *Size-dependent neurotoxicity of β -amyloid oligomers*. *Archives of biochemistry and biophysics*, 2010. **496**(2): p. 84-92.
275. Gorman, P.M., et al., *Alternate aggregation pathways of the Alzheimer β -amyloid peptide: A β association kinetics at endosomal pH*. *Journal of molecular biology*, 2003. **325**(4): p. 743-757.
276. Roher, A.E., et al., *Morphology and toxicity of A β -(1-42) dimer derived from neuritic and vascular amyloid deposits of Alzheimer's disease*. *Journal of Biological Chemistry*, 1996. **271**(34): p. 20631-20635.
277. Ono, K., M.M. Condron, and D.B. Teplow, *Structure-neurotoxicity relationships of amyloid β -protein oligomers*. *Proceedings of the National Academy of Sciences*, 2009. **106**(35): p. 14745-14750.
278. Selkoe, D.J., *Soluble oligomers of the amyloid β -protein impair synaptic plasticity and behavior*. *Behavioural brain research*, 2008. **192**(1): p. 106-113.
279. Larson, M.E. and S.E. Lesné, *Soluble A β oligomer production and toxicity*. *Journal of neurochemistry*, 2012. **120**(s1): p. 125-139.
280. Barghorn, S., et al., *Globular amyloid β - peptide1-42 oligomer- a homogenous and stable neuropathological protein in Alzheimer's disease*. *Journal of neurochemistry*, 2005. **95**(3): p. 834-847.
281. Tran, L., et al., *Structure of ring-shaped A β 42 oligomers determined by conformational selection*. *Scientific reports*, 2016. **6**: p. 21429.
282. Meng, F., et al., *Highly disordered amyloid- β monomer probed by single-molecule FRET and MD simulation*. *Biophysical journal*, 2018. **114**(4): p. 870-884.
283. Buchete, N.-V., R. Tycko, and G. Hummer, *Molecular dynamics simulations of Alzheimer's β -amyloid protofilaments*. *Journal of molecular biology*, 2005. **353**(4): p. 804-821.
284. Schuler, B., E.A. Lipman, and W.A. Eaton, *Probing the free-energy surface for protein folding with single-molecule fluorescence spectroscopy*. *Nature*, 2002. **419**: p. 743.
285. Kasas, S., et al., *Simulation of an atomic force microscope imaging a moving protein*. *Probe Microscopy*, 2000. **2**: p. 37-44.
286. Schuler, B., E.A. Lipman, and W.A. Eaton, *Probing the free-energy surface for protein folding with single-molecule fluorescence spectroscopy*. *Nature*, 2002. **419**(6908): p. 743.
287. Neuman, K.C. and A. Nagy, *Single-molecule force spectroscopy: optical tweezers, magnetic tweezers and atomic force microscopy*. *Nature methods*, 2008. **5**(6): p. 491.
288. Gittens, S.A., et al., *Impact of tether length on bone mineral affinity of protein-bisphosphonate conjugates*. *Pharmaceutical research*, 2004. **21**(4): p. 608-616.

289. Zlatanova, J., S.M. Lindsay, and S.H. Leuba, *Single molecule force spectroscopy in biology using the atomic force microscope*. Progress in biophysics and molecular biology, 2000. **74**(1-2): p. 37-61.
290. Kim, B.-H., et al., *Single-molecule atomic force microscopy force spectroscopy study of A β -40 interactions*. Biochemistry, 2011. **50**(23): p. 5154-5162.
291. Hane, F., S. Attwood, and Z. Leonenko, *Comparison of three competing dynamic force spectroscopy models to study binding forces of amyloid- β (1–42)*. Soft matter, 2014. **10**(12): p. 1924-1930.
292. Hane, F.T., et al., *Effect of copper and zinc on the single molecule self-affinity of Alzheimer's amyloid- β peptides*. PLoS One, 2016. **11**(1): p. e0147488.
293. Schauerte, J.A., et al., *Simultaneous single-molecule fluorescence and conductivity studies reveal distinct classes of A β species on lipid bilayers*. Biochemistry, 2010. **49**(14): p. 3031-3039.
294. Zhang, X., C. Liu, and Z. Wang, *Force spectroscopy of polymers: Studying on intramolecular and intermolecular interactions in single molecular level*. Polymer, 2008. **49**(16): p. 3353-3361.
295. Hortschansky, P., et al., *The aggregation kinetics of Alzheimer's β - amyloid peptide is controlled by stochastic nucleation*. Protein science, 2005. **14**(7): p. 1753-1759.
296. Nag, S., et al., *Measurement of the attachment and assembly of small amyloid- β oligomers on live cell membranes at physiological concentrations using single-molecule tools*. Biophysical journal, 2010. **99**(6): p. 1969-1975.
297. Orte, A., et al., *Direct characterization of amyloidogenic oligomers by single-molecule fluorescence*. Proceedings of the National Academy of Sciences, 2008. **105**(38): p. 14424-14429.
298. Gsponer, J., U. Haberthür, and A. Caflisch, *The role of side-chain interactions in the early steps of aggregation: Molecular dynamics simulations of an amyloid-forming peptide from the yeast prion Sup35*. Proceedings of the National Academy of Sciences, 2003. **100**(9): p. 5154-5159.
299. Fändrich, M., et al., *Myoglobin forms amyloid fibrils by association of unfolded polypeptide segments*. Proceedings of the National Academy of Sciences, 2003. **100**(26): p. 15463-15468.
300. Bucciantini, M., et al., *Inherent toxicity of aggregates implies a common mechanism for protein misfolding diseases*. nature, 2002. **416**(6880): p. 507.
301. Blessed, G., B.E. Tomlinson, and M. Roth, *The association between quantitative measures of dementia and of senile change in the cerebral grey matter of elderly subjects*. Br J Psychiatry, 1968. **114**(512): p. 797-811.
302. Neve, R.L., et al., *Genetics and biology of the Alzheimer amyloid precursor*, in *Progress in brain research*. 1990, Elsevier. p. 257-267.
303. Katzman, R. and T. Saitoh, *Advances in Alzheimer's disease*. The FASEB journal, 1991. **5**(3): p. 278-286.
304. McKee, A., K. Kosik, and N. Kowall, *Neuritic pathology and dementia in Alzheimer's disease*. Annals of Neurology: Official Journal of the American Neurological Association and the Child Neurology Society, 1991. **30**(2): p. 156-165.
305. Selkoe, D.J., *The molecular pathology of Alzheimer's disease*. Neuron, 1991. **6**(4): p. 487-498.
306. Kumar-Singh, S., et al., *Behavioral disturbances without amyloid deposits in mice overexpressing human amyloid precursor protein with Flemish (A692G) or Dutch (E693Q) mutation*. Neurobiology of disease, 2000. **7**(1): p. 9-22.
307. Moechars, D., et al., *Early phenotypic changes in transgenic mice that overexpress different mutants of amyloid precursor protein in brain*. Journal of Biological Chemistry, 1999. **274**(10): p. 6483-6492.
308. Hsia, A.Y., et al., *Plaque-independent disruption of neural circuits in Alzheimer's disease mouse models*. Proceedings of the National Academy of Sciences, 1999. **96**(6): p. 3228-3233.

309. Chui, D.-H., et al., *Transgenic mice with Alzheimer presenilin 1 mutations show accelerated neurodegeneration without amyloid plaque formation*. *Nature medicine*, 1999. **5**(5): p. 560.
310. Shankar, G.M., et al., *Amyloid- β protein dimers isolated directly from Alzheimer's brains impair synaptic plasticity and memory*. *Nature medicine*, 2008. **14**(8): p. 837.
311. Törnquist, M., et al., *Secondary nucleation in amyloid formation*. *Chemical Communications*, 2018. **54**(63): p. 8667-8684.
312. Straub, J.E. and D. Thirumalai, *Toward a molecular theory of early and late events in monomer to amyloid fibril formation*. *Annual review of physical chemistry*, 2011. **62**: p. 437-463.
313. Lee, C.-C., et al., *A three-stage kinetic model of amyloid fibrillation*. *Biophysical journal*, 2007. **92**(10): p. 3448-3458.
314. Jan, A., et al., *A β 42 neurotoxicity is mediated by ongoing nucleated polymerization process rather than by discrete A β 42 species*. *Journal of Biological Chemistry*, 2011. **286**(10): p. 8585-8596.
315. Cohen, S.I., et al., *A molecular chaperone breaks the catalytic cycle that generates toxic A β oligomers*. *Nature structural & molecular biology*, 2015. **22**(3): p. 207.
316. Harper, J.D. and P.T. Lansbury Jr, *Models of amyloid seeding in Alzheimer's disease and scrapie: mechanistic truths and physiological consequences of the time-dependent solubility of amyloid proteins*. *Annual review of biochemistry*, 1997. **66**(1): p. 385-407.
317. Wood, S.J., W. Chan, and R. Wetzel, *Seeding of A β fibril formation is inhibited by all three isotypes of apolipoprotein E*. *Biochemistry*, 1996. **35**(38): p. 12623-12628.
318. Serpell, L.C., M. Sunde, and C.C. Blake, *The molecular basis of amyloidosis*. *Cellular and Molecular Life Sciences CMLS*, 1997. **53**(11-12): p. 871-887.
319. Rochet, J.-C. and P.T. Lansbury Jr, *Amyloid fibrillogenesis: themes and variations*. *Current opinion in structural biology*, 2000. **10**(1): p. 60-68.
320. Burdick, D., et al., *Assembly and aggregation properties of synthetic Alzheimer's A4/beta amyloid peptide analogs*. *Journal of Biological Chemistry*, 1992. **267**(1): p. 546-554.
321. Cavallucci, V., M. D'Amelio, and F. Cecconi, *A β toxicity in Alzheimer's disease*. *Molecular neurobiology*, 2012. **45**(2): p. 366-378.
322. Barrow, C.J., et al., *Solution conformations and aggregational properties of synthetic amyloid β -peptides of Alzheimer's disease: analysis of circular dichroism spectra*. *Journal of molecular biology*, 1992. **225**(4): p. 1075-1093.
323. Shen, C.-L., M.C. Fitzgerald, and R.M. Murphy, *Effect of acid predissolution on fibril size and fibril flexibility of synthetic beta-amyloid peptide*. *Biophysical journal*, 1994. **67**(3): p. 1238-1246.
324. Kaye, R., et al., *Conformational transitions of islet amyloid polypeptide (IAPP) in amyloid formation in vitro*. *Journal of molecular biology*, 1999. **287**(4): p. 781-796.
325. Matsunaga, Y., et al., *Conformational changes preceding amyloid-fibril formation of amyloid-beta and stefin B; parallels in pH dependence*. *Current medicinal chemistry*, 2002. **9**(19): p. 1717-1724.
326. Klug, G.M., et al., *β - Amyloid protein oligomers induced by metal ions and acid pH are distinct from those generated by slow spontaneous ageing at neutral pH*. *European journal of biochemistry*, 2003. **270**(21): p. 4282-4293.
327. Garzon-Rodriguez, W., et al., *Soluble amyloid A β -(1-40) exists as a stable dimer at low concentrations*. *Journal of Biological Chemistry*, 1997. **272**(34): p. 21037-21044.
328. Kirkitadze, M.D., M.M. Condrón, and D.B. Teplow, *Identification and characterization of key kinetic intermediates in amyloid β -protein fibrillogenesis*. *Journal of molecular biology*, 2001. **312**(5): p. 1103-1119.
329. Lomakin, A., et al., *Kinetic theory of fibrillogenesis of amyloid β -protein*. *Proceedings of the National Academy of Sciences*, 1997. **94**(15): p. 7942-7947.

330. Di Fede, G., et al., *A recessive mutation in the APP gene with dominant-negative effect on amyloidogenesis*. *Science*, 2009. **323**(5920): p. 1473-1477.
331. Jonsson, T., et al., *A mutation in APP protects against Alzheimer's disease and age-related cognitive decline*. *Nature*, 2012. **488**(7409): p. 96.
332. Betts, V., et al., *Aggregation and catabolism of disease-associated intra-A β mutations: reduced proteolysis of A β A21G by neprilysin*. *Neurobiology of disease*, 2008. **31**(3): p. 442-450.
333. Carrotta, R., et al., *Inhibiting effect of as1-casein on A β 1–40 fibrillogenesis*. *Biochimica et Biophysica Acta (BBA)-General Subjects*, 2012. **1820**(2): p. 124-132.
334. Ecroyd, H. and J.A. Carver, *Crystallin proteins and amyloid fibrils*. *Cellular and Molecular Life Sciences*, 2009. **66**(1): p. 62.
335. Hoyer, W., et al., *Stabilization of a β -hairpin in monomeric Alzheimer's amyloid- β peptide inhibits amyloid formation*. *Proceedings of the National Academy of Sciences*, 2008. **105**(13): p. 5099-5104.
336. Hughes, E., R.M. Burke, and A.J. Doig, *Inhibition of Toxicity in the β -Amyloid Peptide Fragment β -(25–35) Using N-Methylated Derivatives A GENERAL STRATEGY TO PREVENT AMYLOID FORMATION*. *Journal of Biological Chemistry*, 2000. **275**(33): p. 25109-25115.
337. Grey, M., et al., *Membrane interaction of α -synuclein in different aggregation states*. *Journal of Parkinson's disease*, 2011. **1**(4): p. 359-371.
338. Hellstrand, E., E. Sparr, and S. Linse, *Retardation of A β fibril formation by phospholipid vesicles depends on membrane phase behavior*. *Biophysical journal*, 2010. **98**(10): p. 2206-2214.
339. Cabaleiro-Lago, C., et al., *Inhibition of IAPP and IAPP (20–29) fibrillation by polymeric nanoparticles*. *Langmuir*, 2009. **26**(5): p. 3453-3461.
340. Cabaleiro-Lago, C., et al., *Dual effect of amino modified polystyrene nanoparticles on amyloid β protein fibrillation*. *ACS chemical neuroscience*, 2010. **1**(4): p. 279-287.
341. Cabaleiro-Lago, C., O. Szczepankiewicz, and S. Linse, *The effect of nanoparticles on amyloid aggregation depends on the protein stability and intrinsic aggregation rate*. *Langmuir*, 2012. **28**(3): p. 1852-1857.
342. Vacha, R., S. Linse, and M. Lund, *Surface effects on aggregation kinetics of amyloidogenic peptides*. *Journal of the American Chemical Society*, 2014. **136**(33): p. 11776-11782.
343. Campioni, S., et al., *The presence of an air–water interface affects formation and elongation of α -synuclein fibrils*. *Journal of the American Chemical Society*, 2014. **136**(7): p. 2866-2875.
344. Munishkina, L.A., et al., *Role of protein–water interactions and electrostatics in α -synuclein fibril formation*. *Biochemistry*, 2004. **43**(11): p. 3289-3300.
345. Härd, T. and C. Lendel, *Inhibition of amyloid formation*. *Journal of molecular biology*, 2012. **421**(4-5): p. 441-465.
346. Wahlström, A., et al., *Specific binding of a β -cyclodextrin dimer to the amyloid β peptide modulates the peptide aggregation process*. *Biochemistry*, 2012. **51**(21): p. 4280-4289.
347. Buell, A.K., et al., *Solution conditions determine the relative importance of nucleation and growth processes in α -synuclein aggregation*. *Proceedings of the National Academy of Sciences*, 2014. **111**(21): p. 7671-7676.
348. Nielsen, L., et al., *Effect of environmental factors on the kinetics of insulin fibril formation: elucidation of the molecular mechanism*. *Biochemistry*, 2001. **40**(20): p. 6036-6046.
349. Linse, S., et al., *Nucleation of protein fibrillation by nanoparticles*. *Proceedings of the National Academy of Sciences*, 2007. **104**(21): p. 8691-8696.
350. Meisl, G., et al., *Molecular mechanisms of protein aggregation from global fitting of kinetic models*. *Nature protocols*, 2016. **11**(2): p. 252.
351. Gaspar, R., et al., *Secondary nucleation of monomers on fibril surface dominates α -synuclein aggregation and provides autocatalytic amyloid amplification*. *Quarterly reviews of biophysics*, 2017. **50**.

352. Bemporad, F. and F. Chiti, *Protein misfolded oligomers: experimental approaches, mechanism of formation, and structure-toxicity relationships*. Chemistry & biology, 2012. **19**(3): p. 315-327.
353. Kodali, R. and R. Wetzel, *Polymorphism in the intermediates and products of amyloid assembly*. Current opinion in structural biology, 2007. **17**(1): p. 48-57.
354. Pellarin, R., E. Guarnera, and A. Caflich, *Pathways and intermediates of amyloid fibril formation*. Journal of molecular biology, 2007. **374**(4): p. 917-924.
355. Shire, S.J., J.J. Steckert, and T.M. Schuster, *Mechanism of self-assembly of tobacco mosaic virus protein: II. Characterization of the metastable polymerization nucleus and the initial stages of helix formation*. Journal of molecular biology, 1979. **127**(4): p. 487-506.
356. Avidan-Shpalter, C. and E. Gazit, *The early stages of amyloid formation: biophysical and structural characterization of human calcitonin pre-fibrillar assemblies*. Amyloid, 2006. **13**(4): p. 216-225.
357. Ando, T., T. Uchihashi, and N. Kodera, *High-speed AFM and applications to biomolecular systems*. Annual review of biophysics, 2013. **42**: p. 393-414.
358. Feng, L., et al., *Dynamics of Inter-Molecular Interactions Between Single A β 42 Oligomeric and Aggregate Species by High-Speed Atomic Force Microscopy*. Journal of molecular biology, 2019.
359. Naiki, H. and F. Gejyo, *[20] Kinetic analysis of amyloid fibril formation*, in *Methods in enzymology*. 1999, Elsevier. p. 305-318.
360. Rambaran, R.N. and L.C. Serpell, *Amyloid fibrils: abnormal protein assembly*. Prion, 2008. **2**(3): p. 112-117.
361. Aymard, P., et al., *Static and dynamic scattering of β -lactoglobulin aggregates formed after heat-induced denaturation at pH 2*. Macromolecules, 1999. **32**(8): p. 2542-2552.
362. Brännström, K., et al., *The N-terminal region of amyloid β controls the aggregation rate and fibril stability at low pH through a gain of function mechanism*. Journal of the American Chemical Society, 2014. **136**(31): p. 10956-10964.
363. Haass, C., et al., *Targeting of cell-surface β -amyloid precursor protein to lysosomes: alternative processing into amyloid-bearing fragments*. Nature, 1992. **357**(6378): p. 500.
364. Yamazaki, T., E.H. Koo, and D.J. Selkoe, *Trafficking of cell-surface amyloid beta-protein precursor. II. Endocytosis, recycling and lysosomal targeting detected by immunolocalization*. Journal of Cell Science, 1996. **109**(5): p. 999-1008.
365. Morishima-Kawashima, M. and Y. Ihara, *The presence of amyloid β -protein in the detergent-insoluble membrane compartment of human neuroblastoma cells*. Biochemistry, 1998. **37**(44): p. 15247-15253.
366. Ditaranto, K., T.L. Tekirian, and A.J. Yang, *Lysosomal membrane damage in soluble A β -mediated cell death in Alzheimer's disease*. Neurobiology of disease, 2001. **8**(1): p. 19-31.
367. Pasternak, S.H., et al., *Presenilin-1, nicastrin, amyloid precursor protein, and γ -secretase activity are co-localized in the lysosomal membrane*. Journal of Biological Chemistry, 2003. **278**(29): p. 26687-26694.
368. Liu, R.-Q., et al., *Membrane Localization of β -Amyloid 1-42 in Lysosomes A POSSIBLE MECHANISM FOR LYSOSOME LABILIZATION*. Journal of Biological Chemistry, 2010. **285**(26): p. 19986-19996.
369. Grant, S.A., et al., *In vitro and in vivo measurements of fiber optic and electrochemical sensors to monitor brain tissue pH*. Sensors and Actuators B: Chemical, 2001. **72**(2): p. 174-179.
370. Srinivasan, R., et al., *pH-dependent amyloid and protofibril formation by the ABri peptide of familial British dementia*. Journal of molecular biology, 2003. **333**(5): p. 1003-1023.
371. Huang, T.J., et al., *Structural studies of soluble oligomers of the Alzheimer β -amyloid peptide*. Journal of molecular biology, 2000. **297**(1): p. 73-87.

372. Syme, C.D., et al., *Copper Binding to the Amyloid- β (A β) Peptide Associated with Alzheimer's Disease FOLDING, COORDINATION GEOMETRY, pH DEPENDENCE, STOICHIOMETRY, AND AFFINITY OF A β -(1–28): INSIGHTS FROM A RANGE OF COMPLEMENTARY SPECTROSCOPIC TECHNIQUES*. Journal of Biological Chemistry, 2004. **279**(18): p. 18169-18177.
373. Beeg, M., et al., *A modified protocol to prepare seed-free starting solutions of amyloid- β (A β) 1–40 and A β 1–42 from the corresponding depsipeptides*. Analytical biochemistry, 2011. **411**(2): p. 297-299.
374. Maslova, M., L. Gerasimova, and W. Forsling, *Surface properties of cleaved mica*. Colloid Journal, 2004. **66**(3): p. 322-328.
375. Nishimura, S., et al., *Cationic modification of muscovite mica: an electrokinetic study*. Langmuir, 1995. **11**(1): p. 291-295.
376. Jiang, H., et al., *Interaction forces between muscovite and silica surfaces in electrolyte solutions measured with AFM*. Transactions of Nonferrous Metals Society of China, 2013. **23**(6): p. 1783-1788.
377. Sahoo, B., et al., *On the stability of the soluble amyloid aggregates*. Biophysical journal, 2009. **97**(5): p. 1454-1460.
378. Lee, S.J.C., et al., *Towards an understanding of amyloid- β oligomers: characterization, toxicity mechanisms, and inhibitors*. Chemical Society Reviews, 2017. **46**(2): p. 310-323.
379. Meisl, G., et al., *Quantitative analysis of intrinsic and extrinsic factors in the aggregation mechanism of Alzheimer-associated A β -peptide*. Scientific reports, 2016. **6**: p. 18728.
380. Zhu, M., et al., *Surface-catalyzed amyloid fibril formation*. Journal of Biological Chemistry, 2002. **277**(52): p. 50914-50922.
381. Moores, B., et al., *Effect of surfaces on amyloid fibril formation*. PLoS One, 2011. **6**(10): p. e25954.
382. Petkova, A., et al., *Solid state NMR reveals a pH-dependent antiparallel β -sheet registry in fibrils formed by a β -amyloid peptide*. Journal of molecular biology, 2004. **335**(1): p. 247-260.
383. Levine III, H., *Thioflavine T interaction with synthetic Alzheimer's disease β - amyloid peptides: Detection of amyloid aggregation in solution*. Protein Science, 1993. **2**(3): p. 404-410.
384. Simmons, L.K., et al., *Secondary structure of amyloid beta peptide correlates with neurotoxic activity in vitro*. Molecular Pharmacology, 1994. **45**(3): p. 373-379.
385. Serpell, L.C., *Alzheimer's amyloid fibrils: structure and assembly*. Biochimica et Biophysica Acta (BBA)-Molecular Basis of Disease, 2000. **1502**(1): p. 16-30.
386. Thiyagarajan, P., et al., *pH dependent self assembly of β -amyloid (10-35) and β -amyloid (10-35)-PEG3000*. Journal of applied crystallography, 2000. **33**(3): p. 535-539.
387. Fraser, P.E., et al., *pH-dependent structural transitions of Alzheimer amyloid peptides*. Biophysical journal, 1991. **60**(5): p. 1190-1201.
388. Watanabe-Nakayama, T. and K. Ono, *High-speed atomic force microscopy of individual amyloidogenic protein assemblies*, in *Nanoscale Imaging*. 2018, Springer. p. 201-212.
389. Glenner, G.G. and C.W. Wong, *Alzheimer's disease: initial report of the purification and characterization of a novel cerebrovascular amyloid protein*. Biochemical and biophysical research communications, 1984. **120**(3): p. 885-890.
390. Masters, C.L., et al., *Amyloid plaque core protein in Alzheimer disease and Down syndrome*. Proceedings of the National Academy of Sciences, 1985. **82**(12): p. 4245-4249.
391. Pike, C.J., et al., *Neurodegeneration induced by beta-amyloid peptides in vitro: the role of peptide assembly state*. Journal of Neuroscience, 1993. **13**(4): p. 1676-1687.
392. Gong, Y., et al., *Alzheimer's disease-affected brain: presence of oligomeric A β ligands (ADDLs) suggests a molecular basis for reversible memory loss*. Proceedings of the National Academy of Sciences, 2003. **100**(18): p. 10417-10422.
393. Glabe, C.G. and R. Kaye, *Common structure and toxic function of amyloid oligomers implies a common mechanism of pathogenesis*. Neurology, 2006. **66**(1 suppl 1): p. S74-S78.

394. Sakono, M. and T. Zako, *Amyloid oligomers: formation and toxicity of A β oligomers*. The FEBS journal, 2010. **277**(6): p. 1348-1358.
395. Chauhan, A., et al., *Amyloid β -protein stimulates casein kinase I and casein kinase II activities*. Brain research, 1993. **629**(1): p. 47-52.
396. Flajolet, M., et al., *Regulation of Alzheimer's disease amyloid- β formation by casein kinase I*. Proceedings of the National Academy of Sciences, 2007. **104**(10): p. 4159-4164.
397. Lorenzo, A. and B.A. Yankner, *Beta-amyloid neurotoxicity requires fibril formation and is inhibited by congo red*. Proceedings of the National Academy of Sciences, 1994. **91**(25): p. 12243-12247.
398. Ritchie, C.W., et al., *Metal-protein attenuation with iodochlorhydroxyquin (clioquinol) targeting A β amyloid deposition and toxicity in Alzheimer disease: a pilot phase 2 clinical trial*. Archives of neurology, 2003. **60**(12): p. 1685-1691.
399. Blanchard, B.J., et al., *Efficient reversal of Alzheimer's disease fibril formation and elimination of neurotoxicity by a small molecule*. Proceedings of the National Academy of Sciences, 2004. **101**(40): p. 14326-14332.
400. Yang, F., et al., *Curcumin inhibits formation of amyloid β oligomers and fibrils, binds plaques, and reduces amyloid in vivo*. Journal of Biological Chemistry, 2005. **280**(7): p. 5892-5901.
401. Zhu, M., et al., *The flavonoid baicalein inhibits fibrillation of α -synuclein and disaggregates existing fibrils*. Journal of Biological Chemistry, 2004. **279**(26): p. 26846-26857.
402. Heiser, V., et al., *Inhibition of huntingtin fibrillogenesis by specific antibodies and small molecules: implications for Huntington's disease therapy*. Proceedings of the National Academy of Sciences, 2000. **97**(12): p. 6739-6744.
403. Tjernberg, L.O., et al., *Arrest of-amyloid fibril formation by a pentapeptide ligand*. Journal of Biological Chemistry, 1996. **271**(15): p. 8545-8548.
404. Cairo, C.W., et al., *Affinity-based inhibition of β -amyloid toxicity*. Biochemistry, 2002. **41**(27): p. 8620-8629.
405. Soto, C., et al., *β -sheet breaker peptides inhibit fibrillogenesis in a rat brain model of amyloidosis: implications for Alzheimer's therapy*. Nature medicine, 1998. **4**(7): p. 822.
406. Gordon, D.J. and S.C. Meredith, *Probing the role of backbone hydrogen bonding in β -amyloid fibrils with inhibitor peptides containing ester bonds at alternate positions*. Biochemistry, 2003. **42**(2): p. 475-485.
407. Radwan, S.H. and H.M. Azzazy, *Gold nanoparticles for molecular diagnostics*. Expert review of molecular diagnostics, 2009. **9**(5): p. 511-524.
408. Zhang, L. and T.J. Webster, *Nanotechnology and nanomaterials: promises for improved tissue regeneration*. Nano today, 2009. **4**(1): p. 66-80.
409. Sun, X., et al., *Nano-graphene oxide for cellular imaging and drug delivery*. Nano research, 2008. **1**(3): p. 203-212.
410. Menon, J.U., et al., *Nanomaterials for photo-based diagnostic and therapeutic applications*. Theranostics, 2013. **3**(3): p. 152.
411. Ge, C., et al., *Binding of blood proteins to carbon nanotubes reduces cytotoxicity*. Proceedings of the National Academy of Sciences, 2011. **108**(41): p. 16968-16973.
412. Sahni, J.K., et al., *Neurotherapeutic applications of nanoparticles in Alzheimer's disease*. Journal of Controlled Release, 2011. **152**(2): p. 208-231.
413. Li, M., et al., *Self - Assembled Peptide - Polyoxometalate Hybrid Nanospheres: Two in One Enhances Targeted Inhibition of Amyloid β - Peptide Aggregation Associated with Alzheimer's Disease*. Small, 2013. **9**(20): p. 3455-3461.
414. Cabaleiro-Lago, C., et al., *Inhibition of amyloid β protein fibrillation by polymeric nanoparticles*. Journal of the American Chemical Society, 2008. **130**(46): p. 15437-15443.
415. Gazit, E., *Self-assembled peptide nanostructures: the design of molecular building blocks and their technological utilization*. Chemical Society Reviews, 2007. **36**(8): p. 1263-1269.

416. Le Droumaguet, B., et al., *Versatile and efficient targeting using a single nanoparticulate platform: application to cancer and Alzheimer's disease*. ACS nano, 2012. **6**(7): p. 5866-5879.
417. Shaw, C.P., et al., *Amyloid-derived peptide forms self-assembled monolayers on gold nanoparticle with a curvature-dependent β -sheet structure*. ACS nano, 2012. **6**(2): p. 1416-1426.
418. Liao, Y.H., et al., *Negatively Charged Gold Nanoparticles Inhibit Alzheimer's Amyloid - β Fibrillization, Induce Fibril Dissociation, and Mitigate Neurotoxicity*. Small, 2012. **8**(23): p. 3631-3639.
419. Bastús, N.G., et al., *Peptides conjugated to gold nanoparticles induce macrophage activation*. Molecular immunology, 2009. **46**(4): p. 743-748.
420. Zhang, D., et al., *Gold nanoparticles can induce the formation of protein-based aggregates at physiological pH*. Nano letters, 2009. **9**(2): p. 666-671.
421. Skaat, H., et al., *Effect of maghemite nanoparticles on insulin amyloid fibril formation: selective labeling, kinetics, and fibril removal by a magnetic field*. Journal of Biomedical Materials Research Part A: An Official Journal of The Society for Biomaterials, The Japanese Society for Biomaterials, and The Australian Society for Biomaterials and the Korean Society for Biomaterials, 2009. **91**(2): p. 342-351.
422. Skaat, H., G. Belfort, and S. Margel, *Synthesis and characterization of fluorinated magnetic core-shell nanoparticles for inhibition of insulin amyloid fibril formation*. Nanotechnology, 2009. **20**(22): p. 225106.
423. Skaat, H., G. Shafir, and S. Margel, *Acceleration and inhibition of amyloid- β fibril formation by peptide-conjugated fluorescent-maghemite nanoparticles*. Journal of Nanoparticle Research, 2011. **13**(8): p. 3521-3534.
424. Dugan, L.L., et al., *Carboxyfullerenes as neuroprotective agents*. Proceedings of the National Academy of Sciences, 1997. **94**(17): p. 9434-9439.
425. Kim, J.E. and M. Lee, *Fullerene inhibits β -amyloid peptide aggregation*. Biochemical and biophysical research communications, 2003. **303**(2): p. 576-579.
426. Huang, H.-M., et al., *Blockage of amyloid β peptide-induced cytosolic free calcium by fullereneol-1, carboxylate C60 in PC12 cells*. Life Sciences, 2000. **66**(16): p. 1525-1533.
427. Lee, C.-M., et al., *C60 fullerene-pentoxifylline dyad nanoparticles enhance autophagy to avoid cytotoxic effects caused by the β -amyloid peptide*. Nanomedicine: Nanotechnology, Biology and Medicine, 2011. **7**(1): p. 107-114.
428. Li, H., et al., *Carbon nanotube inhibits the formation of β -sheet-rich oligomers of the Alzheimer's amyloid- β (16-22) peptide*. Biophysical journal, 2011. **101**(9): p. 2267-2276.
429. Fu, Z., et al., *Induced β -Barrel Formation of the Alzheimer's A β 25-35 Oligomers on Carbon Nanotube Surfaces: Implication for Amyloid Fibril Inhibition*. Biophysical journal, 2009. **97**(6): p. 1795-1803.
430. Jana, A.K. and N. Sengupta, *Adsorption Mechanism and Collapse Propensities of the Full-Length, Monomeric A β 1-42 on the Surface of a Single-Walled Carbon Nanotube: A Molecular Dynamics Simulation Study*. Biophysical journal, 2012. **102**(8): p. 1889-1896.
431. Triulzi, R.C., et al., *Photothermal ablation of amyloid aggregates by gold nanoparticles*. Colloids and Surfaces B: Biointerfaces, 2008. **63**(2): p. 200-208.
432. Araya, E., et al., *Gold nanoparticles and microwave irradiation inhibit beta-amyloid amyloidogenesis*. Nanoscale research letters, 2008. **3**(11): p. 435.
433. Kogan, M.J., et al., *Nanoparticle-mediated local and remote manipulation of protein aggregation*. Nano letters, 2006. **6**(1): p. 110-115.
434. Majzik, A., et al., *Functionalization of gold nanoparticles with amino acid, β -amyloid peptides and fragment*. Colloids and Surfaces B: Biointerfaces, 2010. **81**(1): p. 235-241.
435. Yoo, S.I., et al., *Inhibition of amyloid peptide fibrillation by inorganic nanoparticles: functional similarities with proteins*. Angewandte Chemie International Edition, 2011. **50**(22): p. 5110-5115.

436. Palmal, S., et al., *Inhibition of amyloid fibril growth and dissolution of amyloid fibrils by curcumin–gold nanoparticles*. Chemistry–A European Journal, 2014. **20**(20): p. 6184-6191.
437. Gao, N., et al., *Gold - Nanoparticle - Based Multifunctional Amyloid - β Inhibitor against Alzheimer ' s Disease*. Chemistry - A European Journal, 2015. **21**(2): p. 829-835.
438. Pai, A.S., I. Rubinstein, and H. Önyüksel, *PEGylated phospholipid nanomicelles interact with β -amyloid (1–42) and mitigate its β -sheet formation, aggregation and neurotoxicity in vitro*. Peptides, 2006. **27**(11): p. 2858-2866.
439. Rocha, S., et al., *Influence of fluorinated and hydrogenated nanoparticles on the structure and fibrillogenesis of amyloid beta-peptide*. Biophysical chemistry, 2008. **137**(1): p. 35-42.
440. Wu, W.-h., et al., *TiO₂ nanoparticles promote β -amyloid fibrillation in vitro*. Biochemical and biophysical research communications, 2008. **373**(2): p. 315-318.
441. Qu, Z.G., et al., *Advances in the understanding of nanomaterial–biomembrane interactions and their mathematical and numerical modeling*. Nanomedicine, 2013. **8**(6): p. 995-1011.
442. Mills, Z.G., W. Mao, and A. Alexeev, *Mesoscale modeling: solving complex flows in biology and biotechnology*. Trends in biotechnology, 2013. **31**(7): p. 426-434.
443. Ding, H.-m. and Y.-q. Ma, *Computer simulation of the role of protein corona in cellular delivery of nanoparticles*. Biomaterials, 2014. **35**(30): p. 8703-8710.
444. Radic, S., et al., *Contrasting effects of nanoparticle–protein attraction on amyloid aggregation*. RSC advances, 2015. **5**(127): p. 105489-105498.
445. Knowles, B.R., et al., *Carboxybetaine functionalized nanosilicas as protein resistant surface coatings*. Biointerphases, 2020. **15**(1): p. 011001.
446. Knowles, B.R., et al., *Zwitterion functionalized silica nanoparticle coatings: The effect of particle size on protein, bacteria, and fungal spore adhesion*. Langmuir, 2018. **35**(5): p. 1335-1345.
447. Magonov, S., V. Elings, and M.-H. Whangbo, *Phase imaging and stiffness in tapping-mode atomic force microscopy*. Surface science, 1997. **375**(2-3): p. L385-L391.
448. Mun, E.A., et al., *On the role of specific interactions in the diffusion of nanoparticles in aqueous polymer solutions*. Langmuir, 2013. **30**(1): p. 308-317.
449. Mansfield, E.D., et al., *POZylation: a new approach to enhance nanoparticle diffusion through mucosal barriers*. Nanoscale, 2015. **7**(32): p. 13671-13679.
450. Petrie, E., *Adhesive bonding of textiles: principles, types of adhesive and methods of use, in Joining Textiles*. 2013, Elsevier. p. 225-274.
451. Frieden, C., *Protein aggregation processes: in search of the mechanism*. Protein Science, 2007. **16**(11): p. 2334-2344.
452. Ferrone, F.A., et al., *Kinetic studies on photolysis-induced gelation of sickle cell hemoglobin suggest a new mechanism*. Biophysical journal, 1980. **32**(1): p. 361-380.
453. Hock, C., et al., *Antibodies against β -amyloid slow cognitive decline in Alzheimer's disease*. Neuron, 2003. **38**(4): p. 547-554.
454. Sevigny, J., et al., *The antibody aducanumab reduces A β plaques in Alzheimer's disease*. Nature, 2016. **537**(7618): p. 50-56.
455. Wang, J., et al., *Dimensionality of carbon nanomaterial impacting on the modulation of amyloid peptide assembly*. Nanotechnology, 2016. **27**(30): p. 304001.
456. Wang, J., et al., *Size effect of graphene oxide on modulating amyloid peptide assembly*. Chemistry–A European Journal, 2015. **21**(27): p. 9632-9637.
457. Li, C. and R. Mezzenga, *The interplay between carbon nanomaterials and amyloid fibrils in bio-nanotechnology*. Nanoscale, 2013. **5**(14): p. 6207-6218.